CLEANING VISCOPLASTIC SOIL LAYERS FROM FLAT SURFACES USING IMPINGING WATER JETS

Rubens Rosario Fernandes

Department of Chemical Engineering and Biotechnology

University of Cambridge

This thesis is submitted for the degree of

Doctor of Philosophy

St John's College *January 2021*

DECLARATION

This thesis is the result of my own work and includes nothing which is the outcome of work done in collaboration except as declared in the Preface and specified in the text. It is not substantially the same as any that I have submitted, or, is being concurrently submitted for a degree or diploma or other qualification at the University of Cambridge or any other University or similar institution. I further state that no substantial part of my thesis has already been submitted, or, is being concurrently submitted for any such degree, diploma or other qualification at the University of Cambridge or any other University or similar institution. It does not exceed the prescribed word limit for the Engineering Degree Committee.

Rubens Rosario Fernandes

Cambridge, UK - January 2021.

ABSTRACT

Title: *Cleaning viscoplastic soil layers from flat surfaces using impinging water jets.*
Name: *Rubens Rosario Fernandes*

Impinging liquid jets are widely used in industry to clean unwanted soil layers from the internal walls of storage tanks and mixing vessels. Viscoplastic layers are common in a wide range of industrial applications and are challenging to clean due to their yield stress behaviour. When a stationary coherent turbulent perpendicular liquid jet impinges on a flat soiled surface, it generates a roughly circular cleaned region that grows over time.

In this work, different insoluble viscoplastic materials such as petroleum jellies and a white soft paraffin were cleaned by impinging water jets. The rheological investigation of the soil layers indicated that these materials show time-dependent yield stress behaviour. A method to measure the yield stress of soil layers *in-situ* using a blade-scraping device was developed and shown to provide reasonable estimates of the yield stress of different industrial ointments, household items and food spreads. Two distinct regimes were observed in cleaning experiments by impinging jets: for thin soil layers, the liquid film pushed the soil layer radially outwards in a momentum-driven flow. For very thin soil layers, the liquid film flowed over the soil layer. The transition between these two regimes is related to the relative thickness of the liquid film to the soil layer.

A phenomenological model was proposed to describe the transition from fast, momentum-driven to slow, creep-dominated cleaning of thin soil layers, and provided good agreement with experimental results. It required the fitting of a kinetic constant to experimental data to describe the initial fast growth of the cleaned radius close to the impinging point. A detailed model was also developed based on the rate of viscous dissipation in a shallow wedge of material at the cleaning front, which explains the kinetic parameter used in previous models in the literature in terms of measurable quantities, including the rheology of the soil. A shear-driven model was also proposed to describe the cleaning of very thin soil layers. This model gave inconsistent results when compared to experiments, and it is proposed that this results from the model not coupling the flow between the soil layer and the liquid film.

Cleaning viscoplastic soil layers form flat surfaces using impinging water jets – Rubens Rosario Fernandes –January 2021

I would like to dedicate this thesis to Gabi, who has been by my side during happy and difficult times, and to the memory of my grandmother Antonia, who is watching over me from heaven.

The more I study nature, the more I stand amazed at the work of the Creator.

Louis Pasteur

LIST OF PUBLICATIONS

Published journal papers

Fernandes, R. R. & Wilson, D. I. (2020). Modelling the cleaning of viscoplastic layers by impinging coherent turbulent water jets. *J. Non-Newton. Fluid Mech*., **282**, 104314.

Tsai, J. H., Fernandes, R. R. & Wilson, D. I. (2020). Measurements and modelling of the 'millimanipulation' device to study the removal of soft solid layers from solid substrates. *J. Food Eng.,* **285**, 110086.

Fernandes, R. R., Oevermann, D., & Wilson, D. I. (2019). Cleaning insoluble viscoplastic soil layers using static and moving coherent impinging water jets. *Chem. Eng. Sci*., **207**, 752–768.

Yang, J., Bhagat, R. K., Fernandes, R. R., Nordkvist, M., Gernaey, K. V., Krühne, U., & Wilson, D. I. (2019). Cleaning of toothpaste from vessel walls by impinging liquid jets and their falling films: Quantitative modelling of soaking effects. *Chem. Eng. Sci*., **208** (8), 115148.

Oevermann, D., Bhagat, R. K., Fernandes, R. R. & Wilson, D. I. (2019). Quantitative modelling of the erosive removal of a thin soil deposit by impinging liquid jets. *Wear*, **422–423**, 27–34.

Fernandes, R. R., Suleiman, N. B., & Wilson, D. I. *In-situ* measurement of the critical stress of viscoplastic soil layers. (2021) *J. Food Eng.*, **303**, 110668.

Meza, B. E., Fernandes, R. R., Zorrilla, S. E, Wilson, D. I., Peralta, J. M. (2021). Rheological characterisation of full-fat and reduced-fat aerated icings. Submitted to: *LWT,* **142**, 111014.

Conference proceeding

Fernandes, R. R.; Tsai, J-H.; Suleiman, N. B. & Wilson, D. I. Use of a blade scraping device to estimate the yield stress of viscoplastic soil layers. In: *British Society of Rheology mid-winter meeting*, 2021, online conference.

Fernandes, R. R.; Tsai, J-H.; Suleiman, N. B. & Wilson, D. I. *In situ* measurement of the yield stress of viscoplastic fouling and soil layers. In: *18th International Congress on Rheology*, 2020, Rio de Janeiro, Brazil.

Fernandes, R. R. & Wilson, D.I. Modelling the cleaning of a yield stress soil by impinging water jets. In: Viscoplastic Fluids: From Theory to Application 2019, Cambridge, UK.

Wilson, D.I.; Fernandes, R. R.; Tan, X. S. & Wong, E. J. Elucidating studies of purging viscoplastic fluid from pipes. In: Viscoplastic Fluids: From Theory to Application 2019, Cambridge, UK.

Fernandes, R. R. & Wilson, D.I. . Cleaning viscoplastic soil layers with impinging water jets. In: CEB Research Conference, 2019, Cambridge, UK.

Bhagat, R. K.; Chee, M. W. L.; Ahuja, T. V.; Wingmore, R. L.; Taesopapong, N.; Fernandes, R. R.; Wilson, D. I. Effect of jet length and surface curvature on cleaning of tank walls. In: *Fouling and Cleaning in Food Processing*, 2018, Lund, Sweden.

Bhagat, R.K., Hunter, S.N., Mace F.C.M., Fernandes, R.R., and Wilson D.I., 2018. Cleaning tanks by impinging liquid jets, *Chemeca 2018*, Queenstown, New Zealand.

ACKNOWLEDGEMENTS

This thesis is one of the last steps of my amazing PhD journey that started back in October 2017. None of this would be possible without the mentorship and supervision of Prof D. Ian Wilson. I could not ask for a better supervisor. You inspire me with your creativity, physical intuition, enthusiasm and resilience. I am always learning with you, and your patience and encouragement in every meeting, lunch or tea break were extremely important to me. Thank you so much for allowing me to be your student: I will never forget this experience.

I would also like to thank the trust that my supervisor has put in me by allowing me to co-supervise some research projects during my PhD and to work in collaboration with my colleagues. A special acknowledgement should be given to Dirk Oevermann, who performed some of the moving jet experiments reported in Chapter 5. Also, I would like to acknowledge Dr Bart Hallmark and Dr Chris Ness, who trusted me to supervise the Rheology and Processing module.

I am also grateful for the support of all the staff in the Department of Chemical Engineering and Biotechnology. A special thanks to Dr Simon Butler, who provided me with access to many of the tools and devices used in this thesis, and to the mechanical and electronics workshop crew who helped me so many times. The safety team has also done a great job in arranging a safe return to work after the COVID-19 lockdown.

I have received my funding from the *Coordenação de Aperfeiçoamento de Pessoal de Ensino Superior* (CAPES), through the finance code 001, process number 88881.128591/2016-01. I am deeply grateful that my home country invested in my education, and I hope I can help Brazil to develop its science, engineering and technology. I have also received some financial support from St John's College, and I am very grateful for this. A special recognition should also be made to the rheology team at the Federal University of Technology – Parana in my hometown Curitiba, where I learned about rheology and gave my first steps in scientific research before starting my PhD.

I also would like to express my gratitude to all my friends who have been by my side, physically and virtually, during these challenging years. I will list you guys in alphabetical order, so I can rely on a neutral criterion to avoid any trouble. Ana, Anastasia, Cris, Dabwan, George, Harry, Honeyfer, Jamie, Janaki, Jheng-Han, Jenny, Karthik, Lucas, Luis, Melissa, Michael, Pedro, Petar, Rajesh, Ru and Saksham: you are the best! I already miss drinking tea

and eating cake with you guys during our breaks, and the trips to the cinema to watch every single superhero movie. The support of my Brazilian friends, Bruna, Carlos *Gaúcho*, Diogo, Luiz Felipe, Mauro and Tainan during this last challenging year under lockdown has also been extremely important for me. Our video chats have kept me going during the quarantine, and I want you to know that I admire each one of you.

I could not end this section without the most important acknowledgement. I thank and praise the Lord for His wonderful creation, which keeps us scientists busy trying to unveil so many mysteries. I am grateful that His plans for me included doing a PhD, and I hope I can honour Him with my work. I also would like to thank the love, support and companionship of my beautiful wife Gabi, to whom this thesis is dedicated. You supported me since I decided to apply for the PhD, and these last three years have been so much fun having you by my side. I love you, and I want you to know that getting married to you is the best thing that ever happened to me. The love, support and encouragement from my mother Rita, from my father Japiaçú and my brother César were also extremely important for me. I love you so much, and I hope to see you three again soon.

CONTENTS

LIST OF FIGURES

LIST OF TABLES

LIST OF SYMBOLS AND ACRONYMS

Latin symbols

Symbol	Unit	Description
a	[m]	Radial location of the cleaning front
A	[-]	Lumped parameter
a_{o}^{*}	[-]	Dimensionless initial cleaned radius, weak soil model
a_{BP}	[-]	Parameter, Bingham viscous dissipation model
a_{HB}	[-]	Parameter, Herschel-Bulkley viscous dissipation model
$a_{\max}$	[m]	Asymptotic cleaned radius
a_{o}^{+}	[-]	Dimensionless initial cleaned radius, strong soil model
A_{r}	[m^2]	Area of the cleaned region
a_{s}^{+}	[-]	Dimensionless cleaned radius, strong soil model
a_{w}^{*}	[-]	Dimensionless cleaned radius, weak soil model
a_{x}	[m]	Distance from point of reference to cleaning front, moving nozzle
B	[m^{-3}]	Lumped parameter
b_{BP}	[-]	Parameter, Bingham viscous dissipation model
b_{HB}	[-]	Parameter, Herschel-Bulkley viscous dissipation model
b_{MM}	[m]	Length of the accumulated berm, millimanipulation device
c	[$kg^2 \cdot m^{-4} \cdot s^{-1}$]	Lumped parameter ($c = 10\pi^2\rho\mu/3$)
C_1	[-]	Lumped parameter, Eq. (6.74)
C_{i}	[-]	Circularity
d_{N}	[m]	Nozzle diameter
$\dot{E}_{\mathrm{k}}$	[$W \cdot m^{-1}$]	Rate of flow of kinetic energy in the liquid film per unit width
$\dot{E}_{\mathrm{k}'}$	[W]	Rate of flow of kinetic energy in the liquid film
F_{C}	[$N \cdot m^{-1}$]	Critical force per unit of width of the blade, millimanipulation
f_{c}	[-]	Fraction of the jet flow rate that flows in the draining film
$F_{\mathrm{C}'}$	[$N \cdot m^{-1}$]	Critical force per unit of width of the blade, millimanipulation
F_{D}	[$N \cdot m^{-1}$]	Critical force per unit of width of the blade, millimanipulation
F_{w}	[$N \cdot m^{-1}$]	Force per unit width
F_{z}	[N]	Normal force
G	[Pa]	Shear elastic modulus
G'	[Pa]	Elastic modulus
G''	[Pa]	Viscous modulus
H	[m]	Height of the accumulated berm
h	[m]	Thickness of the liquid film
H_{blade}	[m]	Length of the vane tool

h_{MM}	[m]	Height of the accumulated berm, millimanipulation device
h_{Nu}	[m]	Thickness of the liquid film, Nusselt falling film
h_{Ka}	[m]	Thickness of the liquid film, Kapitza falling film
h_{p}	[m]	Thickness of the liquid film at the point of reference P, moving nozzle
$\bar{h}_{\mathrm{Pl}}$	[m]	Space averaged liquid film thickness over a circular plate
h_{plate}	[m]	Gap between parallel plates
$\boldsymbol{I}$	[-]	Identity tensor
k	[ ]	Cleaning rate constant, not defined
k'	[m·s·kg^{-1}]	Lumped cleaning rate constant
k'_{B}	[m·s·kg^{-1}]	Cleaning rate constant, Bingham viscous dissipation model
k'_{BP}	[m·s·kg^{-1}]	Cleaning rate constant, Bingham viscous dissipation model with power-law approximation
k'_{ϕ}	[m·s·kg^{-1}]	Cleaning rate constant, Bingham viscous dissipation model with dissipation along the berm
k'_{R}	[m·s·kg^{-1}]	Cleaning rate constant, Bingham viscous dissipation model with dissipation along the accumulated berm
k_{HB}	[Pa · s$^{n_{\mathrm{HB}}}$]	Consistency index, Herschel-Bulkley fluid
k_{PL}	[Pa · s$^{n_{\mathrm{PL}}}$]	Consistency index, power-law fluid
l	[m]	Distance measured from the base of the accumulated berm
L	[m]	Stand-off distance between nozzle and substrate
M	[N·m^{-1}]	Momentum flow rate per unit of circumferential width
m	[kg]	Mass
$\dot{m}$	[kg·s^{-1}]	Mass flow rate
m_{HB}	[-]	Inverse of the Herschel-Bulkley exponent, $m_{\mathrm{HB}} = n_{\mathrm{HB}}^{-1}$
m_{PL}	[-]	Inverse of the power-law exponent, $m_{\mathrm{PL}} = n_{\mathrm{PL}}^{-1}$
M_{X}	[N·m^{-1}]	Momentum flow rate per unit length of the liquid film at a_{X}, moving nozzle.
M_{y}	[N·m^{-1}]	Momentum flow rate required to yield the soil layer
$M_{\mathrm{y,B}}$	[N·m^{-1}]	Momentum flow rate required to yield the soil layer, Bingham viscous dissipation model
$M_{\mathrm{y,BP}}$	[N·m^{-1}]	Momentum flow rate required to yield the soil layer, Bingham viscous dissipation model with power-law approximation
$M_{\mathrm{y},\phi}$	[N·m^{-1}]	Momentum flow rate required to yield the soil layer, Bingham viscous dissipation model with dissipation along the berm
$M_{\mathrm{y,R}}$	[N·m^{-1}]	Momentum flow rate required to yield the soil layer, Bingham viscous dissipation model with dissipation along the accumulated berm
n	[-]	Exponent
N_1	[Pa]	First normal stress difference
N_2	[Pa]	Second normal stress difference
n_{HB}	[-]	Exponent, Herschel-Bulkley fluid
n_{PL}	[-]	Exponent, power-law fluid

p	[m]	Distance from point of reference, moving nozzle
P	[N·m^2]	Pressure
p^*	[-]	Non-dimensional distance from point of reference, moving nozzle
P_e	[m]	Perimeter
Q	[m^3·s^{-1}]	Volumetric flow rate
Q_D	[W·m^{-1}]	Power per unit of width consumed by viscous dissipation
$Q_{\mathrm{D}'}$	[W]	Power consumed by viscous dissipation
t	[s]	Time
r	[m]	Radial co-ordinate, cylindrical system
r_b	[m]	Boundary-layer zone radius
R_blade	[m]	Radius of the vane tool
R_cone	[m]	Radius of the cone
R_cup	[m]	Radius of the cup, vane tool
r_j	[m]	Radius of the hydraulic jump
r_o	[m]	Radius of the nozzle ($r_\mathrm{o} = d_\mathrm{N}/2$)
r_p	[m]	Radial distance from point of reference P
R_pl	[m]	Radius of a circular plate used by Yeckel and Middleman (1987)
R_plate	[m]	Radius of the plate
r_t	[-]	Turbulent transition radius
r_w	[m]	Radius of the plate used by Yeckel and Middleman (1987)
$\mathcal{T}$	[N·m]	Torque
$t_\mathrm{c,strong}$	[s]	Dimensionless timescale, strong soil model
$t_\mathrm{c,weak}$	[s]	Dimensionless timescale, weak soil model
t_ct	[s]	Characteristic time scale, creep experiments
t_i	[s]	Time when a cleaned radius is first detected
t_s^+	[-]	Dimensionless time, strong soil model
$t_{YM}^\star$	[-]	Dimensionless time used by Yeckel and Middleman (1987)
U	[m·s^{-1}]	Average velocity
u	[m·s^{-1}]	Local velocity
u_c	[m·s^{-1}]	Critical local velocity
U_o	[m·s^{-1}]	Average velocity of the jet
u_s	[m·s^{-1}]	Surface velocity
u_so	[m·s^{-1}]	Local velocity of the soil in the radial direction
v_so	[m·s^{-1}]	Local velocity of the soil in the z-direction
V_bl	[m·s^{-1}]	Velocity of the moving blade, millimanipulation device
v_jet	[m·s^{-1}]	Nozzle traversing velocity
W	[m]	Width of the falling film
w_c	[m]	Width of the cleaned region, moving nozzle
w_c^*	[-]	Non-dimensional width of the cleaned region, moving nozzle
x	[m]	Co-ordinate, Cartesian system
x^*	[-]	Non-dimensional co-ordinate, Cartesian system
x_{δ_o}	[m]	Position along the x axis in which $\delta = \delta_\mathrm{o}$

x_{E}	[m]	x-coordinate of the apex of the accumulated berm
x_{L}	[m]	Position where $\delta = h$, viscous dissipation model
x_{T}	[m]	Position where $\tau_{\mathrm{w}}^{*} = 1$, viscous dissipation model
y	[m]	Co-ordinate, Cartesian system
y^{*}	[-]	Non-dimensional co-ordinate, Cartesian system
z	[m]	Normal co-ordinate, cylindrical system

Greek symbols

α	[$m^5 \cdot s^{-1}$]	Lumped parameter ($\alpha = 3\dot{m}^3/5\pi c$)
β	[rad]	Azimuthal angle, reference frame for moving nozzle
χ	[rad]	Inclination of the wedge-shaped cleaning front
χ	[rad]	Angle of the wedge-shaped cleaning front
δ	[m]	Thickness of the soil layer
δ_{bl}	[m]	Thickness of the boundary layer
δ_{i}	[m]	Thickness of the residual layer
δ_{o}	[m]	Thickness of the undisturbed layer
δ_{ph}	[rad]	Phase angle
$\bar{\delta}_{\mathrm{YM}}^{*}$	[-]	Nondimensional average soil layer thickness, Yeckel and Middleman (1987)
η	[Pa·s]	Apparent viscosity
η_{e}	[-]	Energy efficiency of the cleaning process
γ	[-]	Shear strain
Γ	[$m^2 \cdot s$]	Volumetric flow rate of soil per unit of circumferential width
$\dot{\gamma}$	[s^{-1}]	Shear rate
$\dot{\gamma}_{\mathrm{ch}}$	[s^{-1}]	Characteristic shear rate, millimanipulation
γ_{a}	[-]	Shear strain amplitude
γ_{st}	[$N \cdot m^{-1}$]	Surface tension
κ	[m^{-1}]	Surface curvature
μ	[Pa·s]	Newtonian viscosity
μ_{B}	[$Pa \cdot s^{-1}$]	Bingham viscosity
μ_{so}	[Pa·s]	Viscosity of Newtonian soil
ν	[$m^2 \cdot s^{-1}$]	Kinematic viscosity
ϕ	[rad]	Angle of the cleaning front
ϕ_{o}	[rad]	Slope of the rim for $\delta > h$
ϕ_1	[rad]	Slope measured at the base of the rim
ϕ_2	[rad]	Slope measured at the initial layer height
ϕ_{MM}	[rad]	Cutting angle, millimanipulation
ϕ_{SD}	[rad]	Slope of the soil layer profile, shear-driven model
$\boldsymbol{\Pi}$	[Pa]	Total stress tensor
ψ	[rad]	Inclination angle of the jet
ρ	[$kg \cdot m^{-3}$]	Density of the liquid
σ	[$kg \cdot m \cdot s^{-2}$]	Lumped parameter: $\sigma = 3\dot{m}U_{\mathrm{o}}/5\pi$
τ	[Pa]	Shear stress
$\boldsymbol{\tau}$	[Pa]	Extra stress tensor
τ_{a}	[Pa]	Shear stress amplitude
τ_{c}	[Pa]	Critical stress

$\tau_{c,d}$	[Pa]	Dynamic critical stress
$\tau_{c,s}$	[Pa]	Static critical stress
τ_{el}	[Pa]	Elastic limit shear stress
τ_{ij}	[Pa]	Components of the stress tensor
τ_{int}	[Pa]	Shear stress at the interface between the liquid film and the soil layer
τ_r	[rad]	Residual shear stress
τ_{st}	[Pa]	Critical stress, stress steps
τ_{rp}	[Pa]	Critical stress, stress ramps
τ_{cr}	[Pa]	Critical stress, oscillatory stress amplitude sweeps
τ_w	[Pa]	Local wall shear stress within the soil rim
$\tau_{w,l}$	[Pa]	Liquid film wall shear stress in the RFZ
τ_x	[Pa]	Crossover stress
τ_y	[Pa]	Yield stress
τ_y^{e1}	[Pa]	First estimate of the yield stress, millimanipulation
τ_y^{e2}	[Pa]	Second estimate of the yield stress, millimanipulation
τ_y^{e3}	[Pa]	Third estimate of the yield stress, millimanipulation
τ_{zr}	[Pa]	Shear stress in the radial direction
θ	[rad]	Azimuthal angle
$\dot{\theta}$	[rad·s^{-1}]	Azimuthal angular velocity
ξ	[rad]	Contact angle
ξ_{cone}	[rad]	Angle of the cone-plate tool

Dimensionless groups

Bn	[-]	Approximate Bingham number: $Bn = \tau_y^{e3}/\left(\tau_y^{e1} - \tau_y^{e3}\right)$
Oh	[-]	Ohnesorge number: $Oh = \mu/\sqrt{\rho_L d_N \gamma_{ST}}$
Re_j	[-]	Jet Reynolds number ($Re_j = \rho U_o d_N/\mu$)
We_A	[-]	Weber number for air, $We_A = \rho_A U^2 d_N/\gamma_{st}$
We_L	[-]	Weber number for liquid, $We_L = \rho_L U^2 d_N/\gamma_{st}$

Acronyms

CIP	Cleaning-in-place
COP	Cleaning out-of-place
FDG	Fluid Dynamic Gauging
FMCG	Fast-moving consumer goods
fps	Frames per second
HB	Herschel-Bulkley
HSV	Hue, Saturation and Value
LHS	Left-hand side
PJA	Petroleum jelly, Atom Scientific
PJS	Petroleum jelly, Sasol
PJT	Petroleum jelly, Trilanco
PMMA	Poly(methyl methacrylate)
PVA	Polyvinyl acetate

RFZ	Radial flow zone
RGB	Red, Green and Blue
RHS	Right-hand side
WSP	White soft paraffin

1 Introduction

1.1 Context

Manufacturing fast-moving consumer goods (FMCG) such as foods, beverages, health care products and cosmetics involves mixing these products in a range of vessels, storing in tanks and pumping through pipelines. This can lead to soiling, *i.e.*, the build-up of deposit layers on solid surfaces (Fryer *et al.*, 2006). These layers can affect the efficiency of heat exchangers (Goode *et al.*, 2013), increase the pressure drop in pipelines (Trinh *et al.*, 2017) and lead to cross-contamination between batches (Lelieveld, 2014). This is particularly troublesome for food and pharmaceutical products, where high levels of hygiene are required due to sanitary regulations (Lelieveld, 2014), allergen control (Ward, 2014) and product purity requirements. Decontamination of soiled surfaces is also important for nuclear (McGuire, 1985), biomedical (Grower & Bhaskar, 1972; Park *et al.*, 2015), mining (Kuyumcu & Rolf, 2004), aerospace (Thomas *et al.*, 1996) and defence (Dragolici & Dragolici, 2014) applications. More recently, the effective decontamination of surfaces has become the topic of increasing attention due to the transmission of the SARS-CoV-2 virus through infected surfaces (Malone *et al.*, 2020; Ong *et al.*, 2020; Santarpia *et al.*, 2020).

The cleaning of surfaces is a widespread industrial challenge, and this is often performed with liquids. For confined geometries, such as in pipelines and ducts, it is often possible to recirculate a cleaning solution at a high flow rate, which promotes the detachment of residues from the walls (Palabiyik *et al.*, 2014, 2018; Alba & Frigaard, 2016). Open surfaces, on the other hand, represent a different engineering challenge. Cleaning methods in these cases may involve delivering the cleaning fluid as a falling film (Fuchs *et al.*, 2015), as a spray (Gould, 2003) or by an impinging liquid jet: the latter is the subject of this dissertation. Some examples of cleaning with impinging jets in different scenarios are shown in Figure 1.1.

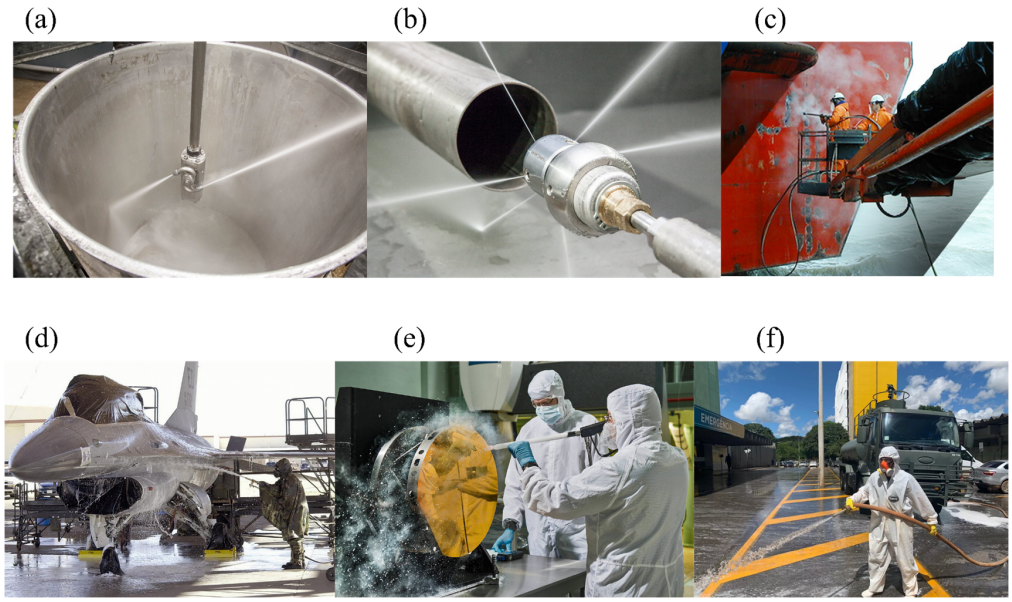

Figure 1.1 – Examples of cleaning and decontamination using impinging jets. (a) Liquid jets impinging on the inner walls of a dairy processing tank (Hammelmann, 2020); (b) Device for sewage pipe cleaning (Hammelmann, 2020); (c) Removal of fouling from a ship hull (SMCjet, 2020); (d) Decontamination of a military aircraft (F-16.net, 2020); (e) cleaning of a gold-coated mirror used in the James Webb Space Telescope with a carbon dioxide spray (NASA, 2015) and (f) washing of a Brazilian street during the COVID-19 pandemic (Globo News, 2020).

Water is widely used, from household chores such as dishwashing and bathroom surface cleaning to industrial applications. According to the Energy Saving Trust (2014), approximately 70% of British household water consumption is employed for cleaning and sanitary applications, including washing machines, dishwashing, as well as bath, shower and toilet use. The average UK per capita water usage is approximately 141 litres of water/day (Wildfowl & Wetlands Trust, 2019), and an estimated 2.4 billion m^3 of water is used annually on household cleaning alone. Cleaning is also responsible for up to 70% of the water consumption in the UK food and beverage manufacturing sectors (IChemE, 2014). Understanding the cleaning mechanisms involved is needed to improve the sustainability of manufacturing operations and the design of household cleaning devices such as dishwashers.

1.2 COP vs CIP

In food and consumer goods processing plants, cleaning out-of-place (COP) is performed by disassembling the production line and taking the soiled components to a cleaning station (Lelieveld, 2014). These operations often involve manual removal of the soil layers by scraping the surfaces with brushes, using high-pressure liquid jets or by submerging the

components in a bath of cleaning solution. Disassembly leads to long production downtimes. Also, in cases where contamination is critical to the quality of the final product, such as in the food and pharmaceutical industries, disassembly introduces an additional risk of contamination from external agents (Wilson, 2005). Cleaning-in-place (CIP) operations are those where cleaning is performed without dismantling the plant, meaning that they can be more easily automated. An example of CIP operation is the regular cleaning of dairy pasteurisation units (Van Asselt *et al.*, 2002).

Unwanted layers of residues also accumulate on the inner walls of processing tanks and vessels. Cleaning these soil layers is a challenging task, as large volumes of cleaning solution are usually required to ensure adequate coverage of the walls. *Fill and soak* methods consist of filling the vessel with a cleaning solution and leaving it for some time (Hui *et al.*, 2003): removal involves diffusion of the cleaning solution into the soil and of the softened soil into the bulk solution. This is a time-consuming method that requires large volumes of liquid. Water is a limited natural resource, and the development of more efficient cleaning strategies is important from both the financial and environmental points of view. An alternative approach for open surface cleaning is to deliver the cleaning solution in the form of an impinging jet so that cleaning is enhanced by the hydraulic action of the liquid. This process can be automated by using spray balls and rotating nozzles, as shown in Figure 1.2, which deliver the liquid across the tank walls.

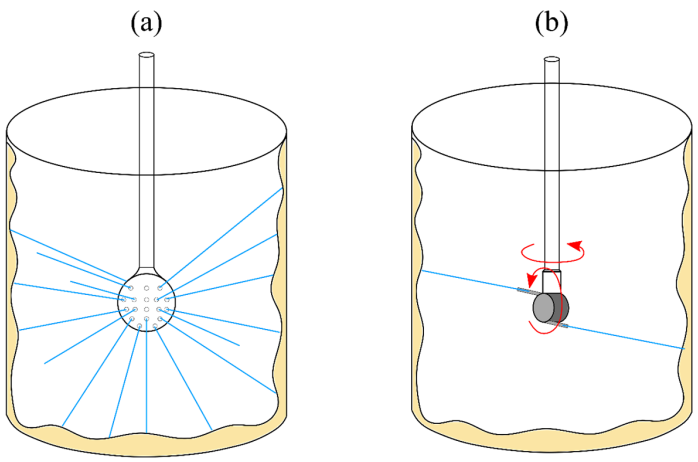

Figure 1.2 - Schematic of (a) spray ball and (b) rotary jet cleaning of tank walls. The liquid is directed onto the inner walls of the tank, which are coated with an unwanted soil layer.

1.3 Factors that affect cleaning: Sinner's circle

Hygienic design involves a balance between the forces responsible for cleaning the layer and the time of exposure to the cleaning solution. The factors determining cleaning efficiency are time, temperature, chemical and mechanical action. This is schematically represented by the Sinner's circle (Basso *et al.*, 2017), Figure 1.3, which was proposed by Herbert Sinner, a German engineer working for the detergent supplier Henkel in 1959 (Duisterwinkel, 2010).

Cleaning operations often employ a combination of the four factors present in the Sinner's circle. Fryer *et al.* (2009) carefully outlined cleaning operations in which temperature, chemical and mechanical action impact the cleaning time. In general, soil removal rates increase with the increase in temperature, as quantified by Bourne and Jennings (1963a, 1963b) during the removal of organic fats from pipelines. Cleaning efficiency can also be enhanced if the soil chemically reacts with the cleaning fluid, such as when whey protein residues are cleaned with water: swelling (Saikhwan *et al.*, 2010; Joppa *et al.*, 2020) and dissolution (Fickak *et al.*, 2011) of the soil contribute to faster cleaning operations. Finally, the mechanical action in the form of a bulk liquid flow can significantly increase cleaning rates. This can result from the liquid promoting erosive mechanisms when strong, cohesive soils are removed such as the dry residues investigated by Kaye *et al.* (1995). It can also result from relocation of the soil, such as during the removal of oil layers with water jets (Yeckel & Middleman, 1987; Yeckel *et al.*, 1990), or from convective mass transfer, such as observed in the removal of reactive contaminants from cracks (Chilukuri & Middleman, 1984) and cavities (Fang, 2003).

These cleaning scenarios are all industrially relevant, but the effects of temperature and chemical reactions significantly increase the complexity of a quantitative analysis from the point of view of modelling these operations. Modelling often requires simplifying assumptions, and the choice of an appropriate cleaning scenario in which the effects of temperature and chemical reactions are not strong when compared to the effects of mechanical action can be an interesting object of study in fluid mechanics.

The cleaning of soiled surfaces using impinging jets is an example of an operation in which the mechanical action plays a major role in the cleaning operation along with time. Depending on the soil and cleaning solution, temperature and chemical action can also be important. For instance, cleaning fat-based materials can be quicker if the temperature of the

liquid is high enough to promote melting of the soil and if surfactants are present in the cleaning solution.

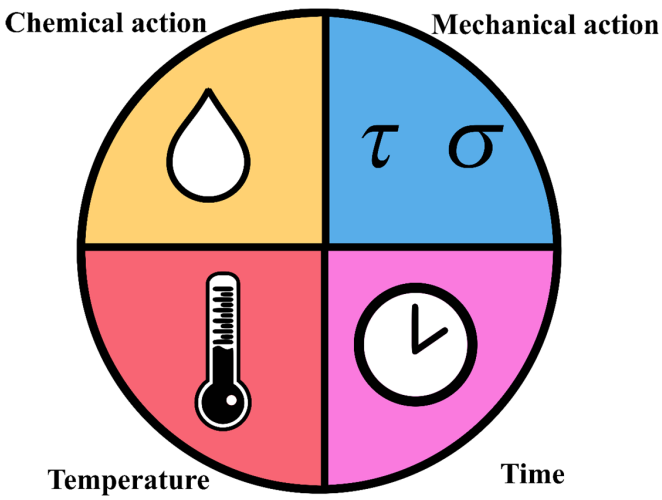

Figure 1.3 – Sinner's circle. Adapted from Basso *et al.* (2017).

The mechanical interactions between the soil and the cleaning solution determine how the residual layer deforms under the forces and stresses imposed by the liquid and by the interactions between the soil and the substrate. In other words, the rheology of the soil layer and the tribological characteristics of the system both play a decisive role in the efficiency of the cleaning process (Bhagat *et al.*, 2017). An understanding of the rheology of the soil layers is essential to optimise, predict and design cleaning operations.

This thesis explores the cleaning of insoluble viscoplastic soil layers using impinging water jets. Being hydrophobic in nature, the soils do not interact with water and are thus challenging to clean sustainably. Additionally, being non-interactive towards the cleaning fluid, these materials allow the interactions between the rheology of the soil and the hydrodynamics of the liquid film to be investigated in the absence of reaction effects and timescales.

1.4 Rheology and cleaning

Many materials of industrial interest are neither Newtonian fluids nor perfectly elastic solids and are broadly classified as non-Newtonian materials. Take, for instance, a toothpaste. It should readily flow when squeezed out of the tube, but the blob of paste retains its shape when resting on the toothbrush. Spreading peanut butter over toast would be a challenge if the material was either a Newtonian fluid or an elastic solid. If it had constant viscosity, it

would simply drain over the bread, and if it was a solid, it would not spread at all. Foods such as yoghurts (Dimonte *et al.*, 1998) and mayonnaise (Tabilo-Munizaga & Barbosa-Cánovas, 2005; Valette *et al.*, 2019), health care products like toothpaste (Ahuja & Potanin, 2018; Ahuja *et al.*, 2018), and cosmetics such as hand creams and lotions (Martinie *et al.*, 2013), are all examples of materials that can display viscoplastic characteristics. This means that these products behave as predominantly elastic solids when subject to low shear stresses, and flow with viscous characteristics at higher shear stresses (Ewoldt *et al.*, 2010). Because of their viscoplastic nature, these products are more prone to adhere to the inner surfaces of tanks when compared to their Newtonian counterparts such as syrups and oils, which tend to drain due to gravity. Cleaning these materials from the walls of tanks and vessels using impinging water jets is, therefore, challenging.

1.5 Aims and overview

The fundamentals of cleaning viscoplastic soil layers by a coherent impinging water jet have not been extensively discussed in the literature and so this is investigated in this thesis. Jets used in industrial practice are often more complex. A simpler flow geometry is used here to provide a fundamental understanding of the process, which can be extended to operating conditions. This will be explored experimentally, using an impinging jet apparatus to clean different soil layers from flat surfaces. Mathematical models are presented which describe the cleaning scenarios using different approaches.

A review of the available literature on rheology, impinging jet hydrodynamics and cleaning by impinging water jets will be presented in Chapter 2. The experimental methods, including a description of the materials, of the impinging jet apparatus, of the methods to characterise the mechanical behaviour of the soil material and of the methods used to process the results are presented in Chapter 3. Cleaning of a number of different soils is reported, so Chapter 4 presents the rheological characterisation of these materials. The rheological characteristics of the materials such as the yield stress and thixotropy are discussed, and a new method to estimate the yield stress using a scraping device is proposed. In Chapter 5, a phenomenological model for cleaning insoluble viscoplastic soil layers from flat surfaces using coherent impinging turbulent water jets is presented. The model is fitted to experimental data obtained with a petroleum jelly for static and moving water jets. In Chapter 6, a detailed model for cleaning viscoplastic soil layers is derived from an argument based on viscous dissipation of the soil at the cleaning front. This model incorporates the

rheological behaviour of the soil layer material and explains features from previous models available in the literature. Some modifications of this model are also discussed, and an attempt to model very thin soil layers is also presented. Finally, the conclusions of this work and suggestions for future investigations are presented in Chapter 7.

2 Literature review

This chapter is organised as follows: basic concepts of rheology are presented in Section 2.1, which is followed by a review of the rheology of viscoplastic fluids in Section 2.2. The hydrodynamic behaviour of water jets impinging on surfaces is discussed in Section 2.3, whilst the cleaning of soil layers from surfaces using water jets is reviewed in Section 2.4.

2.1 Basic concepts of rheology

Rheology is the study of deformation and flow of matter, and much of its scope is focused on the relationship between stresses and strains of elastic solids, Newtonian fluids and non-Newtonian materials.

The shear stress, τ, of an elastic solid is proportional to the shear strain γ, following Hooke's law:

$$\tau = G\gamma \tag{2.1}$$

where G is the shear elastic modulus.

For a Newtonian fluid, on the other hand, the shear stress is proportional to the shear rate, $\dot{\gamma}$:

$$\tau = \mu\dot{\gamma} \tag{2.2}$$

where μ is the viscosity of the Newtonian fluid.

Many fluids are not well described by Hooke's law of elasticity or by Newton's law of viscosity and are therefore labelled non-Newtonian fluids. There are several possible reasons for the deviation from Newtonian behaviour. For instance, the shear stress of a *viscoelastic material,* such as a polymer melt (Bird *et al.*, 1987), is determined by a combination of elastic and viscous contributions.

Other materials behave as inherently viscous materials with the instantaneous apparent viscosity $\eta(\dot{\gamma})$, defined

$$\eta(\dot{\gamma}) = \frac{\tau}{\dot{\gamma}}. \tag{2.3}$$

This quantity depends on the shear rate, with shear-thinning (or pseudoplastic) or shear thickening behaviour both observed (Deshpande *et al.*, 2010). The apparent viscosity of a time-dependent fluid depends on its shear history (Mewis & Wagner, 2009; Geri *et al.*, 2017; Larson & Wei, 2019).

Normal stresses also need to be considered in rheology, so tensorial notation is often used. The stress state of an infinitesimal fluid element is represented by the total stress tensor, **Π**, defined:

$$\boldsymbol{\Pi} = \begin{bmatrix} \tau_{11} + p & \tau_{12} & \tau_{13} \\ \tau_{21} & \tau_{22} + p & \tau_{23} \\ \tau_{31} & \tau_{32} & \tau_{33} + p \end{bmatrix} \tag{2.4}$$

where τ_{ij} are the components of the extra (or deviatoric) stress tensor and p is the pressure.

The extra stress tensor $\boldsymbol{\tau}$, also simply referred to as the stress tensor, is the difference between the total stress tensor and the isotropic pressure $p\boldsymbol{I}$, where $\boldsymbol{I}$ is the identity tensor:

$$\boldsymbol{\tau} = \boldsymbol{\Pi} - p\boldsymbol{I} = \begin{bmatrix} \tau_{11} & \tau_{12} & \tau_{13} \\ \tau_{21} & \tau_{22} & \tau_{23} \\ \tau_{31} & \tau_{32} & \tau_{33} \end{bmatrix}. \tag{2.5}$$

In simple shear flows, such as the shear-driven flow between parallel plates, $\tau_{13} = \tau_{31} = \tau_{32} = \tau_{23} = 0$. The total stress tensor becomes

$$\boldsymbol{\Pi} = \begin{bmatrix} \tau_{11} + p & \tau_{12} & 0 \\ \tau_{21} & \tau_{22} + p & 0 \\ 0 & 0 & \tau_{33} + p \end{bmatrix}. \tag{2.6}$$

It is common practice to refer to the component $\tau_{12} = \tau_{21}$ as the shear stress τ.

In rheometric devices, normal force measurements give values of the first and second normal stress differences, N_1 and N_2 (Morrison, 2001), respectively:

$$N_1 = \Pi_{11} - \Pi_{22} = \tau_{11} - \tau_{22} \tag{2.7}$$

$$N_2 = \Pi_{22} - \Pi_{33} = \tau_{22} - \tau_{33} \tag{2.8}$$

Identification of individual normal components of the total stress tensor requires a combination of techniques (Thompson *et al.*, 2018; de Cagny *et al.*, 2019).

For Newtonian fluids, $N_1 = N_2 = 0$. Materials with elasticity, on the other hand, show non-zero values of N_1 and N_2 which can be measured in rotational rheometers, as discussed in Section 2.1.1. Some materials behave as predominantly elastic solids when subject to small shear stresses, and display viscous characteristics at higher shear stresses. The cleaning of these *viscoplastic* materials is the topic of this thesis, and so their rheology will be covered in greater detail in this section.

2.1.1 Fundaments of rheometry

Rheometers measure the strain generated in a sample by an imposed stress (or torque) or vice versa. The former are labelled stress-controlled devices and the latter, strain-controlled. Several geometrical configurations are in widespread use: this work makes extensive use of rotational devices when a torque $\mathcal{T}$ is imposed or measured. The azimuthal angular displacement is θ, and the angular velocity is $\dot{\theta} = \mathrm{d}\theta/\mathrm{d}t$. The choice of the measuring geometry depends on the characteristics of the sample being tested and on the device. Figure 2.1 shows the measuring geometries used in the current work: (a) cone-plate, (b) parallel plates and (c) vane-in-cup. The vane-in-cup device is useful to reduce the effects of slip at the walls of the measuring tool. At large angular velocities, recirculation of the fluid between the blades of the vane can occur (Barnes & Nguyen, 2001; Marchesini *et al.*, 2015), so measurements with the vane in cup are expected to be more precise at low shear rates.

When materials with elasticity are sheared in cone-and-plate and parallel-plate devices, a normal force F_z in the axial direction is generated. Modern rheometers are equipped with a force transducer in the measuring head, which allows quantification of this force. The normal stress differences, N_1 and $N_1 - N_2$, can then be readily measured in the cone-plate and parallel plate geometries, respectively. The equations that describe $\tau, \gamma, \dot{\gamma}, N_1$ and $N_1 - N_2$ for each of the geometries are presented in Table 2.1.

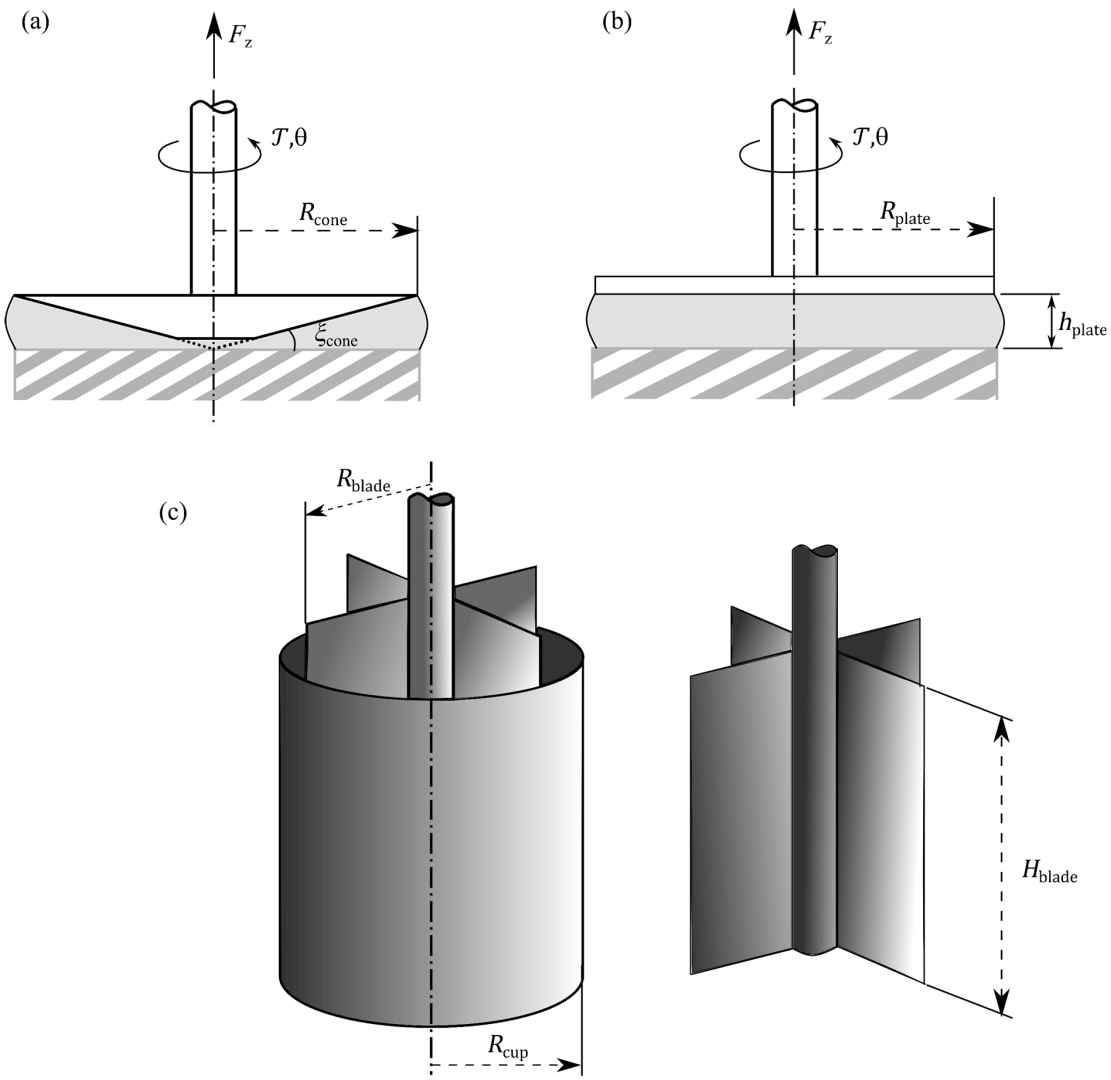

Figure 2.1 - Schematic representation of the measuring geometries employed: (a) Cone-plate, (b) parallel plates and (c) vane-in-cup.

Table 2.1 – Rheometrical equations for cone-plate, parallel plate and vane tools

	Shear strain (γ)	Shear rate ($\dot{\gamma}$)	Shear stress (τ_{12})	Normal stress differences (N_1 and $N_1 - N_2$)
Cone-plate	$\gamma = \frac{\theta}{\xi_{\text{cone}}}$ (2.17)	$\dot{\gamma} = \frac{\dot{\theta}}{\xi_{\text{cone}}}$ (2.14)	$\tau_{12} = \frac{3\mathcal{T}}{2\pi(R_{\text{cone}})^3}$ (2.11)	$N_1 = \tau_{11} - \tau_{22} = \frac{2F_z}{\pi(R_{\text{cone}})^2}$ (2.9)
Parallel plates	$\gamma = \frac{\theta r}{h_{\text{plate}}}$ (2.18)	$\dot{\gamma} = \frac{\dot{\theta} r}{h_{\text{plate}}}$ (2.15)	$\tau_{12} = \frac{\mathcal{T}}{\pi R_{\text{plate}}^3}\left[3 + \frac{\mathrm{d}(\ln \mathcal{T})}{\mathrm{d}\left(\ln(\dot{\gamma}\vert_{r=R_{\text{plate}}})\right)}\right]$ (2.12)	$N_1 - N_2 = \frac{F_z}{\pi R_{\text{plate}}^2}\left[2 + \frac{\mathrm{d}(\ln F_z)}{\mathrm{d}\left(\ln(\dot{\gamma}\vert_{r=R_{\text{plate}}})\right)}\right]$ (2.10)
Vane-in-cup	$\gamma \approx \frac{2\theta}{1 - \left(\frac{R_{\text{blade}}}{R_{\text{cup}}}\right)^2}$ (2.19)	$\dot{\gamma} \approx \frac{2\dot{\theta}}{1 - \left(\frac{R_{\text{blade}}}{R_{\text{cup}}}\right)^2}$ (2.16)	$\tau_{12} = \frac{\mathcal{T}}{2\pi(R_{\text{blade}})^2 H_{\text{blade}}}$ (2.13)	-

If a sinusoidal strain is imposed over time, such that $\gamma(t) = \gamma_a \sin(\omega t)$, where γ_a is the amplitude of the strain and ω the frequency, the shear stress response of a perfectly elastic material is in phase with the strain imposed, *i.e.* $\tau = G'\gamma_a \sin(\omega t)$, where G' is the storage modulus. For a Newtonian fluid, on the other hand, the shear stress response is in antiphase, *i.e.*, $\tau(t) = \eta\dot{\gamma}(t) = \eta\omega\gamma_a \cos(\omega t) = G''\gamma_a \cos(\omega t)$, with G'' the loss modulus. Complex materials often show an intermediate response which can be represented by (Macosko, 1994):

$$\tau(t) = \gamma_a[G'\sin(\omega t) + G''\cos(\omega t)] \tag{2.20}$$

This definition assumes that the shear stress is linearly related to the shear strain: if this is true, the deformation is said to lie within the linear viscoelastic region (LVE). For a given frequency, the values of G' and G'' are constant in the LVE. At large strains and stresses, a non-linear relationship between the stress and the strain exists: the stress response to an imposed strain is periodic but no longer sinusoidal, and the values of G' and G'' change with the strain amplitude.

Oscillatory experiments can be performed by changing the strain amplitude (oscillatory strain sweeps), the shear stress amplitude τ_a (oscillatory stress sweeps), the frequency (oscillatory frequency sweeps) or by keeping the amplitude and frequency constant and tracking the evolution of G' and G'' (oscillatory time sweep). Oscillatory tests are useful to measure the rheological behaviour of viscoplastic fluids, where a change from a predominantly elastic to viscous behaviour induced by shear takes place, as will be discussed in the next section. The stress response can also be represented in terms of the phase angle δ_{ph}:

$$\tan\delta_{ph} = \frac{G''}{G'}. \tag{2.21}$$

For viscous fluids, $\delta_{ph} = \pi/2$, whereas for elastic solids, $\delta_{ph} = 0$. Therefore, for viscoelastic materials, $0 < \delta_{ph} < \pi/2$.

2.1.2 Viscoelastic solids and fluids

Viscoelastic materials are those which show a combination of elastic and viscous behaviours. Non-zero values for the dynamic moduli G' and G'' are a characteristic of viscoelastic behaviour. The response of viscoelastic materials to an imposed shear is time-dependent, and a common way to check if a material is viscoelastic is by performing creep and recovery experiments (Ferry, 1980). Viscoelastic fluids can be distinguished from viscoelastic solids based on their creep-recovery response. Figure 2.2 presents the input of a stress step test and typical responses for Newtonian fluids and elastic solids, as well as viscoelastic fluids and solids. Newtonian fluids deform continuously under an imposed load, whereas elastic solids deform immediately and maintain a constant strain thereafter, Figure 2.2 (b). Viscoelastic materials, on the other hand, show time-dependent behaviour, and the stress-strain relationship is non-linear.

The rheological behaviour of viscoelastic materials can also be described by mechanical analogies with springs and dashpots, where springs represent the elastic behaviour, and dashpots the viscous behaviour (Ferry, 1980). The simplest model to explain the viscoelastic solid behaviour is the Kelvin-Voigt model, consisting of a spring and a dashpot in parallel. Under a constant stress load, the spring limits the maximum strain attainable by the system, whereas the dashpot is responsible for the retarded response in the creep phase illustrated in Figure 2.2 (c). When the external load is removed, the strain of a viscoelastic solid returns to its initial value, the timescale of which being governed by the viscous dashpot.

The Maxwell model consists of a spring and a dashpot in series and is often used to represent viscoelastic fluids. Under a constant stress load in the creep phase, an initial fast elastic deformation is present. At steady-state, the material eventually reaches a constant strain rate (Barnes *et al.*, 1989) as shown in Figure 2.2 (d). In the recovery phase, the residual strain results from the non-recoverable deformation of the viscous dashpot.

These two models demonstrate how viscoelastic solids and viscoelastic fluids differ both in the creep and in the recovery phases.

At low strains, the shear strain of viscoelastic materials is often proportional to the shear stress, and the materials are said to be in the linear viscoelastic regime. At higher strains,

non-linear viscoelasticity is often observed where non-linear relationships between the stress and strain are present (Macosko, 1994; Deshpande *et al.*, 2010).

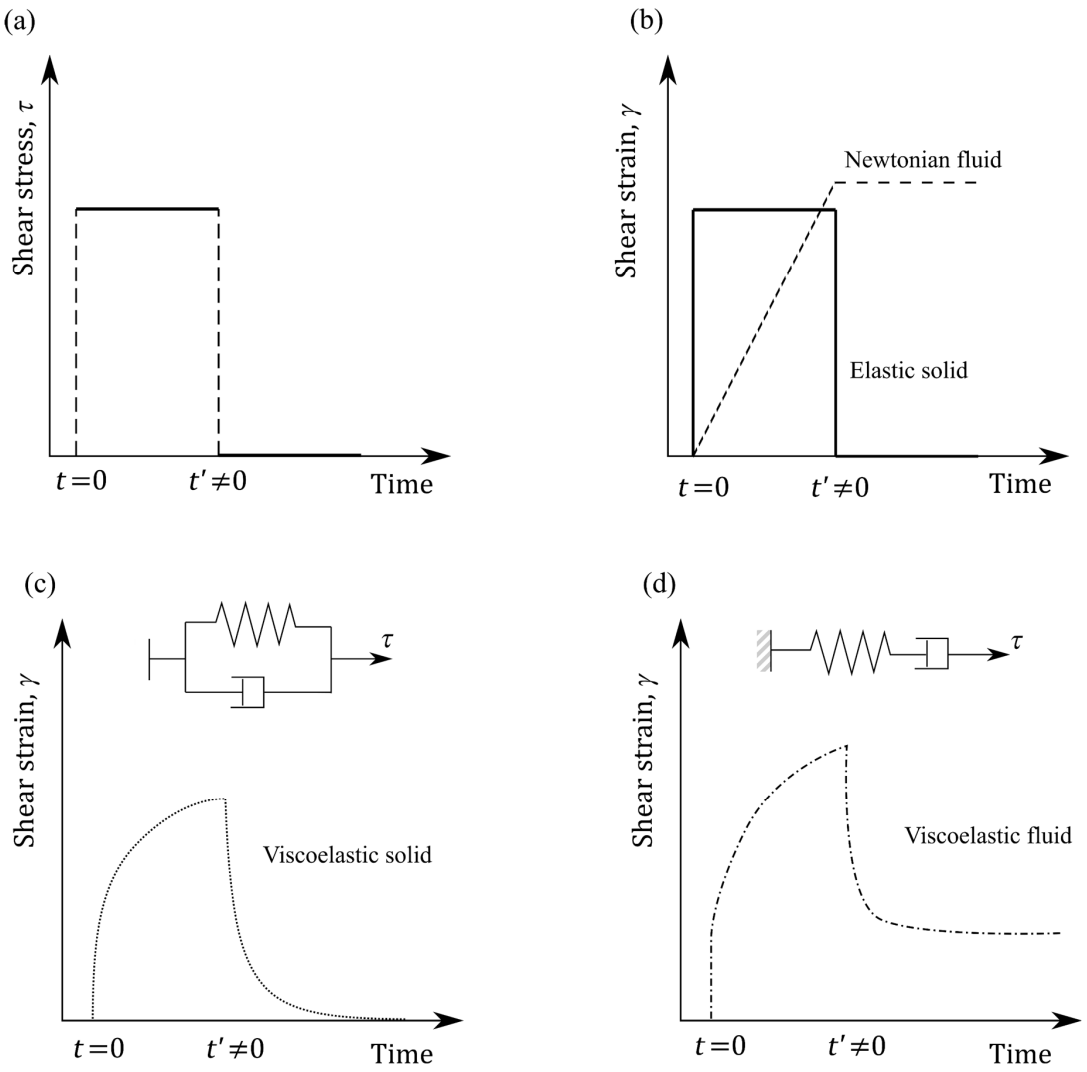

Figure 2.2 – (a) Schematic representation of the input of a creep (constant shear stress) and recovery (null shear stress) experiment and typical results for (b) elastic solid and Newtonian fluid, (c) viscoelastic solid and (d) and viscoelastic fluid behaviour. Insets in (c) and (d) illustrate the mechanical analogies of the Kelvin-Voigt and Maxwell models.

2.2 Rheology of viscoplastic fluids

2.2.1 What is the yield stress?

As discussed in Section 2.1, viscoplastic fluids do not exhibit significant deformation below a critical stress. The study of viscoplastic fluids was pioneered by Bingham (1922), who reported that the behaviour of clays could be expressed as:

$$\begin{aligned} \tau &= \tau_{\mathrm{y}} + \mu_{\mathrm{B}}\dot{\gamma} \qquad & \tau > \tau_{\mathrm{y}} \\ \dot{\gamma} &= 0 \qquad & \tau \leq \tau_{\mathrm{y}} \end{aligned} \tag{2.22}$$

where μ_{B} is the Bingham viscosity and τ_{y} is some yield stress.

This expression indicates that Bingham materials do not flow unless a critical shear stress is exceeded. Other expressions describing the behaviour of viscoplastic fluids exist, the Herschel-Bulkley (HB) model (Herschel & Bulkley, 1926) being one of the most commonly used:

$$\begin{aligned} \tau &= \tau_{\mathrm{y}} + k_{\mathrm{HB}}(\dot{\gamma})^{n_{\mathrm{HB}}} \qquad & \tau > \tau_{\mathrm{y}} \\ \dot{\gamma} &= 0 \qquad & \tau \leq \tau_{\mathrm{y}} \end{aligned} \tag{2.23}$$

where k_{HB} is the consistency index and n_{HB} is the HB exponent.

The Bingham model is a particular case of the HB model, where $n_{\mathrm{HB}} = 1$. In these two expressions, τ_{y} is a key parameter: the yield stress is the stress below which the material does not flow. Many authors use the terminology *yield stress materials* instead of *viscoplastic fluids* to describe materials that exhibit this yielding transition. Both terms are acceptable, with the first being used more by experimentalists, and the second by fluid mechanicists (Balmforth *et al.*, 2014). The term *elastoviscoplastic* materials is also used (Piau, 2007; Saramito, 2007, 2009; Ewoldt *et al.*, 2010; Souza Mendes & Thompson, 2013; Stickel *et al.*, 2013; Fernandes *et al.*, 2017a; Donley *et al.*, 2019) since elastic effects are sometimes observed below the critical stress, as discussed in Section 2.2.5.

Yield stress materials flow with predominantly viscous characteristics when stresses higher than the yield stress are imposed. This is an oversimplification of the problem as there are many other features involved in the yielding of viscoplastic materials, which is rarely a sharp

transition as suggested by Eq. (2.22) and Eq. (2.23) (Balmforth *et al.*, 2014; Bonn *et al.*, 2017). The term *yield stress* will be used in this thesis to refer to the threshold that separates the viscous from the unyielded regime. As discussed in Section 2.2.6, there are many methods to estimate the yield stress in rotational rheometers. Since there is a band of shear stresses over which the yielding transition occurs, these can provide different estimates of the yield stress. The estimate of the yield stress obtained from experiments will be therefore referred to as the critical stress, τ_c. There are several reviews of the topic in the literature (Nguyen & Boger, 1992; Barnes, 1999b; Møller *et al.*, 2006; Denn & Bonn, 2011; Balmforth *et al.*, 2014; Coussot, 2014, 2017; Bonn *et al.*, 2017), and this section is based on these works.

2.2.2 Physical origins of the yield stress

Yield stress materials are often composed of one or more phases dispersed in a continuous medium, and the macroscopic yield stress behaviour is a result of the microstructural configuration of the material. Here, two main cases are considered: those in which the yield stress results from (i) repulsive and (ii) attractive interactions between the dispersed elements (Nelson & Ewoldt, 2017; Nelson *et al.*, 2019).

Repulsion-dominated materials are those in which the dispersed elements do not attract each other. Examples include concentrated suspensions, emulsions and foams, which consist of solid particles, liquid droplets and gas bubbles dispersed in a continuous liquid phase, respectively. At high volume fractions (the ratio of the volume of the dispersed phase to the total volume of the material), a jammed microstructure is formed: dispersed particles are no longer able to freely move across the material, and become trapped in their respective positions by the neighbouring elements. The emergence of yield stress behaviour in dispersed systems is thus associated with a critical volume fraction, which depends on the morphology and physical properties of the particles. Examples include jammed suspensions of hard particles, such as poly(methyl methacrylate) (PMMA) particles (Petekidis *et al.*, 2003) and glass spheres (Richefeu *et al.*, 2006), suspensions of soft particles such as dispersions of Carbopol® in water (Putz & Burghelea, 2009) and crowded emulsions (Cohen-Addad & Höhler, 2014).

In attraction-dominated materials, the forces between the dispersed elements are strong enough to induce a nontrivial structural arrest even at low volume fractions (Bonn *et al.*, 2017). Examples include suspensions of colloidal clays, such as bentonite (Bekkour *et al.*, 2005) and laponite (Willenbacher, 1996; Bonn *et al.*, 1999) in water. The microstructure of these materials is composed of a percolated network which provides elasticity and allows the material to macroscopically sustain a finite stress. Attraction-dominated materials are often time-dependent, as the nature of the interactions between the dispersed particles allows microstructural rearrangement after flow. Suspensions of organic crystals in a continuous phase, such as suspensions of wax in oil, are also attractive-dominated materials. However, the morphology (shape and size) of the suspended crystals depend on the flow and/or temperature history of the sample (Geri *et al.*, 2017; Andrade & Coussot, 2019).

The yield stress can thus be affected by different factors. The most obvious one is the volume fraction of the dispersed phase: at higher volume fractions, the interactions between the dispersed particles are enhanced, increasing the macroscopic yield stress of the material. Materials that crystallize, such as waxy suspensions, are also influenced by temperature: increasing the temperature leads to a decrease in the volume fraction of the wax crystals, and consequently to a decrease in the bulk yield stress. The yield stress of colloidal dispersions is also influenced by surface properties, such as particle size distribution, particle shape, surface charge and solution conditions such as pH and salt concentration (Czibulya *et al.*, 2010). In this thesis, viscoplastic fluids will be used as received, and no changes in their rheology are expected due to changes in their composition.

2.2.3 Viscoplastic fluids with time-dependent behaviour

The origin of the yield stress behaviour in complex fluids resides in their microstructure. This microstructure can be partially disrupted by the flow, leading to a decrease in the particle-particle interactions. Since the viscosity is ultimately a measure of the internal friction of the fluid, the viscosity of multiphase materials can be a function of the shear history experienced by the fluid. This is nicely exemplified by the microscopic imaging of a colloidal get at rest and after flow presented by Bonn and Denn (2009), shown in Figure 2.3. Here, the same colloidal gel, a suspension of 1.3 μm fluorescent PMMA particles in a

mixture of decalin and cyclohexyl bromide shows a percolated structure at rest (a), which is broken down after flow (b).

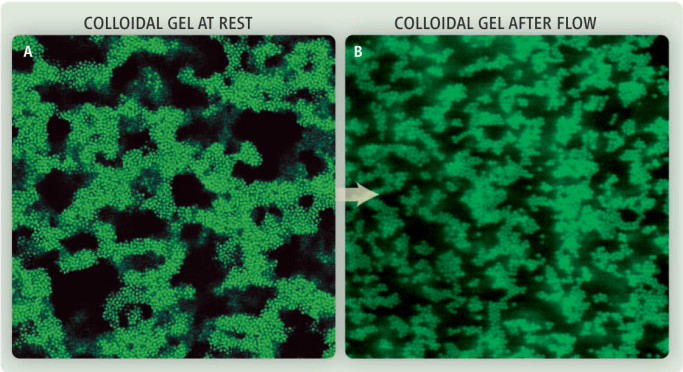

Figure 2.3 – Microscopic images of a colloidal gel (a) at rest and (b) after flow, showing breakdown of the percolated structure. Reproduced from Bonn and Denn (2009).

When a material that had been previously at rest for a long time is submitted to a finite shear, a decrease in viscosity may be observed due to the structural breakdown discussed above. If after flow cessation the original viscosity is recovered over the ageing time, the material is said to exhibit thixotropic behaviour (Mewis & Wagner, 2009; Larson & Wei, 2019). Many materials of scientific and engineering interest are thixotropic, as reviewed by Barnes (1997), Mewis and Wagner (2009) and Larson and Wei (2019), and include many FMCG products, such as ketchup (Coussot & Gaulard, 2005), peanut butter (Citerne *et al.*, 2001), toothpaste (Ahuja & Potanin, 2018), moisturising lotions (Ahuja *et al.*, 2019) and ointments (Stortz & Marangoni, 2014). Some materials, such as waxy crude oils (Mendes *et al.*, 2015; Geri *et al.*, 2017) and wax dispersions (Andrade & Coussot, 2019) show an irreversible viscosity decrease under shear, with the original levels of viscosity not being recovered even after very long ageing times. The characterisation of these materials is challenging, as their rheological properties are a function of the shear history (Legnani *et al.*, 2020). By definition, these materials are not thixotropic, as the viscosity decrease is not reversible, so these are termed more generally as *time-dependent* materials. On the other hand, some materials, termed simple yield stress materials, show little thixotropy, their behaviour being virtually independent of their shear history. Examples include some emulsions, foams and some Carbopol® dispersions (Bertola *et al.*, 2003; Møller *et al.*, 2009a; Ovarlez *et al.*, 2013).

The estimate of the critical stress in a time-dependent yield stress material depends on its shear history. As a result, pre-shearing is usually employed to impose a known shear history on the sample (Dzuy & Boger, 1985; Barnes, 1997; Cloitre *et al.*, 2000; Derec *et al.*, 2000). However, intense pre-shearing can lead to irreversible changes in the rheological behaviour of complex fluids (Mahaut *et al.*, 2008; Fernandes *et al.*, 2017b; Choi & Rogers, 2020), and so needs to be applied with care.

2.2.4 Static vs dynamic critical stresses

During rheometric experiments, the shear stress or the shear rate can be controlled. If the shear stress (or the shear rate) is increased starting from rest, this will promote structural breakdown and a solid-to-liquid transition will eventually be observed. On the other hand, if the shear rate (or stress) is decreased when the material was initially in a flowing state, the flow will eventually stop and a liquid-to-solid transition takes place (Bonn *et al.*, 2017). The viscosity of time-dependent materials changes with time under shear, and this affects the critical stress measurements. The existence of different critical stresses at the solid-to-liquid and at the liquid-to-solid transition was reported by Cheng (1986) in waxy crude oils and was later confirmed by Chang *et al.* (1998). Møller *et al.* (2009b) proposed that the difference between these estimates of the critical stress is due to the time-dependent behaviour, and is a result of the different time scales for ageing and rejuvenation, which depend on the material's microstructure. This is illustrated in Figure 2.4, in which increasing and decreasing stress sweep are performed in (a) a simple and (b) a time-dependent yield stress material. For the simple yield stress material, the static and the dynamic critical stress values ($\tau_{c,s}$ and $\tau_{c,d}$, respectively) are similar, whereas $\tau_{c,s} > \tau_{c,d}$ for the time-dependent material.

Balmforth *et al.* (2014) defined the static critical stress as 'the stress above which unyielded fluid begins to flow', and the dynamic critical stress as 'the stress below which yielded fluid stops flowing'. This definition will be adopted in this thesis, and methods to measure the static and dynamic critical stresses are described in the next section.

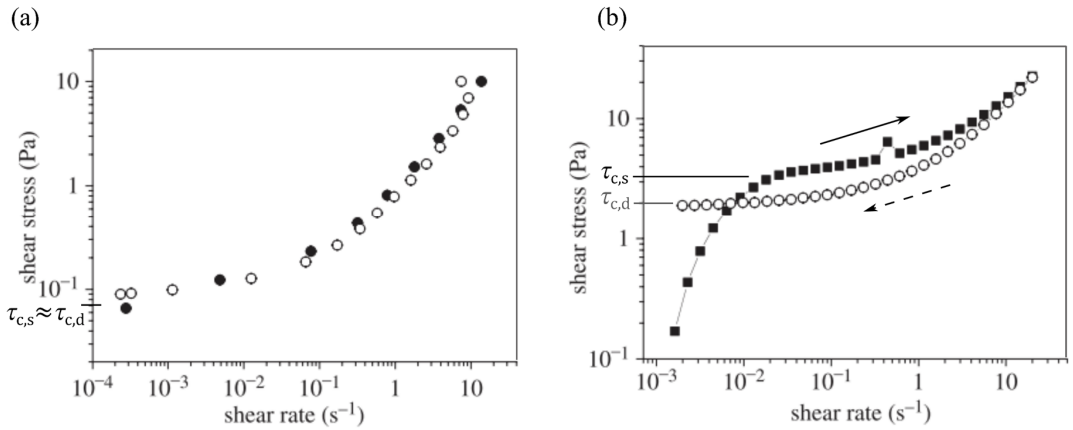

Figure 2.4 – Shear stress as a function of shear rate for increasing (filled symbols) and decreasing (empty symbols) shear stress ramps performed with (a) a simple yield stress material and (b) a time-dependent material. Adapted from Møller *et al.* (2009b).

2.2.5 The yielding process

Barnes and Walters (1985) proposed that viscoplastic materials behave as very viscous fluids at shear stresses below the critical stress, sparking a lengthy discussion on the existence and relevance of the yield stress (Hartnett & Hu, 1989; Astarita, 1990; Schurz, 1990; Evans, 1992). As measurement methods have become more accurate, new insights have been gained but the yielding transition is still the subject of much debate.

As mentioned before, viscoplastic materials are not perfectly rigid bodies below the critical stress. Oldroyd (1947) proposed that viscoplastic materials behave as elastic solids below the yield stress, and as viscous fluids above it. However, a discontinuous, sharp transition is not observed in experiments. Chang *et al.* (1998), for instance, demonstrated that the experiments performed by Wardhaugh and Boger (1991) with gelled waxy crude oil display a series of processes before culminating at fracture, when a constant speed rotation was imposed on the material using a vane tool. The main features of their experimental results are represented schematically in Figure 2.5, which shows the shear stress response as a function of shear strain.

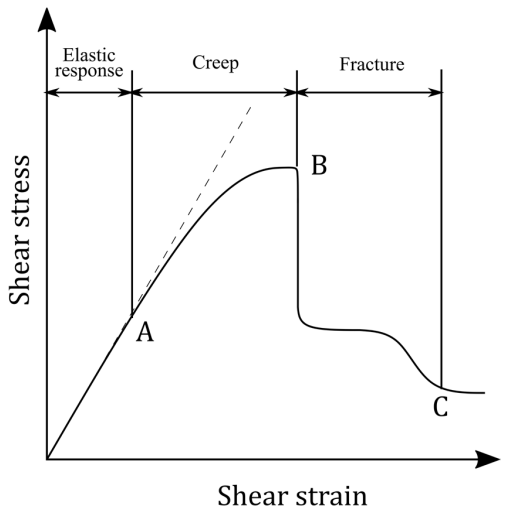

Figure 2.5 – Schematic representation of the stress-strain relationship observed by Wardhaugh and Boger (Wardhaugh & Boger, 1991) (discussed by Chang *et al.* (1998)) for a waxy crude oil under start-up flow using a vane tool.

An initial elastic response was observed, indicated by the linear stress-strain relationship up to point A. Beyond this, the deformation was no longer linear, initiating a creep regime that culminated at fracture, beyond which viscous behaviour predominated. Dinkgreve *et al.* (2017) have recently reported similar elastic effects at the yielding of a Carbopol® dispersion (which is widely used as a model material in the viscoplastic fluids community) under different flow conditions.

The shear stress measured at the limit of the linear stress-strain curve is termed the elastic limit stress, τ_{el}. However, this behaviour is not purely elastic for many materials: the values of G'' under oscillatory flow at stresses lower than τ_{el} for viscoplastic materials are often non-zero (Dinkgreve *et al.*, 2016, 2017; Fernandes *et al.*, 2017a; Donley *et al.*, 2019). The behaviour of viscoplastic materials below the critical stress can be described in terms of a viscoelastic solid (Husband *et al.*, 1993; Saramito, 2007, 2009; Ewoldt *et al.*, 2010), and the stresses and strains observed at the limit of elasticity are similar to the limit of linear viscoelasticity (Fernandes *et al.*, 2017a; Donley *et al.*, 2019). The yielding process thus takes place as a non-linear creeping flow (Lidon *et al.*, 2017) and can be quantified in terms of the phase angle δ_{ph} (Donley *et al.*, 2019).

Attempts have been made to model the pre-yield behaviour of viscoplastic fluids. Based on experimental observations, Dinkgreve *et al.* (2017) argued that the pre-yield behaviour of a

Carbopol® dispersion for $\tau \ll \tau_c$ is appropriately described by the Kelvin-Voigt model. For $\tau \gg \tau_c$, the material should follow the Maxwell model. However, the creeping regime is not described well by either, indicating that the yielding process is a transition from viscoelastic solid to viscoelastic fluid behaviour (Ewoldt *et al.*, 2010). This transition has been incorporated in general constitutive models for viscoplastic fluids, such as those by Souza Mendes and co-workers (Souza Mendes, 2009, 2011; 2013; Marchesini *et al.*, 2019), Saramito (2007), Park and Liu (Park & Liu, 2010), Belblidia *et al.* (2011) and Dimitriou *et al.* (2013). These models rely on fitting many parameters to experimental data sets and require numerical solution to compute complex flows. Other important phenomena observed below the yield stress are the transition from linear to nonlinear viscoelasticity (Fernandes *et al.*, 2017a) and the onset of plastic deformation (N'Gouamba *et al.*, 2019).

2.2.6 Methods to estimate the critical stress in rotational rheometers

Due to the time-dependent nature of viscoplastic materials, different estimates of the critical stress can be obtained if the material is initially at rest or under shear. This leads to the estimates of the static critical stress, $\tau_{c,s}$ and the dynamic critical stress, $\tau_{c,d}$. There are several methods to estimate both $\tau_{c,s}$ and $\tau_{c,d}$ (Nguyen & Boger, 1992). Non-viscometric flow conditions, such as squeeze flow tests (Rabideau *et al.*, 2009), penetrometry tests (Boujlel & Coussot, 2012) or flow on an inclined plane (Coussot *et al.*, 2002a) can be used to estimate the yield stress. However, these methods often involve complex flow conditions which are not easily controlled, and so the use of shear rheometers is preferred. The methods used in this work are discussed in this section.

2.2.6.1 Creep tests

The static critical stress can be estimated in experiments in which the material is probed starting from the solid state, *i.e.*, from rest. A traditional way to estimate the static critical stress is through creep experiments (Coussot *et al.*, 2002b; Da Cruz *et al.*, 2002), where a constant shear stress is applied over time and the strain response is recorded. If the material is an ideal elastic solid, a constant shear strain should be observed, Eq. (2.2). Similarly, Eq. (2.3) indicates that a constant shear rate would be obtained if the material is a Newtonian liquid. Since viscoplastic materials behave as viscoelastic solids below the yield stress and

as viscoelastic fluids above it, a gradual change in behaviour is observed when constant shear stress plateaus are imposed on these materials.

This is illustrated in Figure 2.6, in which Coussot (2018) presented the strain measured over time for several increasing constant shear stress plateaus imposed on a concentrated emulsion. At low stresses, a constant shear strain response is obtained, which is typical of elastic solids. At high shear stresses, a unit gradient in the log-log plot is obtained, which characterises a constant shear rate, typical of Newtonian fluids. Near the static critical stress, a gradual increase in strain is observed, indicating a creep regime in which the material is undergoing yield. This change in behaviour, also known as a viscosity bifurcation, provides a well-defined value for the static critical stress. However, this estimate depends on the duration of the stress plateaus employed (Møller *et al.*, 2006), since delayed yielding can take place at low shear stresses as long as the stress is applied for long enough (Uhlherr *et al.*, 2005; Gibaud *et al.*, 2010). Moreover, the precision of the estimate depends on how many stress plateaus are employed in the vicinity of the critical stress, so this method can be very time-consuming.

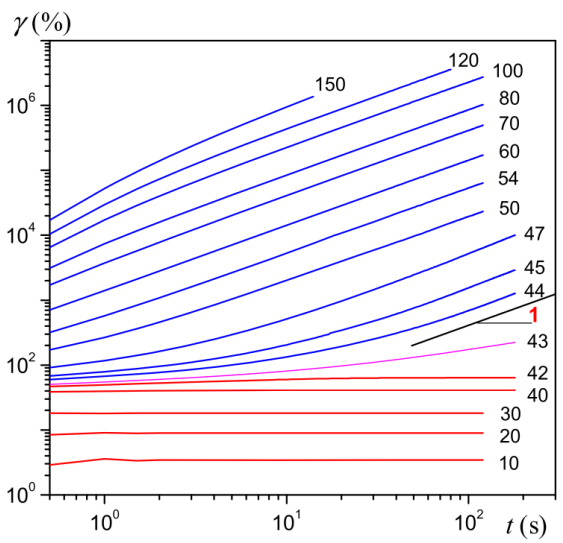

Figure 2.6 – Shear strain as a function of time for creep experiments performed on a concentrated emulsion. Red and blue lines indicate experiments in which the shear stress imposed is below and above the yield stress, respectively. Reproduced from Coussot (2018)

2.2.6.2 Stress ramps and plateaus

Another method to estimate the critical stress is to increase the shear stress over time in a controlled manner. This can be done as a series of shear stress plateaus (or steps), (Visintin *et al.*, 2005; Puisto *et al.*, 2015; Tarcha *et al.*, 2015; Ahuja & Potanin, 2018) or as a stress ramp (Uhlherr *et al.*, 2005; Hou, 2012; Ben Azouz *et al.*, 2016; Liu *et al.*, 2018b; Thompson *et al.*, 2018; Andrade & Coussot, 2019). Ideally, the duration of each shear stress step should be long enough for the shear rate to reach steady-state, which can lead to very long experimental times due to the slow speed of creep effects observed for shear stresses below the critical stress. This can be particularly troublesome for materials with time-dependent characteristics as they might age during the experiment, which leads to an increase in the critical stress (Fernandes *et al.*, 2016; Marinho *et al.*, 2018; Bonacci *et al.*, 2020). The critical stress is then defined as the shear stress at which a jump from low to high shear rates is observed (Tarcha *et al.*, 2015). Stokes and Telford (2004) reported an influence of the time duration of each shear stress step on the measured value of the critical stress for two commercial moisturising creams, reporting that the longer the duration of each stress plateau, the lower the value of the static critical stress.

Shear stress ramps, on the other hand, are inherently unsteady measurements since the shear stress continuously changes over time. However, this method also provides reliable estimates of the static critical stress if the rate of increase of the shear stress is low enough (Thompson *et al.*, 2018). Stress ramps are also useful to determine the critical stress in materials that show brittle fracture, such as wax suspensions (Andrade & Coussot, 2019) and waxy crude oils (Liu *et al.*, 2018a, 2018b), in which the increase in the shear strain immediately above the static critical stress is too rapid for accurate measurements to be obtained. This is discussed in more detail in Chapter 4, where materials with these characteristics are studied. Tarcha *et al.* (2015) compared different methods to estimate the critical stress of a waxy crude oil and reported that stress ramps lead to similar estimates of the static critical stress, unlike stress steps. Similar results were obtained by Andrade and Coussot (2020) with a suspension of paraffin wax in mineral oil.

2.2.6.3 Oscillatory amplitude sweeps

Controlled stress oscillatory experiments are also used to estimate the static critical stress of viscoplastic materials. Oscillatory cycles of stress are imposed with increasing amplitude. Different characteristic points can be associated with the static critical stress, as discussed by Dinkgreve *et al.* (2016). Figure 2.7 presents an example of this type of experiment for a commercial toothpaste (Cavity Protection, Colgate-Palmolive). Figure 2.7 (a) shows the values of G' and G'' as a function of the stress amplitude, whereas Figure 2.7 (b) shows the stress amplitude τ_a as a function of the shear strain amplitude γ_a. There is a crossover in G' and G'' at τ_{cr}, which can be used as an estimate of the static critical stress (Renou *et al.*, 2010; Kugge *et al.*, 2011). However, these measurements are made in the large amplitude oscillatory shear (LAOS) region, and thus beyond the LVE at the crossover (since the dynamic moduli are not constant). Since G' and G'' are based on the first harmonic of the strain response (Hyun *et al.*, 2011), this estimate of the critical stress does not necessarily coincide with the static critical stress evaluated with other methods (Bonn *et al.*, 2017).

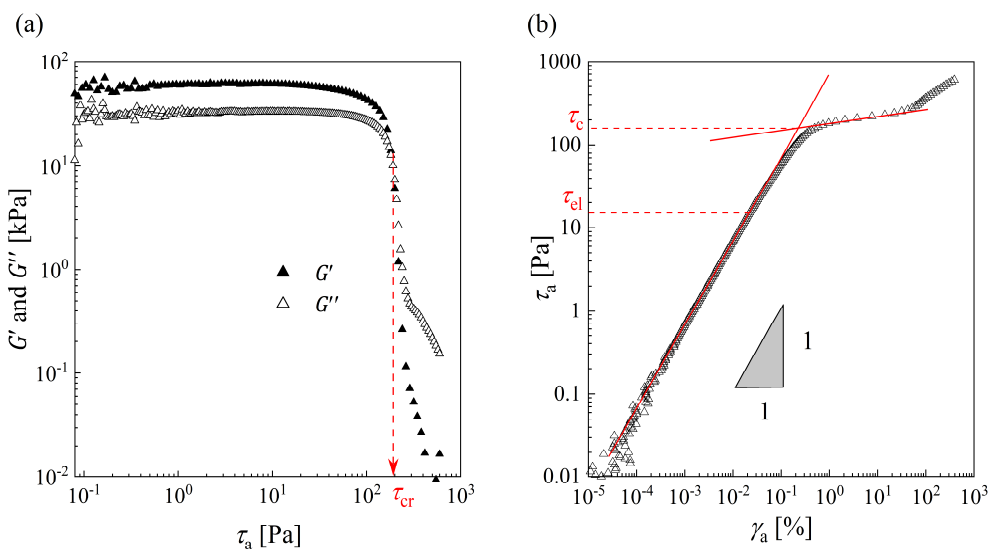

Figure 2.7 – Results for an oscillatory shear stress amplitude sweep performed with a commercial toothpaste at 20 °C. (a) $G'$and G'' as a function of the shear stress amplitude, (b) shear stress amplitude as a function of the shear strain amplitude. Rough parallel plates (20 mm radius, 1 mm gap), ω =1 Hz.

The stress at which the τ_a vs γ_a curve deviates from the unit gradient, indicated in Figure 2.7 (b), indicates the departure from the elastic regime. However, the determination of this

elastic-limit stress, τ_{el}, can be ambiguous since it depends on the criterion adopted for the deviation from the linear elastic behaviour and on the data used in the fit. The stress at the intersection of two power-law curves fitted to the data, one well below and one well above the critical stress, can also be used to estimate the critical stress as indicated in Figure 2.7 (b).

2.2.6.4 Extrapolation of the steady-state flow curve

So far, only methods to estimate the solid-to-liquid transition have been discussed. One method used to estimate the liquid-to-solid transition consists of imposing a steady shear, which can be achieved by controlling the shear stress or the shear rate and decreasing the intensity of this imposed shear until flow eventually stops. This method is usually performed with decreasing shear rate steps, which should be long enough for the shear stress to reach a steady state in each one of them. The dynamic yield stress is then obtained by extrapolating the flow curve at the limit when $\dot{\gamma} \to 0$. This method is widely established to estimate the dynamic critical stress (Kelessidis *et al.*, 2010; Dimitriou *et al.*, 2013; Ovarlez *et al.*, 2013, 2015; Souza Mendes *et al.*, 2014; Donley *et al.*, 2019). Fitting a rheological model, such as the Herschel-Bulkley equation to the $\tau - \dot{\gamma}$ data allows the extrapolation to the $\dot{\gamma} \to 0$ limit. The dynamic yield stress is assumed to be similar to the static yield stress for simple (or non-thixotropic) materials. For these materials, the critical stress obtained by the extrapolation of the steady-state flow curve is expected to be similar to the critical stress measured in increasing stress-controlled methods. However, recent studies (Fernandes *et al.*, 2017a; Dinkgreve *et al.*, 2018) suggest that this might not be the case even with materials that are traditionally assumed to be simple yield stress materials, such as Carbopol® dispersions.

This method suffers from some limitations, particularly at low shear rates. First, the time required for the steady-state shear stress to be reached significantly increases at low shear rates, since a characteristic timescale for the flow is the inverse of the applied shear rate, *i.e.*, $t_{ct} = 1/\dot{\gamma}$. Also, wall slip often occurs in the flow of viscoplastic materials at low shear rates (Bertola *et al.*, 2003; Cloitre & Bonnecaze, 2017), although this effect can be reduced by using measuring geometries with rough surfaces (Dimitriou *et al.*, 2011; Carotenuto & Minale, 2013). Additionally, the precision of this method will depend on the lowest shear rate evaluated, which is usually a hard limit imposed by the rheometer. Time-dependent

viscoplastic materials can also display shear banding in rate-controlled experiments (Møller *et al.*, 2008), meaning that no stable flow is obtained below a critical shear rate that depends on the material.

2.2.6.5 Stress relaxation

Stress relaxation experiments have also been used to estimate the critical stress of viscoplastic materials. In this type of experiment, a constant shear rate (Lidon *et al.*, 2017) or shear stress (Mohan *et al.*, 2013) is applied to the material for long enough for it to reach a steady state, and the material is then left to relax under a null imposed shear strain. The stress decays over time (Mohan *et al.*, 2013) until it reaches a constant residual (or internal) stress τ_r. This value has been used as an estimate of the critical stress (Nguyen & Boger, 1992), but it is important to note that it is often lower than the dynamic critical stress (Keentok, 1982). It has recently been demonstrated that τ_r decreases with the increase of the shear rate (Lidon *et al.*, 2017) and shear stress (Mohan *et al.*, 2013) imposed before the relaxation step. Therefore, this method has to be used with care as it reflects the level of microstructural anisotropy imprinted in the material by earlier shear (Bonn *et al.*, 2017). Stress relaxation effects have been reported in a variety of materials, such as Carbopol® dispersions (Lidon *et al.*, 2017), bentonite, mustard and a hair gel (Coussot *et al.*, 2006). Residual stresses after stress relaxation are also useful to estimate the critical stress in non-viscometric flows. Walder *et al.* (1969) developed a device consisting of a rectangular plate that is submerged in a blood sample. When the plate was rotated, the restoring torque was measured: the deflection angle and restoring torque lead to estimates of the strain and stress, respectively. The residual stress after a finite angular displacement was associated with the critical stress. More recently, Boujlel and Coussot (2012) used the residual forces after submersion of plates and cylinders in baths of Carbopol® dispersions to estimate the critical stress.

2.2.7 Industrial applications of viscoplastic materials

As mentioned, viscoplastic materials have a wide range of industrial applications, particularly for the FMCG industry. Table 2.2 presents a review of typical values for the critical stress of FMCG products, along with the measurement methods employed in each

work. The critical stress of FMCG products can range from less than 1 Pa, such as in fruit pulps, to values of the order of kPa such as butter, lard and margarine. The yield stress is an important parameter in FMCG applications, such as cleaning (Glover *et al.*, 2016; Palabiyik *et al.*, 2018; Tuck *et al.*, 2020), extrusion (Ardakani *et al.*, 2011; Coussot, 2014; Ahuja *et al.*, 2018), pumping through pipelines (Ahuja *et al.*, 2018) and determining food texture characteristics (Joyner (Melito), 2018).

Table 2.2 – Values of the critical stress reported for FMCG products

Material	τ_c [Pa]	Measurement method	Source
Fruit pulps	0.5 - 20	Steady flow curve	(Stafussa *et al.*, 2019)
Body lotion	2	Steady flow curve	(Kwak *et al.*, 2015)
Tomato ketchup	20	Creep experiments	(Tabilo-Munizaga & Barbosa-Cánovas, 2005)
Toothpaste	3 – 250	Stress ramps, oscillatory amplitude sweeps	(Ahuja & Potanin, 2018)
Potato puree	20-110	Steady flow curves	(Rao *et al.*, 1975)
Mayonnaise	20-200	Steady flow curve	(Ma & Barbosa-Cánovas, 1995)
Peanut butter	20-400	Steady flow curves, creep experiments	(Citerne *et al.*, 2001)
Hair gel	60 - 110	Oscillatory amplitude sweeps, creep experiments, steady flow curve	(Souza Mendes *et al.*, 2014; Fernandes *et al.*, 2017a)
Hand cream	100-180	Steady flow curve, creep experiments, increasing stress steps	(Stokes & Telford, 2004; Kwak *et al.*, 2015)
Yoghurt	100-300	Constant shear rate	(Daubert *et al.*, 1998)
Petroleum jelly	100-300	Stress steps	(Duarte *et al.*, 2014)
Cream cheese	400-5000	Constant shear rate	(Breidinger & Steffe, 2001)
Lard	2,000	Oscillatory amplitude sweeps	(Aguilar-Zárate *et al.*, 2019)
Butter	2,000 – 4,500	Constant shear rate	(Daubert *et al.*, 1998)
Margarine	4,200 – 5,500	Constant shear rate	(Daubert *et al.*, 1998)

2.3 Hydrodynamics of impinging liquid jets

The hydrodynamic behaviour of coherent impinging liquid jets is a classic fluid mechanics problem and has been extensively studied (Watson, 1964; Olsson & Turkdogan, 1966; Nakoryakov *et al.*, 1978; Morison & Thorpe, 2002; Wilson *et al.*, 2012; Bhagat & Wilson, 2016; Bhagat *et al.*, 2018). Understanding the hydrodynamic behaviour of a coherent jet impinging on a flat surface is the first step to describe cleaning operations. More complicated hydrodynamic conditions arise in practice, such as impingement on curved surfaces (Chee *et al.*, 2018) or with non-coherent jets (Feldung Damkjær *et al.*, 2017; Chee *et al.*, 2018; Fuchs *et al.*, 2019a, 2019b).

Figure 2.8 shows a schematic representation of a coherent horizontal water jet generated by a circular nozzle with diameter d_N impinging at point 0 on a vertical flat surface which defines the cylindrical frame of reference with coordinates r and z. The liquid, with mass flow rate $\dot{m}$, spreads radially outwards after the impingement in the radial flow zone (RFZ) with local film thickness h. M is the rate of flow of momentum in the liquid film per unit width, which will be hereafter referred to as the momentum of the liquid film. At some radial position, the thickness suddenly increases in a *film jump*. The origin of the film jump resides in the balance of momentum and surface tension in the liquid film (Bhagat *et al.*, 2018). Due to gravity, the fluid then drains down the plate either as a rope or as a draining film with width W (Wang *et al.*, 2013b; Aouad *et al.*, 2016).

Several models of the flow in the RFZ exist for coherent jets perpendicularly impinging on horizontal surfaces. Watson (1964) proposed that a boundary layer develops radially outwards from the jet footprint in the RFZ, in which viscous effects increase until the boundary layer reaches the liquid-air interface. Beyond this point, the liquid flows as a laminar film, which eventually becomes turbulent. Watson's model was used in early works that modelled the removal of Newtonian oil layers from flat surfaces using impinging water jets (Yeckel & Middleman, 1987; Yeckel *et al.*, 1990).

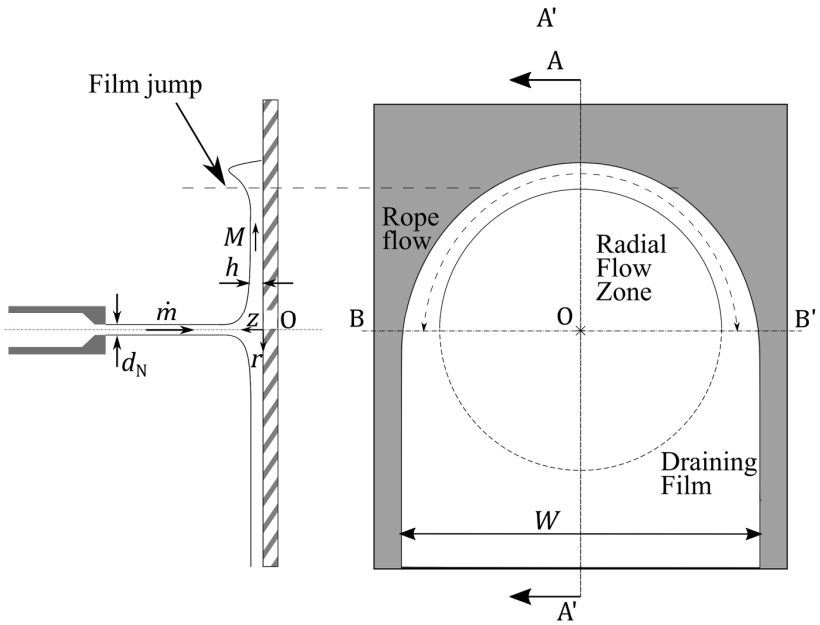

Figure 2.8 - Schematic representation of the flow behaviour of a horizontal, coherent jet impinging on a flat vertical surface. (a) Side view through section AA', (b) front view.

2.3.1 Simple hydrodynamic models

Close to the impinging point, the flow in the liquid film is dominated by diffusion of momentum from the wall to the free surface: a boundary layer is formed near the wall, and its thickness increases with the radial distance from the jet footprint. When the boundary layer reaches the free surface, a laminar flow is present across the film. As the liquid film expands, the flow eventually becomes turbulent.

The transition from laminar to turbulent flow is promoted by instabilities that originate from surface waves (Azuma & Hoshino, 1984) which are propagated from the point of impingement due to the varicose shape of the liquid jet, which is not perfectly cylindrical due to the Rayleigh-Plateau instability (Aouad *et al.*, 2016) induced by surface-tension of the liquid. Although the transition from the boundary-layer to a laminar film flow, and from laminar to turbulent flow along the RFZ is present when a turbulent liquid jet impinges on a surface, describing the flow in these three regions significantly increases the mathematical complexity of the hydrodynamic description of the flow. Simple equations for the average velocity and momentum flow rate can be obtained by modelling the flow in the liquid film as a laminar film flow. Although these equations do not capture the different flowing regimes

present in the liquid film, they are useful for the development of analytical cleaning models, as will be discussed in Figure 2.10.

Wilson *et al.* (2012) modelled the flow in the RFZ generated by an impinging water jet on a flat surface, treating it as a laminar flow with a parabolic velocity profile, with similar characteristics to a Nusselt film flow, where the velocity profile is found by assuming a similarity solution that satisfies three boundary conditions: no-slip at the wall, a given velocity at the free surface and a zero velocity gradient at the free surface (Fox *et al.*, 2011), as indicated in Eq. (2.24).

$$\begin{aligned} u(r,z) &= 0 \quad \text{at} \quad z = 0 \\ u(r,z) &= u_s(r) \quad \text{at} \quad z = h \\ \frac{\partial u(r,z)}{\partial z} &= 0 \quad \text{at} \quad z = h \end{aligned} \tag{2.24}$$

where $u(r,z)$ is the local velocity, z is the distance from the surface, u_s is the surface velocity and $h = h(r)$ is the thickness of the liquid film.

Neglecting gravitational effects and assuming a parabolic (second-order polynomial) velocity profile subject to the conditions outlined in Eq. (2.24), the velocity profile is:

$$u(r,z) = u_s\left(2\frac{z}{h} - \frac{z^2}{h^2}\right). \tag{2.25}$$

Integration of Eq. (2.25) yields the average velocity, U:

$$U(r) = \frac{1}{h}\int_0^h u(r,z)\,\mathrm{d}z = \frac{2}{3}u_s \tag{2.26}$$

The momentum flow rate per unit width, $M = M(r)$, is given by:

$$M(r) = \int_0^h \rho u^2 \mathrm{d}z = \frac{6}{5}\rho U^2 h \tag{2.27}$$

where ρ is the density of the liquid.

A momentum balance performed between radial positions r and $r + \mathrm{d}r$, assuming that the pressure in the layer is atmospheric yields:

$$\frac{\mathrm{d}(Mr)}{\mathrm{d}r} = -r\tau_{\mathrm{w,l}} = -r\frac{3\mu U}{h} \tag{2.28}$$

with $\tau_{\mathrm{w,l}}$ the wall shear stress at the liquid-substrate interface. From Eq. (2.25), $\tau_{\mathrm{w,l}} = \frac{2u_{\mathrm{s}}}{h}$. From Eq. (2.27) and (2.28):

$$\frac{\mathrm{d}(hU^2r)}{\mathrm{d}r} = -\frac{5}{2}\frac{\mu U r}{\rho h}. \tag{2.29}$$

From the conservation of volume, h is given by:

$$h(r) = \frac{Q}{2\pi r U} \tag{2.30}$$

where Q is the volumetric flow rate, given by:

$$Q = U_{\mathrm{o}}\pi\frac{d_{\mathrm{N}}^2}{4}. \tag{2.31}$$

Using Eq. (2.31), Eq. (2.29) can be written as:

$$\frac{\mathrm{d}U}{\mathrm{d}r} = -\frac{10\pi^2\mu}{\rho Q^2}U^2r^2. \tag{2.32}$$

The local value of the average velocity in the radius r is found by integrating Eq. (2.33) and gives:

$$\frac{1}{U} = \frac{1}{U_{\mathrm{o}}} + \frac{10\pi^2\rho\mu}{3\dot{m}^2}(r^3 - r_{\mathrm{o}}^3) \tag{2.33}$$

where μ is the dynamic viscosity of the liquid, $\dot{m} = \rho Q$ is the mass flow rate, U_{o} is the average velocity of the jet and $r_{\mathrm{o}} = d_{\mathrm{N}}/2$, with d_{N} the diameter of the nozzle.

$\tau_{\mathrm{w,l}}$, can be obtained from:

$$\tau_{\mathrm{w,l}}(r) = \mu \left.\frac{\mathrm{d}u(r,z)}{\mathrm{d}z}\right|_{z=0}. \tag{2.34}$$

Substituting Eq. (2.25), (2.26) and (2.30) into Eq. (2.34) yields:

$$\tau_{\mathrm{w,l}}(r) = \mu\frac{3U}{h} = \mu\frac{3U_{\mathrm{o}}}{8r\left[\frac{6.667}{Re_{\mathrm{j}}}\left(\frac{r}{d_{\mathrm{N}}}\right)^2 + \frac{\left(3Re_{\mathrm{j}}-20\right)}{24Re_{\mathrm{j}}}\left(\frac{d_{\mathrm{N}}}{r}\right)\right]^2} \tag{2.35}$$

where

$$Re_{\mathrm{j}} = \frac{\rho U_{\mathrm{o}} d_{\mathrm{N}}}{\mu} \tag{2.36}$$

is the jet Reynolds number.

Eq. (2.27) indicates that the momentum of the liquid film can be obtained from the expression for the average velocity within the liquid film, given by Eq. (2.33). Bhagat *et al.* (2017) proposed three different scenarios for evaluating M:

(i) Small values of r: strong soil case.

At small values of r, $r \approx r_{\mathrm{o}}$ and the second term in the right-hand side (RHS) of Eq. (2.33) is small. This describes the near-field scenario, close to the impinging point, where $U \approx U_{\mathrm{o}}$. Substituting this result in Eq. (2.27) gives:

$$M = \frac{3\dot{m}}{5\pi}\frac{U_{\mathrm{o}}}{r} = \frac{\sigma}{r} \tag{2.37}$$

where $\sigma = \frac{3\dot{m}U_{\mathrm{o}}}{5\pi}$.

(ii) Large values of r: weak soil case.

As discussed by Wang *et al.* (2013a), Wilson *et al.* (2012) assumed that away from the impinging point, $r^3 \gg r_{\mathrm{o}}^3$ and U is small when compared to U_{o}. This describes the far-field scenario, and the term U_{o}^{-1} in Eq. (2.33) can be neglected. This yields a simple expression for U,

$$U = \frac{3}{10}\frac{\dot{m}^2}{\pi^2\rho\mu}\frac{1}{r^3} \tag{2.38}$$

which when combined with Eq. (2.27) gives:

$$M = \frac{3\dot{m}^3}{5\pi c}\frac{1}{r^4} = \frac{\alpha}{r^4} \tag{2.39}$$

where c is a group of parameters characteristic of the liquid: $c = 10\pi^2\rho\mu/3$ and $\alpha = \frac{3\dot{m}^3}{5\pi c}$.

(iii) Intermediate values of r: intermediate strength soil case.

This case arises when Eq. (2.33) is used to describe the average velocity of the liquid film without further assumptions. Eq. (2.33) is rewritten as:

$$U = \frac{U_\mathrm{o}}{A + Br^3} \tag{2.40}$$

where

$$A = 1 - \frac{10\pi\mu}{3\dot{m}}r_\mathrm{o} \tag{2.41}$$

and

$$B = \frac{10\pi\mu}{3\dot{m}r_\mathrm{o}^2} = \frac{20}{3}\frac{1}{r_\mathrm{o}^3}Re_\mathrm{j}^{-1} \tag{2.42}$$

with the jet Reynolds number, $Re_\mathrm{j} = d_\mathrm{N}\rho U_\mathrm{o}/\mu$.

Substituting Eq. (2.40) into Eq. (2.27) yields:

$$M = \frac{3\dot{m}}{5\pi}\frac{U_o}{r(A + Br^3)} = \frac{\sigma}{r(A + Br^3)} \tag{2.43}$$

The performance of these three models is discussed in Figure 2.10, Section 2.3.2

2.3.2 Detailed hydrodynamic model

Although the model developed by Wilson *et al.* (2012) provides simple and useful expressions to describe the hydrodynamic behaviour of impinging liquid jets, it assumes that the flow in the film is laminar throughout the RFZ. Bhagat and Wilson (2016) proposed a

detailed hydrodynamic model to describe the flow in the thin liquid film generated by the impingement of a turbulent liquid jet on a flat smooth surface. Bhagat and Wilson (2016) divided the flow in the thin film in three different regions:

(i) A boundary layer formation zone, that extends from r_o to r_b, the radial position where the boundary layer reaches the free surface:

$$r_b = d_N \left(0.24 Re_j^{1/3}\right) \tag{2.44}$$

where d_N is the diameter of the nozzle.

(ii) A laminar film zone, ranging from $r_b \leq r < r_t$, with r_t the radius that marks the transition from laminar to turbulent flow:

$$r_b = d_N \left(0.2964 Re_j^{1/3}\right) \tag{2.45}$$

(iii) A turbulent region, extending from $r_t < r < r_j$. Here, r_j is the radius of the hydraulic jump, found by the solution of Eq. (2.46), which is implicit in r_j: Eq. (2.46) derives from the balance of momentum and surface tension in the radial direction.

$$\frac{\rho \frac{64}{63} \frac{Q}{2\pi} U_o}{r_j \left[\frac{0.167}{Re_j^{0.25}} \left(\frac{r_j}{d_N}\right)^{9/4} + \left(2.37 - 0.0108 Re_j^{1/2}\right)\right]} = \gamma_{st} \tag{2.46}$$

where γ_{st} is the surface tension of the liquid.

Figure 2.9 presents a schematic representation of the flow pattern due to a vertical jet impinging on a flat horizontal surface. The growth of the boundary layer takes place between r_o and r_b, and a circular hydraulic jump bounds the RFZ at r_t. As will be discussed in Figure 2.12, the hydraulic jump is assumed to result from the balance of the momentum flow rate in the liquid film with surface tension in the radial direction. It should be noted that r_j could be smaller than r_b or r_t. If $r_j < r_b$ or if $r_j < r_t$, the hydraulic jump takes place within the boundary layer formation region or in the laminar flow zone, respectively.

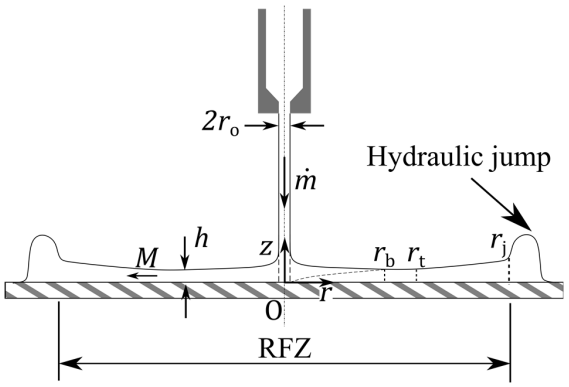

Figure 2.9 – Schematic of the flow pattern generated by a vertical jet impinging on a horizontal flat surface according to the Bhagat and Wilson (2016) model.

The expressions for $U(r)$, $M(r)$, $u(r,z)$, $\tau_{w,l}(r)$ and $h(r)$ for each one of the three regions are given by Eqs. (2.47) to (2.61). A discontinuity in $M(r)$ and $\tau_{w,l}(r)$ arises at the laminar to turbulent transition as a result of the different velocity profiles assumed. However, $h(r)$ is a continuous function along the three regions.

- Boundary layer formation zone - $\frac{d_N}{2} < r < r_b$

$$U(r) = \frac{U_o}{8\frac{r}{d_N}\left[0.125\left(\frac{d_N}{r}\right) + \frac{1.06}{\sqrt{Re_j}}\left(\frac{r}{d_N}\right)^{1/2}\right]} \tag{2.47}$$

$$h(r) = d_N\left[0.125\left(\frac{d_N}{r}\right) + \frac{1.06}{\sqrt{Re_j}}\left(\frac{r}{d_N}\right)^{1/2}\right] \tag{2.48}$$

$$M(r) = -1.37468\rho^{1/2}U_o^{3/2}\sqrt{\mu r} + \rho U_o^2 d_N\left[0.125\left(\frac{d_N}{r}\right) + \frac{1.06}{\sqrt{Re_j}}\left(\frac{r}{d_N}\right)^{1/2}\right] \tag{2.49}$$

$$u(r,z) = \begin{cases} U_o\left[\frac{z}{\delta_{bl}} - \frac{3}{2}\left(\frac{z}{\delta_{bl}}\right)^2 + 4\left(\frac{z}{\delta_{bl}}\right)^3 - \frac{5}{2}\left(\frac{z}{\delta_{bl}}\right)^4\right] & \text{if} \quad 0 < z \le \delta_{bl} \\ U_o & \text{if} \quad \delta_{bl} < z \le h \end{cases} \tag{2.50}$$

$$\tau_{w,l}(r) = \mu\frac{U_o}{2.12\sqrt{\frac{\mu r}{\rho U_o}}} \tag{2.51}$$

- Laminar film zone - $r_b < r < r_t$

$$U(r) = \frac{U_o}{8\frac{r}{d_N}\left[\frac{3.792}{Re_j}\left(\frac{r}{d_N}\right)^2 + 0.1975\left(\frac{d_N}{r}\right)\right]} \tag{2.52}$$

$$h\,(r) = d_N\left[\frac{3.792}{Re_j}\left(\frac{r}{d_N}\right)^2 + 0.1975\left(\frac{d_N}{r}\right)\right] \tag{2.53}$$

$$M\,(r) = \frac{0.3516\rho U_o^2 d_N^3}{16r^2\left[\frac{3.792}{Re_j}\left(\frac{r}{d_N}\right)^2 + 0.1975\left(\frac{d_N}{r}\right)\right]} \tag{2.54}$$

$$u(r,z) = \frac{U_o}{4\frac{r}{d_N}\left[\frac{3.792}{Re_j}\left(\frac{r}{d_N}\right)^2 + 0.1975\left(\frac{d_N}{2}\right)\right]}\left[\frac{z}{h} - \frac{3}{2}\left(\frac{z}{h}\right)^2 + 4\left(\frac{z}{h}\right)^3 - \frac{5}{2}\left(\frac{z}{h}\right)^4\right] \tag{2.55}$$

$$\tau_{w,l}\,(r) = \mu\frac{U_o}{4r\left(\frac{3.792}{Re_j}\left(\frac{r}{d_N}\right)^2 + 0.1975\left(\frac{d_N}{r}\right)\right)^2} \tag{2.56}$$

- Turbulent region - $r_t < r < r_j$

$$U\,(r) = \frac{U_o}{\frac{0.167}{Re_j^{1/4}}\left(\frac{r}{d_N}\right)^{9/4} + 2.37 - 0.0108Re_j^{1/2}} \tag{2.57}$$

$$h\,(r) = d_N\left[\frac{0.0209}{Re_j^{1/4}}\left(\frac{r}{d_N}\right)^{5/4} + \left(0.296 - 0.001356Re_j^{1/2}\right)\left(\frac{d_N}{r}\right)\right] \tag{2.58}$$

$$M\,(r) = \frac{\rho\frac{64}{63}\frac{Q}{2\pi}\,U_o}{r\left[\frac{0.167}{Re_j^{1/4}}\left(\frac{r}{d_N}\right)^{9/4} + \left(2.37 - 0.0108Re_j^{1/2}\right)\right]} \tag{2.59}$$

$$u(r,z) = \frac{8}{7}\left[\frac{U_o}{\frac{0.167}{Re_j^{1/4}}\left(\frac{r}{d_N}\right)^{9/4} + 2.37 - 0.0108Re_j^{1/2}}\right]\left(\frac{z}{h}\right)^{1/7} \tag{2.60}$$

$$\tau_{\mathrm{w,l}}(r) = \frac{0.0478\rho}{Re_{\mathrm{j}}^{1/4}}\left(\frac{U_{\mathrm{o}}}{\frac{0.167}{Re_{\mathrm{j}}^{1/4}}\left(\frac{r}{d_{\mathrm{N}}}\right)^{9/4} + \left(2.37 - 0.0108\,Re_{\mathrm{j}}^{1/2}\right)}\right)^{2}\left(\frac{r}{d_{\mathrm{N}}}\right)^{1/4}. \qquad (2.61)$$

Figure 2.10 compares the different hydrodynamic descriptions from each model for the flow in the liquid film. The plots display (a) M, (b) U and (c) $\tau_{\mathrm{w,l}}$ as a function of the radial position for the strong soil, weak soil and intermediate soil models discussed by Bhagat *et al.* (2017) and for the Bhagat and Wilson (2016) model. Figure 2.10 also shows the values of (a) M and (b) U that would be obtained if the weak soil model (far-field scenario) was used to describe the flow close to the impinging point (near-field scenario). The weak soil model overpredicts U and M by up to two orders of magnitude when outside its range of validity.

Additionally, both the weak and strong soil models fail to describe U in the vicinity of r_{b} when compared to the more accurate intermediate soil model and Bhagat and Wilson (2016) models. However, they provide adequate descriptions of M with simple analytical expressions, Eq. (2.37) and Eq. (2.39). It is important to highlight that the strong, weak and intermediate soil models do not incorporate turbulence in the liquid film, and so should be used with care when describing the flow generated by turbulent liquid jets. The description of $\tau_{\mathrm{w,l}}$ for the Nusselt film approximation, Eq. (2.35), is not reliable for $r < r_t$, showing a maximum in the wall shear stress that is not predicted by the Bhagat and Wilson (2016) model. The region where $r < r_{\mathrm{t}}$ lies within the boundary-layer formation zone, which is not considered by the Wilson *et al.* (2012) model.

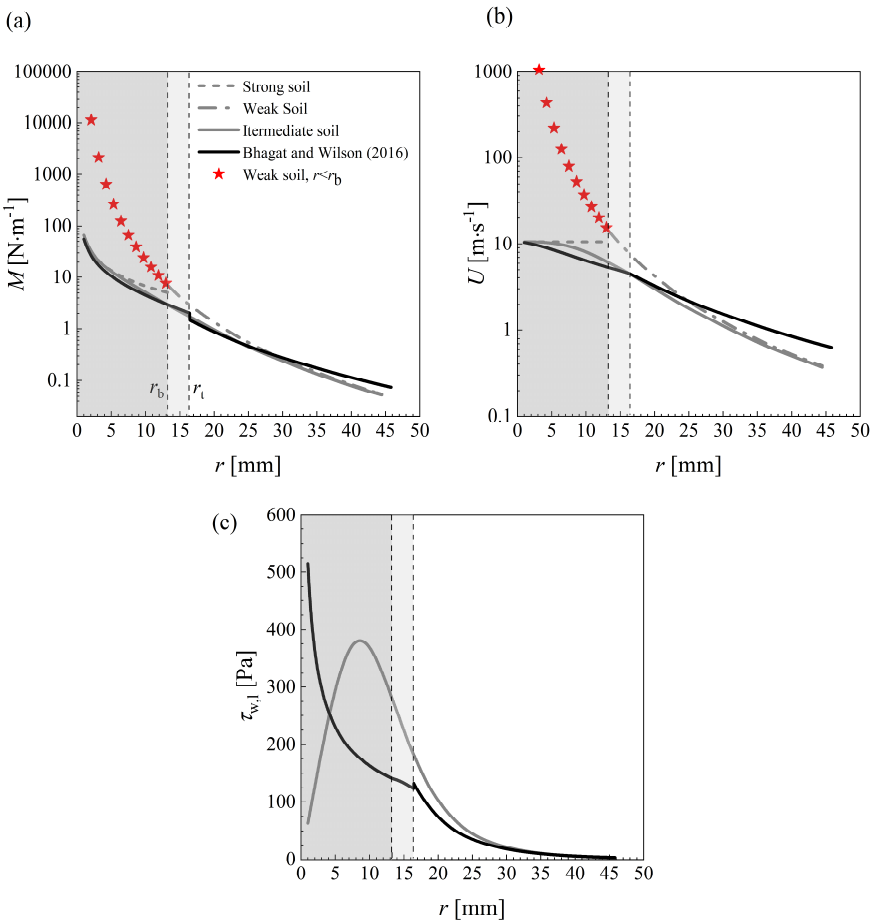

Figure 2.10 – Comparison between the hydrodynamic models. (a) M, (b) U and (c) $\tau_{w,l}$ profiles for the different formulations described in this section. Water jet at 20 °C ($\mu = 1$ mPa·s), $Q = 2.0$ l·min^{-1} and $d_N = 2$ mm. Dashed vertical lines indicate the values of r_b and r_t, according to the Bhagat and Wilson (2016) model, and set the limits for the boundary-layer formation zone (dark grey shaded region), laminar film zone (light grey shaded region) and turbulent region. Red symbols in (a) and (b) denote the values of M and U if the weak soil model is used to describe the flow for $r < r_b$.

Figure 2.11 shows the thickness of the liquid film predicted by the Bhagat and Wilson (2016) model for the same experimental condition in Figure 2.10. The height of the liquid film changes over the cleaned radius as a result of the change in the average velocity across the radially expanding liquid film. Bhagat and Wilson (2016) postulated that h reaches a minimum at r_t, which is evident in Figure 2.11. The liquid film is thin, reaching approximately 100 µm at its thinnest point.

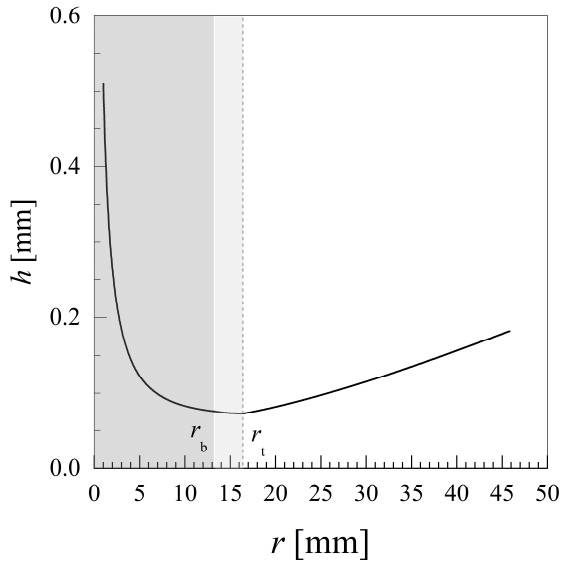

Figure 2.11 - h predicted by the Bhagat and Wilson (2016) model as a function of r for the same hydrodynamic condition described in Figure 2.10 (Water jet, 20 °C, $Q = 2.0$ l·min^{-1} and $d_N = 2$ mm).

2.3.3 Circular hydraulic jumps in impinging jet flows

As described in Section 2.3.2, a hydraulic jump bounds the RFZ when a liquid jet impinges on a flat horizontal surface. This feature has been extensively reported in the literature (Rayleigh, 1914; Tabi, 1949; Watson, 1964; Brechet & Néda, 1999; Morison & Thorpe, 2002; Bush & Aristoff, 2003; Bush *et al.*, 2006; Wilson *et al.*, 2012), and the origin of this phenomenon has been the topic of recent discussion (Bhagat *et al.*, 2018; Duchesne *et al.*, 2019; Fernandez-Feria *et al.*, 2019; Todkari & Kate, 2019; Wang & Khayat, 2019). Wilson *et al.* (2012) proposed that the RFZ in their simple hydrodynamic model stops when the momentum flow is balanced by surface tension forces, as shown in Figure 2.12, where ξ is the contact angle at the liquid/air/substrate interface.

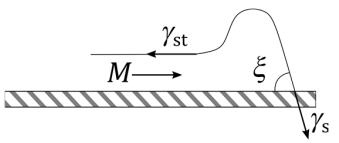

Figure 2.12 - Schematic of the film termination

For the Wilson *et al.* (2012) model the radial location of the film jump, R_j, is given by the solution of:

$$M = \frac{6}{5}\rho U(r)^2 h(r)\Big|_{r=R_j} = \gamma_{st}(1-\cos\xi) \tag{2.62}$$

where γ_{st} is the surface tension of the liquid. For water at 20 °C, $\gamma_{st} \cong 0.074$ N·m^{-1} and $\xi \cong 72.5 \pm 5°$ for Perspex® substrates (Wang *et al.*, 2013b) which were used in the majority of the experiments reported in this thesis.

Eq. (2.62) yields:

$$r_j = 0.276\left[\frac{\dot{m}^3}{\mu\rho\gamma_{st}(1-\cos\xi)}\right]^{1/4}. \tag{2.63}$$

The Bhagat and Wilson (2016) hydrodynamic model defines r_j as the radial position in which $M = \gamma_{st}$, Eq. (2.46). It is important to note that in this thesis, the definition of r_j will be used according to the hydrodynamic description adopted: Eq. (2.46) for the Bhagat and Wilson (2016) model, and Eq. (2.63) for the Wilson *et al.* (2012) model.

2.3.4 Draining film

As described in Figure 2.8, the liquid flow is divided into three distinct regions when a horizontal jet impinges on a vertical surface: the RFZ, the rope and a falling film. Wang *et al.* (2013b) described the draining film based on a Nusselt film laminar flow with a parabolic velocity profile:

$$u = \frac{\rho g}{2\mu}(2hz - z^2). \tag{2.64}$$

The average velocity within the film, U, is given by:

$$U = \frac{1}{h}\int_0^h u\,\mathrm{d}z = \frac{\rho g h^2}{3\mu}, \tag{2.65}$$

which leads to the flow of momentum per unit width,

$$M = \frac{6}{5}\rho U^2 h. \tag{2.66}$$

The thickness of the liquid film comes from Nusselt's theory for purely viscous flow down a flat surface (Bergman *et al.*, 2011),

$$h_{\mathrm{Nu}} = \left(\frac{3\mu f_{\mathrm{c}} Q}{\rho g W}\right)^{1/3} \tag{2.67}$$

where W is the width of the draining film, h_{Nu} is the thickness of the Nusselt draining film and f_{c} is the fraction of the jet flow rate that flows in the draining film (assumed to be 50% (Wang *et al.*, 2013b) for a perpendicular jet).

The draining film is wavy, and according to Kapitza's theory the thickness h_{Ka} of the draining film can be calculated from:

$$h_{\mathrm{Ka}} = \left(\frac{2.4\mu Q}{\rho g}\right)^{1/3} \approx 0.928 h_{\mathrm{Nu}}. \tag{2.68}$$

2.4 Cleaning soil layers

2.4.1 Cleaning maps

The design of cleaning systems depends on the characteristics of the soil, of the cleaning solution, of the substrate and the interaction between these three elements. Fryer and Asteriadou (2009) proposed a cleaning map in which the soils are classified in terms of their reactivity towards the liquid. These can be classified into soils that undergo *fluid mechanical removal*, where the driving mechanism for removal is the mechanical interaction between the soil and the liquid, and those which are cleaned by *diffusion-reaction removal*.

In diffusion-reaction cleaning, the soil reacts with the cleaning solution, promoting a change in the soil properties such as in saponification or reducing the adhesive forces that bind the soil to the substrate. The three main diffusion-reaction mechanisms observed in cleaning operations are dissolution, bulk cohesive failure and surface adhesive failure.

Dissolution by mass transfer (diffusion) takes place when the soil is soluble in the cleaning liquid. Heat transfer (melting) mechanisms can also promote cleaning if the temperature of the solution is higher than the melting point of the deposit (Fryer & Asteriadou, 2009).

Cuskston *et al.* (2019) provided a quantification of the different components of Sinner's circle (mechanical action, chemical action, time and temperature) for the cleaning of a complex burnt food soil.

Bulk cohesive failure takes place when the cleaning liquid promotes breakdown of the cohesive forces in the soil. As a consequence, the soil is gradually removed whilst leaving chunks of deposit adhered to the substrate. Surface adhesive failure happens when the cleaning agent leads to a decrease in the adhesive forces binding the soil to the substrate. Adhesive failure is often desired in cleaning applications, as complete adhesive removal promotes effective cleaning of the surfaces. The cleaning mechanism significantly depends on the reactivity between soil, substrate and cleaning solution and on the time scale of the cleaning process (Fryer & Asteriadou, 2009), which should be taken into account when designing cleaning operations (Herrera-Márquez *et al.*, 2020). For instance, Cuckston *et al.* (2019) demonstrated that cleaning of a complex burnt food soil (containing fats, carbohydrates and proteins) was enhanced by hydration, which promoted swelling of the soil with detergents and increased temperatures. The removal of reactive soils in CIP operations has been numerically investigated by Joppa and co-workers, who investigated the cleaning of soil layers in plane-channel flows (Joppa *et al.*, 2017, 2020) and using impinging water jets (Joppa *et al.*, 2019). They reported that the soils swell with the extended contact with water, promoting diffusion of the liquid into the soil and enhancing the rate of soil removal.

Different mechanisms are observed over different time scales when cleaning reactive soils. This can be exemplified with the removal of toothpaste from pipes by flushing water, such as in the experiments performed by Palabyik *et al*. (2014, 2018). They quantified the evolution of the mass fraction of toothpaste remaining in the pipe m/m_{o}, where m_{o} is the initial amount of toothpaste present, by repeatedly weighing the drained pipe (see Figure 2.13). After an initial phase in which a core of material was removed as toothpaste was displaced by the flushing liquid, cleaning involved the erosion of an annular film on the pipe wall. After some time, individual patches of paste remained on the pipe walls. These were removed slowly, and cleaning was determined by dissolution of the paste into the flushing liquid.

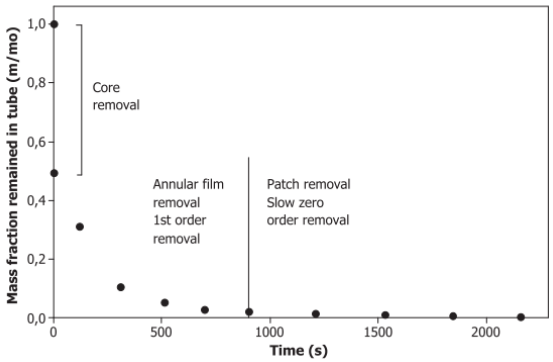

Figure 2.13– Example of result for cleaning toothpaste from a 1 m long pipe with internal diameter 25.4 mm using water (average velocity of 0.55 $m \cdot s^{-1}$, 15 °C) reported by Palabyik *et al*. (2014). Three different mechanisms, core, annular film and patch removal are observed over the cleaning time, indicating different cleaning mechanisms involved. Reproduced from Palabyik *et al*. (2014)

Bhagat *et al.* (2017) proposed a different classification scheme, also adopted by Joppa *et al.* (2020), based on the mobility of the soil, see Figure 2.14. This classification includes contributions from the rheology of the soil, *i.e.*, how the material deforms and flows under the forces imposed by the liquid, and tribology, the interactions at the soil-substrate interface. Mobile soils (a) are those that are displaced by the forces imposed by the liquid. If the time scale for diffusion is shorter than the cleaning time scale, diffusive removal is observed (a-i). If not, viscous shifting or roll-up takes place (a-ii). This is the case in several cleaning scenarios in the cosmetics industry, where hydrophobic materials such as creams and emulsions are cleaned with impinging water jets. The rinsing of Newtonian oils from flat surfaces using impinging liquid jets (Yeckel & Middleman, 1987; Mickaily & Middleman, 1993) is another example of mobile soil removal. Immobile soils (b) are those that do not deform considerably under the action of the liquid. If the cohesion within the soil is strong, the material is eroded by the shear stresses imposed by the liquid (b-i), such as in the experiments reported by Briscoe *et al.* (1995, 1997) where a hard cohesive soil was removed with impinging liquid jets. If the adhesion between the soil and the substrate is weak, peeling or adhesive detachment is observed (b-ii), such as in the removal of glue layers from flat surfaces reported by Wilson and co-workers (2014).

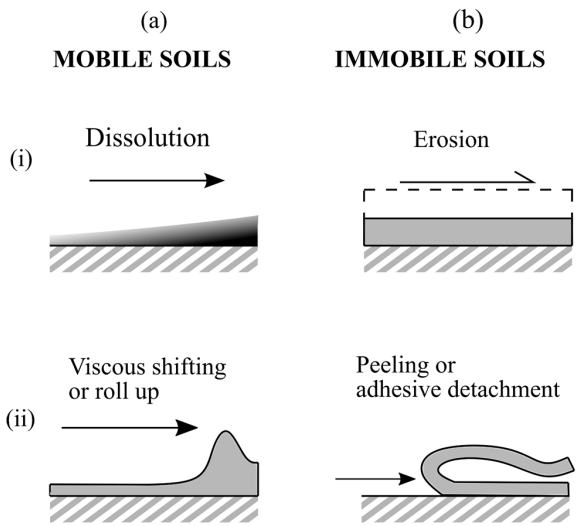

Figure 2.14 - Schematic representation of the different soil removal mechanisms proposed by Bhagat *et al.* (2017). Mobile soils (a) can be removed by (i) dissolution and (ii) viscous shifting or roll-up. Immobile soils (b) can be cleaned by erosion (i) or peeling (ii). Arrows indicate the hydraulic action imposed by the liquid into the soil layer.

2.4.2 Methods to evaluate soil mobility

The cleaning maps indicate that the cleaning mechanisms are a result of complex interactions between the soil, the substrate and the cleaning solution. Soil-substrate interactions dictate whether adhesive removal is involved, whereas the rheology of the soil layer and the nature of the soil and the cleaning solution determine if mobile or immobile soil removal occurs. Methods to evaluate the soil mobility should impose a known force onto a soil layer on a surface and measure the resultant deformation and flow behaviour, or vice-versa. Examples of methods reported in the literature include scraping devices, which promote deformation of layers coated on surfaces by the translation of a blade with the measurement of the associated force. Different length scales have been studied: Liu *et al.* (2002) developed a device, based on the previous work of Zhang *et al.* (1991) in which a T-shaped steel probe pulls fouling deposits of tomato paste from stainless steel surfaces. The gap between the probe and the substrate was of the order of 10 μm, and the cases evaluated consisted of adhesive removal. The same device has been then used to investigate the removal of different soil layers (Liu *et al.*, 2006a, 2006b, 2006c, 2007).

The removal of soils by scraping with substrate-blade gaps of the order of millimetres has also been studied. Ashokkumar and Adler-Nissen (2011) developed and validated a device to investigate the removal of fried pancake from different substrates. The samples were heterogeneous due to air inclusions and dispersed solid particles, so 0.6 mm gaps were employed. Ali *et al.* (2015) developed a similar device, which was used to investigate the cohesive and adhesive removal of different materials (honey, Vaseline® and lard) with blade-substrate gaps ranging from 1 to 8 mm. Magens *et al.* (2017) modified the design to improve precision in the measurements, and Cuckston *et al.* (2019) adapted the device to include a liquid reservoir, so the cleaning of reactive soils could be studied.

Another technique to measure and quantify the cleaning behaviour of layers is fluid dynamic gauging (FDG). In this technique, the flow of liquid through a submerged nozzle, located close to and normal to the surface, is studied. The relationship between pressure drop and mass flow rate then allows quantification of the nozzle-substrate distance (Tuladhar *et al.*, 2000). If fouling layers are present, this technique can provide useful information about the thickness of the layer and its deformation behaviour (Chew *et al.*, 2004a, 2004b; Yang *et al.*, 2014; Tsai *et al.*, 2019).

The rheology of the soil plays a decisive role in the cleaning of mobile fouling layers, particularly for mobile removal. The rheology of the soil is relevant for the cleaning behaviour in millimanipulation (Ali *et al.*, 2015), fluid dynamic gauging (Chew *et al.*, 2004a; Tsai *et al.*, 2019) and cleaning by impinging jets experiments (Hsu *et al.*, 2011, 2014; Walker *et al.*, 2012; Glover *et al.*, 2016; Lu *et al.*, 2020; Tuck *et al.*, 2020; Chee & Wilson, 2021). Soils with higher viscosity are generally more difficult to clean than layers with low viscosity. Viscoplastic layers are also troublesome, as their deformation is limited to the regions where the local stress is larger than the yield stress (Glover *et al.*, 2016; Palabiyik *et al.*, 2018). Therefore, understanding how the rheology of the soil affects its cleaning behaviour is an important topic which has been receiving increasing attention in the literature.

2.4.3 Cleaning with impinging jets

The removal of soils from surfaces using impinging water jets in the RFZ is primarily driven by mechanical interactions between the liquid and the soil. The majority of the studies reported in the literature are on the removal of Newtonian soil layers, such as thin oil layers (Yeckel & Middleman, 1987; Yeckel *et al.*, 1990, 1994), or cohesive layers that are removed by peeling, such as polyvinyl acetate (PVA) layers (Wilson *et al.*, 2014; Glover *et al.*, 2016). This section will describe the main features of soil removal with impinging water jets. Cleaning will be considered from the point where the liquid jet has already fully penetrated the soil layer and reached the substrate. Penetration of liquid jets in soil layers often happens over short time scales (Kaye *et al.*, 1995) and is a complex phenomenon. Uth and Deshpande (2013) have investigated the penetration of thick layers of elastoplastic materials by impinging liquid jets, whereas Yeckel and co-workers (Yeckel & Middleman, 1987; Yeckel *et al.*, 1990, 1994) considered the penetration of thin Newtonian oil layers. The sequence of events that takes when cleaning soils with impinging jets is indicated in Figure 2.15.

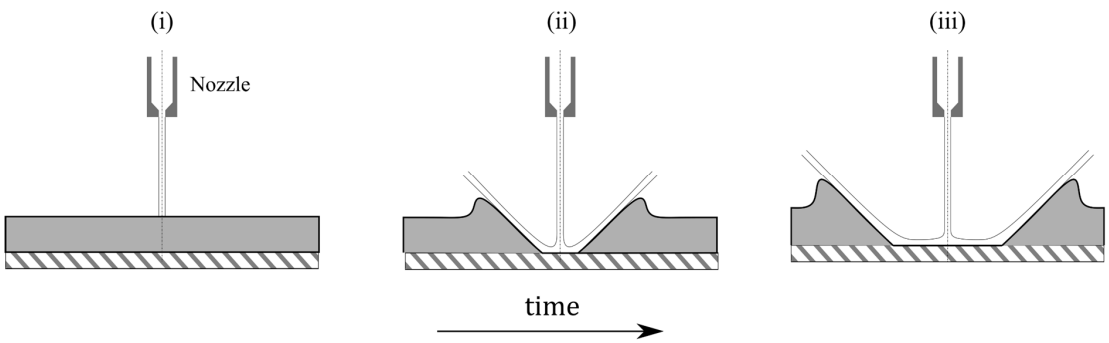

Figure 2.15 – Sequence of the jet impingement experiments. (i) The liquid jet impinges on the soiled surface, (ii) penetrates through the layer and (iii) radially expands cleaning the surface.

At first, the liquid jet impinges on the soil layer (i). If the velocity of the liquid jet is large enough, the liquid reaches the substrate after a short penetration time (ii) and the liquid film spreads radially outwards (iii), leaving behind a roughly circular cleaned region. In this thesis, the cleaning scenarios will be investigated after the jet has penetrated through the soil layer.

Two main mechanisms can be involved in the cleaning of soil layers: shear-driven removal and momentum-driven removal.

2.4.4 Shear-driven removal

Yeckel and Middleman (1987) considered a flat surface coated with a thin oil film, which was contacted by a coherent perpendicular water jet. Since the oil layer was immiscible in water, they assumed that cleaning was promoted by the water jet displacing the oil layer by viscous shifting, driven by the shear stress at the interface between the two fluids. They used the hydrodynamic model of Watson (1964) to calculate the local wall shear stress $\tau_{\mathrm{w,l}}$ imposed by the water film on the oil film, and obtained a partial differential equation (PDE) that described the thickness of the soil layer, δ, over time at different locations.

This mode of removal is expected when cleaning very thin soil layers, where the change in the topography of the layer does not significantly affect the hydrodynamics of the liquid film above it. Also, the work done on the layer does not reduce the kinetic energy of the liquid film substantially. Yeckel and Middleman (1987) provided the experimental conditions for their experiments, including the nozzle diameter, liquid flow rate and soil layer thickness. Circular plates of radius R_{Pl} were coated with silicone oils with viscosities ranging from 0.10 to 1.47 Pa·s, with thicknesses ranging from 60 to 90 μm. Using the Bhagat and Wilson (2016) hydrodynamic model, it is possible to estimate the liquid film thicknesses resulting from the liquid jets employed by Yeckel and Middleman (1987). A space averaged liquid film thickness over the circular plate, $\bar{h}_{Pl}$, can be defined as:

$$\bar{h}_{\mathrm{Pl}} = \frac{1}{R_{\mathrm{Pl}} - r_{\mathrm{o}}} \int_{r_{\mathrm{o}}}^{R_{\mathrm{Pl}}} h(r)\, \mathrm{d}r. \tag{2.69}$$

The values of $\bar{h}_{\mathrm{Pl}}/\delta_{\mathrm{o}}$ for the Yeckel and Middleman (1987) experiments lay between 3.2 and 10.7, indicating that the liquid films employed by them were indeed significantly thicker than the soil layers. The shear-driven model proposed by Yeckel and Middleman (1987) was later modified to describe the removal of the soil layer from the stagnation region (Yeckel *et al.*, 1994) and from roughness patches (Yeckel *et al.*, 1990).

A similar approach has been used to describe the shear-driven removal of thin Newtonian residual oil layers from the inner walls of pipes (Mickaily & Middleman, 1993; Yan *et al.*, 1997). Both these studies assumed that the shear stress imposed on the residual oil layer is equivalent to the wall shear stress in a smooth pipe. Since turbulent water flows were used, the wall shear stress was calculated using the Fanning friction factor (White, 1999). By doing this, the authors did not consider the coupling between the flow in the residual film and the flushing liquid flow.

2.4.5 Momentum-driven removal

Morison and Thorpe (2002) reported experimental observations for the cleaning of washable paint from transparent surfaces using impinging water jets and observed the growth of a circular cleaned region. Wilson *et al.* (2014) presented a model to describe the adhesive removal of these soft soil layers, where the momentum of the liquid film causes detachment (peeling) of the soil layer from the substrate. Cleaning is assumed to take place as the growth of a circular zone with radius a, and the driving force for cleaning was assumed to be a fraction of the momentum flow rate of the liquid film. They postulated that cleaning would follow a first-order kinetic model given by:

$$\frac{\mathrm{d}a}{\mathrm{d}t} = kMf(\delta_\mathrm{o}) = k'M \tag{2.70}$$

where t is time, $f(\delta_\mathrm{o})$ is some function of the initial soil layer thickness δ_o that includes the strength of the soil layer and k is a cleaning rate constant. In the absence of further knowledge about the role of the thickness of the soil layer on the cleaning dynamics, they adopted a lumped cleaning rate parameter k' to relate M to da/dt. In this model, they employed the Wilson *et al.* (2012) hydrodynamic description for the liquid film flow where M was given by Eq. (2.27), the weak soil model.

This yielded:

$$a \approx \left(k'\frac{3\dot{m}^3}{\pi c}\right)^{1/5}(t-t_\mathrm{i})^{1/5} = K\Delta t^{1/5} \tag{2.71}$$

where t_i is the time when a cleaned radius is first detected.

Eq. (2.71) suggests that a scaled with $\Delta t^{1/5}$, which was corroborated by experiments with dry PVA (Wilson *et al.*, 2014; Glover *et al.*, 2016), xanthan gum (Wilson *et al.*, 2015) and paint (Wang *et al.*, 2015) layers.

Lu *et al.* (2020) investigated the displacement of an immiscible oil by a submerged water jet using coupled-flow CFD simulations and reported that $a \propto \Delta t^{0.3}$, suggesting that the dynamics of submerged jets differ from free-surface flows.

The Wilson *et al.* (2014) momentum-driven model has been adapted to describe the cleaning of viscoplastic soil layers. Glover *et al.* (2016) reported that an asymptotic maximum cleaned radius, $a_{\max}$, was reached when cleaning layers of petroleum jelly using impinging water jets. Eq. (2.70) was modified to:

$$\begin{aligned} \frac{\mathrm{d}a}{\mathrm{d}t} &= k'\left(M - M_{\mathrm{y}}\right) \quad \text{if} \quad M > M_{\mathrm{y}} \\ \frac{\mathrm{d}a}{\mathrm{d}t} &= 0 \qquad\quad \text{if} \quad M \leq M_{\mathrm{y}} \end{aligned} \tag{2.72}$$

where M_{y} is the momentum required to yield the soil layer. Growth of the cleaned radius is observed if $M > M_{\mathrm{y}}$. M decreases as a increases: at some radial position, $M = M_{\mathrm{y}}$, so cleaning halts at $a = a_{\max}$.

M_{y} depends on the rheology of the soil layer. Glover *et al.* (2016) proposed that the liquid film flow promotes yielding of the layer at the cleaning front, which advances radially outwards. At $a_{\max}$, the net momentum flux is equal to the force required to overcome the critical stress of the soil layer. Glover *et al.* (2016) assumed that the cross-section of the cleaning front at $a_{\max}$ takes the form of a wedge. A force balance in the radial direction per unit of circumferential width, as indicated in Figure 2.16, equates the change in momentum of the fluid to the force required to yield the soil along a flat shear plane of area per unit of width $\delta \operatorname{cosec} \chi$:

$$M_{\mathrm{y}} - M_{\mathrm{y}} \cos\chi = \tau_{\mathrm{c}}(\delta_{\mathrm{o}} \operatorname{cosec}\chi) \cos\chi \tag{2.73}$$

which can be rearranged to give:

$$M_{\mathrm{y}} = \frac{\tau_{\mathrm{c}}\delta_{\mathrm{o}}}{\tan\chi - \sin\chi} \tag{2.74}$$

where χ is the inclination of the wedge-shaped front.

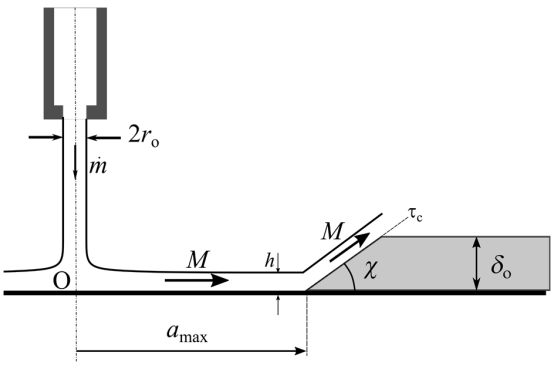

Figure 2.16 – Schematic of the flow at $a_{\max}$ as proposed by Glover *et al.* (2016). The liquid film displaces the soil layer.

Glover *et al.* (2016) made simplifying assumptions that yielded analytical solutions to Eq. (2.72). They used the Wilson *et al.* (2012) hydrodynamic model, which provides a simple expression for M: since this expression is only accurate for $r > r_b$, the model is not expected to be reliable in the boundary-layer formation region, close to the impinging point. They also assumed that the yielding surface at the cleaning front is a flat plane that extends from the substrate to δ_o. The layer rheology was only quantified in terms of a yield stress. Chapters 5 and 6 focus on elucidating Eq. (2.72). This will include relaxing the assumptions made by Glover *et al.* (2016) and proposing models to explain the parameters that influence the cleaning rate constant k'.

The cleaning rate constant k' has been the topic of continuous investigation since it was proposed by Wilson *et al.* (2014). Its dependency on the thickness of the soil layer was explored by Glover *et al.* (2016), who reported that k' shows a weakly decreasing trend with increasing values of δ_o. Wilson *et al.* (2014) evaluated the removal of petroleum jelly at different temperatures by manipulating the temperature of the water in the jet, which decreased the critical stress of the soil. This is illustrated in Figure 2.17. They reported that k' strongly decreases with the increase of τ_c, suggesting that the cleaning rate constant is strongly linked to the rheology of the soil layer. They found that $k' \sim \tau_c^{1.75}$, which is not a simple relationship. An increase in the cleaning rate was also reported by Rodgers *et al.* (2019) on the removal of a white soft paraffin at different temperatures.

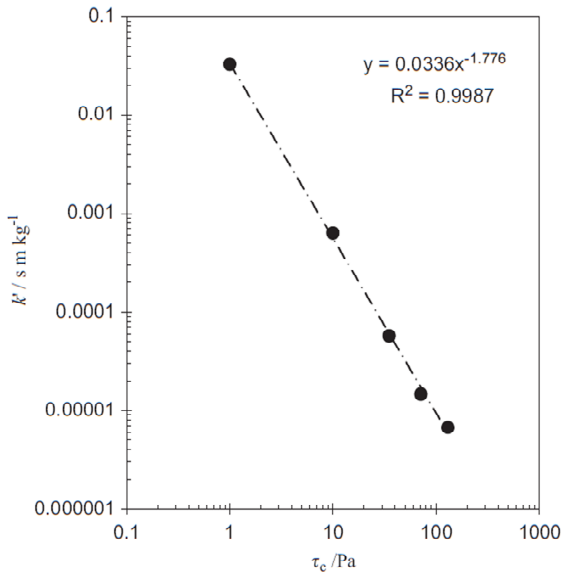

Figure 2.17 – Effect of the critical stress on the cleaning rate constant (Eq. (2.70) for experiments conducted with coherent perpendicular jets impinging on 250 µm thick layers of petroleum jelly coated on glass. Reproduced from Wilson *et al.* (2014)

The removal of soil layers has also been explored for other hydrodynamic conditions. Feldung Damkjær *et al.* (2017) and Chee *et al.* (2018) investigated the effects of jet break-up on the removal of layers of petroleum jelly and Carbopol®, respectively. At large stand-off distances L (the distance between the nozzle and the substrate), jet breakup is observed and a fraction of the liquid splashes back when hitting the surface. Therefore, the effective flow rate at the surface is lower than the jet flow rate, leading to a decrease in k'. Chee *et al.* (2018) also evaluated the removal of Carbopol® from the inner walls of cylinders (*i.e.*, curved surfaces, with curvatures κ ranging from 0 to 9.1 m^{-1}), and did not observe any significant difference in the cleaning dynamics with the curvature of the surfaces.

Cleaning egg yolk, which softens when soaked in water, by horizontal intermittent jets (bursts) was investigated by Yang *et al.* (2019b). The soil below the impingement point was exposed to the draining film between the bursts, which promoted weakening of the soil and increased the cleaning rate during the bursts. More recently, Chee and Wilson (2021) conducted a rigorous study on the cleaning with intermittent jets and reported no significant difference between continuous and intermittent jets for four different soils (tomato ketchup,

petroleum jelly and two different toothpastes) when these were not left to soak between cleaning steps.

2.4.6 Traversing nozzles

The previous section considered cleaning of soiled surfaces by impinging coherent stationary jets. If the point of impingement moves across the surface, it leaves a trail of cleaned material behind. Wilson *et al.* (2015) modelled the shape of this cleaned region left by a normally impinging coherent jet traversing across a flat surface. The jet generates a round-nosed band cleared of soil with width w_c, shown in Figure 2.18. They presented a model to describe the shape of the cleared region for the weak soil model (Eq. (2.39)), and Bhagat *et al.* (2017) extended this model to the strong and intermediate soil cases. Figure 2.18 shows the cleaning pattern left by a jet that traverses at velocity v_{jet}. The impingement point defines the frame of reference. The soil is thus convected towards the jet at velocity v_{jet}: at the nose of the cleared band, point X, the rate of cleaning is equal to v_{jet} such that $|\mathrm{d}a/\mathrm{d}t|_{\mathrm{X}} = v_{\mathrm{jet}}$ at the cleaning front, where the distance from point O to the front is a_{x}. The loci of the cleared path can be defined by describing the rate of cleaning for a point P, located along the cleared surface at angle β and distance p from O.

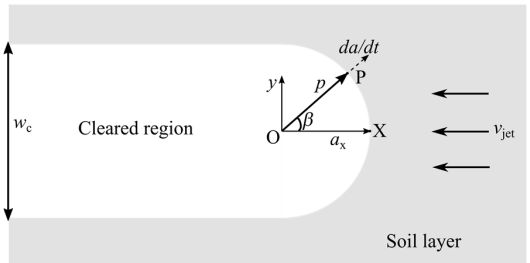

Figure 2.18 - Schematic of region cleaned by a perpendicular jet traversing along a flat soiled surface at velocity v_{jet}. The frame of reference is inverted so that the soil moves towards the jet impingement point

As proposed by Wilson *et al.* (2015), a vector analysis can be performed to describe the shape of the cleaning front in terms of the distance p and angle β, giving:

$$\frac{\mathrm{d}p}{\mathrm{d}\beta} = \left(\frac{\mathrm{d}a}{\mathrm{d}t}\right)_{\mathrm{P}} \frac{p}{v_{\mathrm{jet}} \sin\beta} - \frac{p}{\tan\beta} \tag{2.75}$$

with $\left(\frac{\mathrm{d}a}{\mathrm{d}t}\right)_{\mathrm{P}}$ the rate of cleaning, *i.e.*, the rate of advancement of the cleaning front, at point P.

This can be expressed in non-dimensional terms by writing $p^* = p/a_{\mathrm{x}}$, *i.e.* $p^* \geq 1$ to give:

$$\frac{\mathrm{d}p^*}{\mathrm{d}\beta} = \left(\frac{\mathrm{d}a}{\mathrm{d}t}\right)_{\mathrm{P}} \frac{p^*}{v_{\mathrm{jet}} \sin\beta} - \frac{p^*}{\tan\beta}. \tag{2.76}$$

The solution of this equation depends on the hydrodynamic model employed to describe $\left(\frac{\mathrm{d}a}{\mathrm{d}t}\right)_{\mathrm{P}}$. Three cases are considered:

(i) Weak soil

For the weak soil case, $a_{\mathrm{x}} \geq r_{\mathrm{b}}$, $\left(\frac{\mathrm{d}a}{\mathrm{d}t}\right)_{\mathrm{P}} = \frac{\alpha}{p^4}$ and $v_{\mathrm{jet}} = \alpha/a_{\mathrm{X}}^4$. Substituting these in Eq. (2.76) yields an analytical solution for p^*:

$$p^{*4} \sin^4\beta = \frac{4}{3}\cos^3\beta - 4\cos\beta + \frac{8}{3}. \tag{2.77}$$

The Cartesian coordinates of the point p^* are given by $x^* = \frac{x}{a_{\mathrm{x}}} = p^* \cos\beta$ and $y^* = \frac{y}{a_{\mathrm{x}}} = p^* \sin\beta$. When $\beta \to \pi$, Eq. (2.77) gives the half-width of the cleared region, yielding $w_{\mathrm{c}}^* = w_{\mathrm{c}}/a_{\mathrm{x}} = 3.04$.

(ii) Strong soil

The strong soil case is observed when $a_{\mathrm{x}} < r_{\mathrm{b}}$. Substituting $\left(\frac{\mathrm{d}a}{\mathrm{d}t}\right)_{\mathrm{P}} = \frac{\sigma}{p}$ and $v_{\mathrm{jet}} = \sigma/a_{\mathrm{X}}$ in Eq. (2.76) also yields an analytical solution for p^*:

$$p^* = \beta \operatorname{cosec}\beta. \tag{2.78}$$

Eq. (2.78) gives $w_{\mathrm{c}}^* = 2\pi$ when $\beta \to \pi$.

(iii) Intermediate soil

For the intermediate soil model, $\left(\frac{\mathrm{d}a}{\mathrm{d}t}\right)_{\mathrm{P}} = \frac{\sigma}{p(A+Bp^3)}$ and $v_{\mathrm{jet}} = \frac{\sigma}{a_{\mathrm{x}}(A+Ba_{\mathrm{x}}{}^3)}$. Substitution into (2.76) gives

$$\frac{\mathrm{d}p^*}{\mathrm{d}\beta} = \frac{1}{\sin\beta}\left(\frac{b_{\mathrm{x+1}}}{b_{\mathrm{x}} + p^{*3}}\right) - \frac{p^*}{\tan\beta} \tag{2.79}$$

where $b_{\mathrm{x}} = A/Ba_{\mathrm{x}}^3$. This requires numerical solution.

These models do not include any contribution from M_{y}, which is discussed in Chapter 5.

2.4.7 Removal of Non-Newtonian layers

Fuller and co-workers (Hsu *et al.*, 2011, 2014; Walker *et al.*, 2012) investigated the displacement of different non-Newtonian layers by impinging water jets. An important lesson to be taken from these studies is that the interaction between the Newtonian liquid jet and the non-Newtonian layers depends on the nature of the layer. Figure 2.19 shows the jet region after 0.05 s of impingement on layers of: (a) a Newtonian glycerol-water solution, (b) a viscoelastic polyacrylamide dispersion, (c) a shear-thinning xanthan gum dispersion and (d) an elastic Boger fluid. The Boger fluid is a dilute dispersion of a viscoelastic polymer in a high viscosity liquid, such that the decrease in viscosity due to the addition of polymer is negligible, allowing the effect of elasticity to be evaluated separately from shear-thinning phenomena (James, 2009).

Layers with no significant elasticity (a,c) show a “stepped jump”, as defined by Hsu *et al.* (2014): the liquid jet penetrates through the coating fluid and peels it away layer by layer, and this was attributed to be a result of instabilities due to the different velocities of the jet and coating fluid. The interface between the water from the jet and the coating fluid for coating layers with elasticity (b,d), on the other hand, was different: the elasticity of the coating layer suppresses inertial instabilities but leads to the development of narrow radial fingers.

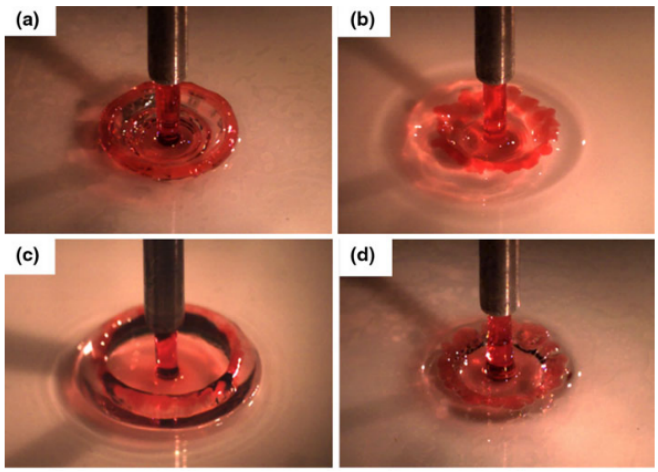

Figure 2.19 – Photographs of water jets (dyed red) impinging on flat surfaces after approximately 0.05 s of jet impingement coated with different layers: (a) Newtonian glycerol-water solution, (b) polyacrylamide dispersion, (c) xantham gum and (d) a Boger fluid. Adapted from Hsu *et al.* (2014).

Hsu *et al.* (2014) also reported instabilities at the liquid-soil interface at longer times after impingement. Figure 2.20 shows the water jet (in white) impinging on blue-dyed (a) Newtonian, (b) viscoelastic, (c) shear thinning and (d) elastic Boger fluid layers. All four materials show unstable interfaces with fingers, which is attributed to instabilities present in displacement flows of fluids with different viscosities. The fingers were narrower for the shear-thinning fluid, Figure 2.20 (c) since the flow at the interface between the two fluids increases the local shear rate and reduces the viscosity of the layer. The viscoelastic fluids, (b) and (c), showed flatter fingers. The fingers grew radially outwards, and the flow in the layer was predominantly extensional in the radial direction. Normal stresses in the azimuthal direction resulting from the elasticity of the layer then contributed to widen the fingers.

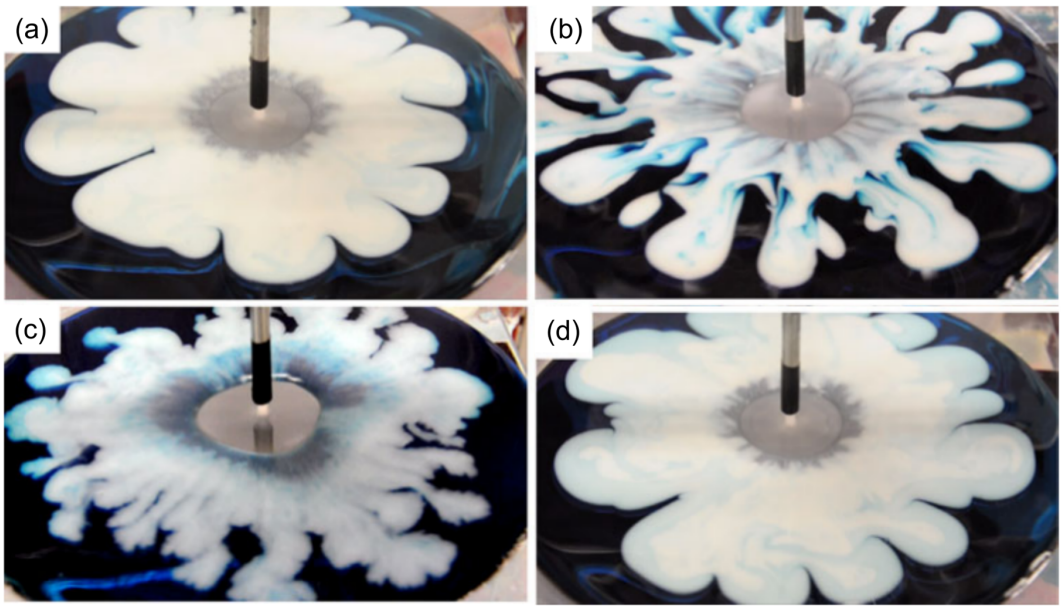

Figure 2.20 – Fingering patterns for water jets (dyed white) impinging on flat surfaces after approximately 3 s of jet impingement coated with fluids (dyed blue) of different rheologies: (a) Newtonian glycerol-water solution, (b) polyacrylamide dispersion, (c) xantham gum and (d) a Boger fluid. Adapted from Hsu *et al.* (2014).

Walker *et al.* (2012) and Hsu *et al.* (2011) also conducted experiments to evaluate the effect of the layer rheology on the position of the hydraulic jump of the jet fluid. In these experiments, the water jet penetrated through the layer. The hydraulic jump of the water was then influenced by the rheology of the soil layer: the hydraulic jump radius increased over time until reaching a stable value when the coating fluid was Newtonian (Walker *et al.*, 2012) and shear thinning (Hsu *et al.*, 2011). With the viscoelastic layer, the hydraulic jump radius increased to a maximum value and subsequently retracted to a smaller value (Hsu *et al.*, 2011, 2014), which was attributed to an elastic recoil effect resulting from the elasticity of the layer.

Rodgers *et al.* (2019) presented an experimental investigation of the cleaning of a white soft paraffin, a hydrophobic viscoplastic material, from flat surfaces using coherent water jets. They reported that the dislodged material accumulated in a berm that is rolled back by the jet flow. They demonstrated this by dyeing a portion of the rim after 60 s of flow and tracking it over time. Figure 2.21 illustrates this phenomenon, which is consistent with the cohesive flow of a viscoplastic material.

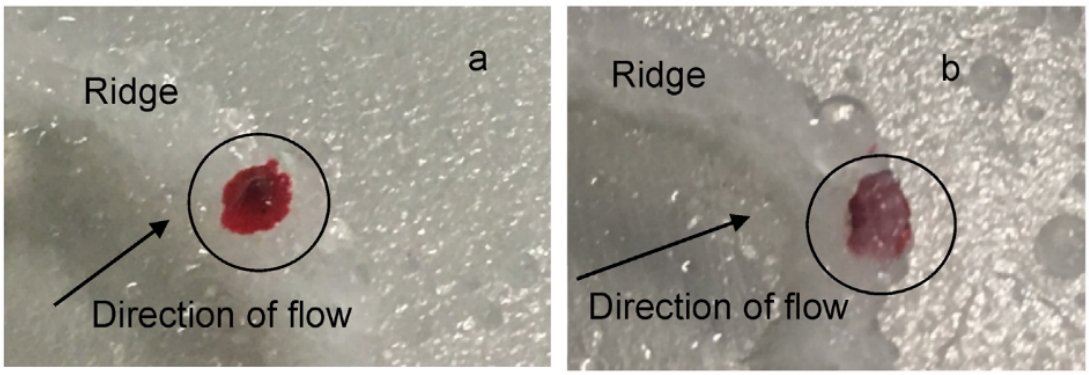

Figure 2.21 – Dyed berm of white soft paraffin at (a) 60 s and (b) 180 s after jet impingement. Image scale not available. Adapted from Rodgers *et al.* (2019).

2.5 Summary

This chapter presented a literature review of the topics relevant to this thesis. The rheology of viscoplastic fluids is an ongoing field of research, and significant advances have been made in the recent literature to understand their behaviour in the pre-yielding regime, below the yield stress. The cleaning of soil layers by impinging jets has also been the topic of recent studies, which have indicated that understanding the role of the rheology of the soil on its cleaning behaviour is a topic that needs further investigation. Although phenomenological descriptions of the adhesive removal of soil layers are available, the understanding of cleaning viscoplastic soils by impinging jets has not been widely explored in the literature. This thesis aims to investigate the cleaning of viscoplastic soil layers by impinging jets, and to provide a deeper understanding of how the rheology of the layer influences the cleaning behaviour.

3 Materials and methods

3.1 Cleaning apparatus

Cleaning experiments were conducted using the impinging jet apparatus used by Glover *et al.* (2016), with some minor modifications. Figure 3.1 shows (a) a schematic representation and (b) a photograph of the impinging jet rig. A 40 l deionised water tank (1) feeds a centrifugal pump (2) that supplies the system. The flow rate is controlled using a ball valve (3) and a rotameter (4), which then directs the water to a 1 m long hose (5) before entering a 150 mm long pipe (internal diameter 9.5 mm), at the end of which is a 55° convergent brass nozzle (6) with diameter $d_{\mathrm{N}} = 2$, 3 or 4 mm. An interrupter plate mechanism activated by a string pull (7) was mounted on the pipe. This allowed the operator to initiate flow onto detachable 150×150×5 mm or large 360×600×5 mm target plates (8), to the floor of the chamber and to drain (9), so the water was not recirculated. The system is contained in a Perspex® walled chamber, of dimensions 1×1×2 m.

Moving jet experiments were primarily performed using the large target plates. Relative motion between the jet and the target was provided by vertical movement of the target. This allowed visualisation of the cleaning patterns by a stationary camera and avoided vibrations and instabilities induced by the motion of the nozzle. The target plate was connected to a variable-speed electrical motor (10) via a rubber-toothed belt that allowed upward and downward movement of the target.

Experiments were filmed at 1920×1080 pixels resolution using either (i) 60 frames per second (fps) with a Nikon D3300 D-SLR digital camera, or (ii) 50 fps with a Sony HX80 camera (11). The Nikon camera was used with a polarizing filter to reduce bright spots caused by reflection. Lighting was provided by two commercial studio light diffusers (12), located behind the camera. Since the target plates (either Perspex® or glass) and the wall chambers are transparent, experiments could be filmed from the dry side of the plate. The tests were performed at room temperature, which was kept between 18 and 22 °C.

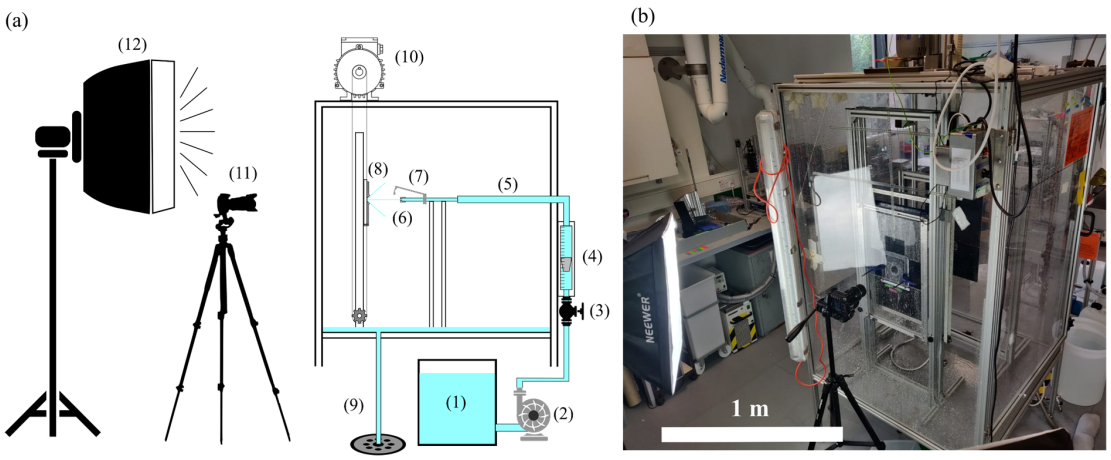

Figure 3.1 (a) Schematic representation and (b) photograph of the impinging jet rig. Numbered items discussed in the text

The nozzle-plate standoff distance was set to 60 mm. The Weber numbers (ratio between forces due to inertia and to surface tension) for the liquid (We_{L}) and air (We_A), as well as the Ohnesorge (Oh) number, which relates viscous forces to inertial and surface tension forces, given by Eq. (3.1) to (3.3), respectively, were calculated to identify the disintegration regime of the liquid jet. Here, ρ_{A} is the density of air.

$$We_{\mathrm{L}} = \frac{\rho_{\mathrm{L}} U_{\mathrm{o}}^2 d_{\mathrm{N}}}{\gamma_{\mathrm{st}}} \tag{3.1}$$

$$We_{\mathrm{A}} = \frac{\rho_{\mathrm{A}} U_{\mathrm{o}}^2 d_{\mathrm{N}}}{\gamma_{\mathrm{st}}} \tag{3.2}$$

$$Oh = \frac{\mu_{\mathrm{L}}}{\sqrt{\rho_{\mathrm{L}} d_{\mathrm{N}} \gamma_{\mathrm{st}}}}. \tag{3.3}$$

The criteria for describing the flow disintegration regimes are given in Table 3.1, which are taken from Ranz (1956) and Sterling and Sleicher (1975). The flow conditions employed used in this work were either in the Rayleigh or in the first wind-induced regimes, with $278 \leq We_{\mathrm{L}} \leq 5{,}700$, $0.3 \leq We_{\mathrm{A}} \leq 7$ and $1.9 \cdot 10^{-3} \leq Oh \leq 2.6 \cdot 10^{-3}$. The jet coherence was also confirmed visually.

Table 3.1 – Criteria for liquid jet disintegration regime. Adapted from Dumouchel (2008)

Disintegration regime	Condition
Rayleigh regime	$We_{\mathrm{L}} > 8$
	$We_{\mathrm{A}} < 0.4$
First wind-induced regime	$1.2 + 3.41\, Oh^{0.9} < We_{\mathrm{A}} < 13$

In the Rayleigh regime, the liquid column is disturbed by a single axisymmetric perturbation, which wavelength is of the same order of d_N. In the first-wind regime, this perturbation grows, although the flow is still relatively axisymmetric near the nozzle exit (Dumouchel, 2008).

3.2 Soil materials

A number of materials were used as soils for experimental investigations. Most experiments were performed with a commercial petroleum jelly (GPC5220-5Y, Atom Scientific, UK), provided by APC Pure, hereafter referred to as PJA. This material was provided in 5 kg containers, ensuring that all experiments were conducted with material from the same batch, thus reducing between-batch variability. Petroleum jelly (or petrolatum) has been used as a model soil material for cleaning experiments (Wilson *et al.*, 2014; Glover *et al.*, 2016; Bhagat *et al.*, 2017; Feldung Damkjær *et al.*, 2017; Fuchs *et al.*, 2019b), as it is commercially available and insoluble in water. Petroleum jellies are used as ointment bases and cosmetic vehicles for the pharmaceutical and cosmetics industries (Ogita *et al.*, 2010). The jelly is a translucent material derived from waxy crude oil, being a mixture of different chain length hydrocarbons, some of which are in the solid and others in the liquid state at room temperature (Park & Song, 2010a). Since the solids fraction is not specified, petroleum jellies provided by different suppliers often exhibit different rheologies. Other experiments were also performed with a second white petroleum jelly (Merkur 500, Sasol, South Africa) and a white soft paraffin, provided by GlaxoSmithKline (UK), hereafter referred to as PJS and WSP, respectively.

Overall, petroleum jellies behave as soft solids at room temperature. Like other waxy materials, such as waxy crude oils (Marchesini, 2012) and waxy oils (Dimitriou *et al.*, 2011), the rheology of petroleum jellies is affected by their thermokinematic memory (Geri *et al.*, 2017). This means that their temperature and deformation histories affect their microstructure and ultimately dictate their rheological behaviour. As a precaution, all materials were stored in the room in which the experiments were performed, which was kept at approximately 20 °C. Additionally, coated plates were left to rest for 30 min before cleaning experiments, as discussed in Chapter 4.

3.3 Rheology

The rheological behaviour of the soil materials was investigated with rotational rheometers. Rough and serrated and smooth parallel plates (40 mm diameter), a 4-blade vane tool ($R_{\text{blade}} = 7$ mm, $R_{\text{cup}} = 13.75$ mm, $h_{\text{blade}} = 61$ mm) and smooth cone-plate (40 mm diameter, 4° angle) geometries were used in a stress-controlled rheometer (Kinexus Lab+, Malvern Instruments, UK). Smooth parallel plates (60 mm diameter) and cone-plate (60 mm diameter, 4° angle) geometries were used in a strain-controlled rheometer (ARES, TA Instruments, USA). The temperature was controlled at 20 °C, matching the room temperature at which cleaning experiments were performed, using Peltier (Kinexus) and water-bath (ARES) systems.

3.4 Coating procedure

Layers of uniform thickness δ_o were prepared on the target plates using the spreader tool shown in Figure 3.2, which was described by Cuckston *et al.* (2019).

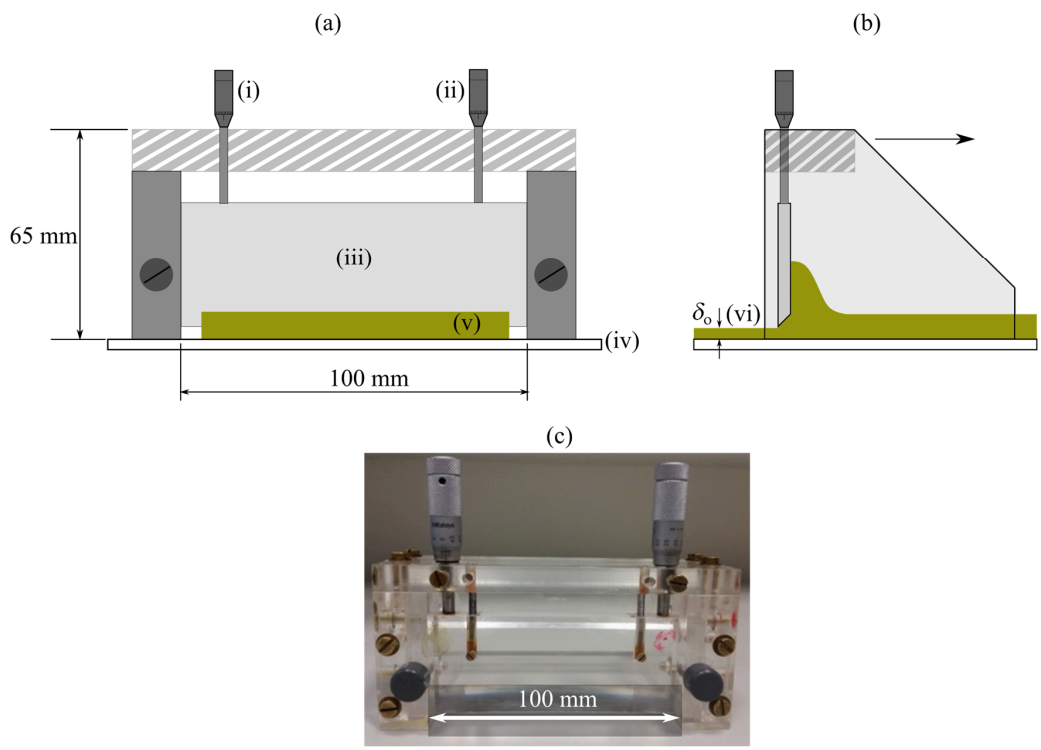

Figure 3.2 – Schematic representation of (a) front and (b) side views and (c) photograph of the front view of the spreader tool. Arrow in (b) indicates the direction of movement of the tool.

Two micrometers (i and ii) set the height of the blade (iii). The spreader is manually dragged over a plate (iv) on which the soil has been previously loaded with a spatula (v). The blade then leaves a layer of given thickness (vi) behind. The average thickness of the soil layer was calculated from the weight of the coated plate and the area coated, measured using the image analysis software ImageJ, and the density of the soil, which was measured by filling Petri dishes of known volume (25.4 mL) and weighing on a digital balance. The majority of the target plates employed were made of Perspex®, and some experiments were performed with glass targets. Both materials were transparent and had an average roughness of approximately 0.03 μm (Lepore *et al.*, 2008).

3.5 Cleaning experiments

3.5.1 Cleaning scenarios considered

The interrupter plate was held in place for at least 30 s after the pump was started to ensure that a stable water jet formed. When the interrupter was lifted, the jet impinged on the soiled surface, leaving behind a roughly circular cleaned region. Figure 3.3 shows typical examples of the cleaning scenarios considered. When a coherent water jet impinges on a soiled surface, it penetrates through the layer (a) and expands radially. The liquid is deflected backwards and leaves a roughly circular cleaned region that grows over time. As will be discussed in Chapters 5 and 6, the initial thickness of the soil layer influences the cleaning mechanisms. If the soil layer is too thin, or if the liquid film generated by the impinging jet is too thick, the liquid flows over the soil layer and a circular cleaned radius is not evident. An example of this case is shown in Figure 3.3 (b). In this work, soil layers of $\mathcal{O}$ (0.1 – 1) mm were investigated, which was sufficient to cover both regimes.

Images were processed using a Matlab™ script that detected the shape of the cleaned region by thresholding the pixels between the cleaned and soiled regions. Both digital cameras generated RGB images, meaning that each pixel contained information from the red, green and blue channels. These were converted to HSV (Hue, Saturation and Value) images, and the third channel (Value) was chosen to perform the image analysis. A contrast correction was performed using the *imcorrect* function, based on the values of the brightest and darkest pixels present in each image.

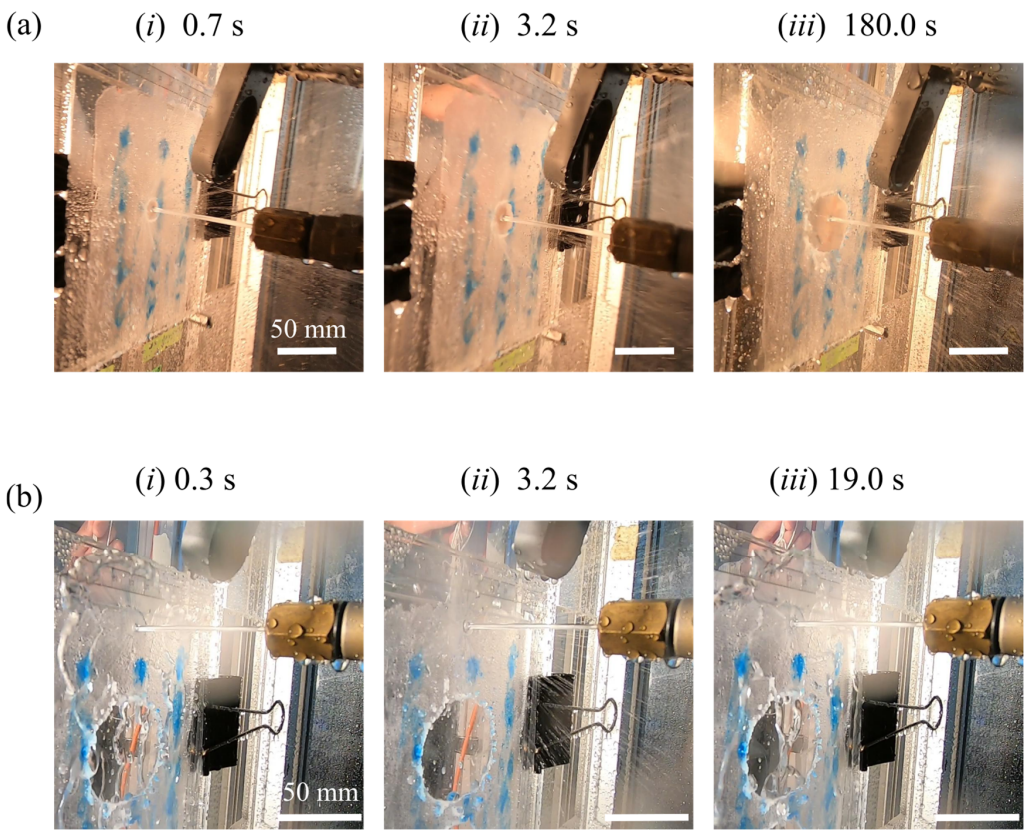

Figure 3.3 – Examples of cleaning scenarios investigated. Cleaning of layers of PJS coated on Perspex® plates by impinging coherent turbulent water jets. (a) Thin soil layer case, when the liquid jet penetrates through the layer and leaves a roughly circular cleaned region. (b) Very thin soil layer case, when the liquid film flows over the soil layer. Labels indicate the time elapsed since jet impingement. The soil layer was dyed for visualisation of the cleaning front.

The first step of the image analysis was to identify the impingement point. A radial band of height corresponding to 10 pixels was then isolated and the average intensity at each radial position along this band was calculated. These mean intensities were then divided by the largest intensity of the pixels along that radial band to give a normalised intensity in each direction. The cleaned radius was identified as the radial position at which the intensity surpassed a given threshold, which had to be calibrated for each experiment and ranged from 0.15 to 0.7. The cleaned radius measurements were taken at 1° intervals, so images were rotated using the *rotatearound* function (Motl, 2017). The effective cleaned radius a was then taken as the average of these 360 measurements, and the standard deviation provided an estimate of the uncertainty of a in each image. Figure 3.4 shows (a) a photograph of a

crater and (b) the detected border along with the circle with effective cleaned radius a. The time corresponding to each image was calculated from the frame rate of the camera used, and the uncertainty in time was approximated from the interval between frames.

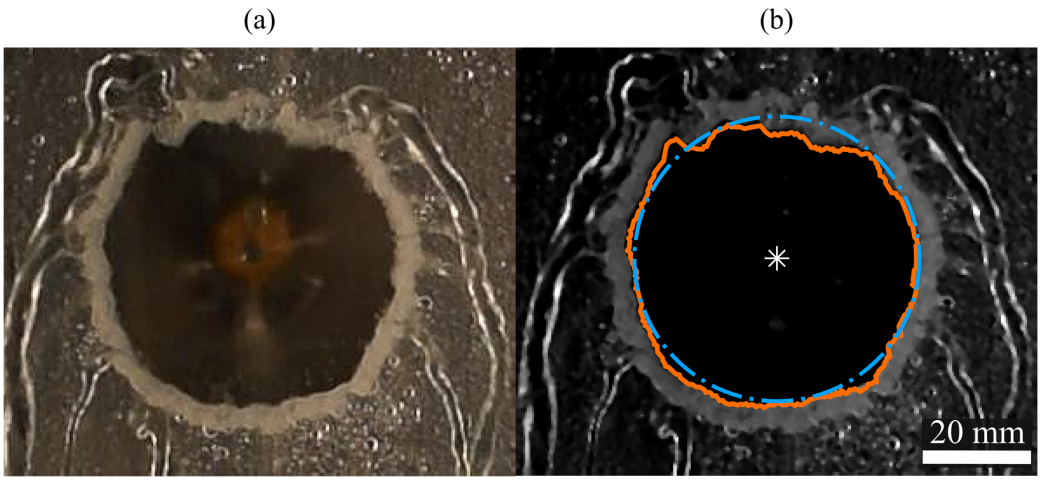

Figure 3.4 - Crater formed after impinging a layer of PJA with thickness δ_0=0.33 mm for 514 s with Q= 2.0 l·min^{-1}. (a) Photograph; (b) Treated image showing the impingement point (white star), the detected border of the cleaned region (continuous orange line) and the circle with equivalent radius a (dash-dotted blue circle).

3.5.2 Profilometry of the soil layers

For tests conducted with small target plates, the plate was detached from the rig after the experiment and the shape of the soil layer was measured by a confocal thickness sensor (ConfocalIDT IFS 2405-3, Micro-Epsilon, Germany) mounted on an automated *x*-*y* positioning stage, shown in Figure 3.5. The system is mounted on a vibration-damping optical bed to reduce external noise. Data acquisition and stage control were performed by a Python code, written by Dr Matthew Bryan and later modified by PhD student Jheng-Han Tsai. The sample was moved in the horizontal plane with step sizes Δx and Δy, and the local thickness was measured with a precision of 36 nm, within a maximum range of 3 mm (Micro-Epsilon, 2018). The thickness of the layer was measured relative to the height of the cleaned plate. A bullseye spirit level was used to ensure that the moving stage was parallel to the confocal scanner.

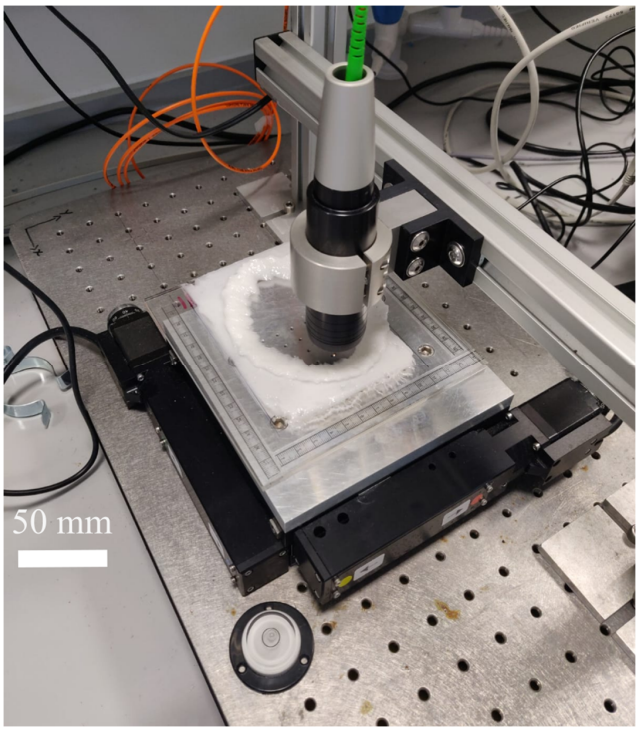

Figure 3.5 – Confocal thickness scanner system.

Figure 3.6 (a) shows a typical scanned crater, generated by a jet with d_N=2 mm and $Q = 2$ l·min^{-1} impinging on a 0.86 mm thick layer of PJA, coated on a vertical target plate. Scans were performed with $\Delta x = \Delta y = 1$ mm. Profiles of the crater were extracted from linear scans performed at four equally spaced azimuthal angles θ with $\Delta x = 0.05$ mm, as shown in Figure 3.6 (c). The θ=270° direction corresponded to the downward direction during the impinging jet experiments. The horizontal axis represents l, the distance from the start of the rim, shown schematically in Figure 3.6 (b). There was a thin residual film of petroleum jelly (thickness of order microns) in the cleared region, indicating that removal did not involve true adhesive detachment from the substrate.

Values of two characteristic angles (gradients) were measured, as indicated in Figure 3.6 (d). These were (*i*) the slope at the base of the rim, labelled ϕ_1, and (*ii*) the gradient of the front at the initial layer height, δ_o, labelled ϕ_2. The Glover *et al.* (2016) model assumed a linear ramp, *i.e.* $\phi_1 = \phi_2$.

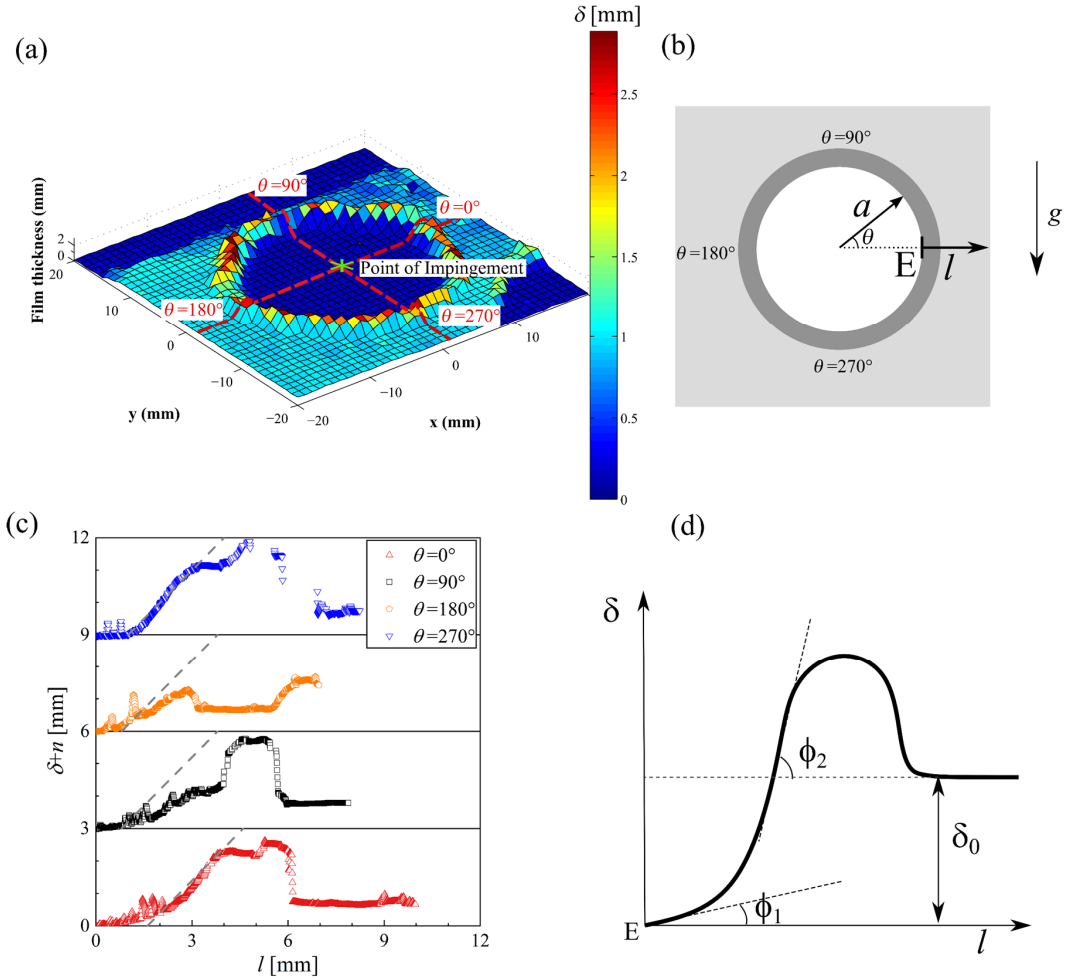

Figure 3.6 - Example of profilometry of the soil layers after cleaning. (a) three-dimensional scan of the crater for $Q = 2$ l·min^{-1}; $\delta_o = 0.86$ mm; t =0.5 s; $\Delta x = \Delta y$ =1 mm; (b) – Coordinates used to describe the shape of the rim in (a); (c) Profiles of the crater in (a). The vertical axis is the thickness of the layers scanned at the four values of θ, shifted to aid visualisation of the data. The horizontal coordinate shows the distance l from the edge of the rim, E, and the grey dashed lines represent an inclination of 45º plotted as a guide to the eye. (d) Schematic representation of the shape of the rim, indicating angles ϕ_1 and ϕ_2.

3.6 Millimanipulation

As discussed in Chapter 2, cleaning can be a result of cohesive or adhesive failure of the soil layer. Scraping devices, in which blades are moved over soiled surfaces, impose a known deformation and induce flow of the soil layer whilst measuring the force required to do so (Ashokkumar & Adler-Nissen, 2011; Maillard *et al.*, 2016). The millimanipulation device

developed by Ali *et al.* (2015) consists of a vertical blade that moves through a layer of material coated on a substrate. By changing the blade-substrate distance, cohesive failure (within the soil) and adhesive failure (between the soil and the substrate) can be induced. By measuring the resultant horizontal force at the blade, it is possible to quantitatively evaluate the removal of the materials from the surface. A similar device was developed by Magens *et al.* (2017) to study the removal of cake from steel surfaces and later modified by Cuckston *et al.* (2019) to study the removal of a burnt complex food soil. Figure 3.7 illustrates the deformation of soils that undergo (a) cohesive and (b) adhesive failure. The type of failure depends on the nature of the soil and of the substrate. Another blade-scraping device was used to investigate the blade coating of Carbopol® from flat surfaces by Maillard *et al.* (2016).

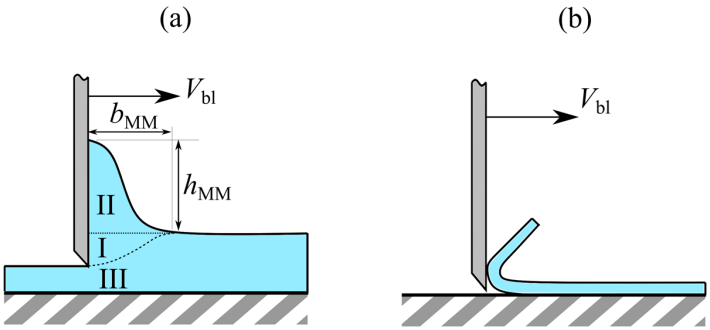

Figure 3.7 – Schematic representation of the millimanipulation device action for (a) cohesive and (b) adhesive removal.

This work focuses mainly on cohesive soil layers. When removing cohesive soils, the horizontal force acting on the blade is composed of three contributions, as indicated in Figure 3.7 (a): that required to deform the layer ahead of the blade (I); that to dislodge the material upwards in a berm that builds up to a height h_{MM} and extends along the length b_{MM} (II); and the force required to overcome the shear resistance at the base of the blade (III). The latter component is reduced by using a blade with a chamfered edge. The millimanipulation device provides local measurements of the flow and deformation behaviour of soil layers. There is a strong need to determine the rheology of such soil layers *in situ* as they are often generated from the original product by the conditions local to the surface, and this is discussed in more detail in Chapter 4.

The millimanipulation device, presented in Figure 3.8, was used to evaluate the cohesive behaviour of the soil removal under an external force. It is similar to that used by Magens *et al.* (2017) and Cuckston *et al.* (2019) and was used to estimate the critical stress of different

soil layers, discussed in Section 4.2. Samples were coated on a stainless steel plate (dimensions 25×100×0.65 mm) using the scraping device in Figure 3.2. The edges of the samples were then trimmed using a metallic spatula to ensure straight edges.

A sample (1) is mounted on a moving platform (2), which is controlled in the x and z-directions using two linear slides (Standa 8MVT40-13-1-MEn1 and Standa 8MT50-100BS1-MEn1, respectively, labelled 3 and 4 in Figure 3.8). A vertical blade (5) (dimensions 25×20×1.5 mm) is positioned at the end of a lever arm, which is mounted on a frictionless pivot, and a force transducer (ME-Meßsysteme GmbH KD40s ±2 N) (6) measures the force as the blade scrapes the material from the substrate. The analogue signal from the force transducer is amplified and logged by an I/O device (National Instruments, USB-6009, 8 AI (14-Bit, 48 kS/s)), then converted to force per unit width of the blade (F_w) using a separate calibration. The data were collected and processed using a Matlab® script. Experiments were visualised from the side of the blade using a digital camera (7) held in place with a retort stand.

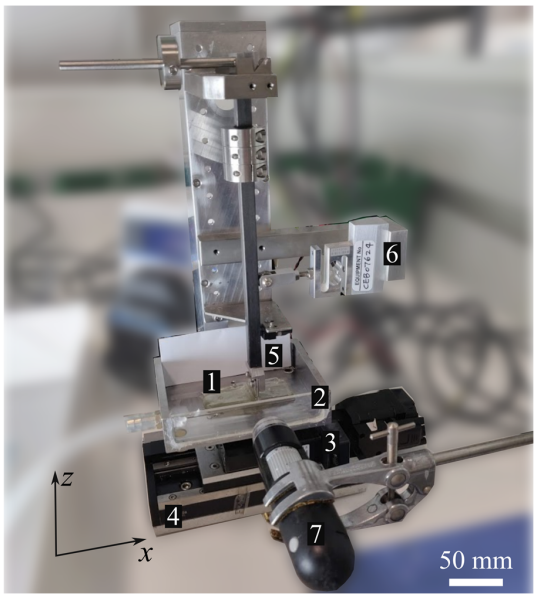

Figure 3.8 – Photograph of the millimanipulation device with the camera visualisation set-up.

4 Rheology of the soil materials

To understand the role of rheology on the cleaning of viscoplastic soil layers, the first step is to characterise the rheology of the soils. In this chapter, two characteristics of the soils will be explored. The first is the ageing behaviour: since the rheology of time-dependent materials depends on their shear history, it is important to impose similar shear histories on samples to obtain repeatable results. The second characteristic is the yielding behaviour. The critical stress directly affects the cleaning rate of viscoplastic soils (see Figure 2.17), and it was investigated using two different techniques. The first, rotational rheometry, is a well-established traditional technique. In the second method, millimanipulation is used to estimate the yield stress of the soil layers *in-situ*.

The rotational rheometry aspects have been reported in Fernandes *et al*. (2019) and Fernandes and Wilson (2020) and are used to support the cleaning models discussed in Chapters 5 and 6. The critical stress estimation using the millimanipulation device has been submitted for publication in the *Journal of Food Engineering* and is currently under review. Preliminary results have been reported in Tsai *et al.* (2020).

4.1 Rheological characterisation of the soil layers

4.1.1 Ageing behaviour

Before conducting cleaning experiments, it is important to ensure that the soil layers on the plates have the same rheological properties as those measured in the rheometer. Many semi-solid materials, such as petroleum jellies (Park & Song, 2010b), exhibit time-dependent behaviour, where the critical stress increases with the ageing time as a result of structural recovery (Fernandes *et al.*, 2016; Marinho *et al.*, 2018). Therefore, it makes sense to coat the plates and let them rest to ensure that the coated material has reached a known state. According to Mewis and Wagner (2009), one non-destructive way to quantify the structural recovery in rotational rheometers is to apply a low amplitude oscillatory shear at constant strain or stress amplitude. If the material is probed in the linear viscoelastic regime, its microstructural recovery is quantified by the evolution of the storage modulus, G', over time. This has been used, for instance, by Mahaut *et al.* (2008) and Bonacci *et al.* (2020) to characterise the ageing behaviour of bentonite dispersions and concentrated PMMA and silica suspensions, respectively.

Figure 4.1 presents the elastic modulus, G', and the loss modulus, G'', for the three materials used in cleaning experiments: the PJA, the PJS and the WSP. These experiments were conducted with a constant stress amplitude of 1 Pa and frequency 1 Hz over 1800 s using rough parallel plates in the Kinexus stress-controlled rheometer. Similar behaviour is observed for the three substances: both G' and G'' increase over time, reaching approximately constant values after approximately 600 s. The values of G' are considerably larger than G'', indicating viscoelastic (semi-solid) behaviour of the materials when at rest (Ewoldt *et al.*, 2010; Ewoldt & McKinley, 2017). Based on these data an ageing (wait) time of 30 min was observed after coating the three materials to ensure that the soils were in a reproducible state at the start of each cleaning experiment.

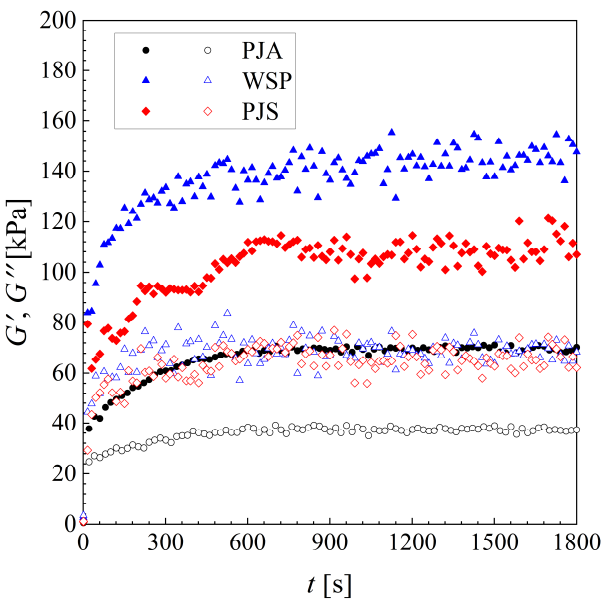

Figure 4.1 – Evolution of dynamic moduli for a constant shear stress amplitude oscillatory sweep at frequency 1 Hz for the materials used in cleaning experiments. Filled symbols G', hollow symbols G''.

4.1.2 Choice of the measuring geometry

It is important to ensure that the measuring geometry is suitable for making measurements on the test materials. Figure 4.2 shows the shear stress as a function of the shear strain for a series of increasing shear stress steps, each lasting for 30 s, performed with the PJA after 30 min of ageing. The protocol was repeated with four measuring geometries: vane, rough plates, serrated plates and smooth cone-plate. All geometries show similar responses at low strains, suggesting that wall slip effects were not present when the material was within the

elastic regime. The yielding transition takes place at a similar shear stress for the vane and the parallel plates. The slight deviation from linear elasticity at low stresses with the vane tool is probably due to insufficient filling of the cup: the material was loaded with a spatula, so voids could have been introduced in the sample. The cone and plate tool shows a yielding transition at a lower shear stress, which is associated to slip effects resulting from the smooth surface of the tool.

Figure 4.2 suggests that both the vane tool and the parallel plates are good candidates for measuring the rheological behaviour of the material. The measurements performed with the vane are not so reliable when the fluid is flowing, as recirculation between the tips of the vane can occur (Marchesini *et al.*, 2015; Owens *et al.*, 2020). Since the parallel plates require a smaller volume of sample to be used in each experiment when compared to the vane, rough and serrated plates were used in the subsequent studies.

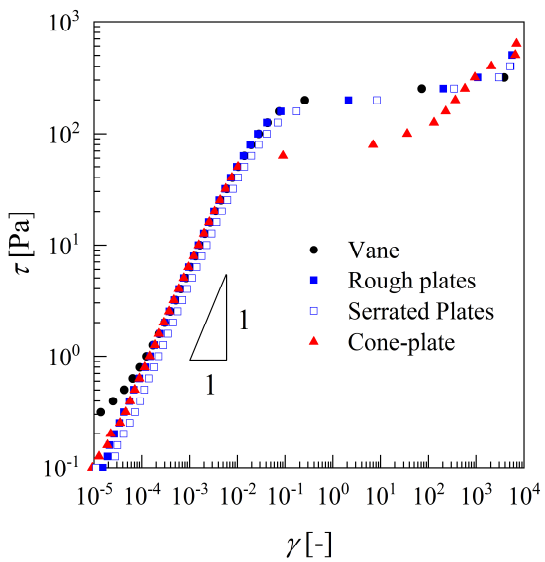

Figure 4.2 – Shear stress as a function of the shear strain for shear stress steps measured with four different tools in the Kinexus rheometer. PJA, 20 °C.

4.1.3 Critical stress measurement

4.1.3.1 Creep tests

As discussed in Chapter 2, creep tests at constant shear stress can be used to evaluate the critical stress of time-dependent yield stress materials (Coussot *et al.*, 2002b). A constant

shear stress step is imposed, and the apparent viscosity is calculated from the resultant shear rate, such that a bifurcation in viscosity evolution is observed at the critical stress. The method is strongly dependent on the duration of the test since delayed yielding can occur below the values associated with the critical stress probed at shorter time scales (Bonn *et al.*, 2017). A characteristic time scale representative of the application must therefore be chosen to estimate the critical stress.

Since cleaning experiments lasted from 0.2 to 600 s, each shear stress was imposed for 300 s. Figure 4.3 presents the shear rate as a function of time for these creep tests under different imposed stresses for the PJA, which is the material used in Chapter 5. There is a noticeable change in behaviour between 212 Pa and 214 Pa, exhibiting the transition reported by Coussot *et al.* (2002b). Below 212 Pa, the material creeps and the shear rate tends to low values, indicating a predominantly elastic regime. Shear stresses above 214 Pa lead to higher values of shear rate, indicating a viscous response (Da Cruz *et al.*, 2002). This gives a critical stress, τ_c, for this material of 212±1 Pa. This is of similar magnitude of the yield stress reported for hand creams (Stokes & Telford, 2004; Kwak *et al.*, 2015), for a fat-free yoghurt (Daubert *et al.*, 1998) and for some toothpastes (Barnes, 1999a; Ahuja & Potanin, 2018).

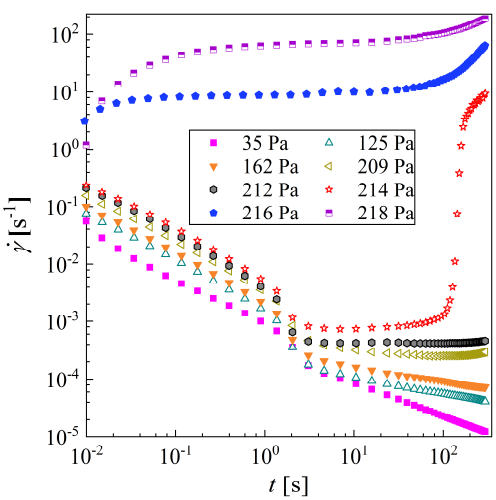

Figure 4.3 - Shear rheometry of the PJA: evolution of shear rate for creep tests, roughened parallel plates.

4.1.3.2 Increasing shear stress ramps

The critical stress can also be determined using increasing steady shear stress ramps starting from rest (Chang *et al.*, 1998; Andrade & Coussot, 2020). The shear stress was increased for the PJA at $\dot{\tau}$ = 10 Pa·min^{-1}, using rough parallel plates. Some experiments were also performed with a (relatively smooth) Perspex® base to check if wall slip is likely to arise with surfaces similar to those used in the cleaning experiments. Dimitriou *et al.* (2011) observed wall slip in model waxy crude oils on smooth surfaces: these partially crystallised materials are similar in nature to the petroleum jelly. Different gaps were used, following the Yoshimura and Prud`homme (1988) protocol for studying wall slip. If significant slip was present, a noticeable difference between the stress-strain curves for different gaps would be observed. Figure 4.4 (a) compares results obtained with the rough base (gap 1.0 mm), and with the smooth Perspex® base, shown in (b), with 0.5 and 1.0 mm gaps. At strains above 0.1%, the material response is roughly independent of both surface and gap, indicating that wall slip is unlikely to occur in the cleaning experiments. However, slip effects were evident at strains below 0.1%, which were enhanced by a (i) smoother surface and (ii) smaller gap.

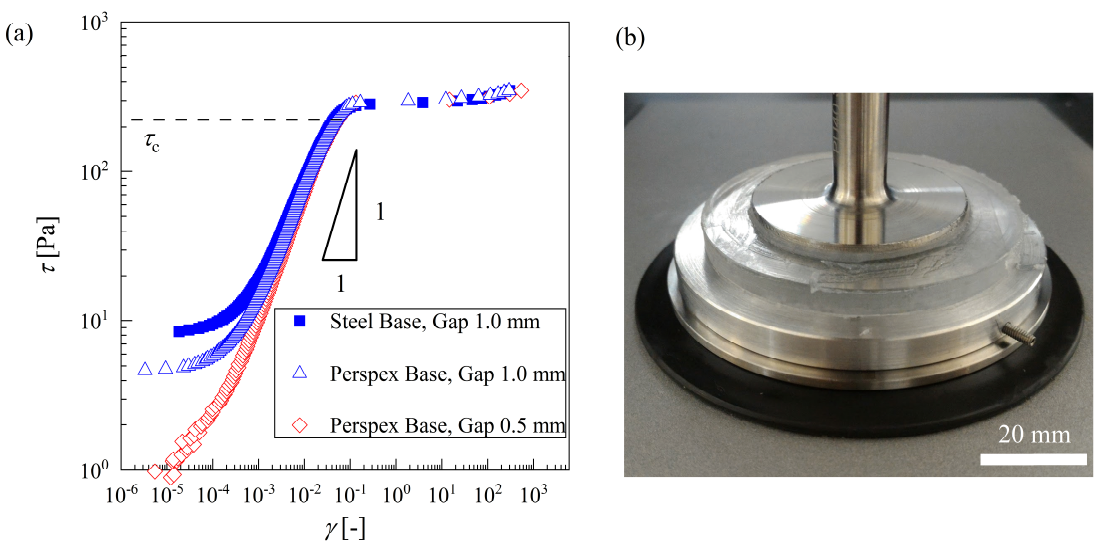

Figure 4.4 – (a) Shear stress as a function of shear strain for shear stress ramps conducted with steel and Perspex® bases for the PJA; (b) Perspex® base adapted to the parallel plate tool used in the Kinexus rheometer for the experiments reported in (a)

The plot shows that the value of τ_c found from the creep experiments, $\tau_c = 220$ Pa, is consistent with the region where significant deformation is taking place during the yield transition. Below τ_c the material shows a predominantly Hookean behaviour (evidenced by

the unit slope in the log-log plot), which is consistent with the elastic behaviour expected when the material is unyielded. It is noteworthy that yielding takes place over a range of stresses and strains since the material starts to creep at $\tau \approx 100$ Pa, below the value of τ_c obtained from Figure 4.3. This is consistent with pre-yielding creep, such as reported by Lidon *et al.* (2017) and Donley *et al.* (2019), and is an important characteristic considered in the cleaning model developed in Chapter 5.

Shear stress ramps at a constant rate of 10 Pa·min^{-1} were also performed with the PJA, PJS and WSP using serrated parallel plates, and these results were used in the detailed cleaning model in Chapter 6. These experiments were conducted almost 2 years after those reported in Figure 4.4, and the behaviour of the PJA had changed due to ageing during storage. Figure 4.5 (a) shows the shear stress as a function of the shear rate for these experiments. Similar behaviour was observed for the three soil materials: the shear rate gradually increases when the materials are below the respective critical stress and increases rapidly as the critical stress is approached. The lines in Figure 4.5 (a) indicate the fits of the Bingham model, Eq. (2.22), to the data for $\tau > \tau_c$.

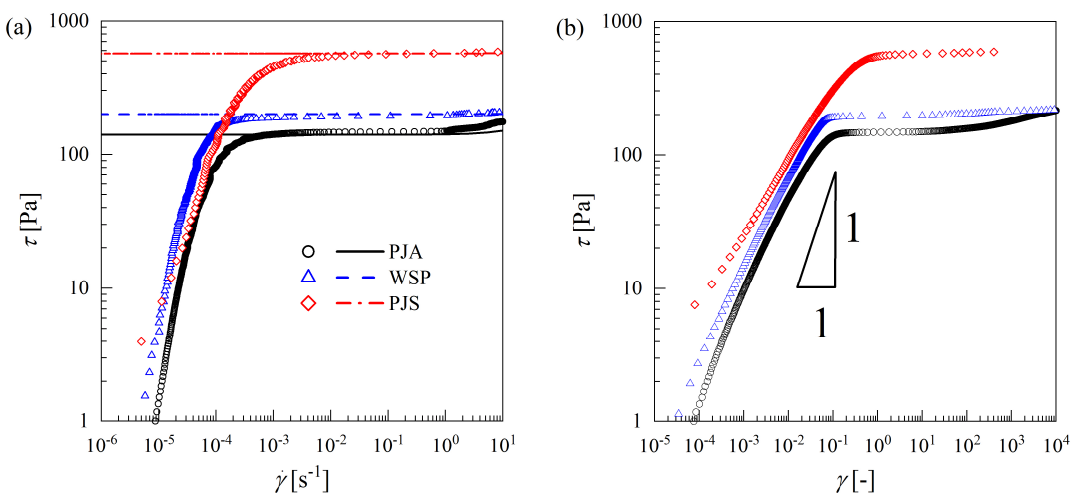

Figure 4.5 – Shear stress as a function of (a) shear rate and (b) shear strain for shear stress ramps ($\dot{\tau} = 10$ Pa·min^{-1}) with the PJA, WSP and PJS. Lines in (a) indicate the Bingham fits above τ_c. The unit gradient within the elastic regime in (b) indicates good agreement with the Hookean behaviour at modest strains

The behaviour at shear stresses below τ_c is again predominantly elastic, as shown in the stress-strain curves in Figure 4.4 (b). Close to the critical stress, the shear rate gradually

increases, indicating that creep is taking place (Coussot *et al.*, 2002b; Da Cruz *et al.*, 2002). This creeping effect is not captured by the Bingham model, which assumes a perfectly rigid state below the critical stress. Above the critical stress, the shear rates sharply increase, indicating that the materials are deforming quickly at these levels of shear stress. The PJS and WSP display predominantly plastic behaviour, indicated by the significant increase in strain over a small increase in shear stress, Figure 4.4 (b). This results in the low values of the Bingham viscosity μ_B in Table 4.1, which also reports the material densities.

Table 4.1 – Soil material properties. Uncertainty in ρ_s was obtained from the standard deviation of triplicate measurements.

Material	Source	Acronym	ρ_s [kg·m^{-3}]	τ_c [Pa]	μ_B [Pa·s]
White petroleum jelly	Atom Scientific, UK	PJA	812±13	140	1
White soft paraffin	GlaxoSmithKline, UK	WSP	838±88	200	0.1
Petroleum jelly Merkur 500	Sasol, South Africa	PJS	826±14	570	0.3

The normal stress differences were also evaluated (Macosko, 1994). The first normal stress difference, N_1, was measured in stress ramps performed with a cone-plate geometry (20 mm radius, 4° angle) with smooth surfaces, and was calculated with Eq. (2.9). The difference between the first and second normal stress differences, $N_1 - N_2$, was obtained using rough parallel plates (20 mm radius, 1 mm gap), using Eq. (2.10).

The stress ramps were performed with the same rate of increase of the shear stress ($\dot{\tau}$ =10 Pa·min^{-1}) at 20 °C, and the results are shown in Figure 4.6 for (a) PJA, (b) WSP and (c) PJS. Cone-plate experiments performed with the PJS presented significant slip, which prevented further analysis of the data, so these results are not reported. All three materials exhibit increasing $N_1 - N_2$. The critical shear stress measured in the stress ramps and reported in Table 4.1 are indicated by the dashed vertical lines in Figure 4.6. The trends are similar to those reported by Thompson *et al.* (2018), de Cagny *et al.* (2019) and Habibi *et al.* (2016), where a non-zero value of the normal stress differences is observed. The increase in $N_1 - N_2$ below the critical stress is consistent with the results of Habibi *et al.* (2016). Thompson *et al.* (2018) argue that the normal stresses in pure-shear flows are significant when compared to the shear component of the stress tensor. However, de Cagny *et al.* (2019) reported that

the normal stress differences had a negligible effect on the equivalent von Mises stress of their three viscoplastic materials, an emulsion, a hair gel and a Carbopol® dispersion. More work is required to describe the influence of the normal stress differences on the equivalent von Mises stress when $\tau = \tau_c$. The cone-plate tool employed had smooth surfaces, so the results obtained with it are subject to slip near the critical stress, which can hinder further analysis of the results.

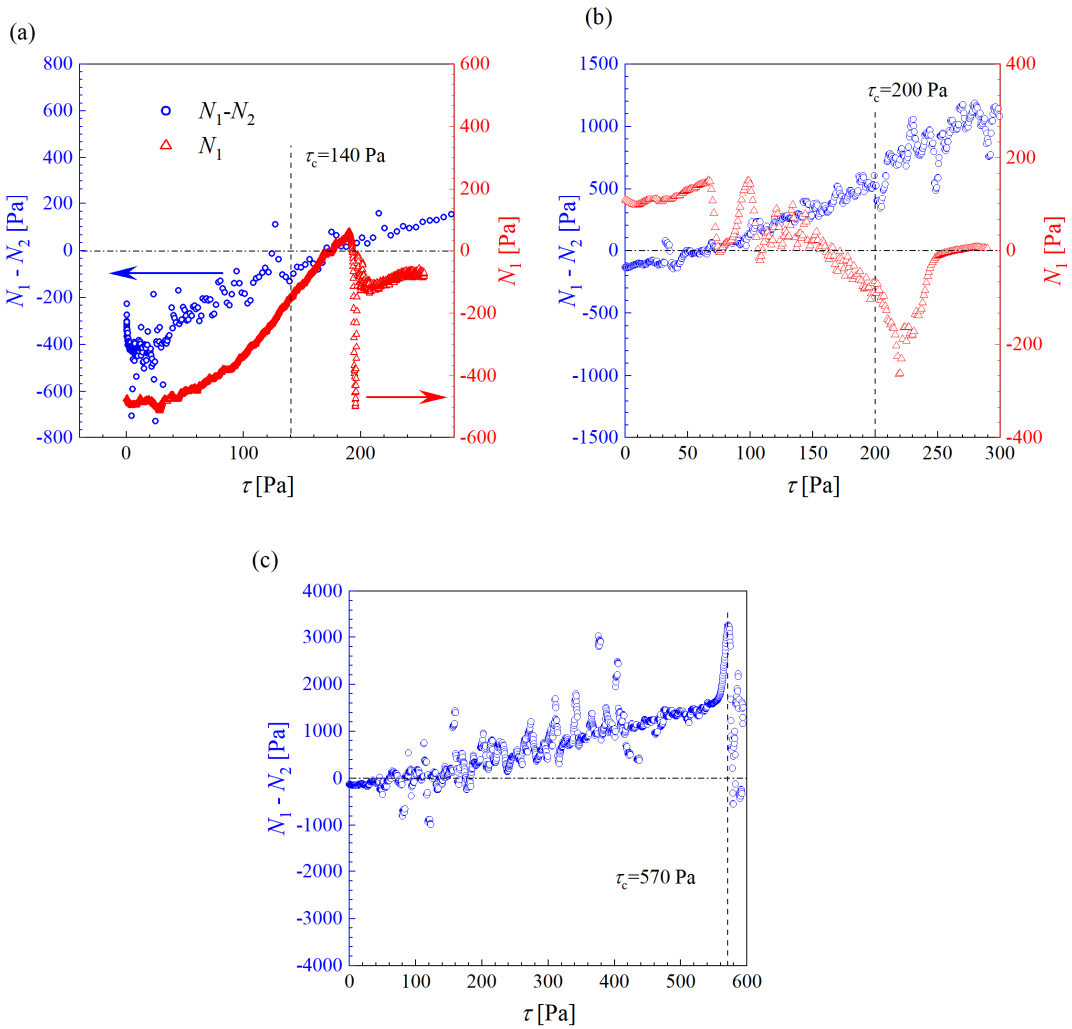

Figure 4.6 – Normal stress differences for stress ramps performed with (a) PJA, (b) WSP and (c) PJS. The horizontal dash-dotted line indicates $N_1 - N_2 = N_1 = 0$ Pa.

The results obtained for the rheological evaluation of the soil layer materials in this section are in agreement with other studies in the literature. For instance, it has been reported that petroleum jellies show time-dependent yield stress behaviour (Park & Song, 2010a, 2010b; Glover *et al.*, 2016), as do many other waxy suspensions (Chang *et al.*, 1998; Visintin *et al.*, 2005; Dimitriou *et al.*, 2011; Dimitriou & McKinley, 2014). Recent developments have also shown that yielding is not a sudden transition from an unyielded to a yielded state, but rather a gradual process dominated by creep (Lidon *et al.*, 2017) that takes place along a range of shear stresses and strains (Fernandes *et al.*, 2017a; Donley *et al.*, 2019, 2020). The materials evaluated in this work exhibited significant creep below the critical stress. This characteristic is relevant for the interpretation of results from cleaning experiments discussed in Chapters 5 and 6.

4.2 In-situ measurement of the critical stress using the millimanipulation device

In Section 4.1, the rheological behaviour of the three soil layer materials used in impinging jet cleaning experiments reported in Chapters 5 and 6 was studied using rotational rheometry. These tests provide detailed information about the materials' yielding behaviour. Oscillatory measurements can also be performed in rotational rheometers, yielding important insight into the viscoelastic properties of the materials. However, viscoplastic fouling layers are often formed as a result of local conditions, such as temperature and shear history, at the surface on which they are formed. These layers often feature a fragile microstructure, so removing a sample for investigation in a standard rheometer can disrupt the structure and result in incorrect estimates of the rheological behaviour. Examples include thixotropic colloidal dispersions, which are often thixotropic or time-dependent (Barnes, 1997; Mewis & Wagner, 2009), waxy suspensions such as those encountered in the manufacturing of creams and ointments (Park & Song, 2010b), food fats (Fitzgerald *et al.*, 2001) and crude oils transported in pipelines (Geri *et al.*, 2017).

It is therefore important to evaluate the rheological behaviour of fouling layers *in situ*, *i.e.* without the need to remove the material for testing in a rheometer. The millimanipulation device, presented in Section 3.6, offers a novel way to investigate the flow and deformation behaviour of viscoplastic soil layers. Although it does not provide the same breadth of functionality of a rheometer, it can test the soil layers *in situ*. Testing in this device requires coating the material on a flat plate using the methodology described in Chapter 3. Also, the

material should offer enough resistance to the movement of the blade to ensure that the force is reliably measured by the force transducer. The tests reported here were all conducted at room temperature. For tests at other temperatures, the device could be mounted in a temperature-controlled chamber.

Fifteen viscoplastic materials of industrial relevance were studied to evaluate the use of the millimanipulation device as a tool to estimate the yield stress. These are listed in Table 4.2: PJA, PJS, and WSP were investigated in Section 4.1. PJT is another petroleum jelly (Gold label, Trilanco, UK), which was used by Glover *et al*. (2016). Food materials that required storage at low temperatures (butter, lard, margarine, cheese spread, cream cheese and mayonnaise) were stored in a fridge at 5 ºC and kept at room temperature for at least 12 h before experiments were performed. Rheological experiments and millimanipulation tests were conducted on the same day with these materials to avoid spoilage. All other materials were stored at room temperature, approximately 20 °C.

Table 4.2 –Materials used in the millimanipulation experiments

	Material	Acronym	Commercial name	Manufacturer
Ointments	White soft paraffin	WSP	-	GlaxoSmithKline
	Petroleum jelly A	PJA	GPS5220	Atom Scientific
	Petroleum jelly S	PJS	Merkur 500	Sasol
	Petroleum jelly T	PJT	Gold label white petroleum jelly	Trilanco
Consumer goods	Nivea hand cream	-	Nivea Creme	Nivea
	Peanut Butter	-	Sainsbury's smooth peanut butter	Sainsbury's
	Toothpaste	-	Colgate cavity protection	Colgate-Palmolive
Foods	Butter	-	Unsalted British butter by Sainsbury’s	Sainsbury's
	Hair Wax	-	V05 styling wax	Unilever
	Lard	-	Sainsbury's basics lard	Sainsbury’s
	Margarine	-	I can't believe it's not butter!	Upfield
	Cheese spread	-	Seriously spreadable	Lactalis McLelland Ltd.
	Cream Cheese	-	Philadelphia original	Mondelez International Inc.
	Mayonnaise	-	Hellmann’s real mayonnaise	Unilever
	Biscoff	-	Lotus biscoff	Lotus Bakeries

4.2.1 Rheological characterisation of the soil layer materials

The rheological behaviour of the materials was evaluated at 20 °C using the Kinexus stress-controlled rheometer with serrated parallel plates to reduce wall slip. The gap between the plates was set to 1 mm in all experiments. Three testing modes, discussed in Chapter 2, were employed: the first was a series of shear stress steps, each lasting 30 s, to evaluate the steady response of the material to an imposed shear stress, and the corresponding shear rate was taken as the average over the last 3 s in each step. The second was an increasing shear stress ramp, with a rate of increase of 50 Pa·min^{-1}, while the third was an oscillatory shear stress amplitude sweep, in which a sinusoidal shear stress was imposed at a frequency of 1 Hz with increasing shear stress amplitude.

4.2.2 Sample preparation

Samples were coated on steel plates (dimensions 25×100×0.65 mm) using the scraping device described in Section 3.4. The thickness of the samples was set at $\delta_o = 5$ mm. These are representative of thick soiling layers found at the base of processing tanks in industrial applications (Tuck *et al.*, 2020). The edges of the samples were carefully scraped using a flat-edged metal spatula to ensure straight sides, and the sample was carefully positioned in the millimanipulation device. The x-axis moving stage was positioned such that at the start of an experiment, the blade was just touching the sample.

4.2.3 Rheological characterisation of the materials

Figure 4.7 shows an example of the rheological results obtained for the white soft paraffin (WSP). Results for the other materials are presented in Appendix A. Figure 4.7 (a) shows the apparent viscosity η as a function of the imposed shear stress τ for the stress ramps and stress steps. The sharp decrease of the viscosity evident around 400 Pa for the stress steps and ramp indicates structural breakdown within the sample and consequent yielding. The estimates of the critical stress, τ_{rp} and τ_{st}, obtained from these tests are indicated by vertical lines. The increase in viscosity for $\tau < \tau_{rp}$ results from the material not being in steady-state during the test. This behaviour was discussed by Møller *et al.* (2009a), who reported that the apparent viscosity in the pre-yielding regime in stress step experiments increases with the duration of the stress steps. Nevertheless, the sharp decrease in the apparent viscosity

happens at roughly the same shear stress, indicating that stress ramp testing gives a reasonable estimate of the yield stress (Chang *et al.*, 1998; Andrade & Coussot, 2020).

Oscillatory amplitude sweeps provide additional information about the yielding transition of viscoplastic materials. This was discussed, amongst others, by Donley *et al.* (2019), who evaluated oscillatory flows of a Carbopol® dispersion and reported that yielding takes place over a range of shear stresses and strains. In Figure 4.7 (b) the storage and loss moduli, G' and G'', are constant at low shear stress amplitudes, indicating that the material is in the linear viscoelastic regime. As the shear stress amplitude increases, a decrease in G' and G'' is observed such that they cross each other at the crossover stress, τ_{cr}, indicated by the vertical dashed line in Figure 4.7 (b). The yielding transition starts at the end of the linear viscoelastic regime, when G' and G'' start to decrease. Different estimates for the yield stress have been defined from oscillatory data: (i) the intersection of power-law fits to G' at low and high stresses (Mason *et al.*, 1996); (ii) the point where $G' = G''$, τ_{cr} (Rouyer *et al.*, 2005); and (iii) the departure from linear elastic behaviour in τ_a vs γ_a plots (Mason *et al.*, 1996). As discussed by Dinkgreve *et al.* (2016), the crossover stress provides an unambiguous estimate for the yield stress from oscillatory data and is used here.

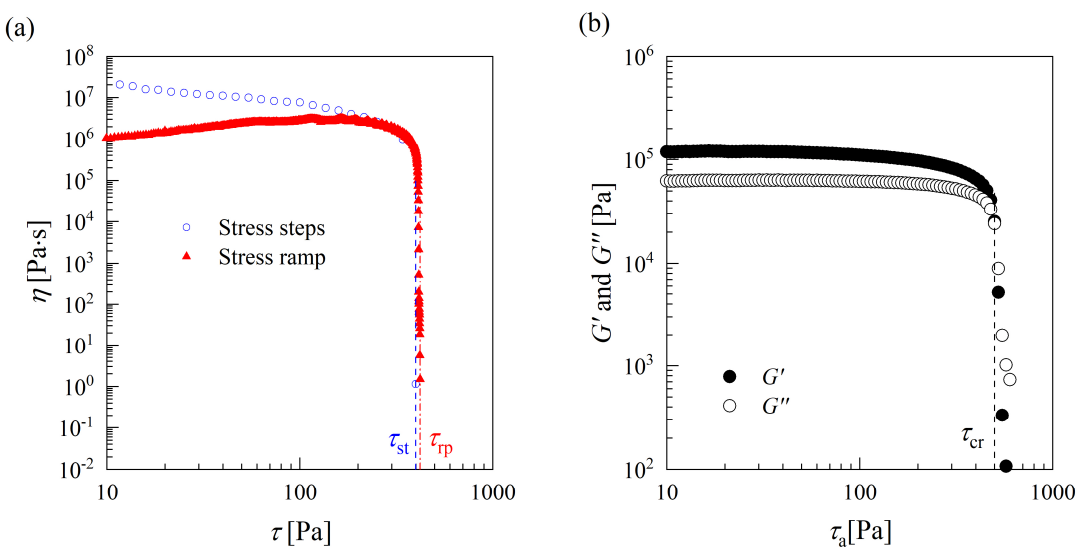

Figure 4.7 - Rheological characterisation of the white soft paraffin. (a) Apparent viscosity as a function of the imposed shear stress for stress steps and stress ramp. (b) Effect of shear stress amplitude on G' and G'' in oscillatory shear stress sweeps. τ_{st} and τ_{rp} were identified as the stress at the sharp drop in η.

Consistent estimates of the yield stress are often not obtained when different methods are used (Stokes & Telford, 2004), particularly for materials with complex microstructures such as waxy deposits (Tarcha *et al.*, 2015). Figure 4.8 compares the values of the critical stress for the materials evaluated in the current work measured from (a) stress ramps, τ_{sr}, and from (b) oscillatory sweeps, τ_{cr}, with the values obtained from the shear stress step tests τ_{st}. The τ_{sr} and τ_{st}values are similar, agreeing within $\pm 15\%$. The crossover values, on the other hand, agree within $\pm 30\%$, with $\tau_{cr} > \tau_{st}$ for most cases. Dinkgreve *et al.* (2016) compared the critical stresses obtained with different techniques for concentrated emulsions and Carbopol® gels, and also found that τ_{cr} was larger than other estimates of the yield stress. τ_{cr} should therefore be viewed as the upper bound of the yielding region and is expected to be larger than other estimates for the critical stress. It should also be noted that the estimate of the yield stress for each experiment is affected by the intrinsic time scale of each test: the rate of increase of the shear stress for the stress ramps (Chang *et al.*, 1998), the duration of each step for the stress steps (Coussot *et al.*, 2002b) and the frequency for the oscillatory sweeps (Perge *et al.*, 2014).

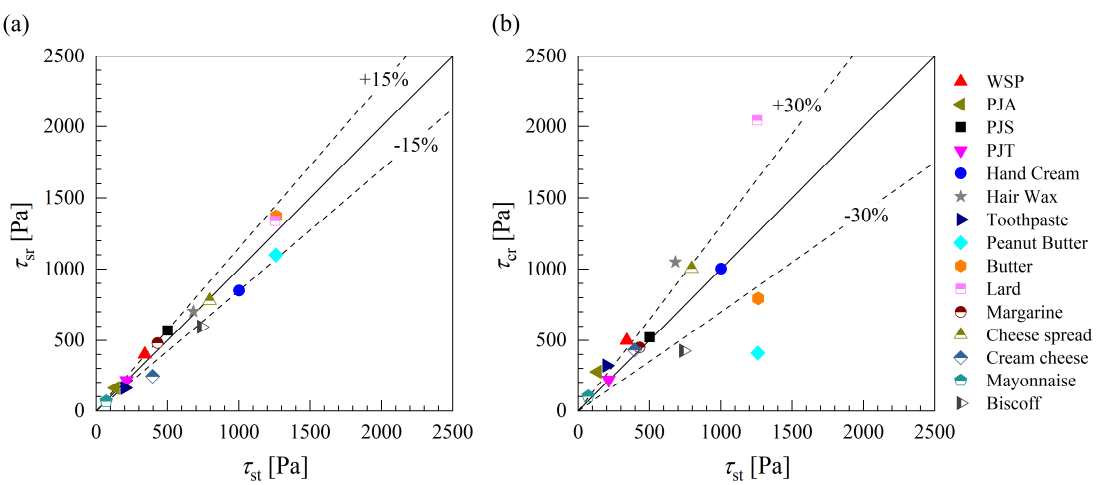

Figure 4.8 – Comparison of measurements of critical stress obtained from rheometer testing: (a) τ_{sr} vs. τ_{st} ; (b) τ_{cr} vs. τ_{st}. Legend is common to both plots.

The value of τ_{cr} for the peanut butter is smaller than τ_{st} and τ_{sr}. Similar behaviour has been reported for smooth and coarse peanut butters by Citerne *et al.* (2001), who attributed this to either (i) shear-thickening effects or (ii) changes in the maximum packing fraction of dispersed solids under oscillatory flow.

4.2.4 Scraping experiments

Experiments in the millimanipulation device consisted of a scraping step, in which the sample moved 10 mm, followed by a relaxation step where the sample was stationary for 120 s. The duration of the scraping step was adjusted according to the scraping velocity, V_{bl}, to ensure a scraping amplitude of 10 mm in each test. Figure 4.9 (a) shows results from two scrape-relaxation sequences for the WSP. The signal is noisy but shows an approximately steady F_w during the scraping step followed by a rapid decay to a finite, residual value during the relaxation step. A slight increase in force is observed in the second scraping step compared to the first one, which is attributed to drag effects associated with the growth of the berm ahead of the blade.

Figure 4.9 (b) shows a closer view of the first scrape-relaxation sequence, highlighting three characteristic force levels. At the end of the scraping stage, a maximum force F_C is evident, which decreases rapidly to $F_{C'}$. During the relaxation step, F_w decayed to a residual value F_D. This residual force is related to the yielding behaviour of the sample, as it reflects the anisotropy imprinted to the material by the previous flow (Bonn *et al.*, 2017). Ali *et al.* (2015) also reported a residual force in interrupted experiments on baked lard but did not associate this behaviour with the yield stress of the material.

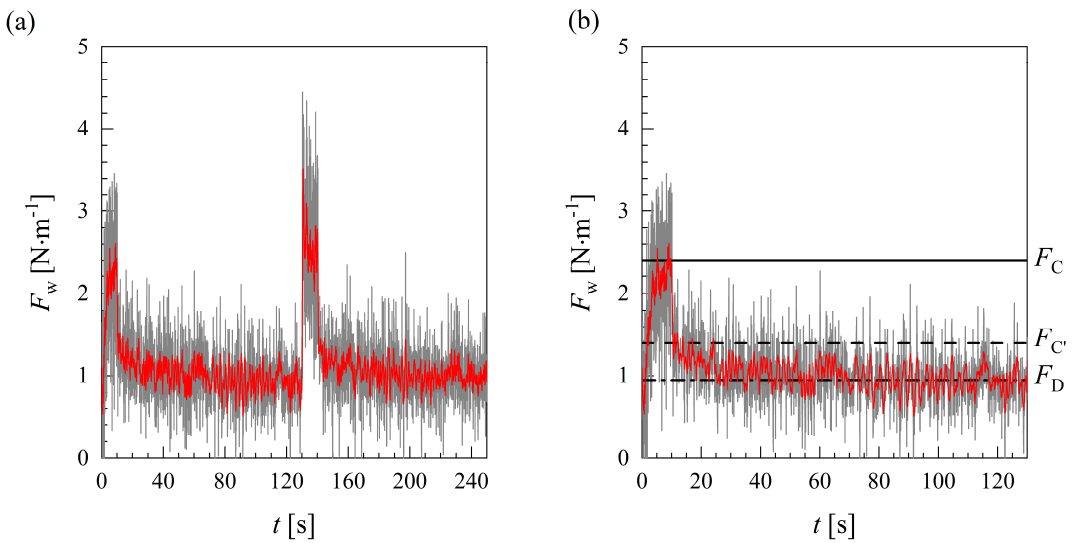

Figure 4.9 – F_w as a function of time for the white soft paraffin: V =1 mm·s^{-1} and s =0.69 mm. (a) Two consecutive scrape-relaxation steps performed with the same sample; (b) closer view of the first scrape-relaxation step, indicating the forces F_C, $F_{C'}$ and F_D. Red lines indicate the signal smoothed using a moving-average filter.

Figure 4.10 (a) presents a schematic of the operation: the blade moves at velocity V_{bl} and scraping depth s, leaving a layer of depth $\delta = \delta_{\mathrm{o}} - s$ behind. The scraping depth s was measured from analysis of the images measured with the digital camera, where the thickness of the blade was used to calibrate the scale. The material ahead of the blade accumulates in a berm of height h_{MM} and length b_{MM}. Tsai *et al.* (2020) performed particle tracking experiments and CFD simulations of these flows and showed that the region where significant deformation takes place is limited to the scraped depth ahead of the blade. These observations suggest the existence of a shear plane inclined at angle $\phi_{\mathrm{MM}} = \angle\mathrm{AOB}$, defined from the tip of the blade to the leading edge of the berm. The boundary of the shear region is unlikely to be a straight plane so this is an approximation, which will limit the accuracy of the approach. Similar approximations are made in metal cutting theory for soft materials (Shaw, 2005). A force balance over plane OA gives an estimate of the shear stress acting along the shear plane, *viz*.

$$\tau = \frac{F_{\mathrm{w}} \tan \phi_{\mathrm{MM}}}{s} \tag{4.1}$$

The length of the berm b_{MM} and cutting angle ϕ_{MM} were evaluated from images captured by the camera (labelled 7 in Figure 3.8), such that $\phi_{\mathrm{MM}} = \tan^{-1}(s/b_{\mathrm{MM}})$. A different approach is required for brittle materials: Akono *et al.* (2011) investigated the scratching of brittle materials, including limestone and cold paraffin wax, using a similar device. There, deformation involved a fracture-dominated process with highly localised plastic deformation at the blade and chip generation rather than the berm formation observed with the ductile materials considered here.

Figure 4.10 (b) shows an image from the experiment in Figure 4.9, in which the geometric features are highlighted. Figure 4.10 (c) shows the evolution of b_{MM}, h_{MM} and ϕ for the same experiment. The berm height increases linearly while b_{MM} is roughly constant, indicating that the cutting angle does not change significantly throughout the test.

Three estimates for the yield stress can be computed:

$$\tau_{\mathrm{y}}^{\mathrm{e1}} = \frac{F_{\mathrm{C}} \tan \phi_{\mathrm{MM}}}{s} \tag{4.2}$$

$$\tau_y^{e2} = \frac{F_{C'} \tan \phi_{MM}}{s} \tag{4.3}$$

$$\tau_y^{e3} = \frac{F_D \tan \phi_{MM}}{s} \tag{4.4}$$

where $F_{C'}$ and F_D are the residual forces identified in Figure 4.9.

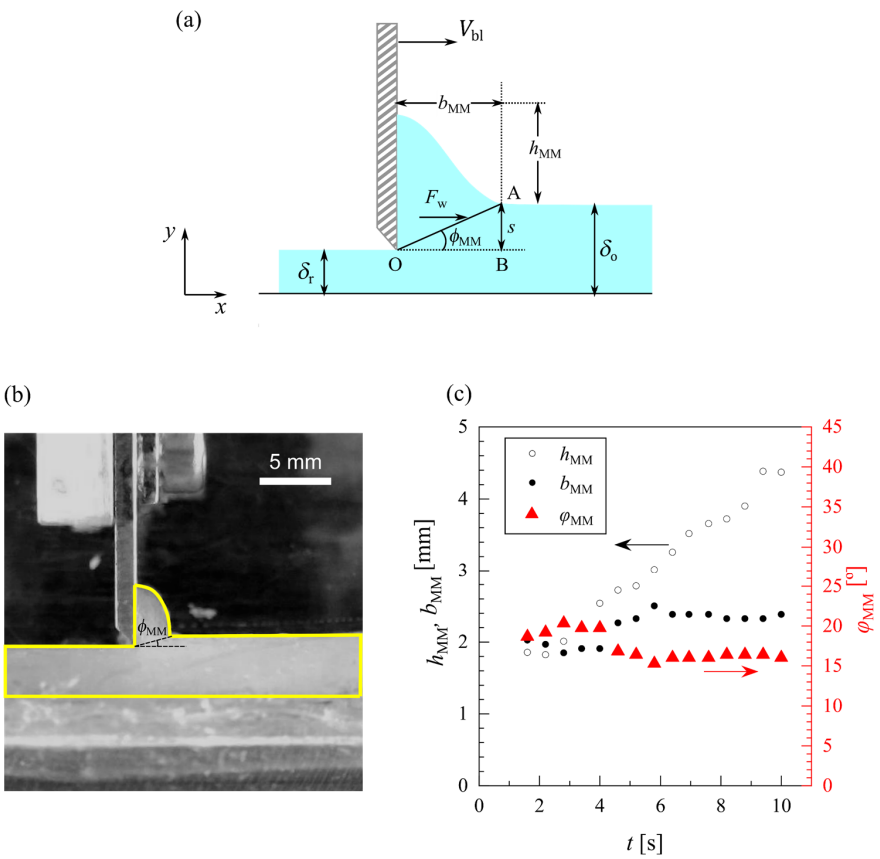

Figure 4.10 – (a) Schematic of the millimanipulation device scraping a viscoplastic soil layer. The cutting angle ϕ_{MM} is formed from the tip of the blade to the end of the displaced berm. (b) Photograph of the berm of the experiment reported in Figure 4.9 at $t = 10$ s. (c) h_{MM}, b_{MM} (left y-axis) and ϕ_{MM} (right y-axis) as a function of scraping time.

τ_y^{e1} includes contributions from the viscous behaviour of the material, since F_C is measured when the material is deforming: τ_y^{e1} is therefore expected to be larger than the estimates of yield stress obtained with the rheometer. τ_y^{e3}, on the other hand, does not include the contributions from the flow and is expected to be closer to the estimates of the yield stress. This is illustrated for the WSP in Figure 4.11, which shows τ_y^{e1} plotted against the

characteristic shear rate for the scraping blade, $\dot{\gamma}_{ch} = V_{bl}/s$ (Maillard *et al.*, 2016), alongside the flow curves obtained on the rheometer (Figure 4.7 (a)). τ_y^{e3} is indicated by the grey band as it is measured with the material at rest: it lies close to the flow curves in the region associated with yielding.

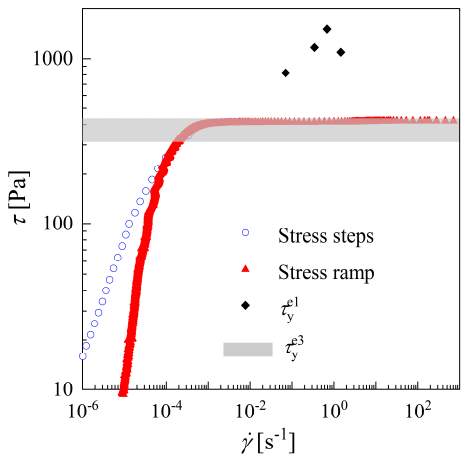

Figure 4.11 – Shear stress as a function of the shear rate for the WSP. τ_y^{e1} and τ_y^{e3} were calculated using Eq. (4.2) and (4.4), respectively.

4.2.4.1 Effect of scraping velocity

The residual stress after flow cessation in rotational rheometers has been used to estimate the yield stress (Tiu & Boger, 1974; Nguyen & Boger, 1983, 1992). Later studies investigated the relationship between the residual stress obtained after imposing different shear stresses (Mohan *et al.*, 2013) and shear rates (Ballauff *et al.*, 2013) and observed that the values obtained depended on the shear rate imposed on the sample. Most of the scraping experiments reported in this section were performed at scraping speeds of 1 mm·s^{-1}. Tests were also performed at 0.1 and 0.5 mm·s^{-1} for WSP to determine the influence of shear rate.

Figure 4.12 (a) to (c) shows examples of residual force decay profiles obtained for different scraping speeds, along with the values of F_C, $F_{C'}$ and F_D identified in each case. The noise is reduced for slower scraping velocities as the mechanical fluctuations in the system are less intense. The results are summarised in Figure 4.12 (d) alongside the estimates of the yield stress obtained from the rheometer as a function of $\dot{\gamma}_{ch}$. The values of τ_y^{e3} are again close to the rheometer measures, and this parameter is insensitive to the scraping velocity, indicating

that viscous contributions are not significant. It can be concluded that τ_y^{e3} provides useful *in situ* estimates of the yield stress for this soft solid.

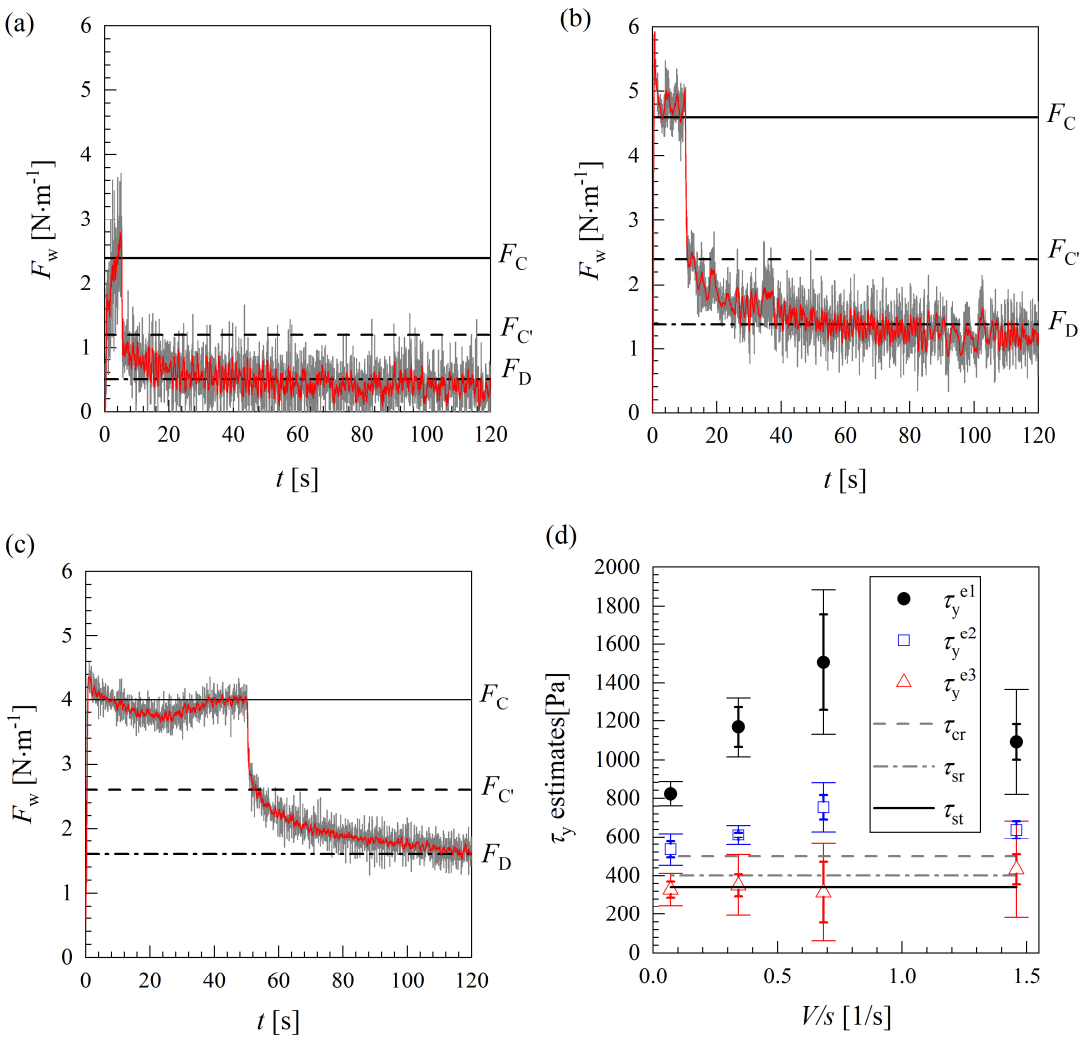

Figure 4.12 – F_w as a function of time for three experiments conducted with different speeds and with the white soft paraffin: (a) V=1 mm·s^{-1}, s =1.43 mm (b) V_{bl} = 0.5 mm·s^{-1}, s=1.46 mm and (c) V_{bl} = 0.1 mm·s^{-1}, s =1.42 mm. (d) τ_y^{e1}, τ_y^{e2} and τ_y^{e3} estimates as a function of V_{bl}/s, where the experiment reported in Figure 4.9 is also included. Horizontal lines indicate the values of τ_{cr}, τ_{sr} and τ_{rp} measured in the rheometer. Error bars in (d) obtained from the local amplitude of the raw (wide cap) and filtered (narrow cap) F_w signal.

It is also possible to estimate the Bingham number for the flow in the millimanipulation device. Since τ_y^{e1} includes contributions from both the yielding and flowing regimes, and

τ_y^{e3} is primarily associated with the yielding behaviour, an approximate Bingham number (Bn, the ratio between the yield stress and the viscous stresses) is given by:

$$Bn = \frac{\tau_y^{e3}}{\tau_y^{e1} - \tau_y^{e3}}. \tag{4.5}$$

Figure 4.13 (a) shows the estimates of the yield stress as a function of Bn for the experiments performed with the WSP reported in Figure 4.12, where $Bn < 1$.

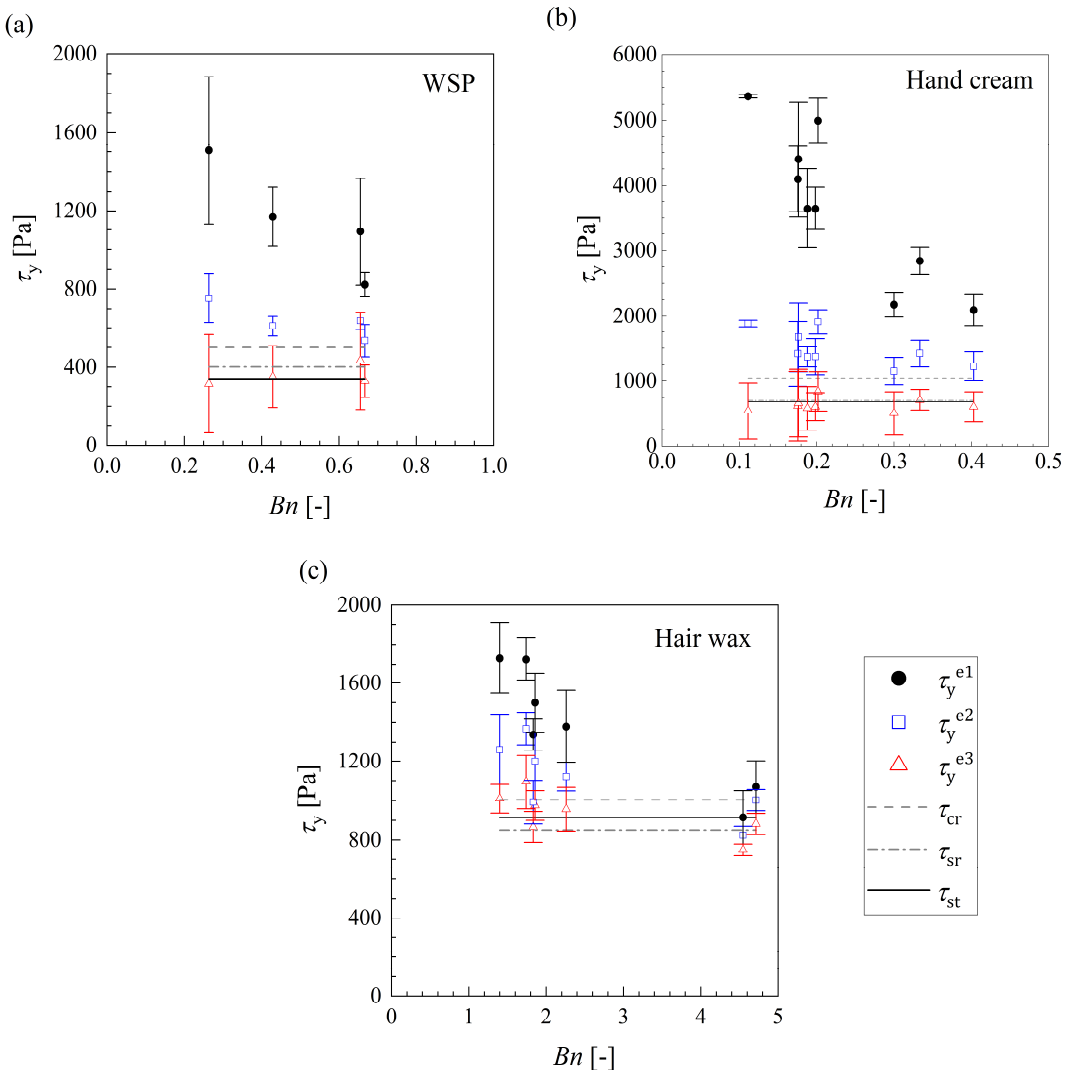

Figure 4.13 – τ_y^{e1}, τ_y^{e2} and τ_y^{e3} estimates as a function of Bn for (a) the WSP, (b) hair wax and (c) hand cream. Legend is common to all plots. Error bars obtained from the local amplitude of the F_w signal.

In general, experiments with larger values of Bn correspond to smaller scraping velocities. τ_y^{e1} and τ_y^{e2} display a decreasing trend, suggesting that the contribution from the viscous stresses to the total stress in the shear plane becomes unimportant when the blade scrapes the material slowly. Similar trends are reported for experiments performed with the hair wax, Figure 4.13 (b), and with the hand cream, Figure 4.13 (c).

The results show that at large Bn, τ_y^{e1}, τ_y^{e2} and τ_y^{e3} collapse and provide values consistent with the critical stresses measured in the rheometer. In practice, this region is only attainable with materials with larger yield stresses. For materials with low yield stresses, the accuracy of the estimate is influenced by signal to noise ratio.

4.2.4.2 Comparing the estimates of the yield stress from the millimanipulation with rheometer measurements

The two estimates of the yield stress obtained with the millimanipulation device, τ_y^{e2} and τ_y^{e3}, are compared with the three measures obtained with the rheometer in Figure 4.14. The horizontal axes report the values of (a) τ_{st}, (b) τ_{sr} and (c) τ_{cr}, and the vertical axes show (i) τ_y^{e2} and (ii) τ_y^{e3}. The values of τ_y^{e1} include significant contribution of the viscous stresses (see Figure 4.13) and so are not included in this figure as they consistently overestimate the yield stress. The dotted loci indicate the line of equality, with range bands at $\pm 30\%$ variation. Some values correspond to the first scraping step, with the blade initially touching the border of a fresh layer: these are indicated by filled symbols. Measurements conducted in subsequent scraping steps are reported with open symbols. Figure 4.14 (i) shows that τ_y^{e2} overpredicts all three rheometer measures, while Figure 4.14 (ii) indicates that τ_y^{e3} provides more accurate estimates. This agrees with the findings for WSP at different scraping velocities in Figure 4.12.

Figure 4.14 (c,ii) shows close agreement between τ_y^{e3} and the crossover stress, τ_{cr}. The latter is a measure of the upper limit of the yielding region and this is consistent with the device probing the characteristics of the material when it has already yielded.

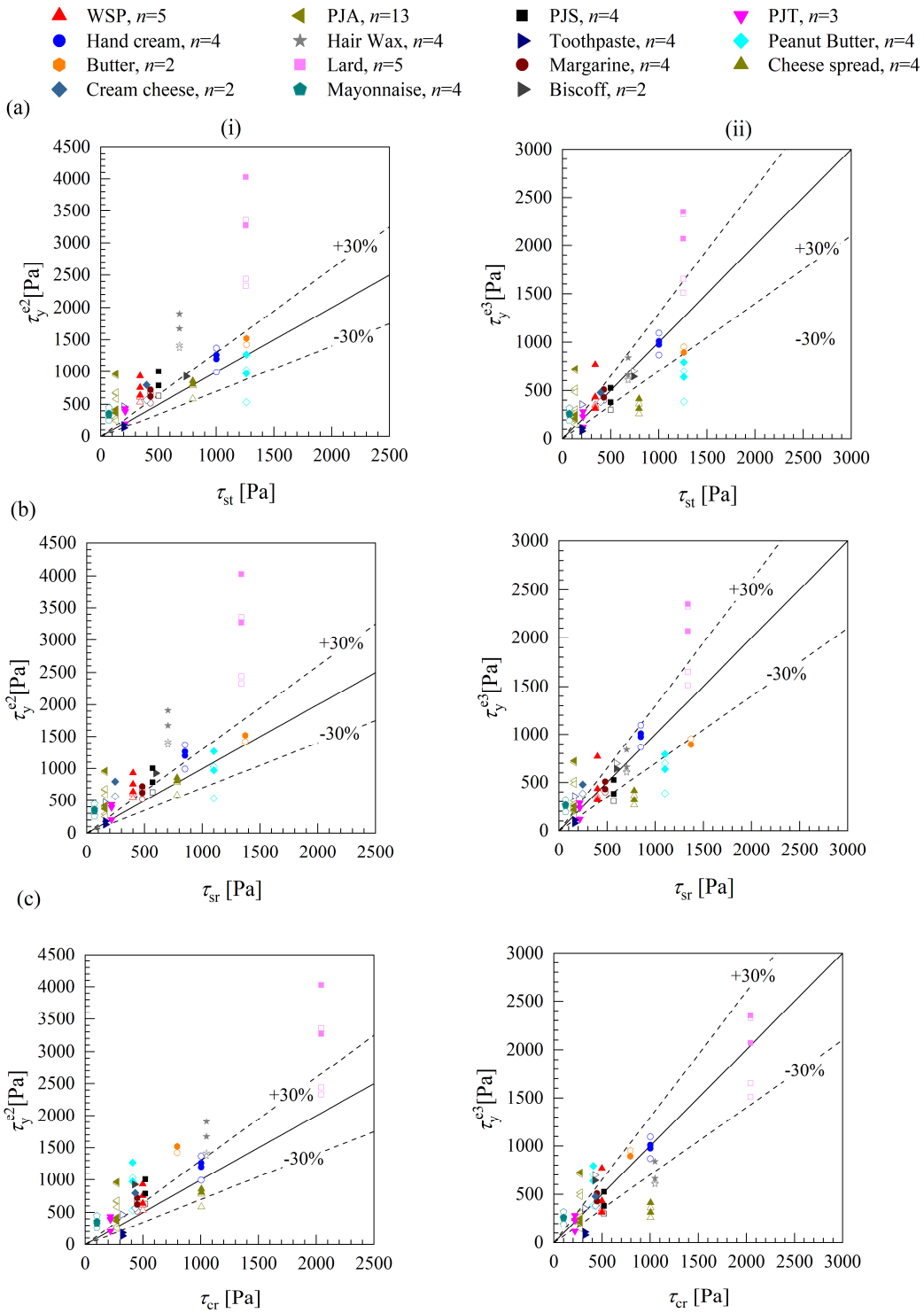

Figure 4.14 – Comparison of the estimates of the yield stress obtained from millimanipulation with the rheometer values. (i) τ_y^{e1} and (ii) τ_y^{e2} as a function of (a) τ_{st}, (b) τ_{sr} and (c) τ_{cr}. Filled symbols denote experiments performed with the first contact of the blade in the samples, open symbols indicate experiments performed in subsequent scraping steps. n is the number of estimates reported for each material.

The uncertainty in the rheometer values is small as this is a commercial, optimised device. The uncertainty in the millimanipulation device values arises from mechanical, sensor and sample effects as well as the degree of approximation in ϕ introduced by assuming a simple flat shear plane. The technique is, however, free from any systematic error associated with moving the sample from the surface and preparing it for test in a rheometer.

Boujlel and Coussot (2012) investigated the penetration of a rectangular plate with constant vertical velocity into a bath of a yield stress fluid. They reported the resistance force during immersion of the blade at low velocities and the residual force after interrupted experiments provided accurate estimates of the yield stress, which was independently measured in a rheometer. The results presented here for the millimanipulation device are consistent with their analysis.

The use of the millimanipulation device as a tool to estimate the yield stress of soil layers *in situ* is encouraging since viscoplastic soil layers with larger yield stresses are usually hard to clean. Additionally, cleaning models such as the one by Glover *et al.* (2016) and the models presented in Chapters 5 and 6 require the value of the yield stress to describe the cleaning by impinging liquid jets. Identifying F_{C}, $F_{\mathrm{C}'}$ and F_{D} was more straightforward for materials with a high yield stress, such as lard, butter and the hand cream, because the signal-to-noise ratio was larger as these materials offered more resistance to the movement of the blade. Materials such as the toothpaste and the mayonnaise exhibited a less sharp drop in apparent viscosity at the yield stress (see Appendix A). They also underwent spatial reconfiguration during deformation and generated complex berm shapes which made it harder to identify ϕ_{MM}. The MM3 technique is, therefore, more appropriate for materials with higher yield stresses, such as troublesome fouling layers found in the FMCG manufacturing.

One of the drawbacks of the current configuration is that it requires layers of consistent thickness on flat substrates. It would require some effort to be adapted on fouling deposits such as those encountered on heat exchanger surfaces as the latter are frequently curved, the layers thin (or order 1 mm or less) and coverage uneven.

The current device is well suited for laboratory studies where layers are generated on test coupons in regular flow geometries, or where coupons are attached to equipment walls for inspection afterwards. It also has potential as a quality control device, as the sample preparation is straightforward.

4.3 Critique and considerations

The three materials that are used along this thesis in the cleaning experiments, PJA, PJS and WSP, show time-dependent and viscoplastic behaviour. A coating protocol was developed based on the time-dependent nature of the soils, which consists of leaving the coated plates to age for at least 30 min before performing further experiments, thus ensuring that the layers are in a similar reproducible state before cleaning. The experiments conducted in the rheometer indicated that the three materials significantly creep near the critical stress.

During the manufacturing of consumer goods, viscoplastic fouling layers are usually formed due to local conditions at the surfaces. A method to estimate the yield stress *in situ,* without the need to remove the materials from the surfaces, is highly desirable. Therefore, the potential of the millimanipulation device as a tool to estimate the yield stress of different soils coated on flat metallic surfaces was evaluated. While the millimanipulation method has limited accuracy when compared with conventional testing, it provides a working estimate of the yield stress which could be used for quick quality tests. Its ability to provide quantitative information for soil layers and fouling deposits *in situ* is noteworthy and provides a useful advance in the field of applied rheology.

5 A phenomenological model for cleaning viscoplastic insoluble soil layers by a coherent impinging liquid jet

This chapter presents an experimental investigation of the cleaning of PJA layers. The shape of the cleaning front at different stages during cleaning is determined experimentally and insights into the mechanism are discussed. The validity of the adhesive removal model proposed by Glover *et al.* (2016), Eq. (2.72), is investigated using the expressions for M reported by Bhagat and Wilson (2016). The experimental data indicate that Eq. (2.72) does not provide an accurate description of removal at late stages of cleaning, and so a revised model is proposed. The parameters obtained by fitting the revised model to data generated for cleaning by jets from static nozzles are discussed. The usefulness of the revised model is demonstrated by its ability to describe the cleaning of similar layers by jets from moving nozzles.

The main aspects of this chapter have been published in Fernandes *et al.* (2019). Some of the results for moving jet experiments reported in Section 5.3.4 were performed by Dirk Oevermann, an MSc student from Technische Universität Dresden who spent the summer of 2018 in the research group.

5.1 Cleaning of a viscoplastic soil, static nozzle

(i) 'Weak soil' case: $r_\mathrm{b} < a_\mathrm{max} < r_\mathrm{j}$

As described in Chapter 2, Glover *et al.* (2016) proposed a cleaning model based on a rate equation, Eq. (2.72), that relates the rate of growth of the cleaned radius, $\mathrm{d}a/\mathrm{d}t$, to the momentum flow rate in the liquid film, M. They considered the case where M is given by Eq. (2.39), the 'weak soil' case, which describes the hydrodynamic behaviour of the liquid jet reasonably well far from the impinging point. This is appropriate for experiments in which k' is large so that initial soil removal, close to the impinging point, is fast. The cleaned radius increases over time and cleaning stops at a radial distance a_max, when $M = M_\mathrm{y}$, where

$$M_{\mathrm{y}} = \frac{3\dot{m}^3}{5\pi c}\frac{1}{a_{\max}^4}. \tag{5.1}$$

Substituting the expression for M from the 'weak soil case', Eq. (2.39), into Eq. (2.72) gives

$$\frac{\mathrm{d}a}{\mathrm{d}t} = k'\frac{3\dot{m}^3}{5\pi c}\left(\frac{1}{a^4} - \frac{1}{a_{\max}^4}\right) = \alpha\left(\frac{1}{a^4} - \frac{1}{a_{\max}^4}\right), \tag{5.2}$$

with $\alpha = k'\frac{3\dot{m}^3}{5\pi c}$. Integration from the initial condition a_{o} at t_{o} and writing $a_{\mathrm{w}}^* = a/a_{max}$ for $a > r_{\mathrm{b}}$ gives

$$\begin{aligned} t - t_{\mathrm{o}} = \frac{1}{4}\frac{a_{\max}^5}{\alpha}\Bigg[&\ln\left(\frac{1+a_{\mathrm{w}}^*}{1-a_{\mathrm{w}}^*}\right) - \ln\left(\frac{1+a_{\mathrm{o}}^*}{1-a_{\mathrm{o}}^*}\right) - 4(a_{\mathrm{w}}^* - a_{\mathrm{o}}^*) + 2\tan^{-1}a_{\mathrm{w}}^* \\ &- 2\tan^{-1}a_{\mathrm{o}}^*\Bigg]. \end{aligned} \tag{5.3}$$

The group $a_{\max}^5/4\alpha$ is a dimensionless timescale, $t_{\mathrm{c,weak}}$, which leads to the dimensionless time $t_{\mathrm{w}}^* = t/t_{\mathrm{c,weak}}$, so Eq. (5.3) can be written:

$$\begin{aligned} t_{\mathrm{w}}^* - t_{\mathrm{w,o}}^* = \Bigg[&\ln\left(\frac{1+a_{\mathrm{w}}^*}{1-a_{\mathrm{w}}^*}\right) - \ln\left(\frac{1+a_{\mathrm{o}}^*}{1-a_{\mathrm{o}}^*}\right) - 4(a_{\mathrm{w}}^* - a_{\mathrm{o}}^*) + 2\tan^{-1}a_{\mathrm{w}}^* \\ &- 2\tan^{-1}a_{\mathrm{o}}^*\Bigg]. \end{aligned} \tag{5.4}$$

(ii) Strong soil: $a_{\max} < r_{\mathrm{b}}$

Glover *et al.* (2016) did not consider 'strong soil' cases, *i.e.*, the cases where cleaning takes place near the impinging point. This is the case where $a_{\max}$ is small, and is associated with thick layers, soils with a high yield stress, or relatively low flow rates. Substituting Eq. (2.37) into Eq. (2.72) yields

$$\frac{\mathrm{d}a}{\mathrm{d}t} = k'\frac{3}{5\pi}\dot{m}U_{\mathrm{o}}\left(\frac{1}{a} - \frac{1}{a_{\max}}\right) = \sigma\left(\frac{1}{a} - \frac{1}{a_{\max}}\right), \tag{5.5}$$

where $\sigma = k'3\dot{m}U_{\mathrm{o}}/5\pi$. Writing $a_{\mathrm{s}}^+ = a/a_{\max}$ for $a < r_{\mathrm{b}}$ gives

$$\frac{\mathrm{d}a_{\mathrm{s}}^+}{\mathrm{d}t_{\mathrm{s}}^+} = \frac{1-a_{\mathrm{s}}^+}{a_{\mathrm{s}}^+}, \tag{5.6}$$

where t_s^+ is a dimensionless time, *viz*:

$$t_s^+ = \frac{\sigma}{a_{max}^2} t \tag{5.7}$$

with timescale $t_{c,strong}$, given by

$$t_{c,strong} = \frac{a_{max}^2}{\sigma}. \tag{5.8}$$

Integrating from the instant where breakthrough is first noticed, a_o^+, at time t_o^+, yields a second implicit relationship

$$t^+ = t_o^+ + \ln\left(\frac{1 - a_o^+}{1 - a_s^+}\right) + a_o^+ - a_s^+ \tag{5.9}$$

which differs noticeably from (5.3) in its early behaviour, as shown in Figure 5.1.

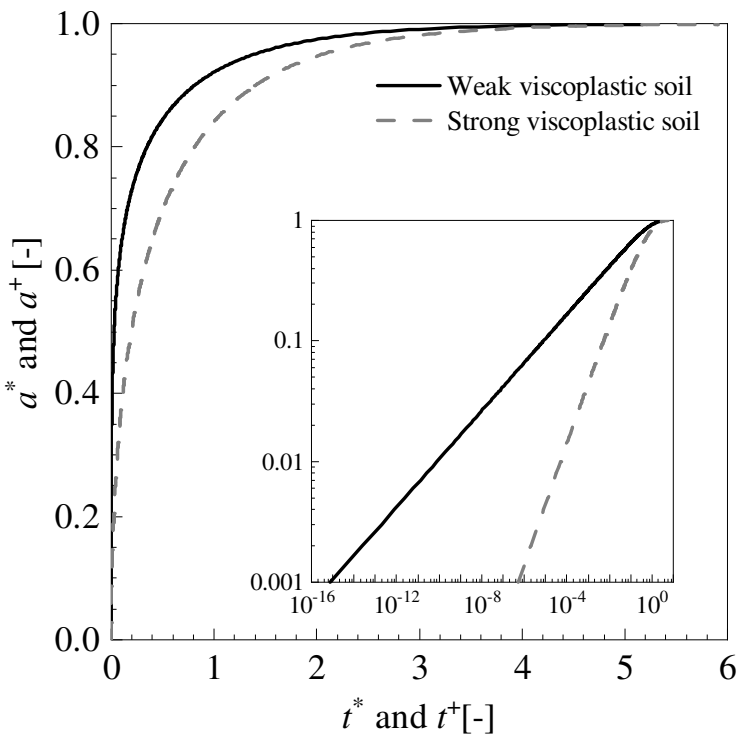

Figure 5.1 – Non-dimensional radius as a function of non-dimensional time for the weak (*, Eq. (5.3)) and strong ($^+$, Eq. (5.9)) soil models with $a_o^* = a_o^+ = 0$, $t_o^* = t_o^+ = 0$.

Figure 5.2 shows sets of experimental data obtained for a layer of the PJA. Figure 5.2 (a) shows the fit to the strong soil model, Eq. (5.9), for a case where $a_{max} < r_b$. In Figure 5.2 (b) the weak soil model, Eq. (5.3), was fitted for a case where $a_{max} > r_b$. In both cases the

appropriate model was fitted to data in the region in which the equations are valid, and fits were performed by selecting appropriated values of k' and using the experimental value of $a_{\max}$. Both models can describe the main features of the data, such as the steep increase in a at the beginning of the cleaning process and the approach to an asymptote. However, they fail to provide a reliable description of the growth of the cleaned radius: both models overestimate $a_{\max}$. Similar behaviour was also reported by Glover *et al.* (2016) when fitting data to Eq. (5.3).

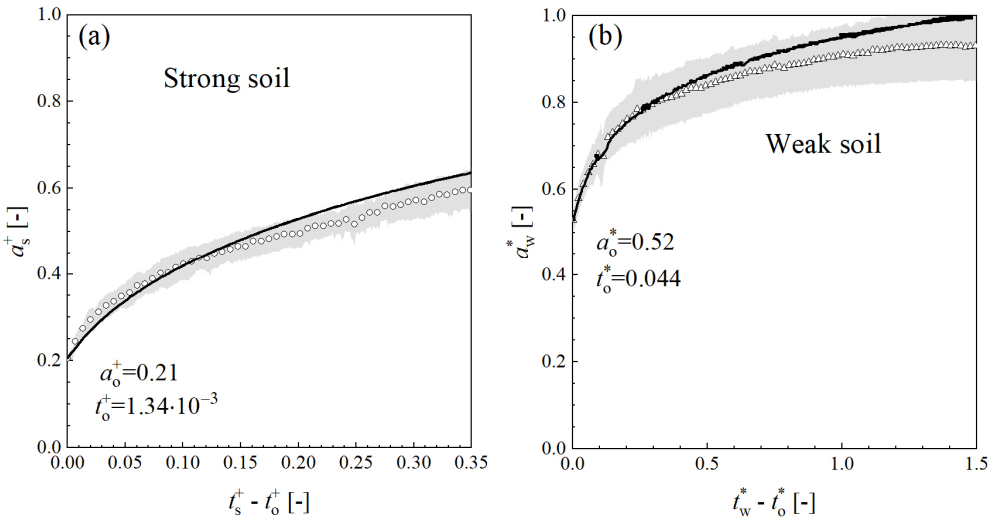

Figure 5.2 - Agreement of analytical models with experimental data. (*a*) strong soil, $a_{\max} < r_b$, Eq. (5.9): Q =3 l·min^{-1}, d_N = 4 mm, δ_o=1.05 mm. $k' = 4.5 \cdot 10^{-4}$ m·s·kg^{-1} (*b*) weak soil, $a_{\max} > r_b$, Eq. (5.3): Q =2 l·min^{-1}, d_N = 2 mm, δ_o=0.85 mm; $k' = 7 \cdot 10^{-4}$ m · s · kg^{-1}. Symbols – experimental data; lines – model. Shaded area represents the normalised standard deviation of the measured radii, $(\text{standard deviation})/a_{\max}$.

The assumption by Glover *et al.* (2016) that the soil-liquid interface, *i.e.* the cleaning front, at $a_{\max}$ takes the form of a wedge yields a relationship between $a_{\max}$ and $\dot{m}$ which can be compared with experimental data. A force balance in the radial direction over the wedge shown in Figure 2.16 yields Eq. (2.74).

Using Eq. (2.37) to estimate $M = M_y$ at $a = a_{\max}$ for the strong soil case yields:

$$a_{\max} = \frac{3}{5\pi}\frac{U_o}{\tau_c \delta_o}(\sec\chi - 1)\,\dot{m}, \tag{5.10}$$

while using Eq. (2.39) for the weak soil case gives

$$a_{\max} = \left[\frac{3}{5\pi c}\frac{1}{\tau_c \delta_o}(\tan\chi - \sin\chi)\right]^{0.25} \dot{m}^{0.75}\,. \tag{5.11}$$

It is possible to explain the deviation from the models by plotting the data in the form of Eq. (2.72), *i.e.*, calculating the local cleaning rate $\mathrm{d}a/\mathrm{d}t$ by numerical differentiation of $a(t)$ and plotting it as a function of M from the Bhagat and Wilson (2016) hydrodynamic model. The trend in Figure 5.3 (a) was observed in all the 50 cleaning experiments with static nozzles reported in this study: Eq. (2.72), which describes a linear relationship between $\mathrm{d}a/\mathrm{d}t$ and M, is followed at higher values of M (corresponding to the early stages of cleaning), with the rate proportional to $M - M_y$, where M_y is the intercept on the *x*-axis. This explains how previous workers were able to describe their results using Eq. (2.72), which is also plotted in Figure 5.3 (a). As a increases and M approaches M_y, however, the rate deviates from the linear relationship. Figure 5.3 (b) shows that the rate approaches zero asymptotically. This interpretation relies on the accuracy of the Bhagat and Wilson (2016) model to describe the hydrodynamics of an impinging liquid jet.

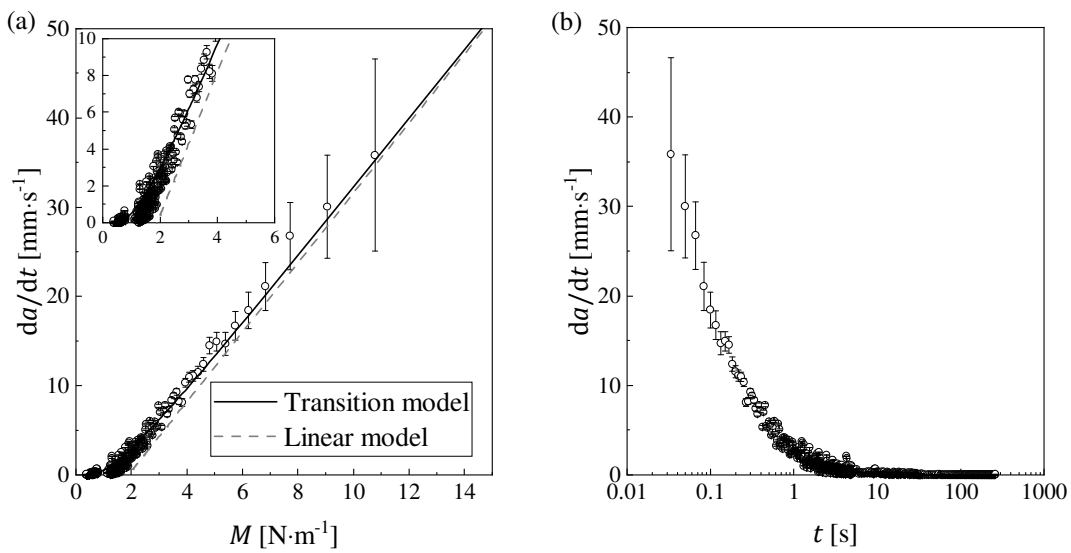

Figure 5.3 - Example of the evolution of the cleaned radius, alongside fits of the linear model, Eq. (2.72), and the transition model, Eq. (5.15). Conditions: $d_N = 2$ mm; $Q = 1.4$ l·min^{-1}; δ_o =0.37 mm. (a) da/dt vs M; (b) $\mathrm{d}a/\mathrm{d}t$ vs t. Error bars represent the propagated uncertainty in $\mathrm{d}a/\mathrm{d}t$.

M_y is an important parameter. Glover *et al*. (2016) linked this quantity to the 'critical stress' of the material by modelling the cleaning front as a ramp of angle χ (Eq. (2.74)) and it will be shown that the shear stress imposed by the liquid film at the surface, $\tau_{w,l}$, for cases such

as in Figure 5.3 gives values similar to those where the petroleum jelly exhibits creep in rheological tests. The equations for $\tau_{w,l}$ proposed by Bhagat and Wilson (2016) are provided in Section 2.3.2.

A simple quantitative model for this transition from fast, momentum-driven cleaning to slow, creep-driven flow is not available in the literature. A suitable expression to describe this behaviour needs to capture the linearity at large M and $\mathrm{d}a/\mathrm{d}t \to 0$ as $M \to 0$. In the absence of a theoretical model, it is desirable to minimise the number of fitting parameters. Two candidates considered were:

(i) Addition of a first-order decay smoothing term, *viz*

$$\begin{aligned}\frac{\mathrm{d}a}{\mathrm{d}t} &= k'\left[\left(M - M_\mathrm{y}\right) + M_\mathrm{y}\exp\left(-\frac{M}{M_\mathrm{y}}\right)\right] \\ &= k' M_\mathrm{y}\left[\left(\frac{M}{M_\mathrm{y}} - 1\right) + \exp\left(-\frac{M}{M_\mathrm{y}}\right)\right].\end{aligned} \tag{5.12}$$

(ii) Addition of a quadratic smoothing term

$$\frac{\mathrm{d}a}{\mathrm{d}t} = k'\left[M - M_\mathrm{y}\left(\frac{M}{M + M_2}\right)^2\right] \tag{5.13}$$

where M_2 is a constant to be defined. Observation of asymptotic behaviour ($\mathrm{d}a/\mathrm{d}t = 0$ at finite M) requires that

$$1 - M_\mathrm{y}\frac{M}{(M + M_2)^2} = 0\,. \tag{5.14}$$

This has one real root, at $M_2 = M_\mathrm{y}/4$. When $M_2 < \frac{M_\mathrm{y}}{4}$ it can be shown that Eq. (5.13) remains positive but passes through a maximum, which is infeasible, so the function is truncated, giving

$$\frac{\mathrm{d}a}{\mathrm{d}t} = k'\left[M - M_\mathrm{y}\left(\frac{M}{M + M_\mathrm{y}/4}\right)^2\right] \qquad M > M_\mathrm{y}/4 \tag{5.15a}$$

$$\frac{\mathrm{d}a}{\mathrm{d}t} = 0 \qquad M \le M_\mathrm{y}/4 \tag{5.15b}$$

Eq. (5.15) is hereafter referred to as the transition model, as it describes the transition from fast cleaning close to the impinging point to slow, creep-dominated cleaning far from it. The two expressions are compared in Figure 5.4, where it can be seen that they are reasonably close to each other.

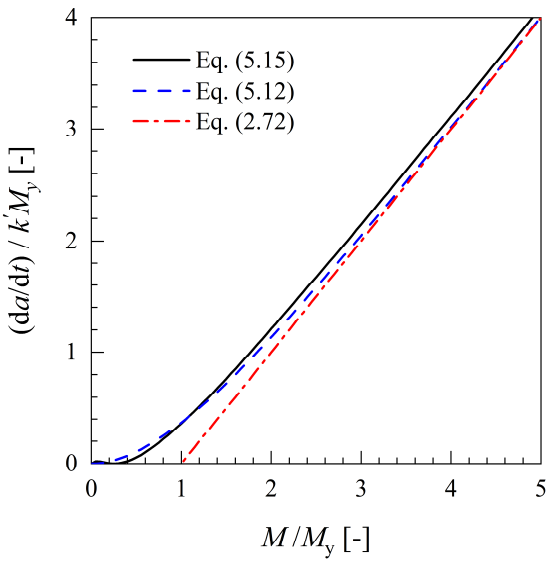

Figure 5.4 - Candidates for the transition model: Eq. (5.15) and Eq. (5.12) are plotted alongside Eq. (2.72), the adhesive removal model proposed by Glover *et al.* (2016).

Eq. (5.15) captures the key features of the transition, namely

(i) A linear dependency of cleaning rate on M at high values of M;

(ii) The rate approaches zero as M approaches zero, and is always positive;

The maximum cleaned radius $a_{\max}$ is reached at $M_y/4$. Inspection of the data indicated that $M > M_y/4$ in all the experiments reported here, so Eq. (5.15) provides a better description of the tests than Eq. (5.12) since in Eq. (5.12) $\mathrm{d}a/\mathrm{d}t \to 0$ only when $M \to 0$, so an asymptotic maximum cleaned radius is not obtained when Eq. (5.12) is fitted to the data. Eq. (5.15) captures the transition in removal from a momentum-driven removal to erosion involving creep. This 'transition model' provides a good description of experimental data obtained with the PJA, the PJS and the WSP, and is also compared to data sets previously reported by other authors. Recently, Chee and Wilson (2021) also showed that Eq. (5.15) described the cleaning of other viscoplastic materials, namely tomato ketchup and two toothpastes.

For cases where $a_{\max} > r_{\mathrm{b}}$ (weak soil), the momentum flow rate of the liquid film can be estimated by Eq. (2.39) and when $a_{\max} < r_{\mathrm{b}}$, M can be described by Eq. (2.37). Substituting these results into Eq. (5.15a) for $a = a_{\max}$, and setting $\frac{\mathrm{d}a}{\mathrm{d}t} = 0$ yields:

$$a_{\max} = \frac{12}{5\pi} \frac{U_{\mathrm{o}} \dot{m}}{M_{\mathrm{y}}} \tag{5.16}$$

for the strong soil, and

$$a_{\max} = \left(\frac{12}{5\pi c}\right)^{1/4} \frac{\dot{m}^{3/4}}{M_{\mathrm{y}}^{1/4}} \tag{5.17}$$

for the weak soil.

These expressions are compared with data from several experiments in Section 5.3.3. They provide a quick way to evaluate if the strong soil and weak soil models can describe the asymptotic growth of the cleaned radius over time.

5.2 Traversing nozzles

As discussed in Section 2.4.6, when a coherent normally impinging jet traverses across a soiled flat surface it generates a round-nosed band of width w_{c} that is clear of soil. Since Eq. (2.76) describes the cleaning by a moving jet without any assumption about the cleaning model employed, it provides a general framework for describing the shape of the cleaned region. Eq. (2.77), (2.78) and (2.79) presented by Bhagat *et al.* (2017) describe the shape of the cleaned region for the weak, strong and intermediate soil cases. To obtain the appropriate equations for the description of cleaning by traversing nozzles, substitution of the corresponding kinetic expressions into Eq. (2.76) is required.

(i) 'Weak viscoplastic soil'

This is the case considered by Glover *et al*. (2016) and requires that $a_{\mathrm{x}} > r_{\mathrm{b}}$, so that the point of the cleaning front immediately ahead of the impinging point lies within the weak soil region (see Figure 2.18). At X

$$\left.\frac{\mathrm{d}a}{\mathrm{d}t}\right|_{\mathrm{X}} = v_{\mathrm{jet}} = \alpha \left(\frac{1}{a_{\mathrm{x}}^4} - \frac{1}{a_{\max}^4}\right) \tag{5.18}$$

This offers a check on the model as it predicts that a_x^{-4} increases linearly with v_{jet}. Substituting this result into Eq. (2.76) to eliminate α gives

$$\frac{dp^*}{d\beta} = \underbrace{\frac{1}{p^{*3}\sin\beta} - \frac{p^*}{\tan\beta}}_{\text{Hydrodynamic term}} + \underbrace{\frac{M'_y}{p^{*3}v_{jet}\sin\beta}\left(1-p^{*4}\right)}_{\text{Yield stress term}} \tag{5.19}$$

where $p^* = p/a_x$ and $M'_y = \alpha/a_{max}^4$. This requires numerical evaluation, with initial condition $p^* = 1$ at $\beta = 0$.

(ii) 'Strong viscoplastic soil'

For Eq. (5.5) to apply, $a_x < r_b$. At X

$$\left.\frac{da}{dt}\right|_X = v_{jet} = \sigma\left(\frac{1}{a_x} - \frac{1}{a_{max}}\right). \tag{5.20}$$

In this case a_x^{-1} increases linearly with v_{jet}. Elsewhere

$$\left.\frac{da}{dt}\right|_P = \sigma\left(\frac{1}{p} - \frac{1}{a_{max}}\right) \tag{5.21}$$

and Eq. (2.76) becomes

$$\frac{dp^*}{d\beta} = \underbrace{\frac{1}{\sin\beta} - \frac{p^*}{\tan\beta}}_{\text{Hydrodynamic term}} + \underbrace{\frac{M'_y}{v_{jet}\sin\beta}\left(1-p^*\right)}_{\text{Yield stress term}} \tag{5.22}$$

where $M'_y = \sigma/a_{max}$.

Both Eqs (5.19) and (5.22) feature a hydrodynamic term and a yield stress term. The hydrodynamic terms are similar to the RHS of the moving jet equations proposed by Bhagat *et al.* (2017).

(iii) 'Transition model'

Eq. (2.75) is combined with a numerical evaluation of M to calculate the local cleaning rate in the integration of Eq. (2.76). It is expected to give a better description of the traversing nozzle profiles as the transition model gives a better description of the local cleaning rate for static nozzles, as shown in Figure 5.3. The dependency of a_x on v_{jet} offers a second way of testing the validity of the models. In this case, at point X:

$$\left.\frac{\mathrm{d}a}{\mathrm{d}t}\right|_{\mathrm{X}} = v_{\mathrm{jet}} = k'\left[M_{\mathrm{X}} - M_{\mathrm{y}}\left(\frac{M_{\mathrm{X}}}{M_{\mathrm{X}}+M_{\mathrm{y}}/4}\right)^2\right] \tag{5.23}$$

where M_{X} is the momentum flow rate per unit length of the liquid film at a_{X}.

5.3 Results for cleaning experiments

5.3.1 Evolution of the cleaning radius

The evolution of the cleaned radius is presented in Figure 5.5 (a) for experiments conducted with the same layer thickness and hydrodynamic conditions. Since the jet impinges normally to the surface, the cleaned front is roughly circular with radius a. Perspex® and glass plates were used, and the average value of a is plotted against the time elapsed since breakthrough of the jet through the layer was first seen. The larger uncertainties at longer times arise from asymmetry in the cleared region. This is evident in the circularity data presented in Figure 5.5 (b) for one of the experiments conducted with the Perspex® substrate.

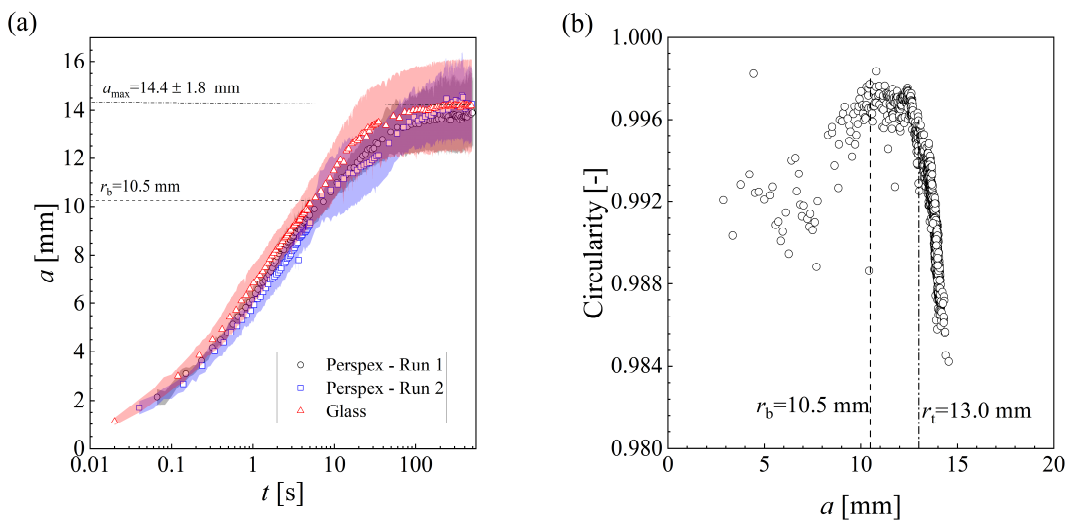

Figure 5.5 – (a) Evolution of the cleaned radius for three experiments with $Q = 1$ l·min^{-1}, $\delta_o = 0.37 \pm 0.02$ mm conducted on Perspex® and glass plates. Shaded regions represent the standard deviation of the data. (b) Circularity vs cleaned radius for one of the experiments reported in (a) with a Perspex® plate.

The effect of the substrate is smaller than the difference between repeats. Perspex® substrates were therefore used for the subsequent experiments reported here. In all cases, the cleaning front reaches a limit, a_{max}, which in the majority of the experiments is larger than r_{b}. One of the cases in which $a_{\mathrm{max}} < r_{\mathrm{b}}$ is reported in Figure 5.2 (b). The cleaning region is initially

circular: at r_t, fingering starts to take place and the cleaning region departs from a circular shape. This can be quantified with the circularity C_i, given by

$$C_i = 4\pi A_r / P_e^2 \tag{5.24}$$

where A_r is the area of the cleaned region and P_e is the perimeter.

Figure 5.6 (a) shows the data from different cleaning experiments presented in the form of Eq. (2.72), where M was calculated using the Bhagat and Wilson (2016) hydrodynamic model. When the momentum flow rate imposed by the liquid film is high, the dependency of $\mathrm{d}a/\mathrm{d}t$ with M is approximately linear, indicating that a simple rate law such as Eq. (2.72) is sufficient to describe the observed behaviour. Non-linear behaviour is observed at large a, as $\mathrm{d}a/\mathrm{d}t$ approaches zero, which is not captured by the model proposed by Glover *et al.* (2016). Also shown are the fits of Eq. (5.15a) to the datasets, indicating that the transition model can describe the variation in $\mathrm{d}a/\mathrm{d}t$ for experiments with different ranges of M. Integration of Eq. (5.15a) leads to the estimate of a over t shown in Figure 5.6 (b). Both the rapid initial growth and the asymptotic behaviour are described well by the transition model. In some cases, the model deviates from the experimental data when $a > r_b$, as shown for the case with $d_N = 4$ mm, $Q = 5$ l·min^{-1} and $\delta_o = 0.50$ mm. This behaviour was also reported by Feldung Damkjær *et al.* (2017), and the reason for this is not currently understood.

Figure 5.6 (c) shows the cleaning rate plotted against the shear stress imposed by the liquid film on the soil surface, $\tau_{w,l}$, for the experimental conditions in Figure 5.6 (a) and (b). The shear stress imposed by the liquid film is lower than τ_c obtained from the rheometry tests. This suggests that the jelly is creeping rather than flowing under the force imposed by the liquid film, leading to the non-linear relationship between $\mathrm{d}a/\mathrm{d}t$ and M reported in Figure 5.6 (a). This non-linear behaviour is captured by the transition model. It also suggests that cleaning is driven by a momentum-driven mechanism rather than a shear-driven mechanism as proposed by Yeckel and Middleman (1987). This is discussed in more details in Section 6.3 where the cleaning of very thin layers is considered, in terms of a shear-driven mechanism.

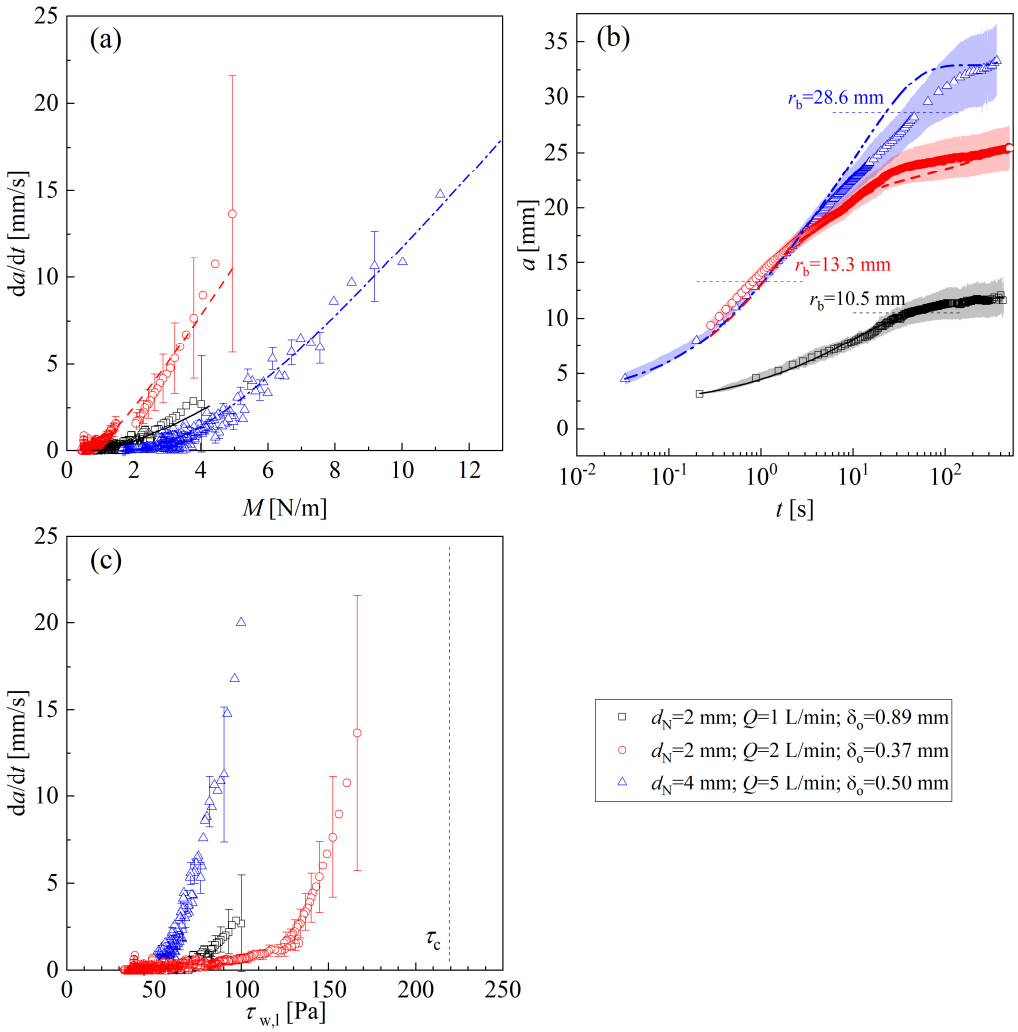

Figure 5.6 - Effect of flow rate on cleaning performance. (a) da/dt as a function of M for three cleaning experiments: M was calculated using the Bhagat and Wilson (2016) model. Error bars represent the propagated uncertainty in da/dt and lines represent the fit of Eq. (5.15a). (b) Evolution of cleaned radius a over time for the experiments in (a). Lines indicate the integration of Eq. (5.15a). (c) $\mathrm{d}a/\mathrm{d}t$ vs $\tau_{w,l}$ for the experiments in (a).

5.3.2 Crater topography

The shape of the rim of the cleaned area was measured with the confocal profilometer. The angles ϕ_1 and ϕ_2, discussed in Section 3.5.2, are reported in Figure 5.7 (a) as a function of the ratio between the thickness of the liquid film h, calculated using Eq. (2.48), (2.53) or (2.58), and the thickness of the undisturbed soil layer, δ_o. Asymptotic cases, in which the soil layers were exposed to the impinging jet until a approached a_{max}, as well as interrupted experiments, are reported.

Two distinct regimes are evident: when $h/\delta_o \leq 0.5$, ϕ_1 and ϕ_2 differ, indicating that the rim shape is not a simple wedge as assumed by Glover *et al.* (2016). For $h/\delta_o > 0.5$, however, the values of ϕ_2 decrease and gradually approach those of ϕ_1. The values of ϕ_2 for $h/\delta_o \leq 0.5$ are close to 45°, whereas with thicker liquid films the slope is more gradual, ranging from 10° to 30°. An angle of 45° suggests that the radial momentum flow of the thin film generates internal yielding within the soil layer.

The thickness of the liquid film generated by an impinging jet changes with radial position (see Figure 2.11), and so the value of h/δ_o changes over the duration of a cleaning experiment. To investigate this, a plate coated with a δ_o=0.37 mm layer was exposed to an impinging jet with $Q = 1$ l·min^{-1} for different lengths of time and the rim shape measured. The values of ϕ_1 and ϕ_2 are presented in Figure 5.7 (b). The same trend is evident, indicating that h/δ_o is the governing factor determining the shape of the rims throughout the cleaning process.

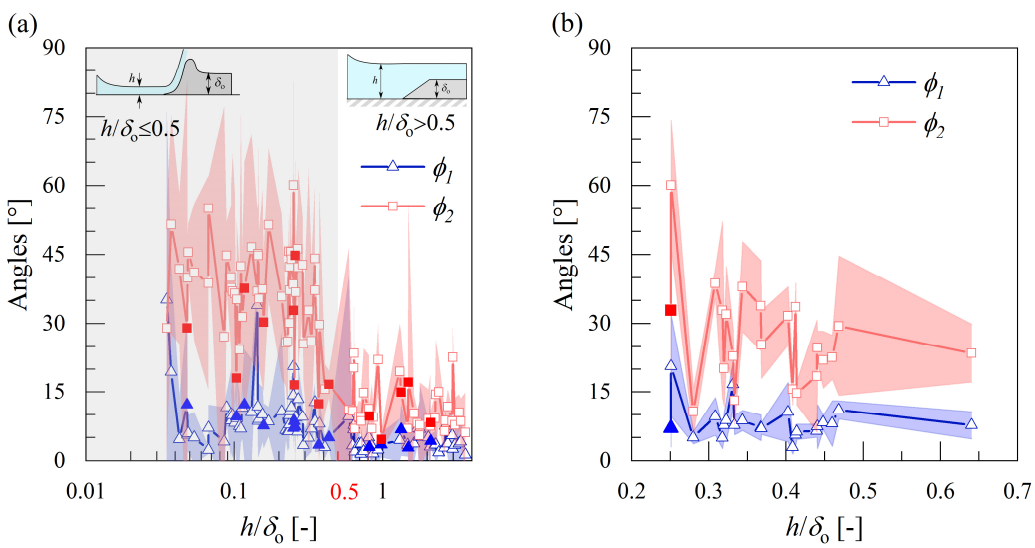

Figure 5.7 - Summary of cleaning front shapes. (a) Effect of h/δ_o on ϕ_1 and ϕ_2 for cleaning experiments conducted with different flow rates, $d_N = 2$ mm. Solid symbols indicate experiments that were run until a approached a_{max}. (b) Evolution of angles ϕ_1 and ϕ_2 during a cleaning test: $d_N = 2$ mm, $Q = 1$ l·min^{-1}, $\delta_o = 0.37$ mm interrupted at different stages and angles measured. Shaded areas represent the 95% confidence interval of the measurements in the four perpendicular directions.

Figure 5.8 (a) presents some of the scanned profiles reported in Figure 5.7 (b). The values of h described by the Bhagat and Wilson (2016) model are also shown. These scans were measured at $\theta = 0°$, and the corresponding values of a are indicated in the evolution of the

cleaned radii reported in Figure 5.8 (b). The berm grows over time, and the morphology of the rim is reasonably close to 45° for $\delta > h$. In the region where $\delta < h$, the shape of the rim changes slightly over the cleaning time, which is reflected in the small changes in ϕ_1 reported in Figure 5.7 (b).

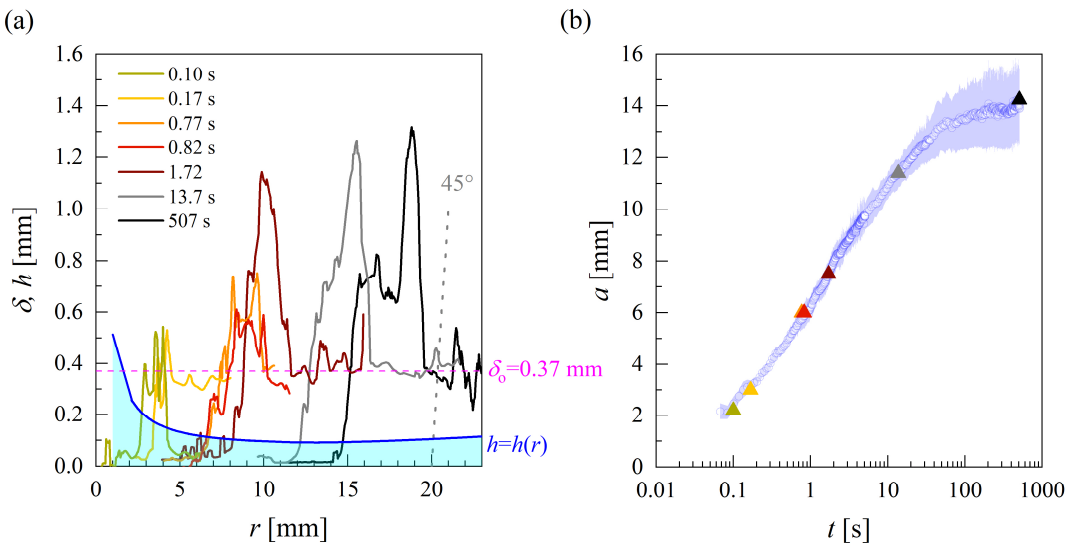

Figure 5.8 – (a) Scanned profiles at different cleaning times and values of h as a function of r for some of the data points reported in Figure 5.7 (b). The dotted grey line indicates a slope of 45°, horizontal dashed magenta line denotes δ_o and the shaded blue region indicates $h(r)$. (b) Evolution of the cleaned radius, indicating the points where the profiles shown in (a) were measured: colours of the symbols in (b) match those in (a). PJA, $d_N = 2$ mm, $Q = 1$ l·min^{-1}, $\delta_o = 0.37$ mm.

5.3.3 Parameter analysis – static nozzles

The transition model was fitted to the experimental data reported in this chapter and those reported by Feldung Damkjær *et al.* (2017) and Glover *et al.* (2016), who used different petroleum jellies. The parameters k' and M_y are compared in Figure 5.9 (a). There is no clear relationship between k' and M_y for each data set, and there is a noticeable difference between the values of k' for each petroleum jelly. This indicates that k' is influenced by the rheology of the layer. Figure 5.9 (b) presents the values of a_{max} and M_y in the form suggested by Eq. (5.17) for cases where $a_{max} > r_b$, *i.e.* in the weak soil region. The inset presents the data in the form proposed by Eq. (5.16) for the strong soil cases. Both show linear trends, indicating that the wedge model with simple hydrodynamics captures some elements of the mechanism.

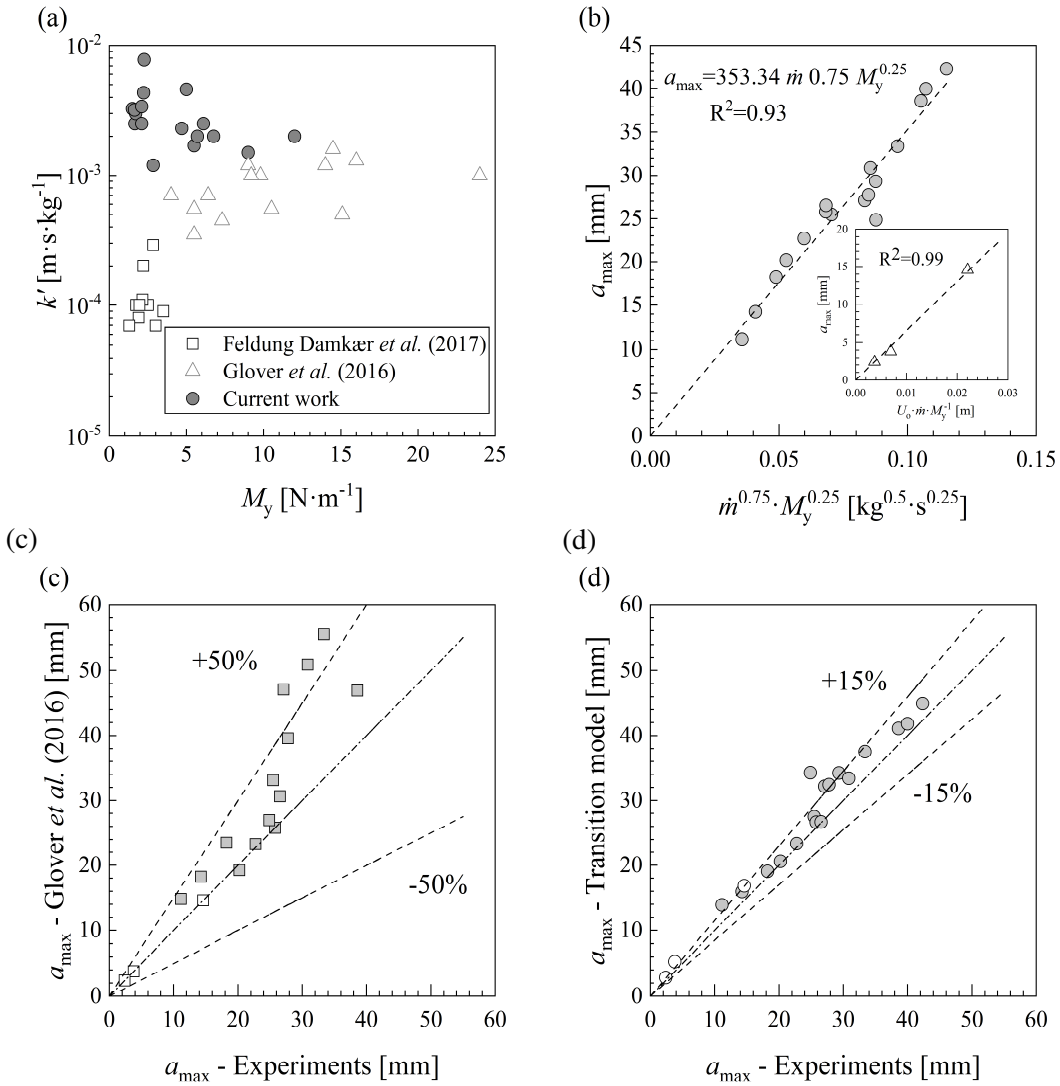

Figure 5.9 - Transition model parameters obtained for different studies of jet cleaning of petroleum jelly. (a) k' and M_y obtained for (*i*) the current work, (*ii*) Glover *et al.* (2016), and (*iii*) Feldung Damkær *et al.* (2017); (b) relationship between a_{max} and M_y plotted in the form suggested by Eq. (5.17) (weak soil). Inset shows the trend for strong soil cases (Eq. (5.16)). (c) agreement between a_{max} estimated with the assumption of linear coupling between da/dt and M, Eq. (5.16) and Eq. (5.17), and experimental values. (d) agreement between a_{max} estimated with the transition model, Eq. (5.16) and (5.17), and experimental values. Solid symbols in (c) and (d) indicate cases where $a_{max} > r_b$, open symbols $a_{max} < r_b$.

Figure 5.9 (c) and (d) compare the performance of the transition model with the model of Glover *et al.* (2016) by comparing the values of a_{max} obtained from each model with the experimental values of a_{max}. Figure 5.9 (c) shows that a_{max} obtained with Eq. (5.16) and Eq. (5.17), corresponding to the assumption of linear coupling between da/dt and M

calculated with the strong and weak soil hydrodynamic models, respectively, give estimates which agree with the experimental values within error bands of ±50 %. The values of $a_{\max}$ calculated for the transition model are the radial position at which $M = M_y/4$, and are compared to the experimental values of $a_{\max}$ in Figure 5.9 (d), agreeing within ±15 %. This indicates that the transition model can describe the evolution of the cleaned radius for a viscoplastic soil layer more reliably than the earlier model, principally because it includes a term to account for the creep seen in the rheological tests. Good agreement was also found in linking the results from static and moving nozzles.

Figure 5.10 compares the measurements of the shape of the cleaning front at $a_{\max}$, ϕ_1 and ϕ_2 in Figure 5.7 (a), with that calculated using the wedge assumption (Eq. (2.74)) of the Glover *et al.* (2016) model. The values of χ in Figure 5.10 were calculated using the momentum of the liquid film calculated with the Bhagat and Wilson (2016) model. These calculations employed the value of the critical stress identified in Section 4.1.3 for τ_c.

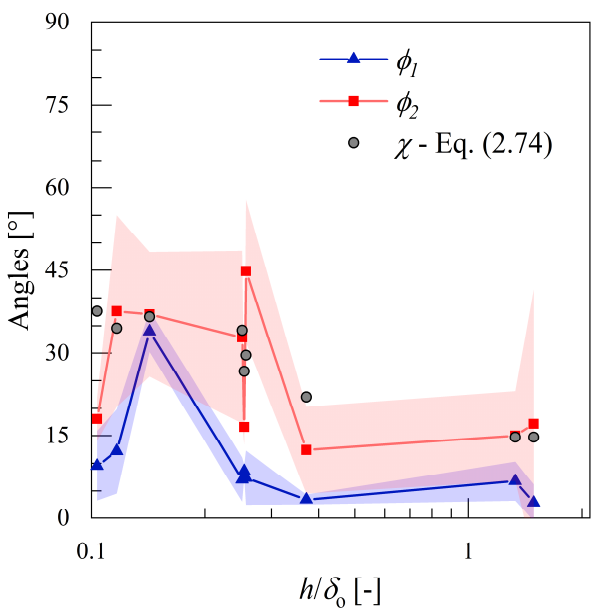

Figure 5.10 – Comparison of measured rim shape for the asymptotic cases with χ calculated using the wedge model of Glover *et al.*, Eq. (2.74): angles ϕ_1 and ϕ_2 are the asymptotic cases reported in Figure 5.7 (a). Shaded areas represent the 95% confidence interval of the measurements in the four perpendicular directions.

The values of χ are comparable to the values of ϕ_2, indicating that the deformation occurring at the rim includes a significant contribution from shear of the viscoplastic fluid. More detailed modelling is required to predict the shape of the rim and to explain the reason for

the change in angle at h/δ_o ~ 0.5. Glover *et al*. (2016) reported χ values in the range 10-25° using the weak soil model to estimate M_y. This tends to overestimate M at smaller a, where asymptotic behaviour is observed (see Figure 2.10), which may explain the difference from the values obtained here.

5.3.4 Cleaning by moving jets

Moving jet experiments were performed with petroleum jelly layers of thickness ranging from 0.194 to 1.05 mm on vertical Perspex® plates. Constant water flow rates were used, with $1 \leq Q \leq 2$ l·min^{-1} and a 2 mm nozzle. The transverse velocity of the target plates ranged from 8.9 to 155 mm·s^{-1}. As discussed by Glover *et al.* (2016), the cleaning front generated by a moving jet impinging on the moving substrate is more stable when the plate moved downwards rather than upwards, due to the jet impinging on an undisturbed layer. Therefore, all the experiments reported here were conducted with the plate moving downwards.

Figure 5.11 (a) presents the shape of the cleaned region generated by a moving jet ($Q = 2$ l·min^{-1}; $\delta_o = 0.33$ mm; $v_{jet} = 15.09$ mm·s^{-1}), along with the estimates of the cleaned region provided by the different cleaning models. The value of k' used in each case was found by fitting the corresponding model to the a vs t data obtained using a static nozzle. Both the strong and the transition soil formulations provide good descriptions of the shape of the cleaned region near the point of impingement, where the cleaned radius is small and $\mathrm{d}a/\mathrm{d}t$ is high. The biggest difference between these two models occurs beyond r_b^* where $\mathrm{d}a/\mathrm{d}t$ is small and the strong soil model fails to describe the non-linear relationship between $\mathrm{d}a/\mathrm{d}t$ and M (see Figure 5.3). The transition model, on the other hand, describes the shape of the cleaned region from the initial stages up to a_{max}^*. Beyond a_{max}^* there is no change and the cleaning front is a horizontal line with width w_c.

The weak viscoplastic soil model did not give a good description of the shape of the cleaned region. This is because this model is fitted for $a > r_b$, where $\mathrm{d}a/\mathrm{d}t$ is lower than in the boundary layer formation region. The value of k' obtained with the weak soil model is thus smaller than the value of k' obtained with the strong soil and with the transition model, resulting in $\left(\frac{\mathrm{d}a}{\mathrm{d}t}\right)_P$ in Eq. (2.75) being underestimated and limiting the value of w_c obtained.

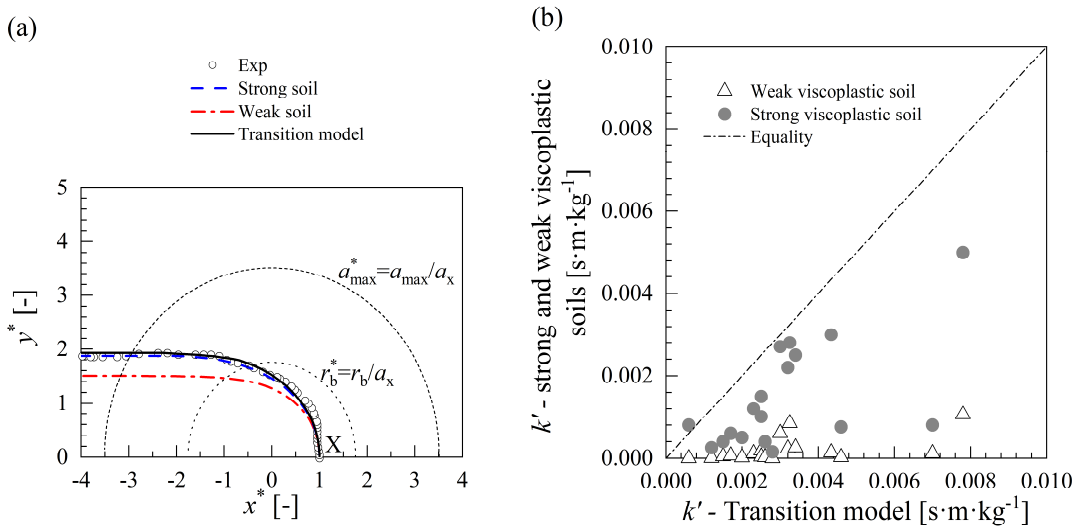

Figure 5.11 - Cleaning by a traversing jet. (a) Half-width of the trail generated by a moving jet with $d_N = 2$ mm; $Q = 2$ l·min^{-1}; $\delta_o = 0.33$ mm; and $v_{jet} = 15.09$ mm·s^{-1}. Fits of the strong viscoplastic soil, weak viscoplastic soil and transition model are shown. Dotted lines denote the loci of r_b/a_x and a_{max}/r_b. (b) k' found by fitting the strong and the weak viscoplastic soil models as a function of k' found by fitting the transition model. Dashed line denotes the line of equality.

This is demonstrated in Figure 5.11 (b), where the values of k' found by fitting the weak and strong viscoplastic soil models are compared with k' found by fitting the transition model to the asymptotic cases. k' estimated with both the weak and strong viscoplastic soils is smaller than k' found by fitting to the transition model. Additionally, the values of k' for the strong viscoplastic soil model are larger than those obtained with the weak version. Care therefore needs to be taken in comparing absolute values of k' obtained using different models.

Eqs. (5.18), (5.20) and (5.23) describe the relationship between a_x and v_{jet} expected for the three models. Figure 5.12 (a)-(d) presents the values of a_x as a function of v_{jet} for moving jet experiments conducted with different soil layer thicknesses and flow rates.

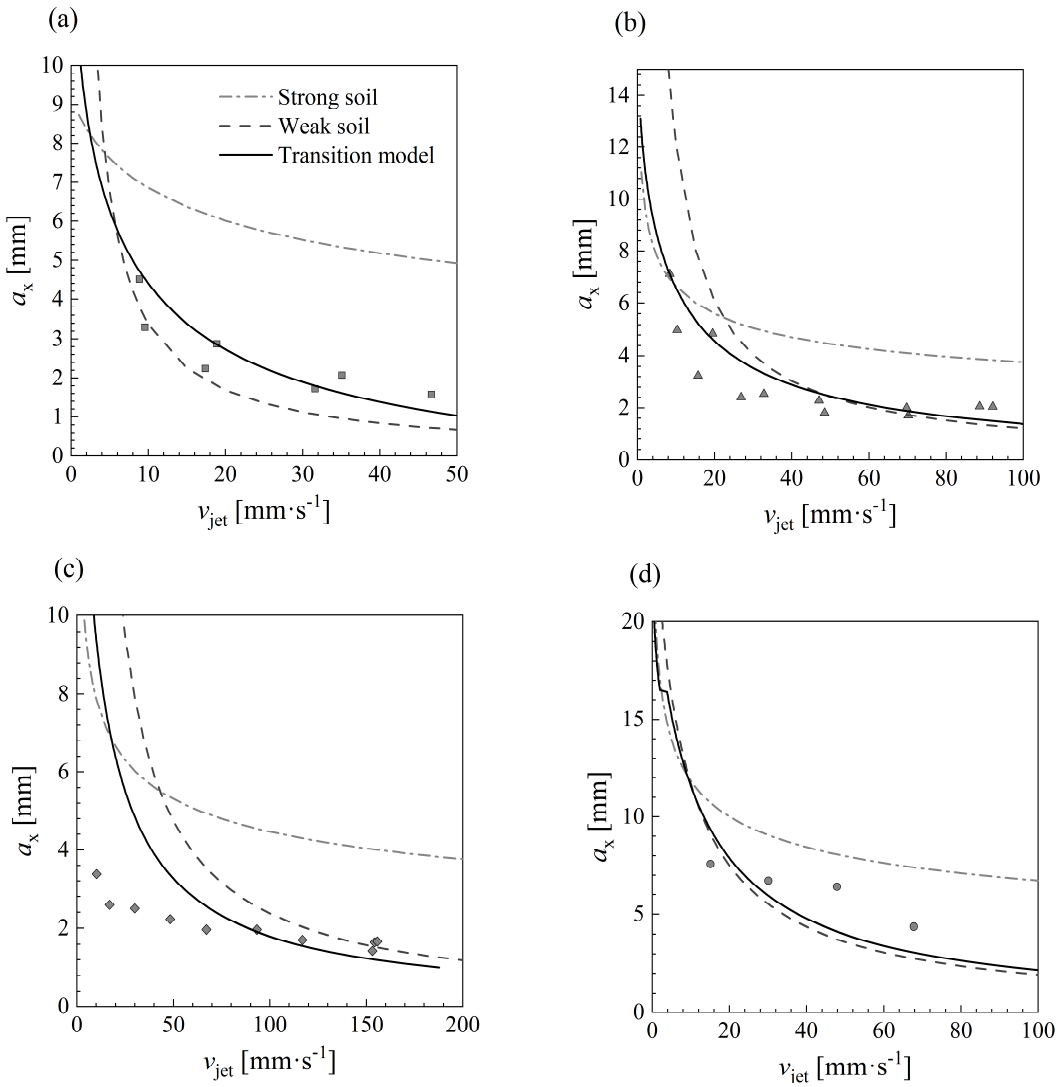

Figure 5.12 - Traversing jet: effect of v_{jet} on a_{x} and w_{c}. $d_{\mathrm{N}} = 2$ mm: (a) $Q = 1$ l·min^{-1}, δ_{o}=0.606 mm; (b) Q=1.2 l·min^{-1}, , δ_{o}=0.382 mm; (c) $Q = 1.6$ l·min^{-1}, δ_{o}=0.606 mm and (d) $Q = 2$ l·min^{-1}, δ_{o}=0.333 mm. Lines denote the results of the strong viscoplastic, weak viscoplastic and transition models, symbols denote the experimental values of a_{x}.

The transition model gives the most reliable description of the dependence of a_{x} on v_{jet}. The strong viscoplastic soil model provides reasonable agreement in two cases. The values of a_{x} all lie below r_{b} for each set of conditions and the weak viscoplastic soil model does not, therefore, describe the data well, since for $r < r_{\mathrm{b}}$ it overestimates M (see Figure 2.10).

Figure 5.13 (a) shows the observed values of w_c plotted against a_x for all the moving jet experiments conducted, with different values of Q, v_{jet} and δ_o. Fitting the data to a linear trend gave $w_c/a_x = 3.04$, which is similar to the result reported by Bhagat *et al.* (2017) using the adhesive failure weak soil model. It should be noted that the latter model would not predict a_x correctly (as $a_x < r_b$ in most cases) so this would appear to be a fortuitous coincidence. Eq. (2.75) was solved numerically, using the transition model, to estimate the rate of cleaning at each point on the front, giving w_c. The results in Figure 5.13 (b) follow the relationship $w_c/a_x = 3$, with noticeable scatter at larger a_x, which represents good agreement with the experimental trend.

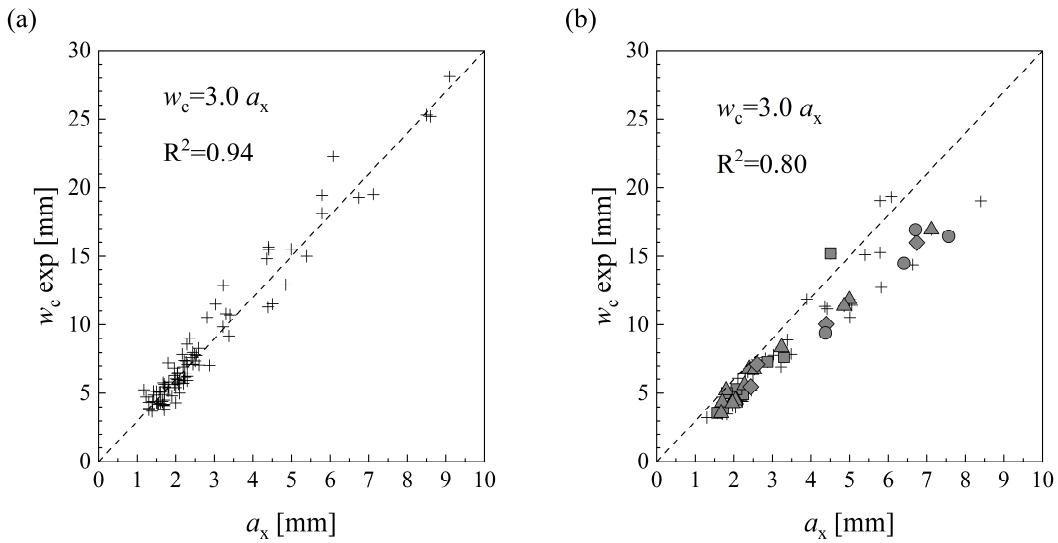

Figure 5.13 - w_c as a function of a_x for the moving jet experiments: (a) w_c measured from image analysis in the experiments, (b) w_c found by fitting the transition model. Symbols are those used in Figure 5.12

5.4 Cleaning other materials

The transition model presented in this chapter was also fitted to experimental data obtained with cleaning the other viscoplastic materials reported in Table 4.2, namely WSP, PJS and PJT, the material used by Glover *et al.* (2016). Figure 5.14 shows the data for cleaning thin soil layers of the three materials using coherent impinging water jets. In Figure 5.14 (a), plots of the cleaned radius as a function of time are presented, whereas in (b) the rate of growth of

the cleaned radius is plotted as a function of M obtained with the Bhagat and Wilson (2016) hydrodynamic model. Good agreement was obtained for the three materials. Recently, Chee and Wilson (2021) have used Eq. (5.12) and showed that it described the cleaning behaviour of tomato ketchup and two toothpastes well.

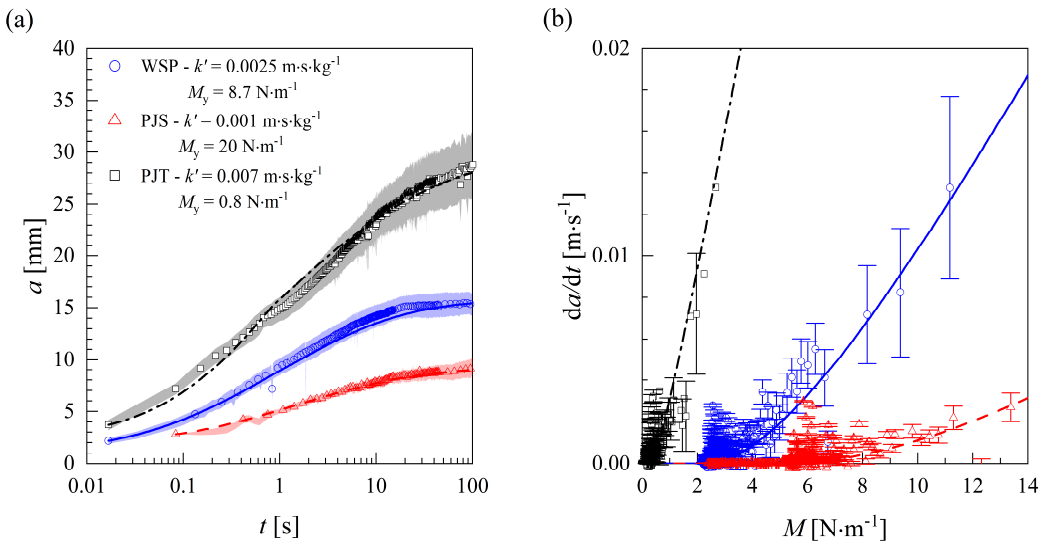

Figure 5.14 – Results for cleaning experiments obtained with the WSP (d_N =2 mm, Q=2 l·min^{-1}, δ_o=0.86 mm) and with the PJS WSP (d_N =2 mm, Q=2 l·min^{-1}, δ_o=0.85 mm). (a) a as a function of t; (b) da/dt as a function of M. Fits of the model are indicated by the continuous and dashed lines.

Cleaning experiments were also performed with the PJS, PJT, WSP and PJA at different soil layer thicknesses and impinging jet conditions. These experiments are summarised in Table 5.1, which also includes the values of k' and M_y obtained from fitting Eq. (5.15) to the data. The values of k' presented are plotted in Figure 5.15 as a function of (a) τ_c and (b) μ_B, where τ_c and μ_B were obtained by fitting the Bingham equation, Eq. (2.22), to increasing stress ramps at $\dot{\tau} = 50$ Pa·min^{-1}, reported in Chapter 4. Also plotted are the results of the fit of Eq. (5.15) to the cleaning of tomato ketchup (Heinz, UK) and toothpaste (Cavity Protection, Colgate-Palmolive, UK) reported by Chee and Wilson (2021), and for a further toothpaste (Advanced White, Colgate-Palmolive, UK) reported by Yang *et al.* (2019a).

Table 5.1 – Experimental conditions for data reported in Figure 5.15

Material	τ_c [Pa]	μ_B [Pa]	Q [l·min^{-1}]	d_N [mm]	δ_o [mm]	k' [m·s·kg^{-1}]	M_y [N·m^{-1}]
PJA	140	1	2	1.0	0.37	0.0017	0.82
			2	1.4	0.37	0.0040	1.50
			2	1.4	0.89	0.0047	1.45
			2	1.8	0.9	0.0030	2.06
			2	2.0	0.89	0.0030	1.37
			2	2.0	0.37	0.0030	1.46
			2	2.2	0.9	0.0047	0.82
			3	3.0	1.05	0.0020	2.15
			3	4.0	1.05	0.0022	6.36
			3	5.0	1.05	0.0026	4.92
			4	3.0	1.05	0.0016	6.10
			4	4.0	0.5	0.0019	2.56
			4	4.0	0.18	0.0033	2.64
			4	4.0	0.36	0.0010	2.51
			4	5.0	0.5	0.0024	7.50
			4	7.0	0.5	0.0015	8.72
			4	7.0	0.13	0.0080	11.4
WSP	200	0.1	2	1.2	0.86	0.0020	13.0
			2	1.6	0.86	0.0022	9.00
			2	2	0.89	0.0025	8.00
			2	2	0.85	0.0002	5.00
			3	1.4	0.86	0.0020	13.0
			3	2.2	0.86	0.0030	11.0
			3	3	0.86	0.0030	9.50
			4	4	0.86	0.0020	22.0
PJS	570	0.3	2	1.6	0.85	0.0008	15.0
			2	1.6	0.50	0.0007	23.0
			2	1.6	0.10	0.0007	18.0
			2	2	0.50	0.0007	18.0
			2	2	0.10	0.0007	13.0
			4	6	0.86	0.0002	17.5
PJT	213	0.04	2	1.6	0.10	0.0060	0.70
			2	2	0.45	0.0060	0.80
			2	2	0.10	0.0060	0.70
			2	2	0.86	0.0060	1.20
Tomato ketchup (Chee & Wilson, 2021).	26	0.5	2	2	0.60	0.300* 0.800†	0.12* 0.35†
Toothpaste (Chee & Wilson, 2021).	200	3	2	2	0.40	0.011	4.0
Oral B toothpaste, (Yang *et al.*, 2019a)	179	3	2	2	0.50	0.0068	1.15

*Value obtained by fitting Eq. (5.15) of the current work.
†Value reported by Chee and Wilson (2021)

Figure 5.15 (a) shows a general decreasing trend of k' with τ_c, which is consistent with the relationship $k' \propto \tau_c^{-1.75}$ reported by Wilson *et al.* (2014), Figure 2.17. The data also fit the trend $k' \propto \tau_c^{-2.00}$ reasonably well. The value of k' for tomato ketchup reported by Chee and Wilson (2021) is slightly larger than the value reported in Figure 5.15, and both fittings provided a good description of the data. There is no clear trend for how k' changes with μ_B: the Bingham model does not incorporate non-linearities below and above τ_c, which are present in some of the materials. The Bingham description of the soil layer materials is used here, as it is used in the detailed cleaning model discussed in Chapter 6. k' is therefore expected to depend not only on the rheology of the soil layer, but also on the interaction between the layer and the liquid film. This will be discussed further in Chapter 6.

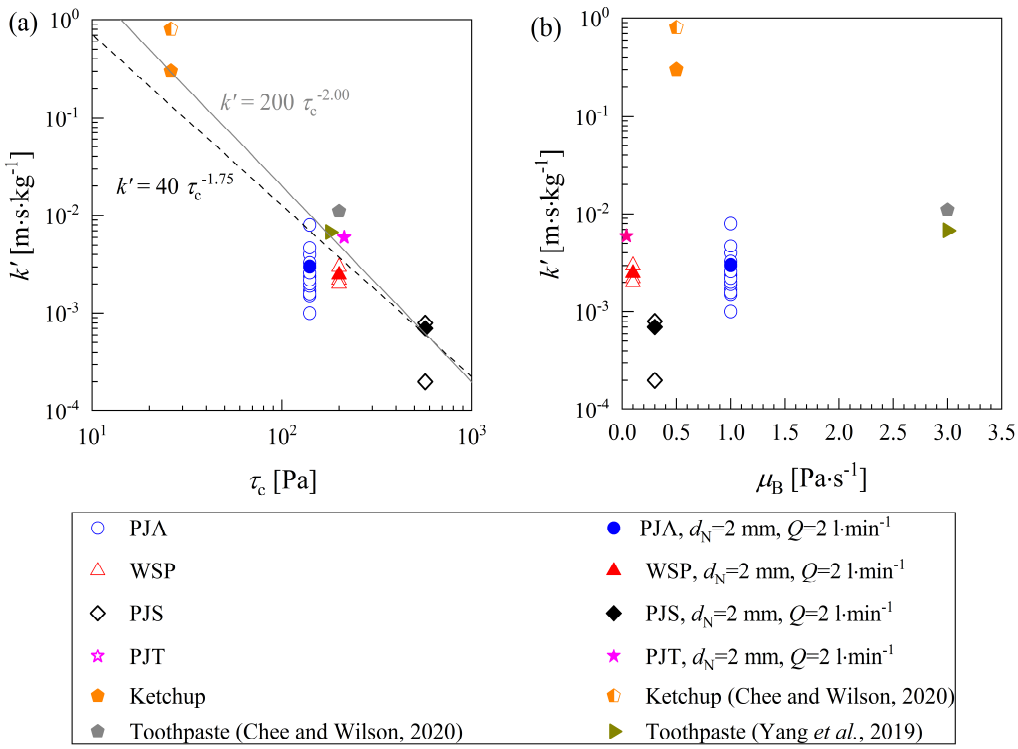

Figure 5.15 – Dependency of k' on (a) τ_c and (b) μ_B for experiments conducted with the PJA, WSP, PJS and PJT at the conditions outlined in Table 5.1 for tomato ketchup and Colgate toothpaste reported by Chee and Wilson (2021) and for the advanced white toothpaste reported by Yang *et al.* (2019a). Filled symbols denote experiments conducted with similar jet hydrodynamics: $d_N = 2$ mm and $Q = 2.0$ l·min^{-1}; empty symbols denote other hydrodynamic conditions. Half-filled symbol for tomato ketchup indicates the value of k' reported by Chee and Wilson (2021).

Figure 5.16 shows the relationship between M_y and τ_c. In addition to the materials reported in Figure 5.15, the results of fits of Eq. (5.15) to the data reported by Wilson *et al.* (2014) for cleaning of a petroleum jelly and by Chee *et al.* for cleaning of Clearglide (a commercial Carbopol® dispersion) are also shown. As expected, M_y increases with τ_c when soils of different rheologies are cleaned with liquid jets of similar d_N and Q: layers with larger yield stresses are more difficult to clean, reaching a smaller maximum cleaned radius, where the values of M_y are larger.

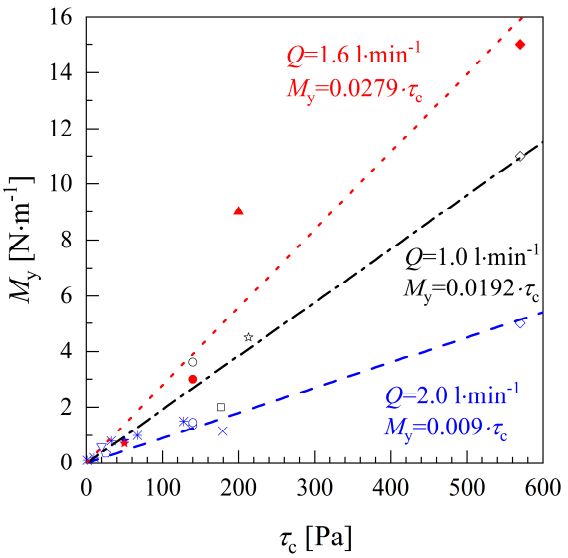

Figure 5.16 - M_y as a function of τ_c for the PJA, WSP, PJT, PJS, tomato ketchup (Chee & Wilson, 2021), toothpaste (Yang *et al.*, 2019a), the petroleum jelly reported by Wilson *et al.* (2014) (∗) and Clearglide (Chee *et al.*, 2018) (▽) at three flow rates and $d_N = 2$ mm. All other symbols follow those of Figure 5.15.

The data in Figure 5.16 were obtained with soil layers of different thicknesses, ranging from 0.1 to 0.9 mm. According to the Glover *et al.* (2016) model, which assumes that the cleaning front is a wedge of constant angle χ, Eq. (2.74), the relationship between M_y and δ_o is expected to depend strongly on the soil layer thickness. However, Figure 5.16 suggests that M_y is significantly more affected by the rheology of the soil layer than by its thickness.

5.5 Effect of the soil layer thickness

Wilson *et al.* (2014) and Glover *et al.* (2016) proposed that the cleaning rate constant k' depends on δ_o. Cleaning experiments were performed on PJA layers, using an impinging liquid jet with d_N = 2 mm, $Q = 3$ l·min^{-1} and δ_o values ranging from 0.038 to 1.45 mm. The jelly was dyed with a white oil-soluble food dye to assist identification of the cleaned radius for experiments involving very thin soil layers. The evolution of the cleaned radius for these experiments is presented in Chapter 6, where these results are further discussed. $h/\delta_o < 0.5$ for $\delta_o > 0.23$ mm (see Figure 6.24 (b)): this value is indicated in the plots reported in Figure 5.17.

The values of k' and M_y obtained from these tests are presented in Figure 5.17 (a) as a function of δ_o. M_y decreases with δ_o, particularly for very thin soil layers, while k' is roughly constant. This suggests that the initial thickness of the soil layer does not influence the cleaning behaviour significantly close to the impinging point. M_y is roughly constant for $\delta_o > 0.23$ mm, where $h/\delta_o < 0.5$. This suggests that the thickness of the soil layer does not significantly affect the cleaning dynamics when $h/\delta_o < 0.5$.

The thickness of the liquid film for the impinging jet used for the experiments reported is shown as a function of the radial coordinate in Figure 5.17 (b). Figure 5.17 (c) shows the values of a_{max} as a function of δ_o, and indicates that thinner layers reach a smaller value of a_{max}. For δ_o>0.45 mm, there is no significant effect on a_{max}. Understanding what influences k' and M_y is one of the aims of the next chapter, in which a detailed model for the flow behaviour at the cleaning front is proposed.

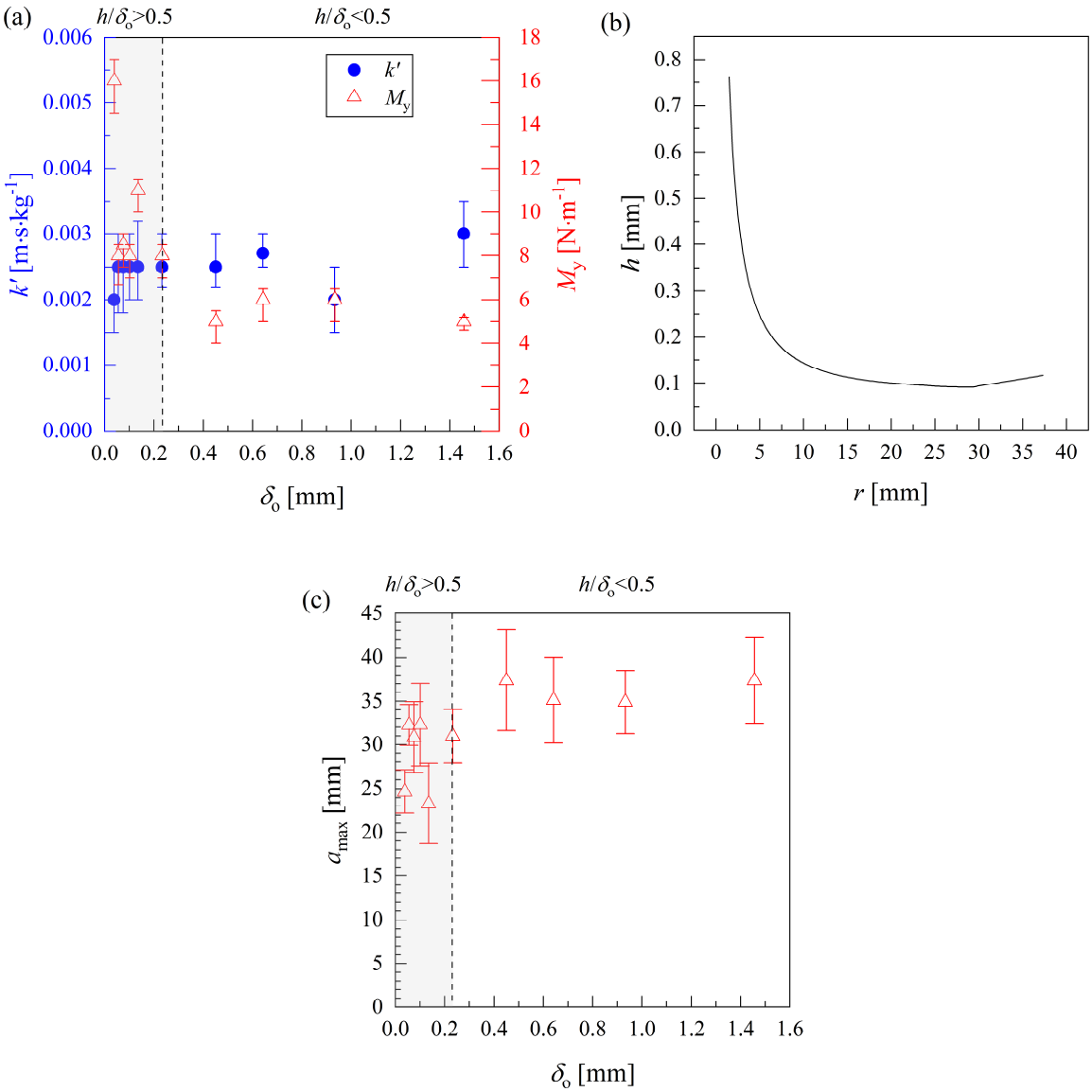

Figure 5.17 – (a) Effect of layer thickness δ_o on k' (left y-axis) and M_y (right y-axis) for dyed PJA, Q = 5 l·min^{-1} and d_N = 3 mm. (b) h as a function of r for for the liquid jet used in the experiments reported in (a). (c) a_{max} as a function of δ_o.Vertical dashed line indicates in (a) and (c) indicates the value of δ_o which corresponds to $h/\delta_o \approx 0.5$. Error bars in (a) show the estimated uncertainty in the gradient from the fitting, error bars in (c) show the standard deviation of the radii at $a = a_{max}$.

5.6 Critique and considerations

In this chapter, the model for momentum-driven cleaning of viscoplastic soil layers by Glover *et al.* (2016) was revisited using more precise estimates for M. The results indicate that the linear model proposed by Glover *et al.* (2016) model does not describe removal well

when $M \to M_y$ due to creeping of the soil layer. A semi-empirical term was included to describe the transition from fast to slow cleaning. This 'transition model' is not a predictive tool in the sense that the parameters k' and M_y are obtained by fitting of experimental data. Measurements of the shape of the cleaning front indicated that the simple wedge-shaped model of Glover *et al.* (2016) does not give a full description of the cleaning mechanism. It is, however, a useful engineering model as it allows cleaning by traversing nozzles to be predicted reliably.

The fitted parameter k' was compared for soils of different rheologies: k' shows a decreasing dependency on τ_c and is not influenced significantly by μ_B. It is roughly independent of the initial thickness of the soil layer, particularly for cases where $h/\delta_o > 0.5$. Therefore, further work is required to link the cleaning behaviour of the soil to the liquid film hydrodynamics, and this will be explored in the next chapter.

6 Detailed modelling of cleaning of a viscoplastic soil layer by a coherent impinging water jet

Chapter 5 presented a phenomenological model that describes the experimental results in terms of a momentum-driven mechanism. This was done by modifying the linear rate model of Glover *et al.* (2016) to include the slow cleaning that takes place far from the impinging point. The cleaning rate constant k' was obtained by fitting to experimental data. In Section 6.1, an argument based on viscous dissipation in the soil layer at the cleaning front is proposed which provides insights into how the layer rheology affects k'. This is not a truly predictive model, but it provides perspectives on how cleaning occurs. The work in Section 6.1 has been published in the Journal of non-Newtonian Fluid Mechanics (Fernandes & Wilson, 2020).

This model is extended in Section 6.2 to include dissipation in the accumulated berm. Section 6.3 presents an alternative modelling approach, based on that of Yeckel and Middleman (1987), to model the cleaning of very thin layers of a viscoplastic soil through a shear-driven mechanism.

6.1 Momentum-driven cleaning of viscoplastic soil layers

It was shown in Section 5.3.2 that the ratio of the thickness of the liquid film, h, to that of the soil layer, δ_o, influences the cleaning dynamics. Figure 6.1 presents three distinct cases:

(a) Very thin soil layers, for which $\delta_o \ll h$, where the film flows over the layer and removal is primarily by viscous drag, as modelled by Yeckel and Middleman (1987).
(b) Thin soil layers, for which $\delta_o \sim h$, and where the film is deflected away from the wall by the displaced soil and removal involves a moving front.
(c) Thick soil layers, when $\delta_o \gg h$. Tuck *et al.* (2020) reported blister formation and bursting with thick layers of FMCG products, including dispersions of Carbopol® in

water. The liquid jet initially burrows into the soil layer and accumulates in a blister which eventually ruptures.

The area cleaned is approximately circular for a jet impinging normally. The cleaned radius, a, is the radial position where the residual layer thickness is negligible. Cases (a) and (b) were investigated experimentally in Chapter 5 and are commonly observed on the sidewalls of processing tanks and vessels. Case (c) is more likely to be observed at the base of such vessels. This chapter considers cases (a) and (b).

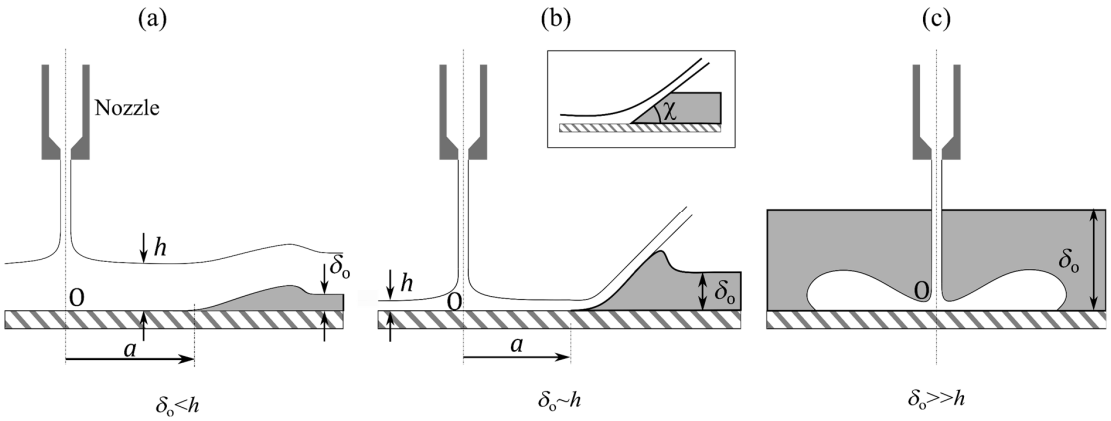

Figure 6.1 – Schematic of jet cleaning for different soil layer scenarios. (a) Very thin soil layer, (b) thin soil layer and (c) thick soil layer. Inset in (b) shows the wedge construction employed by Glover *et al.* (2016)

Glover *et al.* (2016) investigated the removal of viscoplastic thin soil layers from flat surfaces by coherent, turbulent impinging water jets. Their empirical model, Eq. (2.72), differs from film erosion models such as those presented by Yeckel and Middleman (1987) and Yeckel *et al.* (1990), where the flow exerts a shear stress on top of the layer causing it to flow downstream. The local thinning rate is then determined by the shear stress exerted on the layer. Figure 5.6 indicated that a shear driven mechanism (as in (Yeckel & Middleman, 1987; Yeckel *et al.*, 1990)) is unlikely to apply to case (b) as the shear stress imposed by the liquid film is smaller than the critical stress of the soil.

In Chapter 5, the shape of the berm of PJA soil generated at the cleaning front was reported. The petroleum jelly was hydrophobic and cohesive, and so it collected in a berm of dislodged material which moved steadily downstream with the cleaning front (Rodgers *et al.*, 2019). The shape of the berm was characterised by two angles, ϕ_1 and ϕ_2, measured at the cleaning

front (at a, where $l = 0$, see Figure 6.2 (a-i)), and at the level of the initial layer, where $\delta = \delta_o$, Figure 6.2 (a-ii). Figure 6.2 (b) shows the data from Chapter 5 alongside data sets obtained with two other viscoplastic materials investigated further in this chapter. The angles are plotted against the dimensionless film thickness, h/δ_o, at the location where the measurements were made.

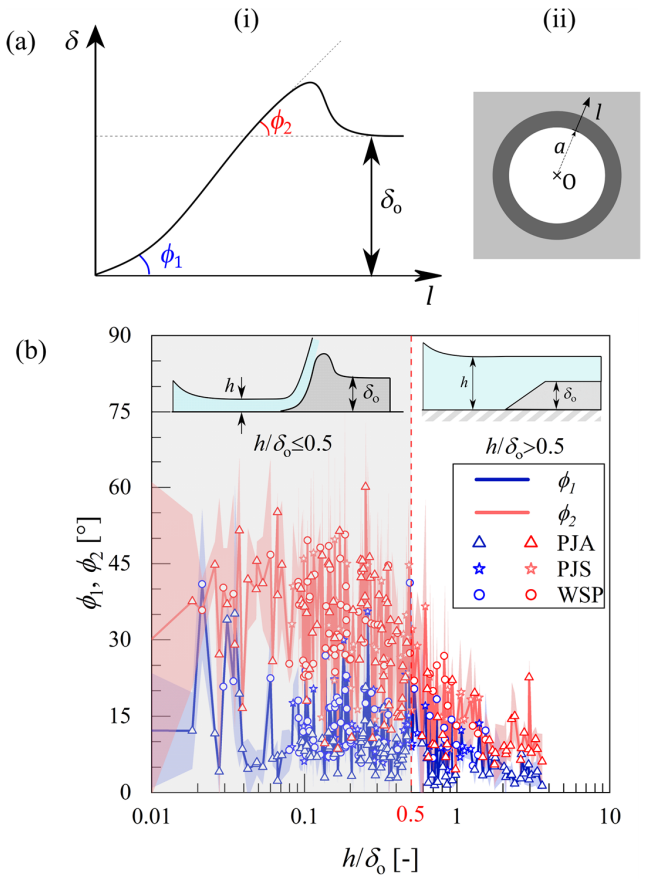

Figure 6.2 – (a-i) Coordinates used to describe the shape of the cleaning front in the soil layer. (a-ii) Schematic representation of the shape of the rim, indicating the locations where angles ϕ_1 and ϕ_2 were measured. (b) Effect of h/δ_o on angles ϕ_1 and ϕ_2 measured for cleaning experiments conducted with different flow rates, nozzle diameters, layer thicknesses and materials. Shaded areas represent the 95% confidence interval of the measurements in the four perpendicular directions. d_N = 2, 3 and 4 mm; 6,300≤ Re ≤42,300; 0.1 ≤ δ_o ≤ 2 mm. Properties of layer materials PJA, PJS and WSP are given in Table 4.1.

Two regimes are evident. When h/δ_o< 0.5, the angle increased with distance from the cleaning front, from ϕ_1 at the leading edge with values similar to the χ values reported by Glover *et al*, to $\phi_2 \sim \pi/4$ at δ_o. The latter is associated with yielding under simple shear caused by the shear stress imposed by the flow of the liquid film. For thicker liquid films,

$h \sim \delta_o$, the angle was almost constant, with $\phi_1 \sim \phi_2$. Similar behaviour is evident for all three materials.

Table 6.1 summarises works that have used the momentum-driven approach, Eq. (2.72), and have combined it with hydraulic models of the flow in the film generated by an impinging jet to predict the cleaning performance. In Chapter 5, a phenomenological approach has been taken to modify Eq. (2.72) to describe the cleaning of viscoplastic soil layers. The cleaning rate constant k' was found by experimental fits to the $\mathrm{d}a/\mathrm{d}t$ vs M data in all works reported in Table 6.1, except for Lu *et al.* (2020) who performed a numerical study for cleaning with submerged jets. In this chapter, a rationalisation of this model will be proposed such that the parameters k' and M_y are related to the soil layer rheology.

Table 6.1 – Studies that have used Eq. (2.72) to describe the removal of soil layers by impinging water jets

Source	Materials removed	Water jet characteristics	Soil layer thicknesses [μm]
Wilson *et al.* (2014)	Polyvinyl acetate (PVA), xanthan gum and petroleum jelly	Coherent perpendicular stationary jet	70 - 300
Wilson *et al.* (2015)	Xanthan gum	Coherent, perpendicular, stationary and moving jet	Not reported
Wang *et al.* (2015)	Paint	Coherent, perpendicular and angled jet	60
Bhagat *et al.* (2017)	Petroleum jelly, PVA, xantham gum	Coherent, stationary and moving, perpendicular and angled jet	322 - 409
Feldung Damkjær *et al.* (2017)	Petroleum jelly	Coherent and non-coherent perpendicular jet	250 - 1,490
Glover *et al.* (2016)	PVA and petroleum jelly.	Coherent, perpendicular, stationary and moving jet	100 - 1,900
Chee *et al.* (2018)	Petroleum jelly and Carbopol®	Coherent and non-coherent, perpendicular stationary jet – flat and curved surfaces.	0.2 and 1,300
Yang *et al.* (2019a)	Toothpaste	Coherent, stationary, perpendicular jet	0.5
Tuck *et al.* (2020)	Thick layers of Carbopol®	Coherent, stationary, perpendicular and angled jet	2,000 – 8,000
Chee and Wilson (2021)	Toothpastes, petroleum jelly, tomato ketchup	Coherent, perpendicular, stationary jet	400 - 600
Lu *et al.* (2020)	Numerical study: removal of a Newtonian fluid layer	Submerged perpendicular laminar jet	100 - 1000

An argument based on viscous dissipation, which has been used to describe flows involving the translation of a contact line, such as the spread of droplets (De Gennes, 1985) and film draining (Peralta *et al.*, 2019), is presented here which yields similar forms to Eq. (2.72) and provides predictive insight into the parameters k' and M_y. Simplifying assumptions are made in order to obtain a tractable result. In particular, the coupling of the liquid flow and soil deformation is not included, such that the shape of the cleaning front is not predicted *a priori*.

6.1.1 Mathematical modelling

The Bhagat and Wilson (2016) hydrodynamic model described in Chapter 2 is used to calculate M. Figure 6.3 presents the geometry of the cleaning model. Modifications of this geometry are explored in Section 6.2. An impinging cylindrical liquid jet generates a liquid film of thickness h and momentum flow rate M at radial distance a from the point of impingement. Point F is the location of the cleaning front, where the thickness of the soil layer is some small value δ_i: for hydrophobic substances such as the PJA discussed in Chapter 5, a thin layer of thickness of order microns remained on the substrate. The physics of a moving contact line are complex (Smith *et al.*, 2018) and the model focuses on the bulk of the layer.

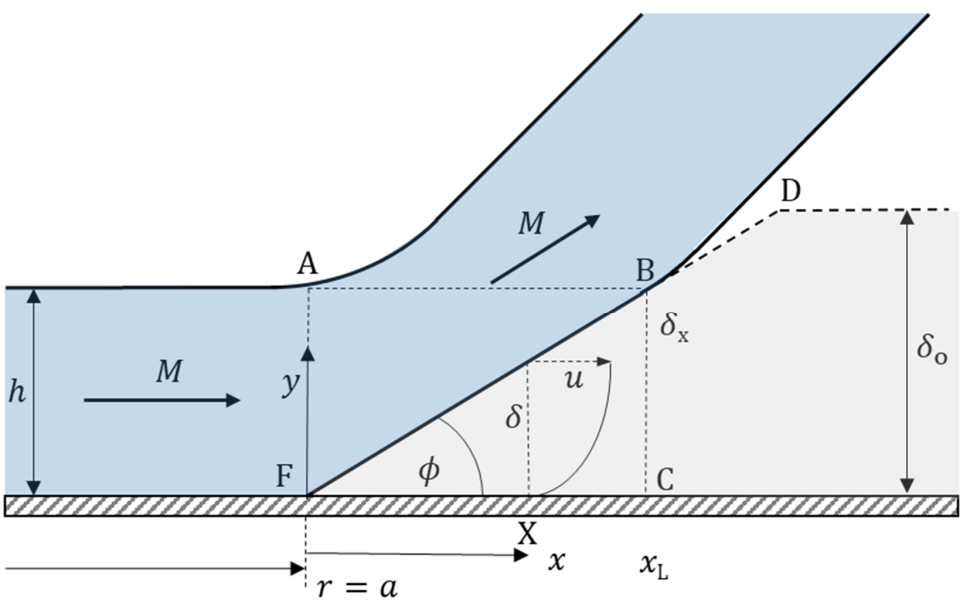

Figure 6.3 – Schematic of the idealised cleaning front

Impingement of the liquid film on the soil layer creates a wedge inclined at angle ϕ to the substrate which extends to point B (with horizontal coordinate x_{L}), corresponding to the height of the liquid film: beyond B, the slope is expected to steepen. A momentum balance in the horizontal direction over FABC gives the net force per unit width F_{w} acting on the soil layer, generated by the pressure acting on FB:

$$F_{\mathrm{w}} = M(1 - \cos\phi). \tag{6.1}$$

This assumes that the magnitude of M does not change significantly between OA and AB, and that ϕ does not change with a. The work done in moving the soil will reduce the kinetic energy of the film and thereby M. This is assumed to be small and is checked in subsequent calculations. We consider thin layers, where δ/a and $|\mathrm{FC}|/a$ are small so contributions from the change in circumferential length are small and the system can be described in Cartesian coordinates x and y.

Let the front FB advance at velocity V with approximately constant shape. The flow path by which material beyond BC is advected upwards and removed or builds up a berm of dislodged material is not modelled. The material in region FBC is moved by force F_{w}, whereas that beyond BC is dragged by the shear stress $\tau_{\mathrm{w,l}}$ acting on the top surface. The rate at which work is done per unit width is equated with Q_{D}, the power consumed by viscous dissipation per unit width within region OBC, viz.

$$F_{\mathrm{w}}V = \int_0^{x_{\mathrm{L}}} \int_0^{\delta(x)} \tau\dot{\gamma}\,\mathrm{d}y\,\mathrm{d}x = Q_{\mathrm{D}}. \tag{6.2}$$

Eq. (6.2) is evaluated for different rheological relationships, *i.e.* $\tau(\dot{\gamma})$. The models for Newtonian and Bingham soil layers are described in Sections 6.1.1.1 and 6.1.1.3, respectively. The results for a power-law fluid and a Herschel-Bulkley material are also reported.

6.1.1.1 Newtonian soil

This is the simplest case, with constant viscosity, μ, and is used to illustrate the concepts. Consider the vertical plane at X, height δ, located at distance x downstream from O illustrated in Figure 6.3. The mean velocity across the plane is V. The local stress distribution is not known and is modelled as a pressure-driven flow with the pressure gradient $\mathrm{d}P/\mathrm{d}x$ being

uniform over the plane, and varying with x. The shear stress profile is assumed to be linear, *viz*

$$\tau = \tau_{\mathrm{w}}\left(1 - \frac{y}{\delta}\right). \tag{6.3}$$

where $\tau_{\mathrm{w}}(x)$ is the shear stress within the soil layer at the soil-substrate interface.

The constitutive relation for Newtonian fluids is:

$$\tau = \mu\frac{du}{dy} \tag{6.4}$$

where u is the local horizontal velocity. With no slip at the substrate (which may not be correct for complex soils and/or surfaces), $u = 0$ when $y = 0$. From Eq. (6.3) and (6.4):

$$u = \frac{\tau_{\mathrm{w}}}{\mu}\left(y - \frac{y^2}{2\delta}\right). \tag{6.5}$$

Continuity requires

$$V\delta = \int_0^{\delta} u\,\mathrm{d}y \tag{6.6}$$

which combined with Eq. (6.5) gives the velocity profile for a viscous flow,

$$u = \frac{3V}{\delta^2}\left(\delta y - \frac{1}{2}y^2\right) \tag{6.7}$$

and the shear rate distribution,

$$\dot{\gamma} = \frac{du}{dy} = \frac{3V}{\delta^2}(\delta - y). \tag{6.8}$$

The rate of viscous dissipation is obtained by substituting Eq. (6.3) and (6.8) into Eq. (6.2),

$$F_{\mathrm{w}}V \approx 9\mu V^2\int_0^{x_{\mathrm{L}}}\left\{\int_0^{\delta(x)}\frac{1}{\delta^4}(\delta - y)^2 dy\right\}dx \tag{6.9}$$

$$F_{\mathrm{w}} \approx 3\mu V\int_0^{x_{\mathrm{L}}}\frac{dx}{\delta}. \tag{6.10}$$

For a simple wedge, $\delta = x\tan\phi$, and thus

$$M(1 - \cos\phi) = 3V\cot\phi\,\ln(h/\delta_{\mathrm{i}}). \tag{6.11}$$

The cleaning velocity is then given by

$$V = \frac{(\tan\phi - \sin\phi)}{3\mu}\frac{1}{\ln(h/\delta_\mathrm{i})}M \qquad h \le \delta_\mathrm{o}. \tag{6.12}$$

This expression is of the form of Eq. (2.70), with a linear dependency on M. The film thickness h varies gradually with r (see Figure 2.11). The rate of cleaning decreases with the viscosity of the soil, which is expected. The dependency of the rate on the soil layer thickness is not straightforward, with two scenarios anticipated:

(i) $h > \delta_\mathrm{o}$, the 'very thin layer': in Eq. (6.12), $\ln(h/\delta_\mathrm{i})$ would be replaced by $\ln(\delta_\mathrm{o}/\delta_\mathrm{i})$ (assuming that little work is done in translating the removed material). M is defined as the total momentum flow rate in the liquid film in this scenario, and a fraction of this quantity will impinge directly on the soil layer (See Figure 6.1 (a)).

(ii) $h \le \delta_\mathrm{o}$, the 'thin layer'. The work done in dislodging the material beyond BC needs to be estimated. In the absence of knowledge of the flow pattern in the soil, this is approximated as either (a) the wedge with angle ϕ extending to D (Figure 6.3), so that $\ln(h/\delta_\mathrm{i})$ is again replaced by $\ln(\delta_\mathrm{o}/\delta_\mathrm{i})$, or including a change in the wedge angle to $\phi_2 \sim \frac{\pi}{4}$ as indicated in Figure 6.2 (b) when $h/\delta_\mathrm{o} > 1/2$, so that $\cot\phi\ln(h/\delta_\mathrm{i})$ in (6.11) is replaced by $\cot\phi\ln(h/\delta_\mathrm{i}) + \ln(\delta_\mathrm{o}/h)$, giving

$$V = \frac{1}{3\mu}\frac{(\tan\phi - \sin\phi)}{\ln(h/\delta_\mathrm{i}) + \tan\phi\ \ln(\delta_\mathrm{o}/h)}\ M\,. \tag{6.13}$$

Since $h/\delta_\mathrm{i} > \delta_\mathrm{o}/h$ and $\tan\phi < 1$, the first term in the denominator is expected to dominate.

6.1.1.2 Power-law soil

This case describes the cleaning of shear thinning and shear thickening soil layers. The stress profile is again assumed to be linear, following Eq. (6.3). The constitutive relation for power-law fluids is

$$\tau = k_\mathrm{PL}\dot{\gamma}^{n_\mathrm{PL}} \tag{6.14}$$

where k_PL is the constitutive index and n_PL is the power-law exponent. From Eq. (6.3) and Eq. (6.14),

$$\dot{\gamma} = \frac{\mathrm{d}u}{\mathrm{d}y} = \left(\frac{\tau_\mathrm{w}}{k_\mathrm{PL}}\right)^{m_\mathrm{PL}}\left(1 - \frac{y}{\delta}\right)^{m_\mathrm{PL}} \tag{6.15}$$

where $m_\mathrm{PL} = n_\mathrm{PL}^{-1}$.

Integration of Eq. (6.15) gives the velocity profile,

$$u = \left(\frac{\tau_{\mathrm{w}}}{k_{\mathrm{PL}}\delta}\right)^{m_{\mathrm{PL}}} \frac{1}{m_{\mathrm{PL}}+1}\left[\delta^{m_{\mathrm{PL}}+1} - (\delta - y)^{m_{\mathrm{PL}}+1}\right] \tag{6.16}$$

which yields the Newtonian velocity profile, Eq. (6.13), when $m_{\mathrm{PL}} = 1$ and $k_{\mathrm{PL}} = \mu$.

The assumption of continuity (see Eq. (6.6)) with the velocity profile given by Eq. (6.15) yields

$$\tau_{\mathrm{w}} = (m_{\mathrm{PL}}+2)^{1/m_{\mathrm{PL}}}\, k_{\mathrm{PL}} \left(\frac{V}{\delta}\right)^{1/m_{\mathrm{PL}}}. \tag{6.17}$$

The rate of viscous dissipation is found by substituting Eqs. (6.15) and (6.17) in Eq. (6.2),

$$F_{\mathrm{w}}V \approx (m_{\mathrm{PL}}+2)^{\frac{1}{m_{\mathrm{PL}}}}\, k_{\mathrm{PL}}\, V^{\frac{m_{\mathrm{PL}}+1}{m_{\mathrm{PL}}}} \int_0^{x_{\mathrm{L}}} \left\{ \int_{x_{\mathrm{i}}}^{\delta(x)} \frac{1}{\delta^{\left(\frac{m_{\mathrm{PL}}^2+2m_{\mathrm{PL}}+1}{m_{\mathrm{PL}}}\right)}} (\delta - y)^{m_{\mathrm{PL}}+1}\, dy \right\} \mathrm{d}x \tag{6.18}$$

$$F_{\mathrm{w}} \approx (m_{\mathrm{PL}}+2)^{\frac{1}{m_{\mathrm{PL}}}}\, k_{\mathrm{PL}}\, V^{\frac{1}{m_{\mathrm{PL}}}} \int_{x_{\mathrm{i}}}^{x_{\mathrm{L}}} \frac{\mathrm{d}x}{\delta^{1/m_{\mathrm{PL}}}}. \tag{6.19}$$

with x_{i} the position where $\delta = \delta_{\mathrm{i}}$.

Substituting $\delta = x\tan\phi$ and $F_{\mathrm{w}} = M(1-\cos\phi)$ yields

$$M(1-\cos\phi) = \left(\frac{m_{\mathrm{PL}}+2}{\tan\phi}\right)^{\frac{1}{m_{\mathrm{PL}}}}\, k_{\mathrm{PL}}\, V^{1/m_{\mathrm{PL}}} \frac{m_{\mathrm{PL}}}{m_{\mathrm{PL}}-1}\left[x_{\mathrm{L}}^{\left(\frac{m_{\mathrm{PL}}-1}{m_{\mathrm{PL}}}\right)} - x_{\mathrm{i}}^{\left(\frac{m_{\mathrm{PL}}-1}{m_{\mathrm{PL}}}\right)}\right]. \tag{6.20}$$

Cases of different thickness are now considered.

(i) If $h > \delta_{\mathrm{o}}$, x_{L} in Eq. (6.28) is replaced by $\delta_{\mathrm{o}}/\tan\phi$ and x_{i} is replaced by $\delta_{\mathrm{i}}/\tan\phi$, yielding the expression for the cleaning rate,

$$V = \left\{ M(\tan\phi - \sin\phi)\frac{m_{\mathrm{PL}}-1}{m_{\mathrm{PL}}} \frac{1}{k_{\mathrm{PL}}(m_{\mathrm{PL}}+2)^{1/m_{\mathrm{PL}}}\left[\delta_{\mathrm{o}}^{\left(\frac{m_{\mathrm{PL}}-1}{m_{\mathrm{PL}}}\right)} - \delta_{\mathrm{i}}^{\left(\frac{m_{\mathrm{PL}}-1}{m_{\mathrm{PL}}}\right)}\right]} \right\}^{m_{\mathrm{PL}}}. \tag{6.21}$$

(ii) If $h \leq \delta_o$, x_L in Eq. (6.20) can be replaced by $x_h = h/\tan\phi$, *i.e.*, the position along the x axis in which $\delta = h$. In this case, the viscous dissipation is limited to $0 \leq y \leq h$, and the solution of Eq. (6.20) yields

$$V = \left\{ M(\tan\phi - \sin\phi)\frac{m_{PL}-1}{m_{PL}} \frac{1}{k_{PL}(m_{PL}+2)^{\frac{1}{m_{PL}}}\left[h^{\left(\frac{m_{PL}-1}{m_{PL}}\right)} - \delta_i^{\left(\frac{m_{PL}-1}{m_{PL}}\right)}\right]} \right\}^{m_{PL}} . \quad (6.22)$$

The viscous dissipation can be extended to include the change in the wedge angle to $\phi_2 \sim \frac{\pi}{4}$ as indicated in Figure 6.2 when $\delta > h$. Eq. (6.19) is then re-written to give

$$M(1-\cos\phi) \approx (m_{PL}+2)^{\frac{1}{m_{PL}}} k_{PL} V^{\frac{1}{m_{PL}}} \left[\int_{x_i}^{x_h} \frac{dx}{\delta^{1/m_{PL}}} + \int_{x_h}^{x_{\delta_o}} \frac{dx}{\delta^{1/m_{PL}}}\right] \quad (6.23)$$

where x_{δ_o} is the position along the x axis in which $\delta = \delta_o$. Solution of Eq. (6.23) yields, after some algebraic manipulation:

$$V = \left\{ M(\tan\phi - \sin\phi)\frac{m_{PL}-1}{m_{PL}} \frac{1}{k_{PL}(m_{PL}+2)^{1/m_{PL}}\left[h^{\left(\frac{m_{PL}-1}{m_{PL}}\right)} - \delta_i^{\left(\frac{m_{PL}-1}{m_{PL}}\right)} + \tan\phi\left(\delta_o^{\left(\frac{m_{PL}-1}{m_{PL}}\right)} - h^{\left(\frac{m_{PL}-1}{m_{PL}}\right)}\right)\right]} \right\}^{m_{PL}} . \quad (6.24)$$

Figure 6.4 shows that Eq. (6.24) approaches the Newtonian case, Eq. (6.13), when $n_{PL} \to 1$ and $k_{PL} = \mu$. This corresponds to a linear relationship between V and M. Additionally, V increases with a decrease in n_{PL}: for lower values of n_{PL}, the soil shows enhanced shear-thinning behaviour, meaning that it is more easily mobilised by the liquid film flow. Describing the soil as a shear-thinning fluid incorporates some non-linearity to the curves, which still cross the *x*-axis at $M = 0$, so an asymptotic maximum cleaned radius is not expected.

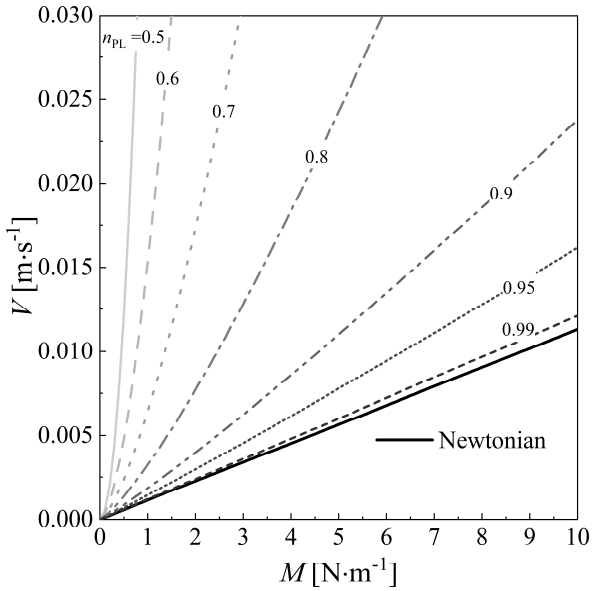

Figure 6.4 - Effect of power-law behaviour on cleaning rate given by Eq. (6.24). Model parameters. ϕ =20°, $k_{\mathrm{PL}} = \mu$ =1 Pa·s, $\delta_{\mathrm{i}} = 10^{-3}$ mm, δ_{o}=1 mm and h=1/2 mm.

6.1.1.3 Bingham soil

The Bingham model, Eq. (6.25), is the simplest description of viscoplastic fluid behaviour. Here, μ_{B} is the Bingham viscosity.

$$\begin{aligned} \tau &= \tau_{\mathrm{c}} + \mu_{\mathrm{B}}\dot{\gamma} \ \text{ if } \ \tau > \tau_{\mathrm{c}} \\ \dot{\gamma} &= 0 \qquad \text{if } \ \tau \le \tau_{\mathrm{c}} \end{aligned} \tag{6.25}$$

The local wall shear stress within the soil layer rim, τ_{w}, is related to the local pressure gradient in the soil by $\tau_{\mathrm{w}} = \delta \, \mathrm{d}P/\mathrm{d}x$ and the shear stress in the layer is again assumed to be given by Eq. (6.3). When $\tau < \tau_{\mathrm{c}}$, corresponding to $y > y_{\mathrm{c}}$ (with $\frac{y_c}{\delta} = 1 - \frac{\tau_{\mathrm{c}}}{\tau_{\mathrm{w}}}$), the fluid moves as a plug: shearing occurs in the lower part of the plane, and the shearing zone reaches the substrate when $\tau_{\mathrm{c}} = \tau_{\mathrm{w}}$. This yields the velocity profile

$$u = \left(\frac{\tau_{\mathrm{w}} - \tau_{\mathrm{c}}}{\mu_{\mathrm{B}}}\right) y - \frac{\tau_{\mathrm{w}}}{2\mu_{\mathrm{B}}} \frac{y^2}{\delta}. \tag{6.26}$$

Conservation of volumetric flow rate requires

$$V\delta = \int_0^{\delta} u \, \mathrm{d}y = \int_0^{y_{\mathrm{c}}} u \, \mathrm{d}y + \int_{y_{\mathrm{c}}}^{\delta} u_{\mathrm{c}} \, \mathrm{d}y \tag{6.27}$$

where

$$u_c = \frac{\tau_w \delta}{2\mu_B}\left(1 - \frac{\tau_c}{\tau_w}\right)^2. \tag{6.28}$$

Writing $\tau_w^* = \tau_w/\tau_c$, integration yields, with some rearrangement,

$$V = \frac{\tau_c \delta}{6\mu_B}\left(1 - \frac{1}{\tau_w^*}\right)^2 (1 + 2\tau_w^*). \tag{6.29}$$

The RHS increases monotonically with τ_w^* . Since V is constant in the front and δ increases with x, this indicates that the local pressure gradient (and hence τ_w^*) decreases with distance from F and at some location flow horizontally will stop.

This result can also be written in the form of a dimensionless characteristic velocity, V^*:

$$V^* = \frac{6\mu_B V}{\tau_c \delta} = \left(1 - \frac{1}{\tau_w^*}\right)^2 (1 + 2\tau_w^*) \tag{6.30}$$

which approaches the linear result $V^* = 2\tau_w^* - 3$ at large τ_w^* (see Figure 6.5).

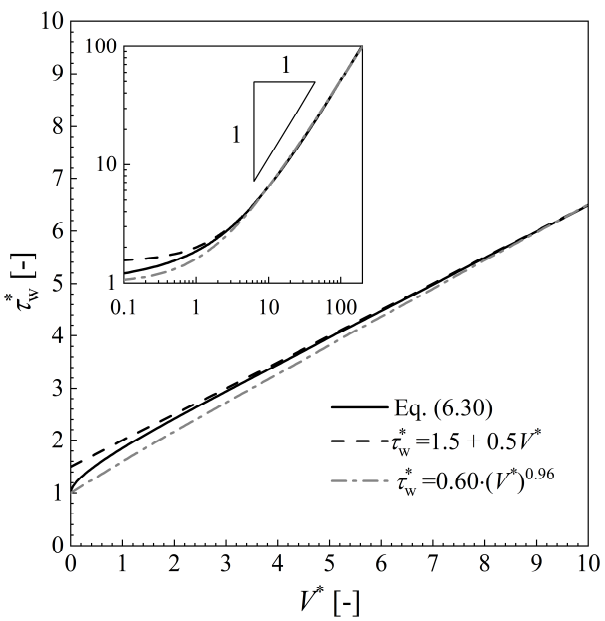

Figure 6.5 – Relationship between τ_w^* and V^* given by Eq. (6.30) alongside two simple fitted expressions.

The rate of viscous dissipation Q_{D} can now be evaluated. For the element between x and x + dx,

$$\frac{\mathrm{d}Q_{\mathrm{D}}}{\mathrm{d}x} = \int_0^{\delta} \tau\dot{\gamma}\,\mathrm{d}y = \int_0^{y_{\mathrm{c}}} \tau\dot{\gamma}\,\mathrm{d}y = \frac{\tau_{\mathrm{w}}^2}{\mu_{\mathrm{B}}} \int_0^{y_{\mathrm{c}}} \left(1 - \frac{y}{\delta}\right)\left(\frac{y_{\mathrm{c}}}{\delta} - \frac{y}{\delta}\right)\mathrm{d}y \tag{6.31}$$

giving

$$\frac{\mathrm{d}Q_{\mathrm{D}}}{\mathrm{d}x} = \frac{\delta\tau_{\mathrm{w}}^2}{6\mu_{\mathrm{B}}} \frac{1}{\tau_{\mathrm{w}}^*} \left(1 - \frac{1}{\tau_{\mathrm{w}}^*}\right)^2 (1 + 2\tau_{\mathrm{w}}^*). \tag{6.32}$$

Substituting the terms in brackets from Eq. (6.30) yields

$$\frac{\mathrm{d}Q_{\mathrm{D}}}{\mathrm{d}x} = \frac{\delta\tau_{\mathrm{w}}^2}{6\mu_{\mathrm{B}}} \frac{1}{\tau_{\mathrm{w}}^*} \frac{6\mu_{\mathrm{B}}V}{\tau_{\mathrm{c}}\delta} = \tau_{\mathrm{w}}V. \tag{6.33}$$

The total rate of viscous dissipation is estimated by integrating Eq. (6.33) over the wedge

$$Q_{\mathrm{D}} = \int_0^{x_{\mathrm{T}}} \tau_{\mathrm{w}}V\,\mathrm{d}x = \tau_{\mathrm{c}}V \int_0^{x_{\mathrm{T}}} \tau_{\mathrm{w}}^*\,\mathrm{d}x \tag{6.34}$$

where x_{T} is set by the location where $\tau_{\mathrm{w}}^* = 1$ and there is no further horizontal motion. The viscous dissipation is thus limited to the region where $\tau_{\mathrm{w}}^* \geq 1$, and the dissipation that occurs beyond BC is not included. Equating this with the rate of work done by the liquid film gives

$$M(1 - \cos\phi)V = \tau_{\mathrm{c}}V \int_0^{x_{\mathrm{T}}} \tau_{\mathrm{w}}^*\,\mathrm{d}x \tag{6.35}$$

or

$$\frac{M(1-\cos\phi)}{\tau_{\mathrm{c}}} = \int_0^{x_{\mathrm{T}}} \tau_{\mathrm{w}}^*\,\mathrm{d}x. \tag{6.36}$$

Eq. (6.30) states that τ_{w}^* is related to a scaled velocity so Eq. (6.36) contains the relationship between the momentum in the film and the cleaning rate. The form of this relationship can be extracted by setting $x_{\mathrm{T}} = x_{\mathrm{L}}$, with x_{L} the position where $\delta = h$, and approximating the locus by the asymptotic form $\tau_{\mathrm{w}}^* = 1.5 + ½V^*$, *viz.*

$$\frac{M(1 - \cos\phi)}{\tau_{\mathrm{c}}} = \int_0^{x_{\mathrm{L}}} \left(\tfrac{3}{2} + ½V^*\right)\mathrm{d}x \tag{6.37}$$

$$\frac{M(1 - \cos\phi)}{\tau_{\mathrm{c}}} = \frac{3}{2}x_{\mathrm{L}} + \frac{3\mu_{\mathrm{B}}V}{\tau_{\mathrm{c}}} \int_0^{x_{\mathrm{L}}} \frac{1}{\delta}\,\mathrm{d}x. \tag{6.38}$$

Setting $\delta = \delta_{\mathrm{i}} + x\tan\phi$ and $x_{\mathrm{L}} = h\cot\phi$, gives

$$\frac{M(1-\cos\phi)}{\tau_c} = \frac{3}{2}h\cot\phi + \frac{3\mu_B V}{\tau_c \tan\phi}\ln\left(1+\frac{h}{\delta_i}\right). \tag{6.39}$$

Rearranging gives an expression similar to Eq.(2.72),

$$V = \frac{(\tan\phi - \sin\phi)}{3\mu_B \ln\left(1+\frac{h}{\delta_i}\right)}\left\{M - \frac{3}{2}\frac{\tau_c h}{(\tan\phi - \sin\phi)}\right\} \tag{6.40}$$

yielding an expression for the cleaning rate constant

$$k'_B = \frac{(\tan\phi - \sin\phi)}{3\mu_B \ln\left(1+\frac{h}{\delta_i}\right)} \tag{6.41}$$

and the limiting momentum flow rate

$$M_{y,B} = \frac{3}{2}\frac{\tau_c h}{(\tan\phi - \sin\phi)}. \tag{6.42}$$

The latter is identical in form to Glover *et al.*'s result, Eq. (2.72), with $3h/2$ replacing δ_o. The values of χ reported by Glover *et al.* correspond to ϕ values in the range 9-30° evaluated using Eq. (6.42). These expressions encapsulate the expected physics, namely M_y increasing with the soil critical stress and k' decreasing with μ_B. The dependency of k'on h is modest as viscous dissipation is concentrated at the front of the ramp: h/δ_i is expected to be $\gg 1$, so $\ln(1 + h/\delta_i) \approx \ln(h/\delta_i)$ and h varies slowly with r (Bhagat & Wilson, 2016). Furthermore, Eq. (6.40) collapses to the result for a Newtonian fluid, Eq. (6.12), when $\tau_c = 0$.

The cleaning rate constant k'_B is not explicitly written as a function of τ_c, since τ_c and ϕ are coupled at the maximum cleaned radius by Eq. (6.42). However, substituting $\tan\phi - \sin\phi$ from Eq. (6.42) into Eq. (6.41) yields:

$$k'_B = \frac{h}{2\mu_B \ln\left(1+\frac{h}{\delta_i}\right)}\frac{\tau_c}{M_y} \tag{6.43}$$

which suggests that k'_B increases with τ_c/M_y.

This is the opposite trend to that shown in Figure 5.15 (a), *i.e.*, k'_B was expected to decrease with the increase of τ_c. The probable reason for this discrepancy is that the wedge angle ϕ is not constant throughout the cleaning process: Figure 5.7 (b) and Figure 5.8 show that the

morphology of the rim evolves during the experiment, particularly over the region where $\delta < h$, in which the wedge angle ϕ is defined. Assuming a constant angle ϕ for all radial positions is required to yield an analytical solution of the model. Although the rim in the current model is assumed to have a constant angle ϕ over the cleaning process, solution of the coupled liquid-soil flow is required to predict any changes in ϕ during an experiment, which is expected to change the relationship suggested by Eq. (6.42).

Figure 6.5 shows that other expressions relating V^* to τ_{w}^* can be identified and capture the behaviour at lower values of V^*. For instance, a simple power-law fitting $\tau_{\mathrm{w}}^* = 1 + a_{\mathrm{BP}} V^{*b_{\mathrm{BP}}}$ gives good agreement (R^2 =0.993) for $V^* < 200$ where $a_{\mathrm{BP}} = 0.60$ and $b_{\mathrm{BP}} = 0.96$. Substituting this expression into Eq. (6.36) gives

$$\frac{M(1-\cos\phi)}{\tau_{\mathrm{c}}} = \int_0^{x_{\mathrm{L}}} \left(a_{\mathrm{BP}} V^{*b_{\mathrm{BP}}} + 1\right) \mathrm{d}x. \tag{6.44}$$

Substituting $\delta = \delta_{\mathrm{i}} + x\tan\phi$ and $x_{\mathrm{L}} = h\cot\phi$, yields after some rearrangement

$$V = \left[\frac{\tau_{\mathrm{c}}^{b_{\mathrm{BP}}-1}(1-b_{\mathrm{BP}})(tan\,\phi - sin\,\phi)}{a_{\mathrm{BP}}(6\mu_{\mathrm{B}})^{b_{\mathrm{BP}}}[(\delta_{\mathrm{i}}+h)^{1-b_{BP}} - (\delta_{\mathrm{i}})^{1-b_{\mathrm{BP}}}]}\right]^{1/b_{\mathrm{BP}}} \left(M - \frac{h\tau_{\mathrm{c}}}{\tan\phi - \sin\phi}\right)^{1/b_{\mathrm{BP}}} \tag{6.45}$$

which follows the form:

$$V = k'_{\mathrm{BP}} \left(M - M_{\mathrm{y,BP}}\right)^{1/b_{\mathrm{BP}}} \tag{6.46}$$

with

$$k'_{\mathrm{BP}} = \left[\frac{\tau_{\mathrm{c}}^{b_{\mathrm{BP}}-1}(1-b_{\mathrm{BP}})(\tan\phi - \sin\phi)}{a_{\mathrm{BP}}\left(6\mu_{\mathrm{B}}\right)^{b_{\mathrm{BP}}}[(\delta_{\mathrm{i}}+h)^{1-b_{\mathrm{BP}}} - (\delta_{\mathrm{i}})^{1-b_{\mathrm{BP}}}]}\right]^{1/b_{\mathrm{BP}}} \tag{6.47}$$

and

$$M_{\mathrm{y,BP}} = \frac{h\tau_{\mathrm{c}}}{\tan\phi - \sin\phi}. \tag{6.48}$$

Both versions of the model, Eq. (6.40) and (6.45), require the Bingham parameters, τ_{c} and μ_{B}, which can be obtained from the flow curve of the material. The performance of the Newtonian and linear Bingham model are compared to the Glover *et al.* (2016) model in Section 6.1.3.2.

6.1.1.4 Herschel-Bulkley soil

For completeness, the model for cleaning of a Herschel-Bulkley soil layer is also derived. As the soil materials studied in the current work are described adequately by the Bingham equation, the Bingham soil formulation was considered for comparison with experimental data. The Herschel-Bulkley model is given by Eq. (2.23), which can be written as

$$\dot{\gamma} = \frac{\mathrm{d}u}{\mathrm{d}t} = \left(\frac{\tau - \tau_\mathrm{c}}{k_\mathrm{HB}}\right)^{m_\mathrm{HB}} \tag{6.49}$$

where similarly to the power-law fluid, $m_\mathrm{HB} = n_\mathrm{HB}^{-1}$.

The shear stress profile within the soil layer rim is similar to the stress profile for the Newtonian, power-law and Bingham fluids, Eq. (6.3). Eq. (6.49) yields the velocity profile within the sheared region,

$$u = \left(\frac{\tau_\mathrm{w}}{k_\mathrm{HB}\delta}\right)^{m_\mathrm{HB}} \frac{1}{m_\mathrm{HB}+1}\left[y_\mathrm{c}^{m_\mathrm{HB}+1} - (y_\mathrm{c}-y)^{m_\mathrm{HB}+1}\right] \tag{6.50}$$

which collapses to the Bingham velocity profile, Eq. (6.18), when $m_\mathrm{HB} = 1$ and $k_\mathrm{HB} = \mu_\mathrm{B}$.

Following the steps discussed for the previous cases yields

$$V = \left(\frac{\tau_\mathrm{c}}{k_\mathrm{HB}}\right)^{m_\mathrm{HB}} \frac{\delta}{(m_\mathrm{HB}+1)(m_\mathrm{HB}+2)} \frac{(\tau_\mathrm{w}^*-1)^{m_\mathrm{HB}+1}}{(\tau_\mathrm{w}^*)^2}[\tau_\mathrm{w}^*(m_\mathrm{HB}+1)+1]. \tag{6.51}$$

As with the Bingham case, the RHS also increases monotonically with τ_w^*. Writing this in terms of a dimensionless characteristic velocity, V^*, gives

$$\begin{aligned} V^* &= \frac{(m_\mathrm{HB}+1)(m_\mathrm{HB}+2)}{\delta}\left(\frac{k_\mathrm{HB}}{\tau_\mathrm{c}}\right)^{m_\mathrm{HB}} V \\ &= \frac{(\tau_\mathrm{w}^*-1)^{m_\mathrm{HB}+1}}{(\tau_\mathrm{w}^*)^2}[\tau_\mathrm{w}^*(m_\mathrm{HB}+1)+1] \end{aligned} \tag{6.52}$$

which is similar to the Bingham characteristic velocity, Eq. (6.30), when $m_\mathrm{HB} = 1$ and $k_\mathrm{HB} = \mu_\mathrm{B}$.

The rate of viscous dissipation Q_D for the element between x and $x + \mathrm{d}x$, is given by

$$\frac{\mathrm{d}Q_\mathrm{D}}{\mathrm{d}x} = \int_0^\delta \tau\dot{\gamma}\,\mathrm{d}y = \int_0^{y_\mathrm{c}} \tau\dot{\gamma}\,\mathrm{d}y. \tag{6.53}$$

Substituting the expressions for τ and $\dot{\gamma}$, Eq. (6.3) and (6.49), into Eq. (6.53), yields

$$\frac{\mathrm{d}Q_\mathrm{D}}{\mathrm{d}x} = \frac{\tau_\mathrm{w}\delta}{(m_\mathrm{HB}+1)(m_\mathrm{HB}+2)}\left(\frac{\tau_\mathrm{c}}{k_\mathrm{HB}}\right)^{m_\mathrm{HB}}\left\{\left[\frac{(\tau_\mathrm{w}^*-1)^{m_\mathrm{HB}+1}}{{\tau_\mathrm{w}^*}^2}\right][\tau_\mathrm{w}^*(m_\mathrm{HB}+1)+1]\right\}. \tag{6.54}$$

Substituting the term between braces in Eq. (6.54) by the left-hand side (LHS) of Eq. (6.52) gives

$$\frac{\mathrm{d}Q_\mathrm{D}}{\mathrm{d}x} = \frac{\tau_\mathrm{w}\delta}{(m_\mathrm{HB}+1)(m_\mathrm{HB}+2)}\left(\frac{\tau_\mathrm{c}}{k_\mathrm{HB}}\right)^{m_\mathrm{HB}}\frac{(m_\mathrm{HB}+1)(m_\mathrm{HB}+2)}{\delta}\left(\frac{k}{\tau_\mathrm{c}}\right)^{m_\mathrm{HB}}V = \tau_\mathrm{w}V\,. \tag{6.55}$$

The total rate of viscous dissipation is found by integration of Eq. (6.55) over the wedge, similarly to the Bingham case, Eq. (6.34).

From an energy balance in the system, the rate of viscous dissipation has to be equal to the rate of work done by the liquid film into the soil layer, giving

$$\frac{M(1-\cos\phi)}{\tau_\mathrm{c}} = \int_0^{x_\mathrm{L}} \tau_\mathrm{w}^*\,\mathrm{d}x. \tag{6.56}$$

Similarly to the Bingham case, Eq. (6.56) contains the relationship between the momentum of the liquid film and the cleaning rate, as τ_w^* is related to the scaled velocity, Eq. (6.52). However, Eq. (6.52) also indicates that the exponent index $n_\mathrm{HB} = m_\mathrm{HB}^{-1}$ from the Herschel-Bulkley model will affect the relationship between V^* and τ_w^*, as shown in Figure 6.6 (a). It is possible to fit power functions of the form $\tau_\mathrm{w}^* = a_\mathrm{HB}{V^*}^{b_\mathrm{HB}} + 1$ to the V^* and τ_w^* curves obtained with each value of n_HB using the least square method, as shown by the red lines in Figure 6.6 (a). These fits give a good description of the curves, apart from the region where $\tau_\mathrm{w}^* < 5$ and $V^* < 5$, as shown in the inset of Figure 6.6 (a). The values of the parameters a_HB and b_HB found by different fittings as a function of n_HB are shown in Figure 6.6 (b).

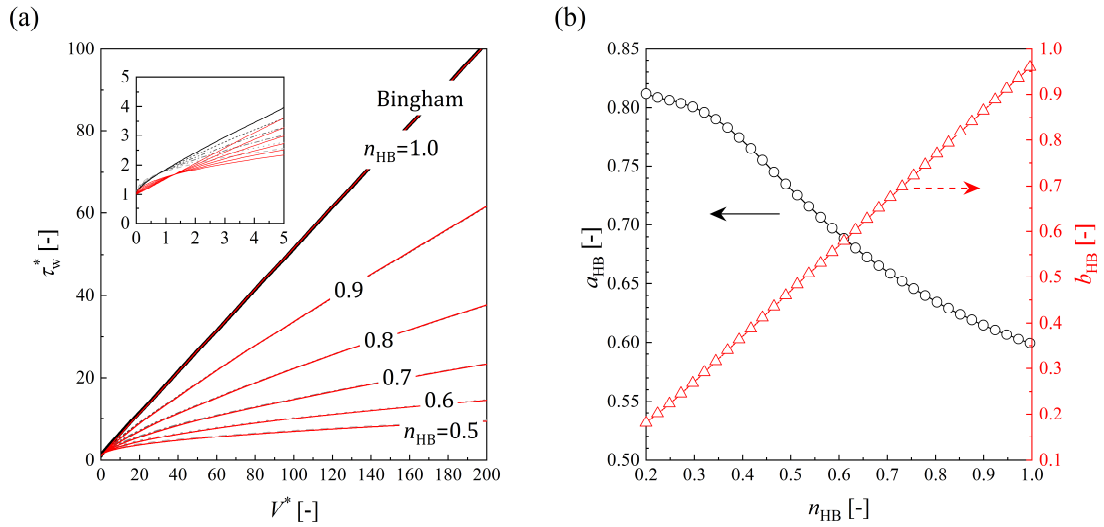

Figure 6.6 – (a) Plots of τ_w^* as a function of V^* for the Herschel-Bulkley soil, given by Eq. (6.52), for given values of n_{HB}. When $n_{HB} = 1$, the solution is the same as for the Bingham soil, Eq. (6.45). Red lines show best fits of $\tau_w^* = a_{HB} V^{*b_{HB}} + 1$. (b) Values for the parameters a_{HB} and b_{HB} of the power-law fits shown in (a) for different values of n_{HB}.

Substituting $\tau_w^* = a_{HB} V^{*b_{HB}} + 1$ in Eq. (6.56) yields

$$\frac{M(1-\cos\phi)}{\tau_c} = \int_0^{x_L} \left\{ a_{HB} \left[\frac{(m_{HB}+1)(m_{HB}+2)}{\delta} \left(\frac{k_{HB}}{\tau_c} \right)^{m_{HB}} V \right]^{b_{HB}} + 1 \right\} dx. \tag{6.57}$$

Again, setting $\delta = \delta_i + x\tan\phi$ and $x_L = h\cot\phi$ gives

$$\frac{M(1-\cos\phi)}{\tau_c} = \int_0^{x_L} \left\{ a_{HB} \left[\frac{(m_{HB}+1)(m_{HB}+2)}{\delta} \left(\frac{k_{HB}}{\tau_c} \right)^{m_{HB}} V \right]^{b_{HB}} + 1 \right\} dx \tag{6.58}$$

$$\frac{M(1-\cos\phi)}{\tau_c} = a_{HB} \left[\left(\frac{k_{HB}}{\tau_c} \right)^{m_{HB}} (m_{HB}+1)(m_{HB}+2) \right]^{b_{HB}} V^{b_{HB}} \frac{cot\,\phi}{1-b_{HB}} \left[\left(\frac{1}{\delta_i - h} \right)^{b_{HB}-1} - \left(\frac{1}{\delta_i} \right)^{b_{HB}-1} \right] + h\cot\phi\,. \tag{6.59}$$

Rearranging Eq. (6.59) yields the cleaning evolution function for a Herschel-Bulkley soil,

$$V = \left\{ \frac{\tau_c^{m_{HB} b_{HB} - 1} (1 - b_{HB})(\tan\phi - \sin\phi)}{a_{HB}[(m_{HB} + 1)(m + 2) k_{HB}^{m}]^{b_{HB}} \left[((\delta_i + h)^{1 - b_{HB}} - \delta_i^{1 - b_{HB}} \right]} \left[M - \frac{h\tau_y}{\tan\phi - \sin\phi} \right] \right\}^{1/b_{HB}} \tag{6.60}$$

which reduces to the Bingham estimate for V using the power-law relationship between τ_w^* and V^*, Eq. (6.45), when $m_{HB} = 1$ and $k_{HB} = \mu_B$. Figure 6.7 presents plots of V vs M found using Eq. (6.59) with different values of n and with k_{HB} = 1 Pa·s^{n}, along with the expression for the Bingham soil, Eq. (6.45). Again, the Herschel-Bulkley cleaning model approaches the Bingham cleaning model when $n_{HB} \to 1$.

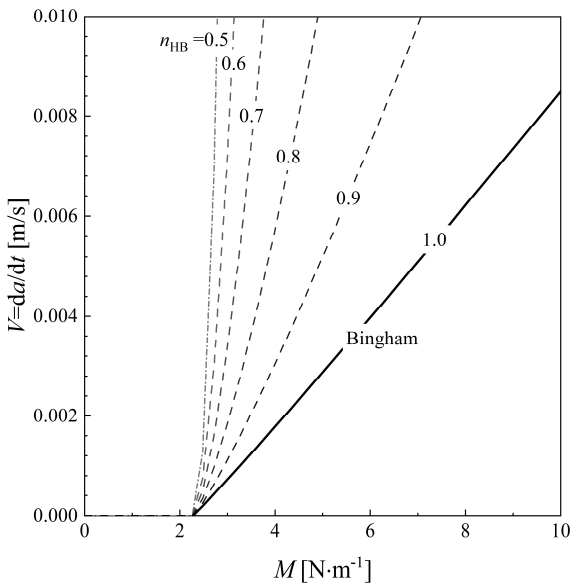

Figure 6.7 - V as a function of M for the Herschel-Bulkley soil, given by Eq. (6.60), with different values of consistency index n_{HB}. $\phi = 20°$, $k = \mu_B$ =1 Pa·s^{m}, $\delta_i = 10^{-3}$ mm, δ_o=1 mm, h=0.5 mm.

The equations for cleaning of a Herschel-Bulkley soil are complex, and significantly depend on the values of the parameters a_{HB} and b_{HB} reported in Figure 6.6. Since the soil layers studied here are sufficiently well described by the Bingham equation (see Chapter 4), the Bingham cleaning model is considered in this Section.

6.1.1.5 Energetic considerations

The energetic efficiency of the cleaning process can be calculated. The rate of viscous dissipation per unit width is given by

$$Q_{\mathrm{D}} = F_{\mathrm{w}} V = M(1 - \cos\phi)V. \tag{6.61}$$

The change in the flow of kinetic energy in the film as a result of moving the cleaning front can be estimated. The rate of flow of kinetic energy in the liquid film per unit width, $\dot{E}_{\mathrm{k}}$, is given by

$$\dot{E}_{\mathrm{k}} = \frac{\dot{m}}{2\pi a}\frac{U^2}{2}. \tag{6.62}$$

The ratio of these two quantities yields the energetic efficiency of the cleaning process, η_{e}, *viz.*

$$\eta_{\mathrm{e}} = \frac{4\pi a M(1 - \cos\phi)V}{\dot{m}U^2}. \tag{6.63}$$

The energetic efficiency observed in the experiments is found by calculating M for a given value of a using the film flow model, and setting V equal to the observed value of $\left.\frac{\mathrm{d}a}{\mathrm{d}t}\right|_{r=a}$ or estimating V using Eq. (6.40). Eq. (6.63) is compared to data from cleaning experiments in Section 6.1.3.4.

The models presented in this section do not include slip or deformation beyond $\overline{\mathrm{BC}}$, so some differences from the experimental data are expected. Additionally, all the models discussed here assume generalised Newtonian fluid formulations for the soils. Both the Newtonian and Bingham models yield linear relationships between $V = \mathrm{d}a/\mathrm{d}t$ and M, Eq. (6.13) which match experimental observations for a Newtonian soil layer. The assumption of a power-law relationship between τ_{w}^* and V^* for a Bingham soil generates slightly non-linear V vs M curves, Eq. (6.45).

Neither of these models capture creep effects that occur at shear stresses below the critical stress (Lidon *et al.*, 2017), which was cited for the strong curvature at lower M observed in Chapter 5. Creep is expected to occur in cleaning experiments when the soil layer is exposed

to the shear stresses and forces imposed by the liquid film for long periods. The models are therefore expected to deviate from experimental data at longer observation times.

6.1.2 Materials and methods

6.1.2.1 Materials, image analysis and crater profilometry

Layers of PJA, PJS and WSP, all insoluble in water, were studied. All have been discussed in previous chapters. Layers of uniform thickness δ_o were coated on Perspex® target plates using the spreader device described in Chapter 4. The rheological behaviour of the materials was investigated using the Kinexus stress-controlled rheometer, presented in Chapter 4, using rough 40 mm diameter parallel plates at 20 °C. An ageing time of at least 30 min was employed after coating the layers in all materials based on the oscillatory time sweeps reported in Figure 4.1. The values of μ_b and τ_c obtained with the fits of the Bingham equation are shown in Table 4.1.

6.1.3 Results and discussion

6.1.3.1 Cleaning experiments – performance of the models

In this section, the performance of the models is discussed in detail for a selection of experimental conditions. The Bingham linear model, Eq. (6.40), was also fitted to a larger number of experiments, and these are discussed in Section 6.1.3.3. Figure 6.8, Figure 6.9 and Figure 6.10 present the results for some of the cleaning experiments, and the values of ϕ and δ_i used in each fitting are shown on the plot labels. Figure 6.8 (a) and Figure 6.9 (a) show the evolution of the non-dimensional cleaned radius, a/δ_o, over time for experiments conducted with the PJA, along with the fit for the Bingham fluid model using the linear (Eq. (6.40)) and power-law (Eq. (6.45)) approximations. The right-hand axis shows the values of h/δ_o. The calculations employed the hydrodynamic model of Bhagat and Wilson (2016) to calculate h and M.

The early stages of the cleaning process are described well by both models, which is also reflected in the good gradient estimations in the $\mathrm{d}a/\mathrm{d}t$ vs M plots (Figure 6.8 (b) and Figure 6.9 (b)). Since h changes with a (see Figure 2.11), the gradient of the $\mathrm{d}a/\mathrm{d}t$ vs M curves changes gradually with a. The asymptotic behaviour, where the cleaned radius approaches a maximum value, a_{max}, is also captured by the models.

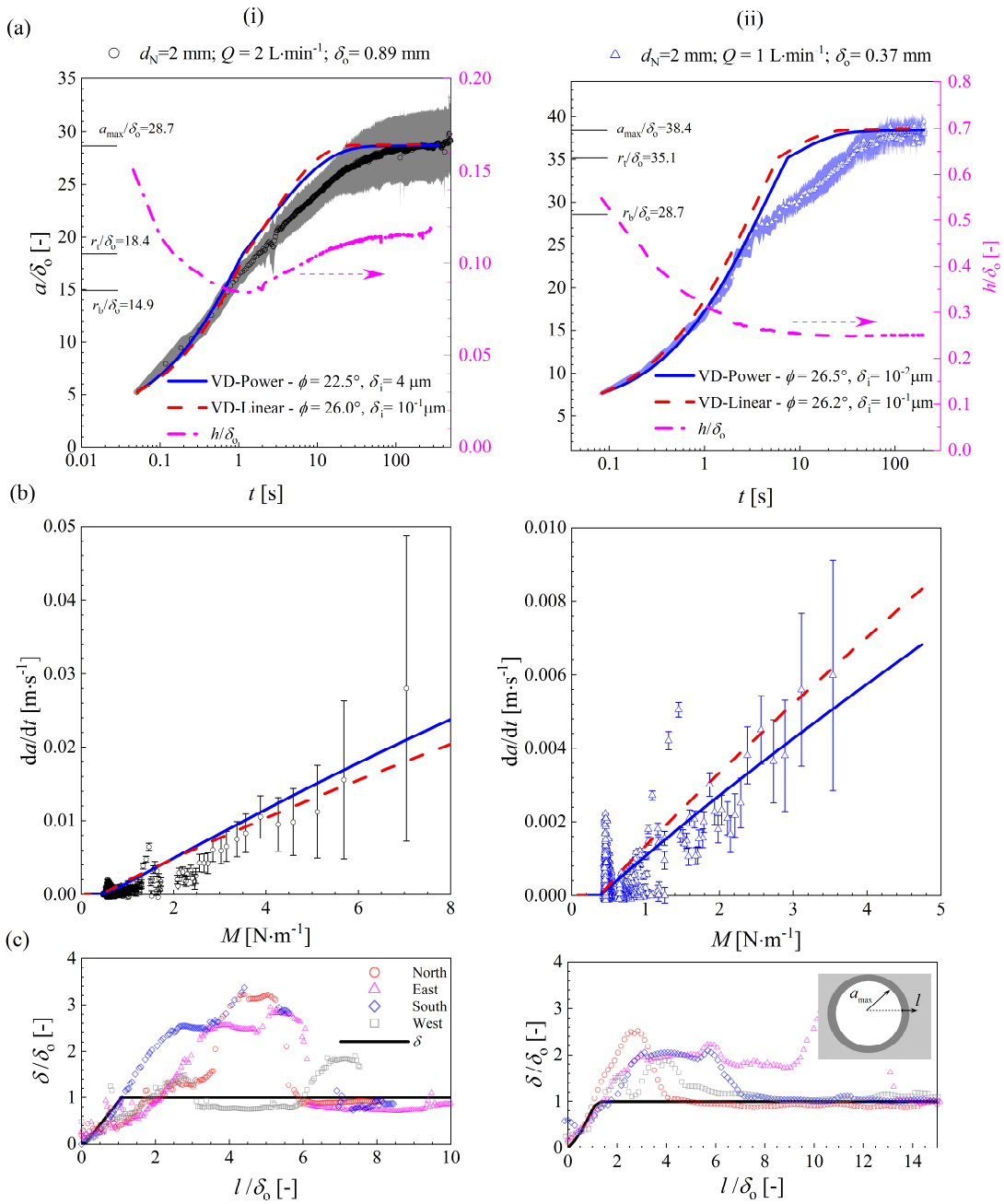

Figure 6.8 – Results for cleaning experiments obtained with PJA, d_N=2 mm. (a) a/δ_o (left y-axis) and h/δ_o (right y-axis) as a function of time. (b) da/dt as a function of M and (c) profilometry of the crater, along with the shape of the rim given by the Bingham linear model. Column (i) Q=2 l·min^{-1}, δ_o=0.89 mm. Column (ii) Q=1 l·min^{-1}, δ_o=0.37 mm. Shaded regions in (a) represent the standard deviation of the radii, error bars in (b) represent the propagated uncertainty in da/dt and are used in remaining plots in this chapter.

At intermediate times, from approximately 1 to 30 s, the models overestimate the cleaned radius. Similar behaviour was reported by Glover *et al.* (2016), and this is attributed to creep

effects that are not captured by the generalised Newtonian fluid formulation adopted to describe the soil materials.

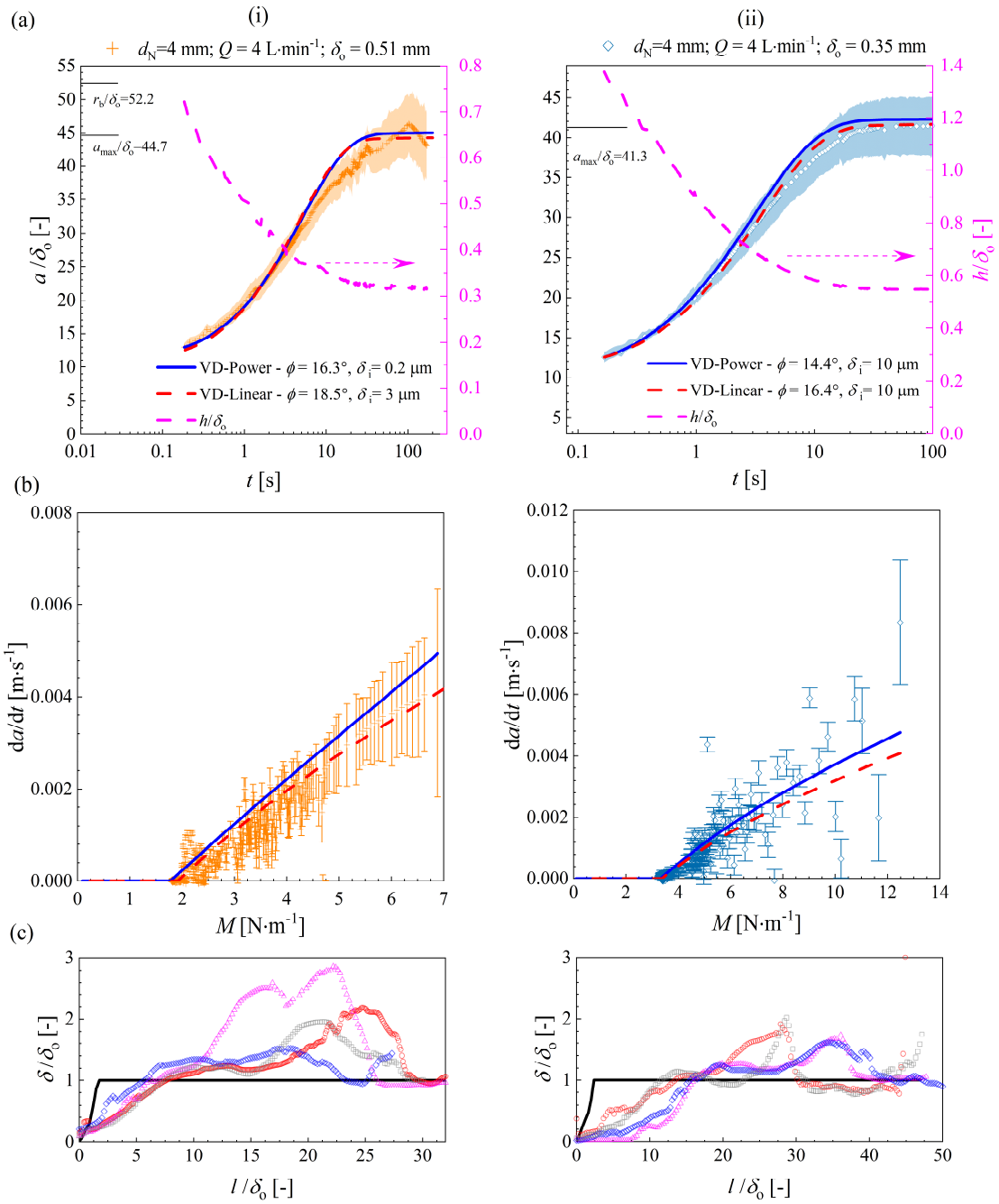

Figure 6.9 – Results for cleaning experiments obtained with PJA, d_N=4 mm, Q=4 l·min^{-1}. (a) a/δ_o (left y-axis) and h/δ_o (right y-axis) as a function of time; (b) da/dt as a function of M and (c) profilometry of the crater, along with the shape of the rim given by the Bingham linear model. (i) δ_o=0.51 mm, (ii) δ_o=0.35 mm.

The measured shape of the berm can be compared with the values of ϕ obtained with the Bingham linear model. Figures 6.8 (c) and 6.9 (c) present the shapes of the rim for the cleaning experiments: the horizontal axis shows the non-dimensional distance from the cleaning front at $a_{\max}$, l/δ_{o} as indicated in Figure 6.8 (c-ii). The measurements were taken along four lines equally spaced at 90° from each other. The cardinal notation indicates the direction of measurement, where South points downwards and North upwards. The lines shown in the plots were constructed using Eq. (6.64), where ϕ is the angle obtained with the Bingham viscous dissipation model, Eq (6.64).

$$\begin{aligned} &\delta = l\tan\phi && \text{if} \quad 0 < l \le h\cot\phi \\ &\delta = l + h(1-\cot\phi) && \text{if} \quad h\cot\phi < l \le \delta_o + h(\cot\phi - 1) \\ &\delta = \delta_{\mathrm{o}} && \text{if} \quad l > \delta_{\mathrm{o}} + h(\cot\phi - 1)\,. \end{aligned} \tag{6.64}$$

The Bingham linear model gives a good description of the initial berm shape for the experiments performed with the 2 mm nozzle in Figure 6.8. The 45° angle for $h < \delta < \delta_{\mathrm{o}}$ arises from the assumption of simple shear in the region where the liquid film is not causing any compression in the rim. A theory to explain the angle of the rim for $\delta \le h$ is not yet available.

For the experiments performed with PJA and a 4 mm nozzle in Figure 6.9, the description of the rim shape is not accurate. In these cases, $h/\delta_{\mathrm{o}} > 1/2$ and so they belong to the very thin soil layer case. As a result, the model is not expected to give a reliable description of the shape of the cleaning front.

Figure 6.10 presents results for the evolution of the cleaned radius and berm shape for experiments performed with WSP and PJS. As with the PJA, the main features of the cleaning process are adequately described by the models. The Bingham model with the linear approximation for τ_{w}^{*}, Eq. (6.40), provides a good description of the experimental data.

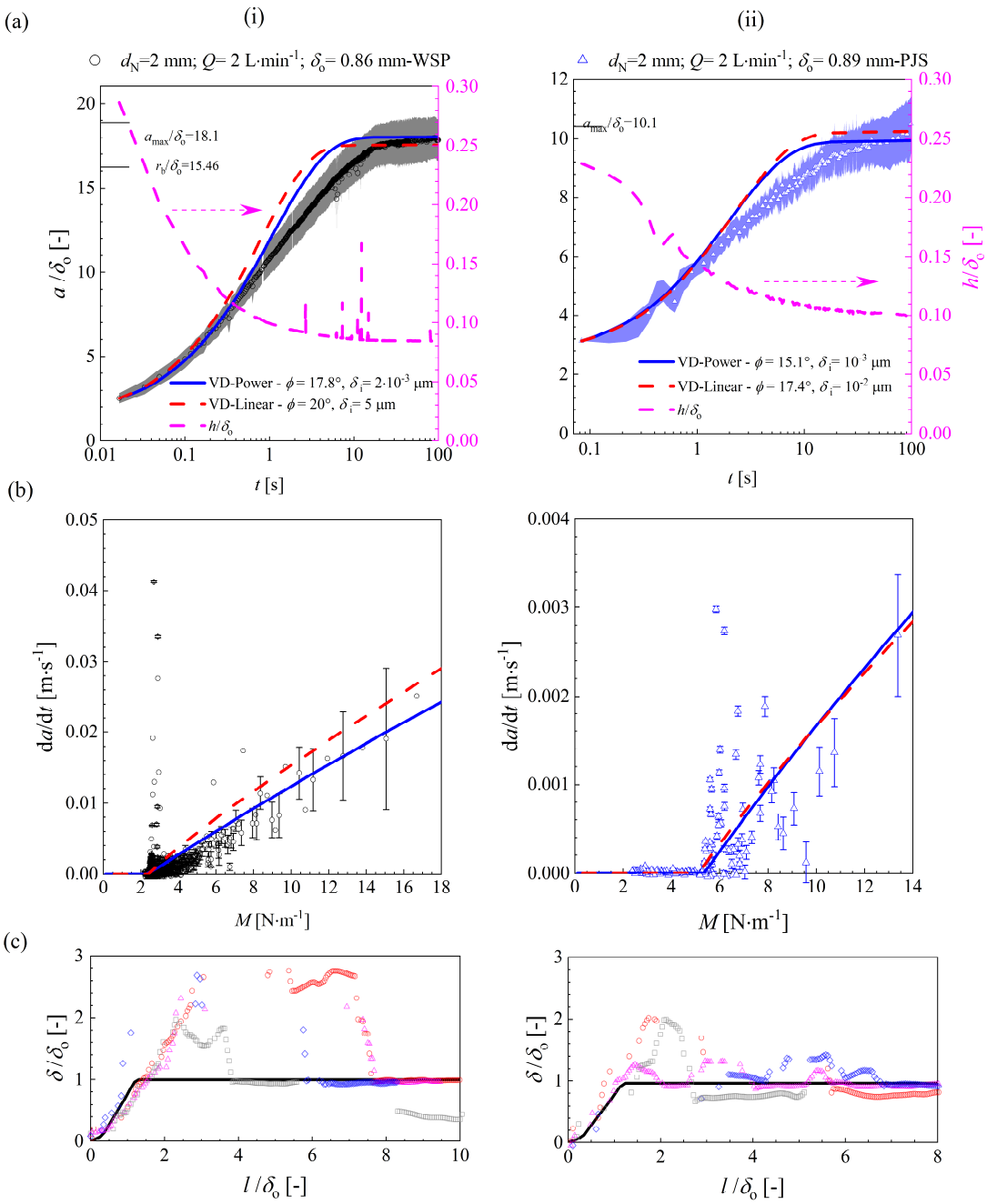

Figure 6.10 – Cleaning of WSP and PJS layers. (a) a/δ_o (left y-axis) and h/δ_o (right y-axis) as a function of time; (b) d$a/$dt as a function of M and (c) measured shape of the berm, along with the profile given by the Bingham linear model. Conditions: d_N=2 mm, Q=2 l·min-1 and (i): δ_o=0.86 mm; (ii): δ_o=0.89 mm.

Since the model was fitted to the experimental data by tuning ϕ and $\ln(\delta_i)$, it is important to establish the sensitivity of the model to these two parameters. Figure 6.11 presents results

for a sensitivity analysis performed with the Bingham linear model for another experiment performed with the PJA. The best fit was found with $\phi = 20°$ and $\delta_i = 0.5$ µm.

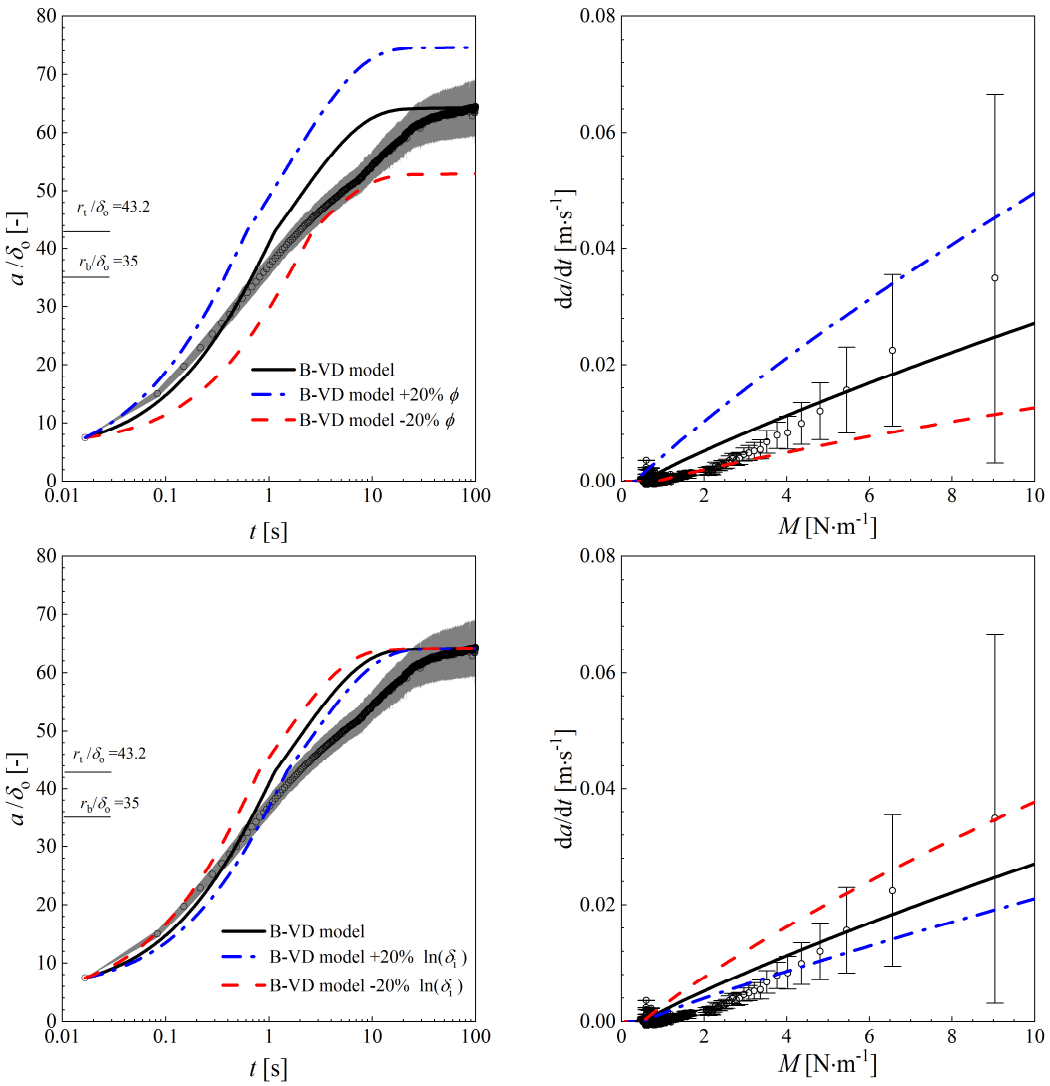

Figure 6.11 – Sensitivity of the linear Bingham model, Eq. (6.40) to ±20% variation in (a) ϕ and (b) $\ln(\delta_i)$. (i) a/δ_o vs t plots and (ii) da/dt vs M plots. Experimental conditions: d_N=2 mm, Q=2 l·min^{-1} and δ_o=0.38 mm.

Figure 6.11 (a) shows the effect of changing ϕ by ±20%, and Figure 6.11 (b) of changing $\ln(\delta_i)$ by ±20%. The model is more sensitive to ϕ than to δ_i, as expected from the form of Eq. (6.40).

6.1.3.2 Performance of different models

The Newtonian and Bingham linear models are compared to the Glover *et al.* (2016) model in Figure 6.12 for the case presented in Figure 6.8 (i). Whereas the former models employed the Bhagat and Wilson (2016) hydrodynamic description, the latter used the weak soil (Wilson *et al.*, 2012) model to calculate M, Eq. (2.38), which is accurate for $r_\mathrm{b} < a < r_\mathrm{t}$, when the film is in laminar flow. The Glover *et al.* (2016) model was therefore fitted to data where $a > r_\mathrm{b}$. The dashed orange locus in Figure 6.12 shows the extrapolation to earlier times.

The Newtonian model does not give a good description as it does not predict the observed approach to an asymptotic value of a. The Glover *et al.* (2016) model provides a good description of the cleaning behaviour at longer times (even though the result for M, Eq. (2.38), is being extrapolated into the region where the film is turbulent). However, it does not describe the early stages well. It assumes constant parameters and requires direct fitting of the parameters k' and M_y to the data. It should be noted that the Bhagat and Wilson (2016) hydrodynamic description does not describe the transition between the laminar and turbulent regions well and this needs to be considered in future work.

The results presented in this section demonstrate that the momentum-driven viscous dissipation model using the Bingham formulation can describe the cleaning of thin viscoplastic soil layers by these impinging water jets. The next section explores the main features of this model when fitted to other experimental conditions.

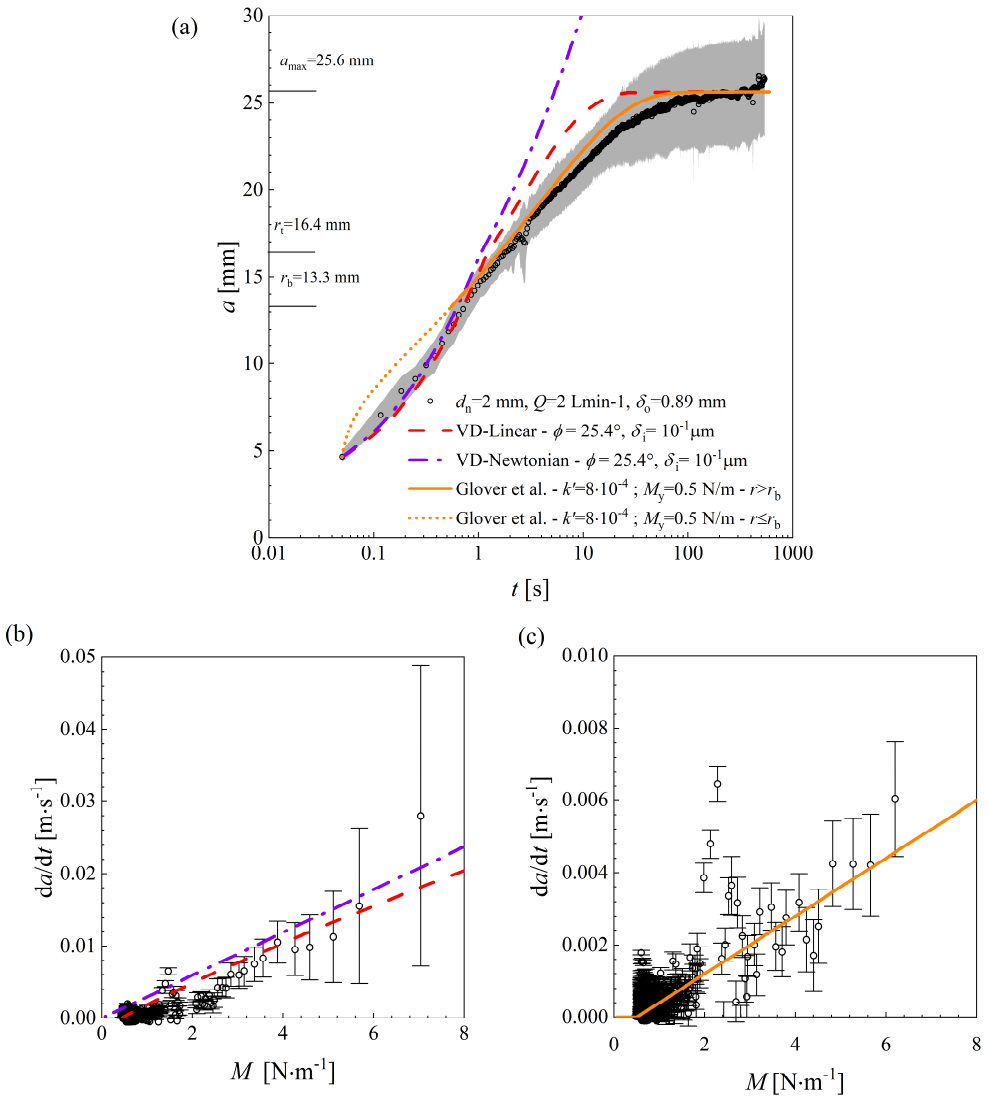

Figure 6.12 - Fit of cleaning models to the experimental data reported in Figure 6.8 (i). (a) Cleaned radius as a function of time, (b) $\mathrm{d}a/\mathrm{d}t$ as a function of M for the Bingham linear and Newtonian models, (c) $\mathrm{d}a/\mathrm{d}t$ as a function of M for the Glover *et al.* (2016) model (note different scale on the ordinate axis).

6.1.3.3 Parametric analysis

Since h changes throughout a cleaning test, Eq. (6.41) and Eq. (6.42) indicate that both k'_{B} and $M_{\mathrm{y,B}}$ also change. We introduce the space averaged values of h, k'_{B} and $M_{\mathrm{y,B}}$, defined:

$$\bar{h} = \frac{1}{a_{\max} - a_{\mathrm{o}}} \int_{a_{\mathrm{o}}}^{a_{\max}} h(r)\, \mathrm{d}r \tag{6.65}$$

$$\bar{k}'_{\mathrm{B}} = \frac{1}{a_{\max} - a_{\mathrm{o}}} \int_{a_{\mathrm{o}}}^{a_{\max}} k'_{\mathrm{B}}(r)\ \mathrm{d}r \tag{6.66}$$

$$\bar{M}_{\mathrm{y,B}} = \frac{1}{a_{\max} - a_{\mathrm{o}}} \int_{a_{\mathrm{o}}}^{a_{\max}} M_{\mathrm{y,B}}(r)\ \mathrm{d}r \tag{6.67}$$

where a_{o} is the first cleaned radius detected. Results are grouped relative to the experimental conditions employed: (i) d_{N}=2 mm and Q=1 l·min^{-1}; (ii) d_{N}=2 mm and Q=2 l·min^{-1} and (iii) d_{N}=4 mm and Q=4 l·min^{-1}. The remaining results refer to a selection of experimental conditions, with ranges 15,000 ≤ *Re* ≤ 37,000, 2 ≤ d_{N} ≤ 4 mm, and 0.4 mm ≤ δ_{o} ≤ 1.1 mm. A summary of the experimental conditions investigated with PJA is presented in Table 6.2, which also reports the values of ϕ and δ_{i} obtained when fitting Eq. (6.40) to the data sets.

Figure 6.13 shows the values of ϕ as a function of $\bar{h}/\delta_{\mathrm{o}}$ for the PJA experiments. The former lie between 15° and 32°, which is consistent with the χ values reported by Glover *et al*. ϕ tends to decrease with increasing $\bar{h}/\delta_{\mathrm{o}}$, approaching 15-20° as $\bar{h}/\delta_{\mathrm{o}}$ increases. The experimental data in Figure 6.2 (b) indicate that a single value of ϕ in the range 5-15° described the berm shape at higher $\bar{h}/\delta_{\mathrm{o}}$.

Table 6.2 – Experimental conditions of the cleaning experiments conducted with PJA to which Eq. (6.40) was fitted

Q [l·min^{-1}]	d_N [mm]	δ_o [mm]	Re	ϕ [°]	δ_i [µm]
		0.10		19.5	1
		0.14		18.3	0.5
		0.34		18.4	1
		0.37		25.6	0.5
1.0	2	0.37	10,600	26.2	0.1
		0.45		23.0	0.5
		0.90		20.8	0.01
		1.45		21.5	0.001
		2.02		25.0	0.005
		0.11		21.5	5
		0.30		20.9	5
2.0	2	0.39	21,200	24.0	5
		0.62		23.5	1
		0.86		25.7	0.3
		1.85		21.0	1
		0.35		16.4	10
		0.36		19.6	1
4.0	4	1.05	21,200	20.5	10
		1.49		20.5	8
		1.97		19.0	1
1.40	2	0.38	14,800	26.0	1
1.40	2	0.91	14,800	26.2	0.1
3.00	4	0.50	16,000	24.5	2
1.80	2	0.90	19,000	18.5	5
3.00	3	1.05	21,200	18.5	5
5.00	4	1.05	26,500	19.0	5
4.00	3	1.05	28,200	20.3	5
5.00	3	1.05	35,300	18.0	10
7.00	4	0.50	37,000	15.0	12

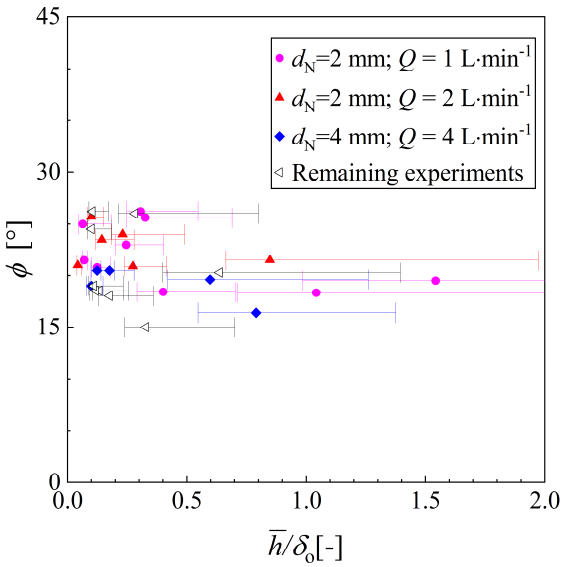

Figure 6.13 – Effect of $\bar{h}/\delta_o$ on fitted wedge angle ϕ. Range bars indicate the minimum and maximum values of h/δ_o.

Figure 6.14 compares the parameters obtained by fitting Eq. (6.40) to the data obtained with PJA for the dependencies given by the model. Wilson *et al.* (2014) hypothesised that the cleaning rate constant k' was a function of the soil layer thickness, while Glover *et al.* (2016) reported a decrease of k' with increasing δ_o. Figure 6.14 (a) presents the values of $\bar{k}'_B$, given by Eq. (6.66), as a function of $\bar{h}/\delta_o$, showing a decreasing trend, somewhat mirroring the predicted dependency on $\ln(1 + h/\delta_i)$. The $\bar{M}_{y,B}$ values increase with $\tau_c\bar{h}$, as suggested by Eq. (6.41), Figure 6.14 (b). Eq. (6.41) and Eq. (6.42) state that k'_B and $M_{y,B}^{-1}$ are both related to $(\tan\phi - \sin\phi)$, but show different dependencies on h and δ_i. If follows from Eq. (6.41) and Eq. (6.42) that $\bar{k}'_B \propto \bar{h}/\ln(1 + \bar{h}/\delta_i)$, as demonstrated in Figure 6.14 (c). The trends therefore show reasonable agreement with the model.

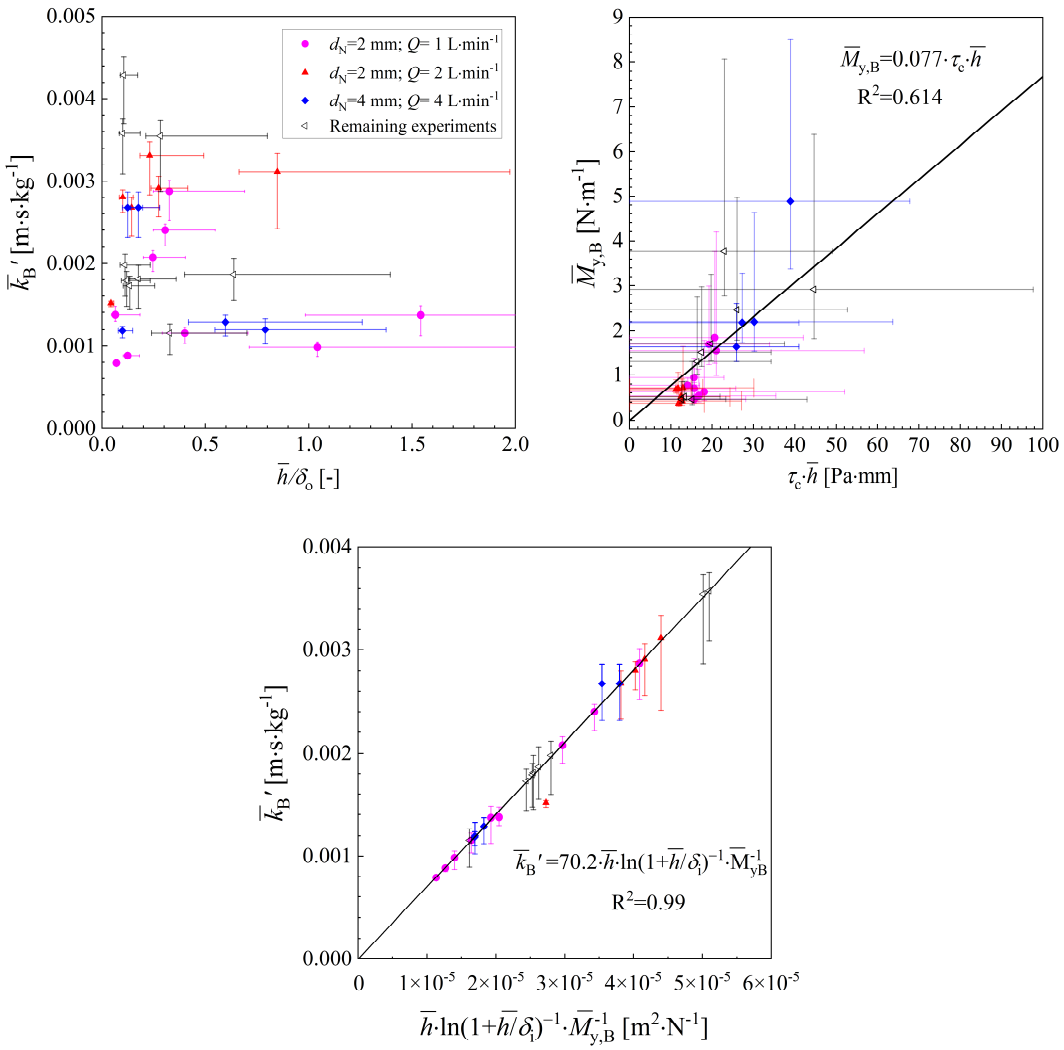

Figure 6.14 –Summary of the parameters obtained for PJA cleaning experiments. (a) Effect of $\overline{h}/\delta_o$ on $\overline{k}_B'$ (b) $\overline{M}_{y,B}$ as a function of $\tau_c \cdot \overline{h}$ and (c) $\overline{k}_B'$ as a function of $\overline{M}_{y,B}$. Range bars indicate the maximum and minimum values for each quantity along the test, whereas symbols indicate the average values given by Eq. (6.65), (6.66) and (6.67).

Figure 6.15 compares the values of (a) $\overline{k}_B'$, (b) $\overline{M}_{y,B}$ and (c) ϕ obtained with the Bingham linear model with the values of k', M_y and χ obtained by fitting the semi-empirical Glover *et al.* (2016) model to the same data sets. The latter assumed a simple laminar velocity profile for the liquid film.

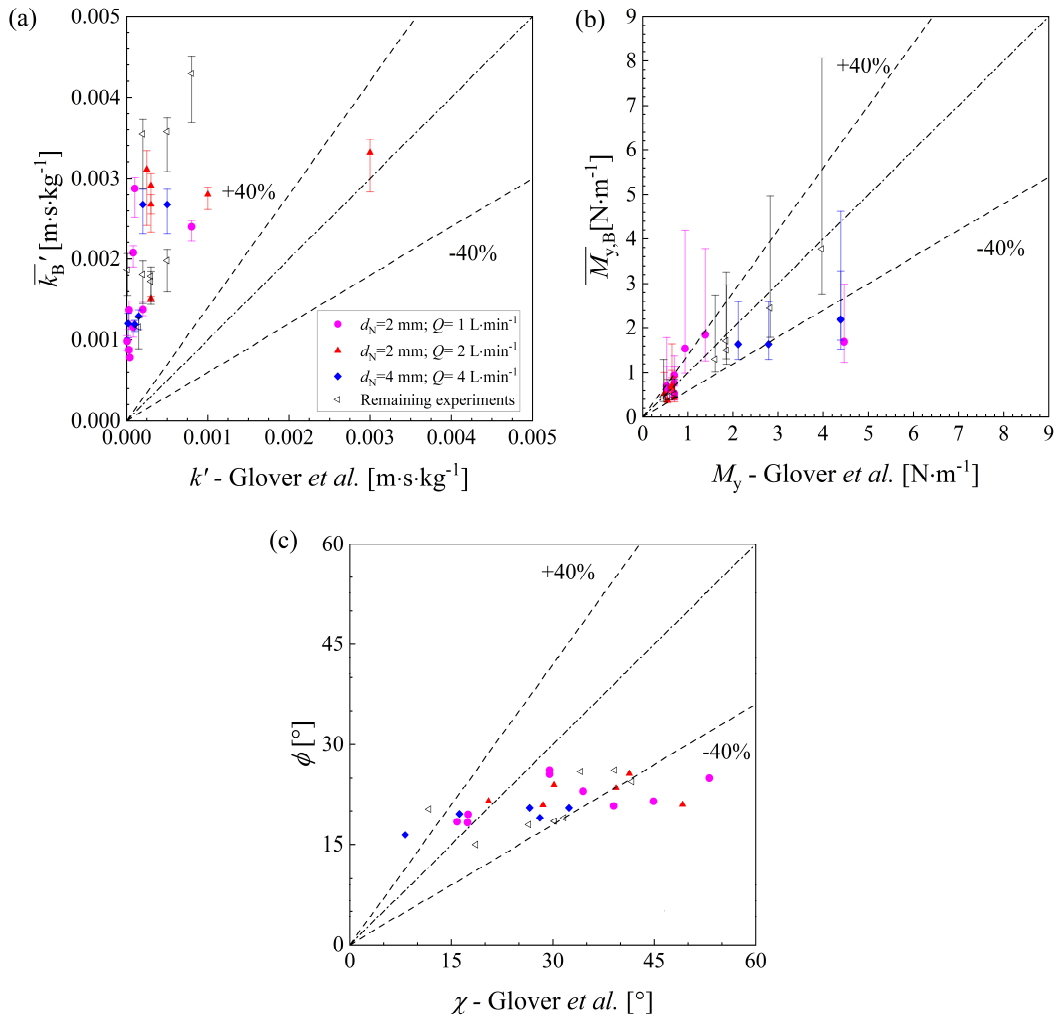

Figure 6.15 – Comparison of the parameters obtained for the linear Bingham model and the Glover *et al.* (2016) model fitted to PJA tests. (a) $\overline{k}_B'$ and k'; (b) $\overline{M}_{y,B}$ and M_y; (c) ϕ and χ. Range bars indicate the maximum and minimum values for each quantity along the cleaning experiment, whereas symbols indicate the spatially averaged values given by Eq. (6.65), (6.66) and (6.67). The values of k', χ and M_y were found by fitting the Glover *et al.* (2016) model to the same data sets.

For the majority of these cleaning tests $a_{max} > r_t$, where both hydraulic models give similar estimates of M, and the values of $\overline{M}_{y,B}$ and M_y are therefore similar (see Figure 6.15 (b)). The wedge angles ϕ and χ differ, with $\phi < \chi$ (Figure 6.15 (c)), with the ϕ values closer to the measured values presented in Figure 6.2 (b). One reason why the Glover *et al.* angle χ is larger is that the static force balance result in Eq. (2.74) employs the layer thickness δ_o rather

than the thickness of the liquid film: if the liquid film thickness was used χ would be smaller. This is one of the insights arising from this work.

The values of $\bar{k}'_{\mathrm{B}}$ are mostly larger than the values of k': this happens because the Glover *et al.* (2016) model overestimates M at the initial stages of cleaning (see Figure 2.10). Therefore, the Glover *et al.* (2016) model gives a poorer description of cleaning at early times (see Figure 6.12), and does not offer any predictive capacity. As discussed above, at later times the cleaning rate is expected to be subject to creep effects which are not included in the viscous dissipation model.

6.1.3.4 Energetic considerations

Figure 6.16 shows the variation of η_{e} with cleaned radius for the experimental conditions reported in Figure 6.8 (a). The data points denote where the measured value of $\mathrm{d}a/\mathrm{d}t$ is used to estimate V in Eq. (6.63), while the dashed lines indicate the result where the Bingham linear model is used to predict V. The values of η_{e} are small, of the order of 10^{-3}, indicating that the change in the kinetic energy of the liquid in the film is small as it moves over the layer and the angled rim. Far from the impinging point, where the rate of cleaning is small, η_{e} reaches values of $\mathcal{O}(10^{-8})$, as shown in the inset of Figure 6.16.

More of the kinetic energy is employed in cleaning at small values of a, *i.e.*, when $\mathrm{d}a/\mathrm{d}t$ is high. This indicates that the most efficient way to clean a viscoplastic soil with impinging water jets is by using traversing nozzles, when the liquid film is continuously exposed to fresh soil (Wilson *et al.*, 2015; Bhagat *et al.*, 2017; Fernandes *et al.*, 2019; Oevermann *et al.*, 2019). The discontinuity in the predicted efficiency loci in Figure 6.16 arises from the jump in M at r_{t} (Bhagat & Wilson, 2016) (see Figure 2.10-a).

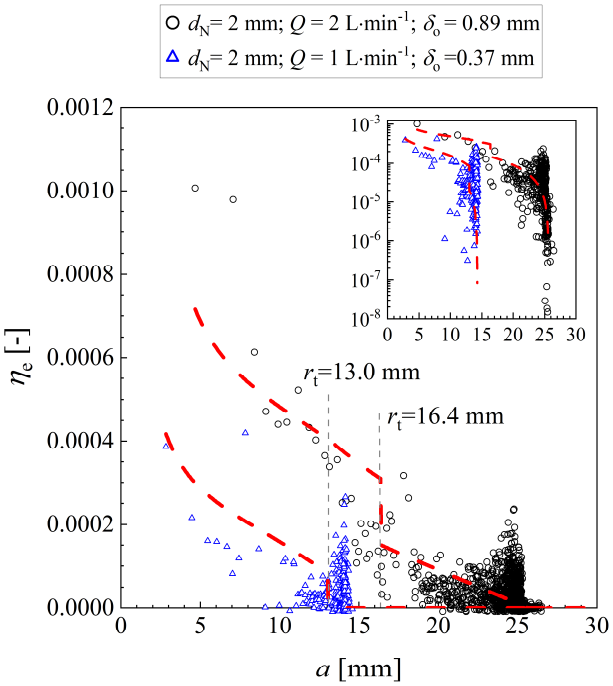

Figure 6.16 – Evolution of energetic efficiency of the cleaning experiments reported in Figure 6.8. Data points: V in Eq. (6.63) taken from experimental data. Red loci – V predicted using model. Dashed vertical lines indicate the location of r_t, inset shows the data with the vertical axis in logarithmic scale

6.2 Including additional dissipation along the moving front

In Section 6.1, a simple wedge geometry was assumed for the derivation of the cleaning model (Figure 6.3). Dissipation was assumed to be limited to the region where $\delta(x) < h$, corresponding to $x < x_L$. The model is extended here to some more complex cases, including dissipation along the rim or the accumulation of mobilised material downstream of the wedge.

6.2.1 Including dissipation for $h < \delta < \delta_o$

For thin soil layers, case (b) illustrated in Figure 6.1, $\delta_o > h(r)$. It is therefore possible to develop the cleaning model assuming dissipation along the whole rim, including the region where $h < \delta \leq \delta_o$. A modified schematic of the cleaning front is shown in Figure 6.17.

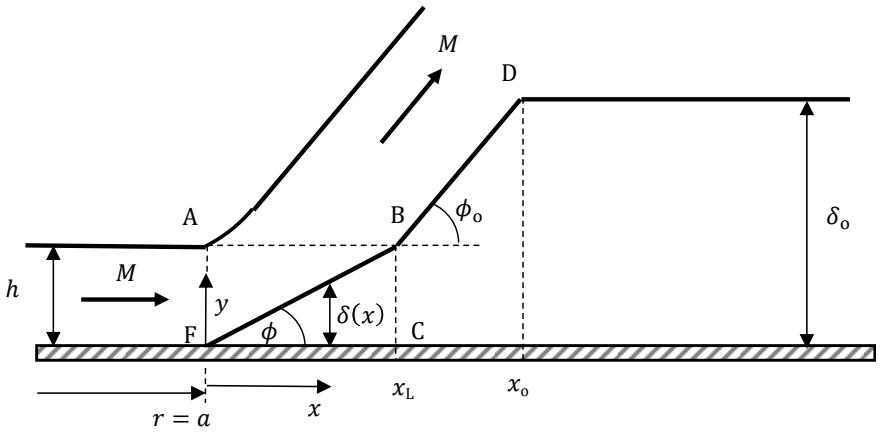

Figure 6.17 – Schematic of the rim corresponding to Eq. (6.73) where dissipation is extended to the region where $h < \delta \leq \delta_o$.

The deforming region is extended across the layer thickness along the line labelled FBD in Figure 6.17. In this case the slope angle changes to a larger value, ϕ_o. This assumption is based on measurements of the shape of the cleaning front, which indicated that for $\delta < h$, $\phi_o \approx \pi/4$ (see Figure 6.2).

Dissipation then takes place up to x_o:

$$x_o = \frac{h}{\tan\phi} + \frac{\delta_o - h}{\tan\phi_o}. \tag{6.68}$$

The power per unit width consumed by viscous dissipation along the rim is:

$$Q_D = \tau_c V \int_0^{x_o} \tau_w^* \, dx = \tau_c V \left[\int_0^{x_T} \tau_w^* \, dx + \int_{x_T}^{x_o} \tau_w^* \, dx \right]. \tag{6.69}$$

Substituting $Q_D = M(1 - \cos\phi)V$, $\tau_w^* = \frac{3}{2} + \frac{1}{2}V^*$ and setting $x_T = x_L = \frac{h}{\tan\phi}$ in Eq. (6.69) gives:

$$\frac{M(1-\cos\phi)}{\tau_c} = \frac{3}{2}x_o + \frac{1}{2}\left[\int_0^{x_L} V^* \, dx + \int_{x_L}^{x_o} V^* \, dx \right]. \tag{6.70}$$

Since $V^* = \frac{6\mu_B V}{\tau_c \delta}$, Eq. (6.70) yields:

$$\frac{M(1-\cos\phi)}{\tau_c} = \frac{3}{2}x_o + \frac{3\mu_B V}{\tau_c}\left[\int_0^{x_L}\frac{1}{\delta}\,dx + \int_{x_L}^{x_o}\frac{1}{\delta}\,dx\right] \tag{6.71}$$

where δ is the local height of the rim, defined as:

$$\delta = \begin{cases} \delta_i + x\tan\phi & \text{if} \quad 0 < x \le x_L \\ h + \left(x - \frac{h}{\tan\phi}\right)\tan\phi_o & \text{if} \quad x_L < x \le x_o \end{cases} \tag{6.72}$$

Solving for V yields:

$$V = \frac{da}{dt} = \frac{\tan\phi - \sin\phi}{3\mu_B C_1}\left[M - \frac{2}{3}\frac{\tau_c x_o}{(1-\cos\phi)}\right] \tag{6.73}$$

where C_1 is given by:

$$C_1 = \ln\left(1 + \frac{h}{\delta_i}\right) + \frac{\tan\phi}{\tan\phi_o}\ln\left[\frac{x_o\tan\phi_o + h\left(\frac{\tan\phi - \tan\phi_o}{\tan\phi}\right)}{x_L\tan\phi_o + h\left(\frac{\tan\phi - \tan\phi_o}{\tan\phi}\right)}\right]. \tag{6.74}$$

Again, Eq. (6.73) takes the form of the Glover *et al.* (2016) model, with the parameters k'_ϕ and $M_{y,\phi}$ given by:

$$k'_\phi = \frac{\tan\phi - \sin\phi}{3\mu_B C_1} \tag{6.75}$$

and

$$M_{y,\phi} = \frac{2}{3}\frac{\tau_c x_o}{(1-\cos\phi)} \tag{6.76}$$

6.2.2 Including dissipation in the berm

The second case extends the single slope to include a contribution from the material in the berm. This material, having been sheared, is likely to exhibit different rheological behaviour (Møller *et al.*, 2009b) since the soil layers are time-dependent. However, it will be assumed to have the same rheology as the undisturbed layer and is considered here for completeness. The shape of the berm is modelled as an isosceles triangle in section inclined at ϕ_o, as shown

in Figure 6.18. Viscous dissipation is then calculated over the region FE. The size of the berm changes with time so its height H varies with a.

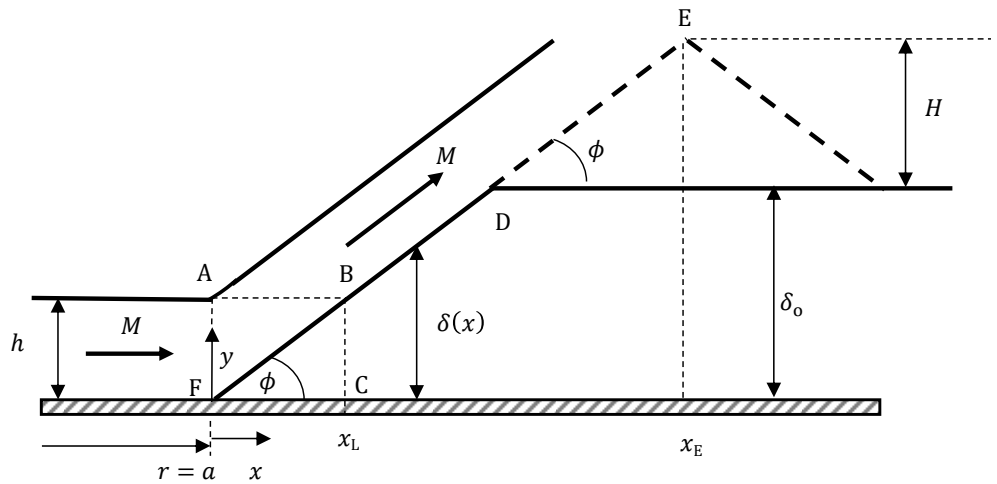

Figure 6.18 – Schematic of the rim corresponding to Eq. (6.82). The material removed accumulates as an isosceles rampart, and dissipation takes place up to x_{E}

Assuming that all the material removed from a circular frustum of height δ_{o}, radius a and angle ϕ_{o} forms such a rampart, it can be shown that H is given by the largest positive root of

$$H^{*3} + \frac{a^*}{\cot\phi}\, H^{*2} + \frac{1}{6\cot^2\phi}\{3a^*\cot\phi - 3a^{*2} - \cot^2\phi\} = 0 \qquad (6.77)$$

where $H^* = H/\delta_{\mathrm{o}}$ and $a^* = a/\delta_{\mathrm{o}} + \cot\phi$.

Curves for a range of ϕ values are shown in Figure 6.19: H^* increases non-linearly with a^*.

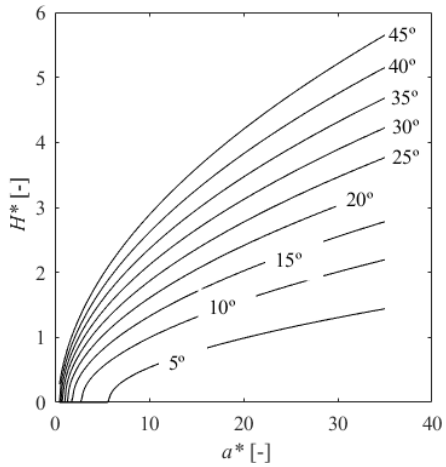

Figure 6.19 – Effect of ϕ on the evolution of the berm height. The angle ϕ is found from the largest positive root of Eq. (6.77).

The x-coordinate of the apex of the accumulated berm, x_E, is given by:

$$x_\mathrm{E} = \frac{\delta_\mathrm{o} + H}{\tan\phi}. \tag{6.78}$$

The power consumed by viscous dissipation along the rim is calculated including the contribution up to $x = x_\mathrm{E}$:

$$Q_\mathrm{D} = \tau_\mathrm{c} V \int_0^{x_\mathrm{E}} \tau_\mathrm{w}^* \,\mathrm{d}x\,. \tag{6.79}$$

Substitution of $Q_\mathrm{D} = M(1-\cos\phi)V$, $\tau_\mathrm{w}^* = \frac{3}{2} + \frac{1}{2}V^*$ and $V^* = \frac{6\mu_\mathrm{B}V}{\tau_\mathrm{c}\delta}$ in Eq. (6.79) gives:

$$\frac{M(1-\cos\phi)}{\tau_\mathrm{c}} = \frac{3}{2}x_\mathrm{A} + \frac{3\mu_\mathrm{B}V}{\tau_\mathrm{c}} \int_0^{x_\mathrm{E}} \frac{1}{\delta}\,\mathrm{d}x \tag{6.80}$$

with δ the local height of the rim, defined as:

$$\delta = \delta_\mathrm{i} + x\tan\phi\,. \tag{6.81}$$

Substitution of Eq. (6.81) in Eq. (6.80) gives, after some rearrangement:

$$V = \frac{\mathrm{d}a}{\mathrm{d}t} = \frac{(\tan\phi - \sin\phi)}{3\mu_\mathrm{B}\ln\left(1 + \frac{x_\mathrm{E}\tan\phi}{\delta_\mathrm{i}}\right)}\left[M - \frac{3}{2}\frac{x_\mathrm{E}\tan\phi\,\tau_\mathrm{c}}{(\tan\phi - \sin\phi)}\right]. \tag{6.82}$$

Again, Eq. (6.82) assumes the form of the Glover *et al.* (2016) model, with

$$k'_{\mathrm{R}} = \frac{(\tan\phi - \sin\phi)}{3\mu_{\mathrm{B}} \ln\left(1 + \frac{x_{\mathrm{E}} \tan\phi}{\delta_{\mathrm{i}}}\right)} \tag{6.83}$$

$$M_{\mathrm{y,R}} = \frac{3}{2} \frac{x_{\mathrm{E}} \tan\phi\, \tau_{\mathrm{c}}}{(\tan\phi - \sin\phi)} \tag{6.84}$$

Figure 6.20 shows the fits of the original model, Eq. (6.40), alongside the two above versions that include dissipation along the rest of the rim, Eq. (6.73) and Eq. (6.82). Fits are presented for the rheological behaviour described by the static flow curve of the PJA, and the corresponding fitted parameters are shown in the plot legends. Figure 6.20 (a) shows the evolution of the cleaned radius over time, whereas Figure 6.20 (b) presents the rate of growth of the cleaned radius as a function of the momentum flow rate per unit of width. Plots are presented for two experimental conditions, (i) d_{N} = 2 mm, Q = 2 l·min^{-1}, δ_{o} = 0.89 mm and (ii) d_{N} = 2 mm, Q = 1 l·min^{-1}, δ_{o} = 0.90 mm. Neither of the modified equations yielded a good description of the experiments. Large values of ϕ were assumed due to the additional dissipation that takes place along the rim for $\delta > h$. As a result, the value of k' is also overestimated, which reflects on the incorrect description of the early stages of cleaning in the a vs t plots, Figure 6.20 (a), and of the $\mathrm{d}a/\mathrm{d}t$ vs M plots in Figure 6.20 (b).

The model considering dissipation across the two-angled rim, Eq. (6.73), provides a good description of the data at the later stages of cleaning. This is because the term corresponding to $M_{\mathrm{y},\phi}$, Eq. (6.76), does not change as a increases, such that it can be adjusted by chosing an appropriate value for ϕ. On the other hand, the $M_{\mathrm{y,R}}$ term for the model that considers the accumulated rampart, Eq. (6.84), increases with the cleaned radius and limits the maximum cleaned radius obtained at long cleaning times. Therefore, the assumption made in Section 6.1 that dissipation is limited to $\delta \leq h$ seems to be correct, as considering dissipation along the whole extent of the rim yields results that do not correspond to the experiments.

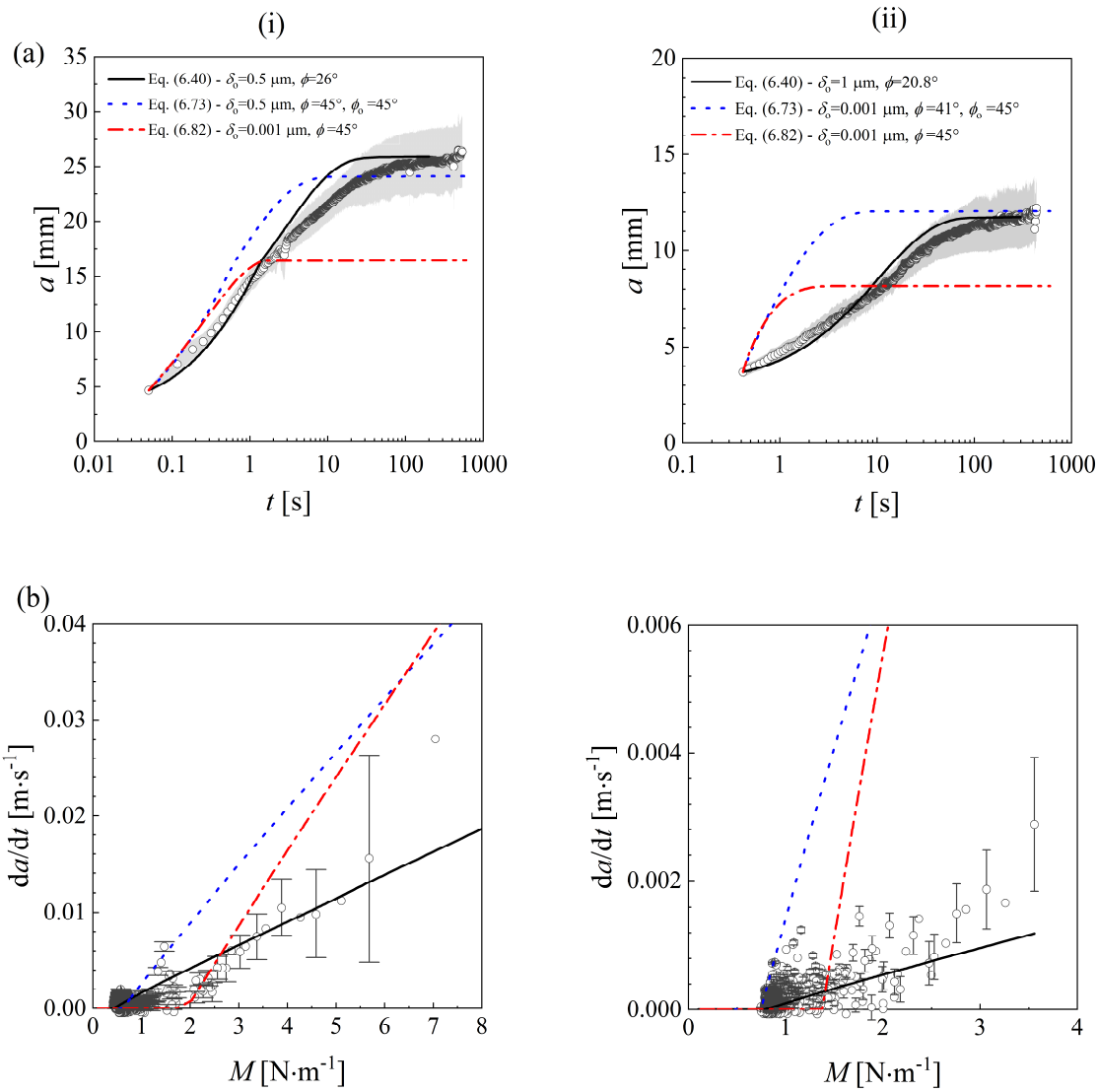

Figure 6.20 – Comparison of the cleaning models, Eq. (6.40), (6.73) and (6.82), for cleaning PJA with d_N =2 mm jets: (a) a as a function of time; (b) da/dt as a function of M. Column (i): Q = 2 l·min^{-1}, δ_o = 0.89 mm; Column (ii): Q =1 l·min^{-1}; δ_o = 0.90 mm.

6.3 Modelling the cleaning of very thin soil layers: shear driven removal

Figure 6.1 showed that the relative thicknesses of the soil layer and of the liquid film define the dynamics of the cleaning process. For very thin soil layers, the liquid film flows over the soil layer and so this scenario is expected to be limited to when $\frac{h}{\delta_o} > 1/2$. In this section a different modelling approach is considered, following the shear-driven mechanism proposed by Yeckel and Middleman (1987).

Yeckel and Middleman (1987) started by writing the equation for conservation of momentum and mass for the soil layer in cylindrical coordinates, Eqs. (6.85) and (6.86), respectively:

$$\frac{\partial P}{\partial r} = \frac{\partial \tau_{rz}}{\partial z} \tag{6.85}$$

$$\frac{\partial (r u_{\mathrm{so}})}{\partial r} + \frac{\partial (r v_{\mathrm{so}})}{\partial z} = 0 \tag{6.86}$$

where τ_{zr} is the shear stress in the radial direction, P is the pressure, u_{so} and v_{so} are the velocities of the soil in the r and z directions, respectively. Their soils were Newtonian, so τ_{zr} is given by

$$\tau_{rz} = \mu_{\mathrm{so}} \frac{\partial u_{\mathrm{so}}(r,z)}{\partial z} \tag{6.87}$$

with μ_{so} the viscosity of the Newtonian soil layer.

Assumption of no-slip at the soil-substrate interface and of continuity of the shear stress at the soil-liquid interface gives the boundary conditions:

$$u_{\mathrm{so}} = v_{\mathrm{so}} = 0 \ \text{ at } \ z = 0 \tag{6.88}$$

$$\tau_{rz} = \tau_{\mathrm{w,l}} \ \text{ at } \ z = \delta(r,t)\,. \tag{6.89}$$

Solution of Eq. (6.85) and (6.86) subject to the boundary conditions (6.88) and (6.89) gives expressions for the velocity u_{so} and v_{so} in the r and z directions, respectively. Applying conservation of volume to the Newtonian soil layer yields a PDE of the form:

$$\frac{\partial \delta}{\partial t} + \frac{1}{\mu_{\mathrm{so}}}\left(\frac{\delta^2}{2}\frac{\mathrm{d}P}{\mathrm{d}r} + \tau_{rz}\delta\right)\frac{\partial \delta}{\partial r} + \frac{1}{\mu_{\mathrm{so}}}\left[\frac{\delta}{3r}\frac{\mathrm{d}\left(r\frac{\mathrm{d}P}{\mathrm{d}r}\right)}{\mathrm{d}r} + \frac{1}{2r}\frac{\mathrm{d}(r\tau_{rz})}{\mathrm{d}r}\right]\delta^2 = 0 \tag{6.90}$$

subject to the boundary and initial conditions:

$$\frac{\partial \delta}{\partial r} = 0 \ \text{ at } \ r = 0 \tag{6.91}$$

$$\delta = \delta_{\mathrm{o}} \ \text{ at } \ t = 0 \tag{6.92}$$

Eq. (6.90) was solved numerically, assuming that $\frac{\partial P}{\partial r} = 0$ in the radial flow zone and the pressure distribution within the jet footprint was the empirical correlation proposed by Chin and Tsang (1978). In the RFZ Eq. (6.90) becomes:

$$\frac{\partial \delta}{\partial t} + \left(\frac{\tau_{rz}}{\mu_{so}}\delta\right)\frac{\partial \delta}{\partial r} + \left[\frac{1}{2r\mu_{so}}\frac{\mathrm{d}(r\tau_{rz})}{\mathrm{d}r}\right]\delta^2 = 0\,. \tag{6.93}$$

Yeckel and Middleman (1987) did not report local layer thicknesses: they reported the average layer thickness obtained by weighing the plates after interrupted cleaning experiments. They reported the average mean liquid film thickness expressed in dimensionless form, $\bar{\delta}^*_{YM}$,

$$\bar{\delta}^*_{YM} = \frac{2}{\delta_o R_{Pl}^2}\int_0^{R_{Pl}} r\delta dr \tag{6.94}$$

where R_{Pl} is the radius of the circular target plate used in their experiments. For the case selected for analysis here, R_{Pl} = 37.5 mm and δ_o=0.09 mm.

Results were presented in terms of a non-dimensional time $t^\star_{YM}$:

$$t^\star_{YM} = \frac{0.089\rho\nu^{0.2}U_o^{1.8}\delta_o}{\mu_{so}R_{Pl}^{1.2}}t \tag{6.95}$$

where μ_{so} =0.48 Pa·s, U_o = 3.35 m·s^{-1}, ρ = 998 kg·m^{-3} and $\nu = \mu/\rho \approx 10^{-6}$ m^2·s^{-1}. Their timescale was derived from the solution of Eq. (6.93) for $\frac{d_N}{2} < r < r_j$, with the shear stress at the interface between the liquid film and the soil layer described by a power-law approximation to Watson's (1964) hydrodynamic model.

A selection of their experimental results is presented in Figure 6.21, along with the solution of Eq. (6.93) obtained using Matlab®. The agreement of the model with the experimental results is similar to that reported by Yeckel and Middleman (1987) and indicates that the numerical method employed is accurate.

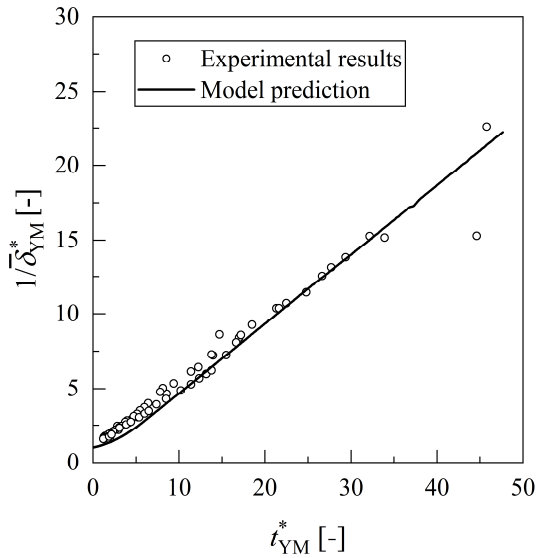

Figure 6.21 – Experimental results presented by Yeckel and Middleman (1987), alongside the Matlab^{TM} solution of Eq. (6.93).

A similar approach is taken here to describe the shear-driven removal of a very thin viscoplastic soil layer. Figure 6.22 presents a schematic of the model in cylindrical coordinates. The liquid film imposes a shear stress on the interface with the soil layer, $\tau_{\mathrm{int}}(r)$, which promotes flow in the layer. The layer thickness then changes as a function of space and time. In the absence of more detailed information on the hydrodynamic interactions between the liquid and the soil, τ_{int} is assumed to be similar to the wall shear stress imposed by the liquid film on a flat surface, $\tau_{\mathrm{w,l}}(r)$, given by the Bhagat and Wilson (2016) model. A similar assumption was made by Yeckel and co-workers (Yeckel & Middleman, 1987; Yeckel *et al.*, 1994) in their description for the removal of immiscible Newtonian liquid layers from flat surfaces. The soil layer is initially modelled as a Herschel-Bulkley material, Eq. (2.23).

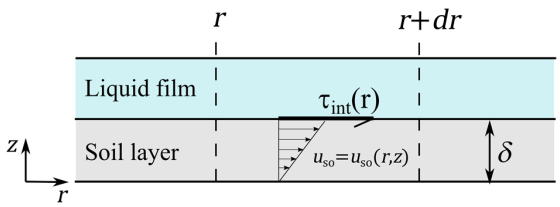

Figure 6.22 – Schematic of the shear driven model in cylindrical coordinates

Conservation of volume in the layer between r and $r + \mathrm{d}r$ requires

$$\frac{\partial \delta}{\partial t} + \frac{1}{r}\frac{\partial (r\Gamma)}{\partial r} = 0 \tag{6.96}$$

where $\Gamma(r)$ is the volumetric flow rate of soil per unit of circumferential width,

$$\Gamma(r) = \int_0^{\delta} u_{\mathrm{so}}\, \mathrm{d}z. \tag{6.97}$$

In the absence of slip (see Figure 4.4), the velocity profile is given by:

$$u_{\mathrm{so}}(r,z) = \left[\frac{\tau_{\mathrm{int}}(r) - \tau_{\mathrm{c}}}{k_{\mathrm{HB}}}\right]^{m_{\mathrm{HB}}} z \tag{6.98}$$

with $m_{\mathrm{HB}} = 1/n_{\mathrm{HB}}$, so $\Gamma(r)$ is given by:

$$\Gamma(r) = \left[\frac{\tau_{\mathrm{int}}(r) - \tau_{\mathrm{c}}}{k_{\mathrm{HB}}}\right]^{m_{\mathrm{HB}}} \frac{\delta^2}{2}\ . \tag{6.99}$$

An important aspect of Eq. (6.99) is that the volumetric flow rate of the soil increases with δ^2.

Substitution of Eqs. (6.98) and (6.97) in Eq. (6.96) yields the following partial differential equation (PDE) for $\delta(r,t)$:

$$\begin{aligned} &\frac{\partial \delta}{\partial t} + \left[\left(\frac{\tau_{\mathrm{int}}(r) - \tau_{\mathrm{c}}}{k_{\mathrm{HB}}}\right)^{m_{\mathrm{HB}}} \delta\right]\frac{\partial \delta}{\partial r} \\ &+ \left[\frac{1}{2r}\left(\frac{\tau_{\mathrm{int}}(r) - \tau_{\mathrm{c}}}{k_{\mathrm{HB}}}\right)^{m_{\mathrm{HB}}} + \frac{\mathrm{m}_{\mathrm{HB}}(\tau_{\mathrm{int}}(r) - \tau_{\mathrm{c}})^{m_{\mathrm{HB}}-1}}{2k_{\mathrm{HB}}^{m_{\mathrm{HB}}}}\frac{\mathrm{d}}{\mathrm{d}r}\left(\tau_{\mathrm{int}}(r)\right)\right]\delta^2 = 0 \end{aligned} \tag{6.100}$$

which requires numerical solution. Eq. (6.100) is non-linear, as it includes a quadratic term for the computed variable (δ^2). This term implies that the volumetric flow rate of the soil is larger where the thickness of the soil is larger. This is not consistent with experimental observations, indicating that the model is unlikely to give a reliable prediction of cleaning rates.

Eq. (6.100) was solved in Matlab™ using QUICK space discretisation (Leonard, 1979, 1995), with initial condition $\delta = \delta_{\mathrm{o}}$ at $t = t_{\mathrm{o}}$ and boundary condition $\delta = 0$ at $r = a_{\mathrm{o}}$. The model is not solved within the jet stagnation region. The Bhagat and Wilson (2016) model

describes the behaviour of the liquid film beyond the jet footprint, so Eq. (6.100) will only be solved within the RFZ, where $\frac{d_N}{2} < r < r_j$.

6.3.1 Rheological characterisation of the soil

Very thin soil layers of the undyed petroleum jelly are translucent, so the PJA was dyed with a white oil-soluble food dye (White icing colour, Wilton Industries, USA) to facilitate detection of the cleaned radius. Petroleum jellies are crystalline materials (Park & Song, 2010b; Duarte *et al.*, 2014), so changes in the rheological behaviour after intense shearing, such as that required to incorporate the dye into the material, are expected to occur. Therefore, the rheological characterisation of the dyed and undyed petroleum jelly are presented separately.

Figure 6.23 shows the effect of flow history on the rheological behaviour of the (a) undyed and (b) dyed jellies. A series of 100 s long increasing shear stress steps performed in the stress-controlled rheometer was used to estimate the static flow curve of the materials. This corresponds to the flow curve of the material in a structured state. Initially, a predominantly elastic response is observed, corresponding to the pre-yielding regime. At a shear stress of approximately 100 Pa the shear rate slowly increases with the shear stress, indicating a slow creep of the material such as previously discussed in Chapter 4. At $\tau \approx 140$ Pa, a sharp increase in the shear rate is observed for both materials, which is associated with the structural breakdown and yielding of the material at the static critical stress $\tau_{c,s}$. Dyeing the petroleum jelly did not affect the static flow curves significantly.

Dynamic (or steady-state) flow curves were obtained with the material starting from high shear rates. Here, decreasing shear rate steps ranging from 100 to 0.025 s^{-1} (the lower limit of the strain-controlled rheometer) were applied over 360 s to keep track of the shear stress response of the materials. This corresponds to the flow curve of the material in an unstructured state, so the estimate of the yield stress obtained in these tests is the dynamic critical stress, $\tau_{c,d}$. Figure 6.23 shows a significant difference between the static and dynamic flow curves, as expected for time-dependent materials (Barnes, 1997; Mewis & Wagner, 2009; Dimitriou & McKinley, 2014; Geri *et al.*, 2017). There is also a noticeable difference between the shear stresses measured in the decreasing shear rate steps for the dyed and undyed jellies, particularly at low shear rates.

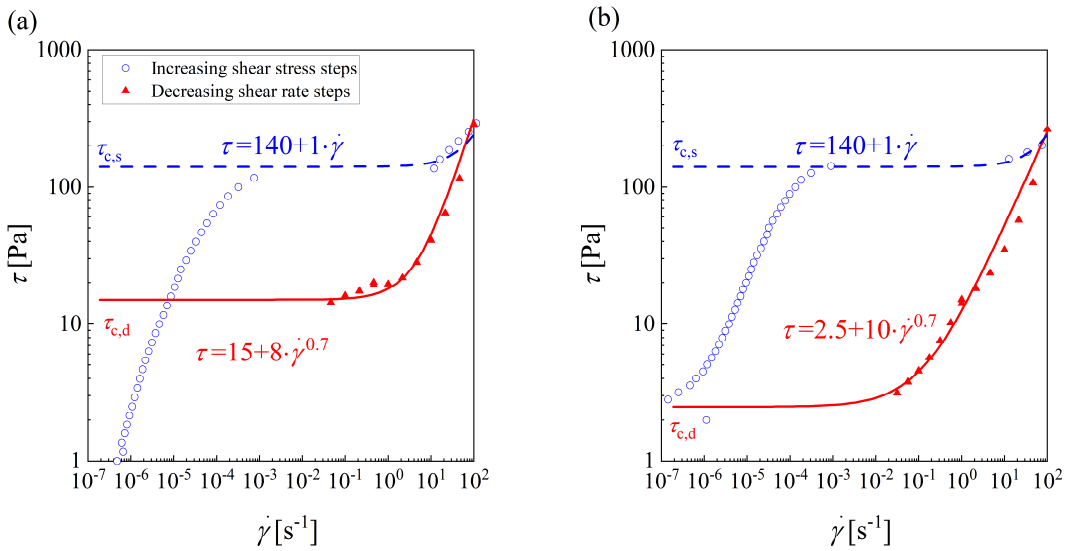

Figure 6.23 - Static flow curves, obtained with increasing shear stress steps, and dynamic flow curves, obtained with decreasing shear rate steps, for the (a) undyed and (b) dyed petroleum jelly. Legend is common to both plots.

6.3.2 Cleaning very thin soil layers

Figure 6.24 (a) shows the evolution of the cleaned radius for soil layers of various thicknesses reproduced from Figure 5.17. Figure 6.24 (b) shows the corresponding values of h/δ_o over time. Two distinct behaviours are evident: soil layers with thicknesses $\delta_o \leq 0.23$ mm, corresponding to $\frac{h}{\delta_o} > 1/2$ reached a maximum cleaned radius of $a_{max} \approx 30$ mm, whereas thicker soil layers reached $a_{max} \approx 35$ mm. Figure 6.2 indicated that there is a significant change in the morphology of the rim at $\frac{h}{\delta_o} \approx 1/2$, and in this case there is a slight effect on the cleaning dynamics for a given impinging jet. Also, it is evident from Figure 6.24 that there is a common rate of growth of the cleaned radius for different initial thicknesses of the soil layer. This observation is not in agreement with the behaviour predicted by Eq. (6.99). It is, however, consistent with the momentum-driven cleaning model presented in Section 6.1, where dissipation is limited to $0 \leq \delta \leq h$, and explains the constant values for k' obtained for different thicknesses reported in Figure 5.17.

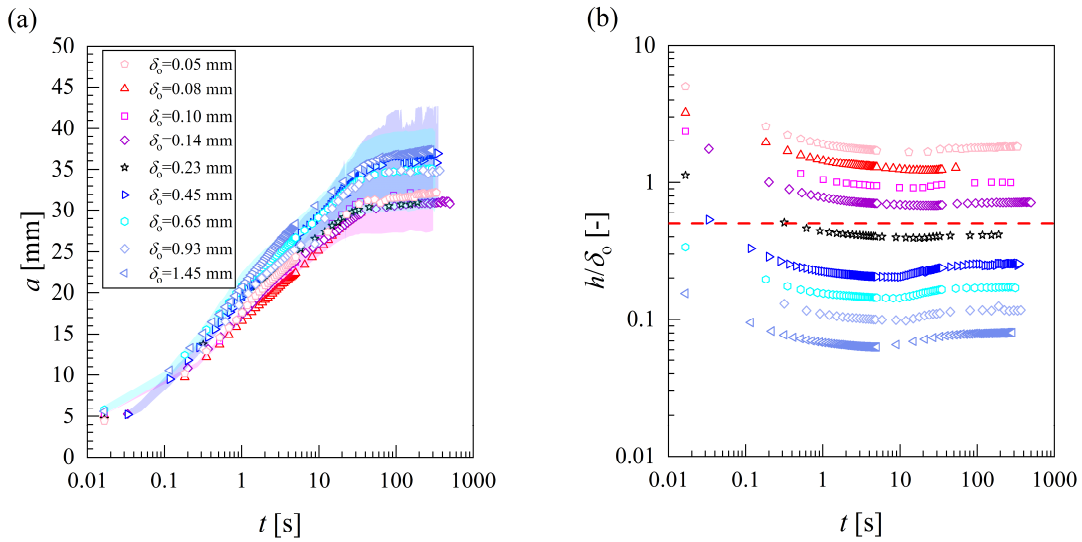

Figure 6.24 – (a) Cleaned radius as a function of time for experiments conducted with $d_N = 3$ mm, $Q = 5$ l·min^{-1} and $0.08 \leq \delta_o \leq 0.93$ mm. Representative range intervals shown for $\delta_o = 0.10$ mm, $\delta_o = 0.45$ mm and $\delta_o = 0.65$ mm. (b) h/δ_o as a function of time for the experiments in (a). Dashed horizontal red line in (b) shows $h/\delta_o = 0.5$.

One of the cases in Figure 6.24 was selected for further investigation, namely d_N=3 mm, Q=5 l·min^{-1} and δ_o=0.08 mm. The PDE was discretised in space, with 500 equally distributed elements ranging from $r = a_o$, the smallest cleaned radius detected from experiments at $t = t_o$, to r_j. The PDE was solved in Matlab^{TM} using the function *ode45*.

Figure 6.25 (a) shows the profiles computed at different time steps. The parameters of the Herschel-Bulkley equation used in Eq. (6.100) were those obtained with the dynamic flow curve of the material, as in this model the soil layer is in motion where $\tau > \tau_c$. The displacement of the soil results in a thin residual layer on the substrate, which is consistent with experimental observations. The region where the material accumulates, however, extends far beyond the value of a_{max} measured from experiments, reported in Figure 6.25 (a) and (c), since $\tau_{w,l} = \tau_{c,d}$ at $r \approx 79$ mm, as denoted by the shaded regions in Figure 6.25 (a), (b) and (d).

It is possible to calculate the angle of the cleaning front for the shear driven model, ϕ_{SD}, by numerical differentiation of δ:

$$\phi_{SD} = \tan^{-1}\left(\frac{d\delta}{dr}\right). \quad (6.101)$$

The values of ϕ_{SD} for the soil profiles are reported in Figure 6.25 (b). The values of ϕ_{SD} are smaller than 1° for most of the time steps reported (see inset in (b)), and these are considerably smaller than the experimental values of ϕ_1 (Figure 6.2).

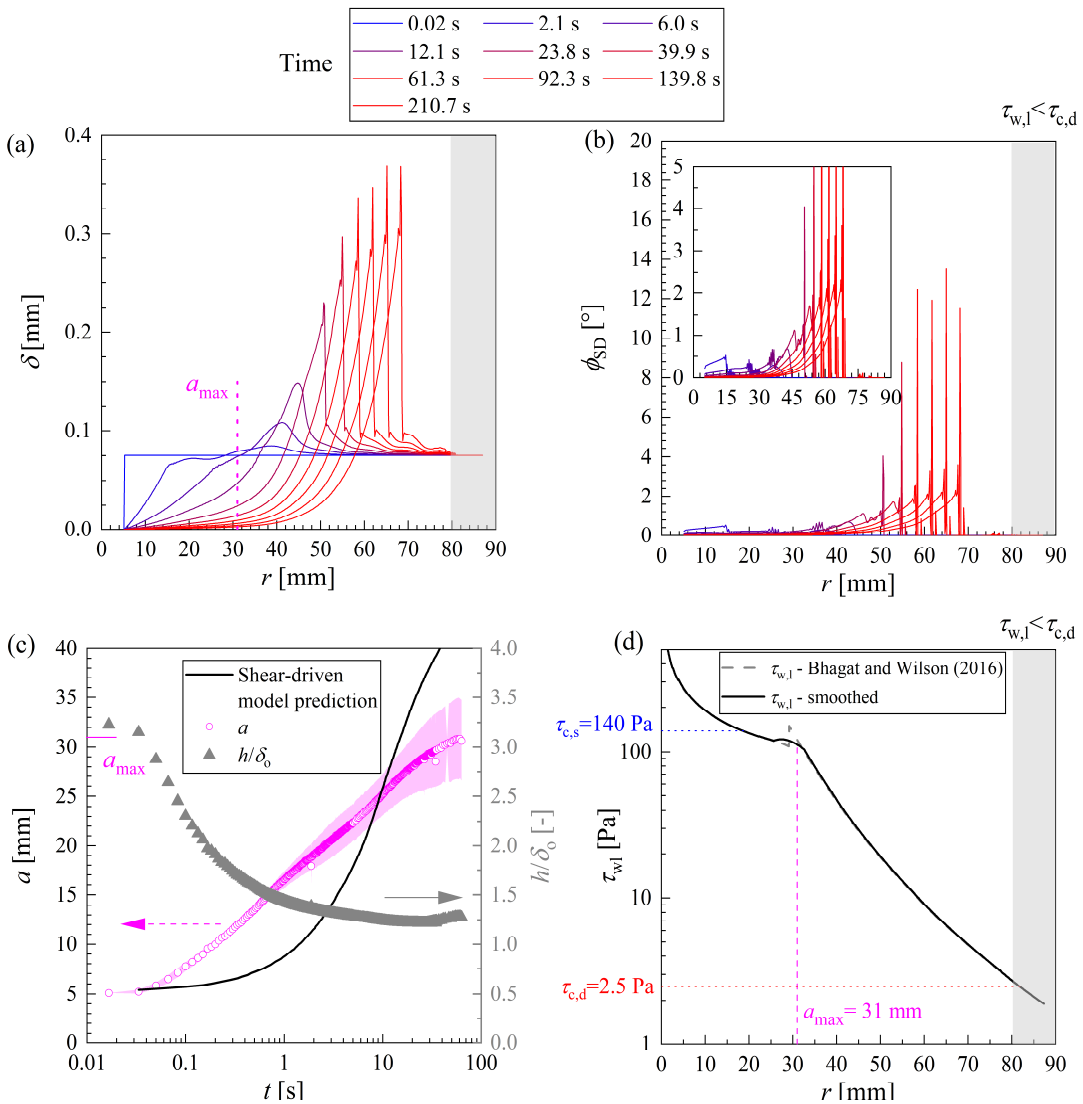

Figure 6.25 – (a) Evolution of the cleaned profiles for d_N=3 mm, Q=5 l·min^{-1} and δ_o=0.075 mm, using rheological parameters for the dynamic flow curve of the dyed petroleum jelly. (b) Values of ϕ_{SD} for the profiles reported in (a). (c) a (left y-axis) and h/δ_o (right y-axis) as a function of time for the experiment reported in (a). (d) $\tau_{w,l}$ as a function of r. Shaded region in (a), (b) and (d) indicates where $\tau_{w,l} < \tau_{c,d}$. Value of a_{max} reported in (a) and (d) extracted from (c).

A criterion is needed to determine when the layer has been removed, *i.e.* is equivalent to being visually clean. This was taken to be when $\delta(r,t) = \delta_o/2$. Figure 6.25 (c) shows the evolution of a over time along with the response predicted by the shear-driven model. It also

reports the values of h/δ_o taken from the experiments. The model does not reach an asymptotic cleaned radius close to the experimental value of a_{max}: this is consistent with Eq. (6.99), which states that the flow rate of the soil increases with the local thickness of the layer. Figure 6.25 (d) plots the values of $\tau_{w,l}$ for the liquid film flow used in the simulations reported in (a). The value of a_{max} taken from the experiment in (c) is shown, as well as the values of $\tau_{c,s}$ and $\tau_{c,d}$ taken from the rheological characterisation of the soil. Since the $\tau_{w,l}$ profile is discontinuous at the laminar-turbulent transition, a smoothed curve is presented. At the experimental value of a_{max}, $\tau_{w,l} \approx$125 Pa, which is close to the static critical stress measured in the increasing stress steps, Figure 6.23 (b). However, this appears to be a coincidence: in other experiments, the soil was removed even when $\tau_{w,l} < \tau_{c,s}$, as will be discussed in Figure 6.27.

A second inconsistency is that the whole layer is assumed to be mobilised at all times since it is subject to the shear stress imposed by the liquid film. Figure 6.26 shows the cleaning of a very thin layer of dyed PJA at different stages. The layer is translucent and the film jump is visible above the point of impingement, which indicates that the liquid film flows over the soil layer instead of splashing backwards. Small indentations (marked in yellow) in the soil layer are present between the berm of accumulated material and the film jump. These indentations did not move ahead of the cleaning front, indicating that the assumption of a mobile soil throughout the RFZ is not correct: the layer beyond the cleaning front was essentially static.

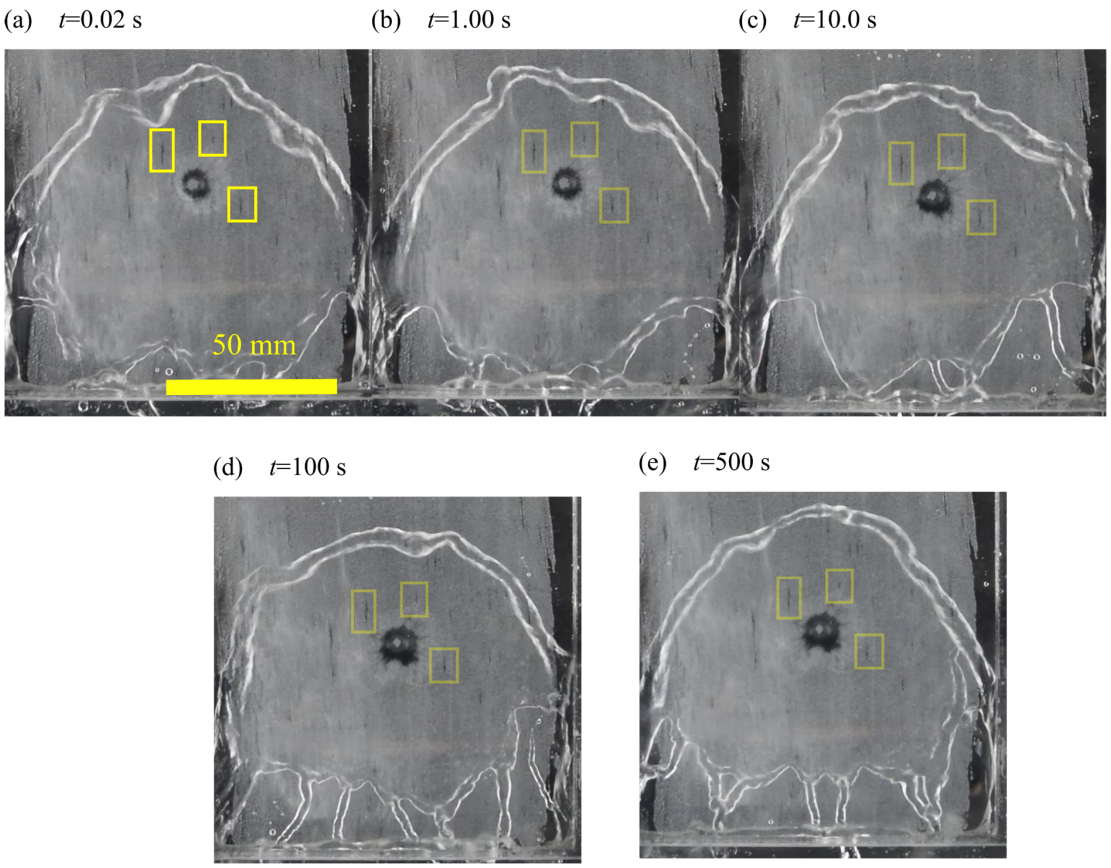

Figure 6.26 – Photographs of the cleaning of a very thin layer of PJA ($d_N = 3$ mm, $Q = 2$ l·min^{-1}, $\delta_o = 0.05$ mm) at different times after penetration of the liquid jet through the layer. Rectangles indicate indentations in the soil layer, which do not move over the cleaning time.

Figure 6.27 shows the results of the model alongside experiments conducted with different nozzle diameters, flow rates and soil layer thicknesses. All experiments reported in Figure 6.27 correspond to very thin soil cases, with $h/\delta_o > 0.5$. Although Figure 6.27 (c) shows good agreement with the model at the early stages of the cleaning process in this case, poor agreement is evident in the other cases. These results indicated that the shear-driven model approach proposed by Yeckel and Middleman (1987) does not give a reliable prediction of cleaning of these thin viscoplastic soil layers. The rate of cleaning predicted by the model at long cleaning times is faster than experimentally observed, which is consistent with Eq. (6.99): the volumetric flow rate of the berm increases with δ^2.

The values of $\tau_{w,l}$ at a_{max} are reported in each case. The values of $\tau_{w,l}$ decrease with r (see Figure 2.10), so the values of $\tau_{w,l}$ imposed by the liquid film on the mobilised layer are larger

than $\tau_{w,l}$ at a_{max}. These values of $\tau_{w,l}$ lie between $\tau_{c,d}$ for the unstructured material and $\tau_{c,s}$ for the fully structured material. Other cleaning experiments were also conducted with very thin soil layers and with the dyed jelly. The values of $\tau_{w,l}$ at $r = a_{max}$ for these experiments are shown in Table 6.3, and again lie between $\tau_{c,s}$ and $\tau_{c,d}$.

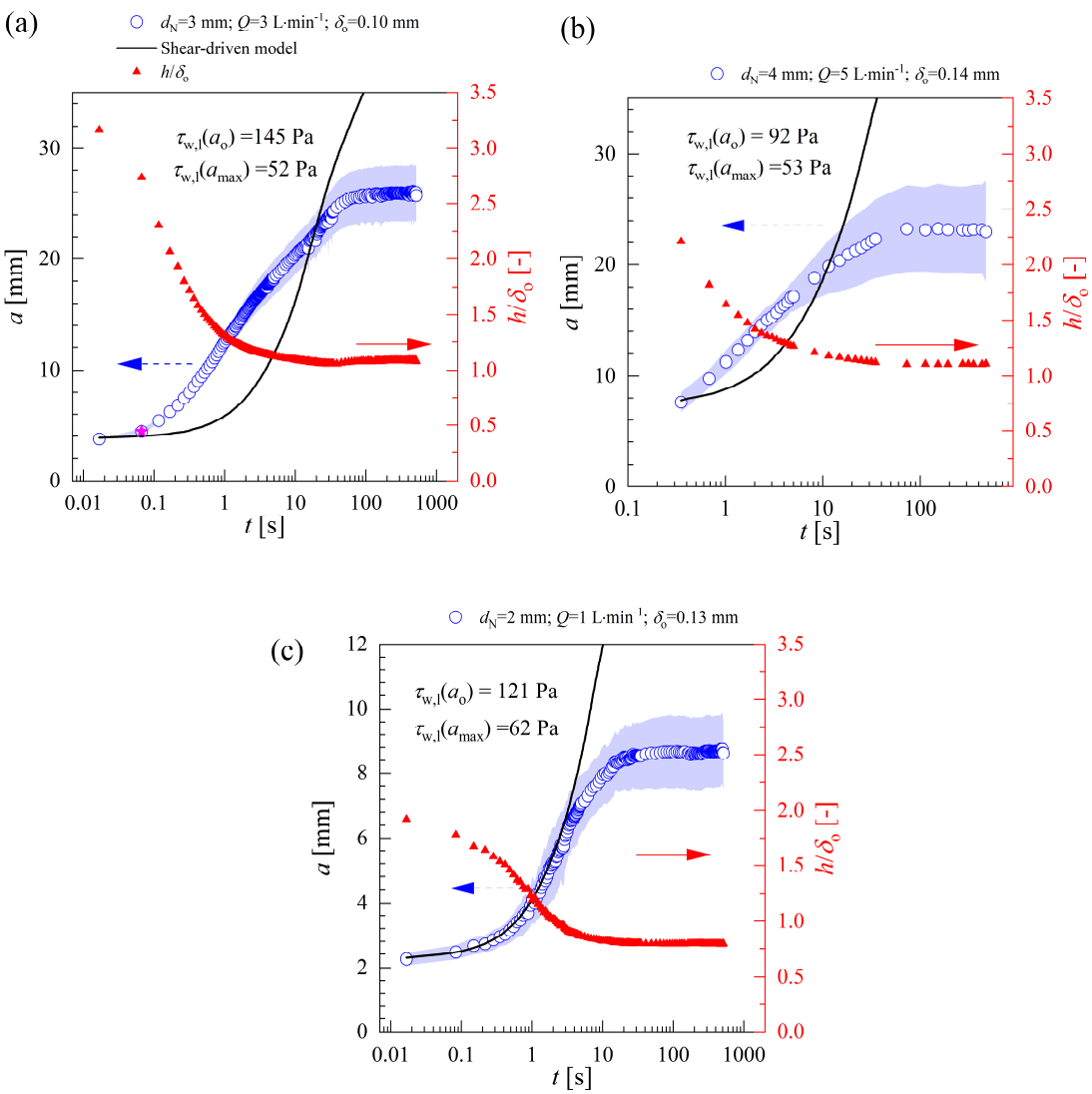

Figure 6.27 – Evolution of a (left y-axis) and h/δ_o (right y-axis), dyed petroleum jelly. (a) d_N = 3 mm, Q= 3 l·min^{-1}, δ_o = 0.103 mm; (b) d_N = 4 mm, Q= 5 l·min^{-1}, δ_o = 0.135 mm and (c) d_N = 2 mm, Q= 1 l·min^{-1}, δ_o = 0.127 mm. Magenta star in (a) indicates location where $\tau_{w,l} \approx \tau_{c,s}$ = 140 Pa.

Table 6.3 – Cleaning experiments with very thin layers of the dyed PJA

Experimental conditions			Results*	
d_N [mm]	Q [l·min^{-1}]	δ_o [mm]	$\tau_{w,l}$ at a_{max} [Pa]	h/δ_o at a_{max} [-]
2	1.0	0.13	62.0	0.8
2	1.4	0.16	79.1	0.5
2	2.0	0.06	83.4	1.4
3	3.0	0.10	52.6	1.1
3	4.0	0.04	90.1	2.7
3	4.0	0.13	99.4	0.8
3	5.0	0.04	124.5	2.5
3	5.0	0.06	105.5	1.8
3	5.0	0.08	126.6	1.3
3	5.0	0.10	104.5	1.0
4	4.0	0.16	54.0	1.4
4	5.0	0.14	53.1	1.1
4	6.0	0.09	65.0	1.5
4	7.0	0.05	86.4	2.9
4	7.0	0.13	88.5	1.1

*Calculated with the Bhagat and Wilson (2016) hydrodynamic model

The material might not be completely unstructured during the cleaning process. If this is the case, its rheological behaviour should not be described by the dynamic flow curve. The rheology of the soil has been described as the unstructured material in the simulations reported in Figure 6.25 and in Figure 6.27. If the result for the previously unyielded material (static flow curve, Figure 6.23) was used, the cleaning rate should approach zero at the point in which $\tau_{w,l} = \tau_{c,s}$, which is smaller than a_{max} in the experiments reported in Figure 6.27. An arbitrary flow curve, lying between the static and dynamic flow curves, could be used, but this would represent a mathematical fitting of the cleaning model with no physical significance. Examples of such a curve-fitting exercise are further explored in Figure 6.31. Time-dependent materials can be described by non-equilibrium flow curves when the material is at an intermediate structural state (Thompson, 2020). A rationale to describe the decrease in τ_c, k_{HB} and n_{HB} with the shear stress over time is needed, and this could possibly be achieved with a thixotropic kinetic model such as that of Mujumdar *et al.* (2002).

The dynamic flow curve represents a lower bound for the viscosity of the fluid. Close to the impinging point, the shear stress imposed by the liquid film is large, so higher cleaning rates are expected in this region, where the material should be close to an unstructured state. The cleaning rate predicted by the model using the dynamic flow curve is slower than the

experimental cleaning rate at short times, indicating that the dynamics of the process are not well described by the shear-driven mechanism discussed here.

One way to further investigate whether the time dependency of the layer is the cause for the deviations between the experimental results and the predictions obtained from the model is to evaluate the cleaning of a thin layer of a non-thixotropic material. Hair gels are dispersions of Carbopol® in water, and their thixotropic time scale is very short – meaning that for practical purposes they behave as non-thixotropic viscoplastic fluids (Dinkgreve *et al.*, 2018).

Figure 6.28 (a) shows the stress as a function of the shear rate for a series of increasing 30 s long shear stress steps performed with a hair gel (Professional max hold styling gel, Eco Style, UK). Results obtained from increasing and decreasing shear rate ramps ($\dot{\gamma} = 0.167$ s^{-2}) are also presented. All curves coincide above the critical stress, indicating that the material is not thixotropic over the time scale considered, and $\tau_{c,s} \approx \tau_{c,d}$.

Cleaning experiments were performed with very thin layers of this hair gel. Figure 6.28 (b) and (c) show the cleaning profiles alongside the solution of Eq. (6.100) with the parameters of the Hershel-Bulkley equation found from the fit of Eq. (2.23) to the data in Figure 6.28 (a). The model again does not describe the experimental results, indicating that the thixotropic nature of the petroleum jelly is not responsible for the failure of the model.

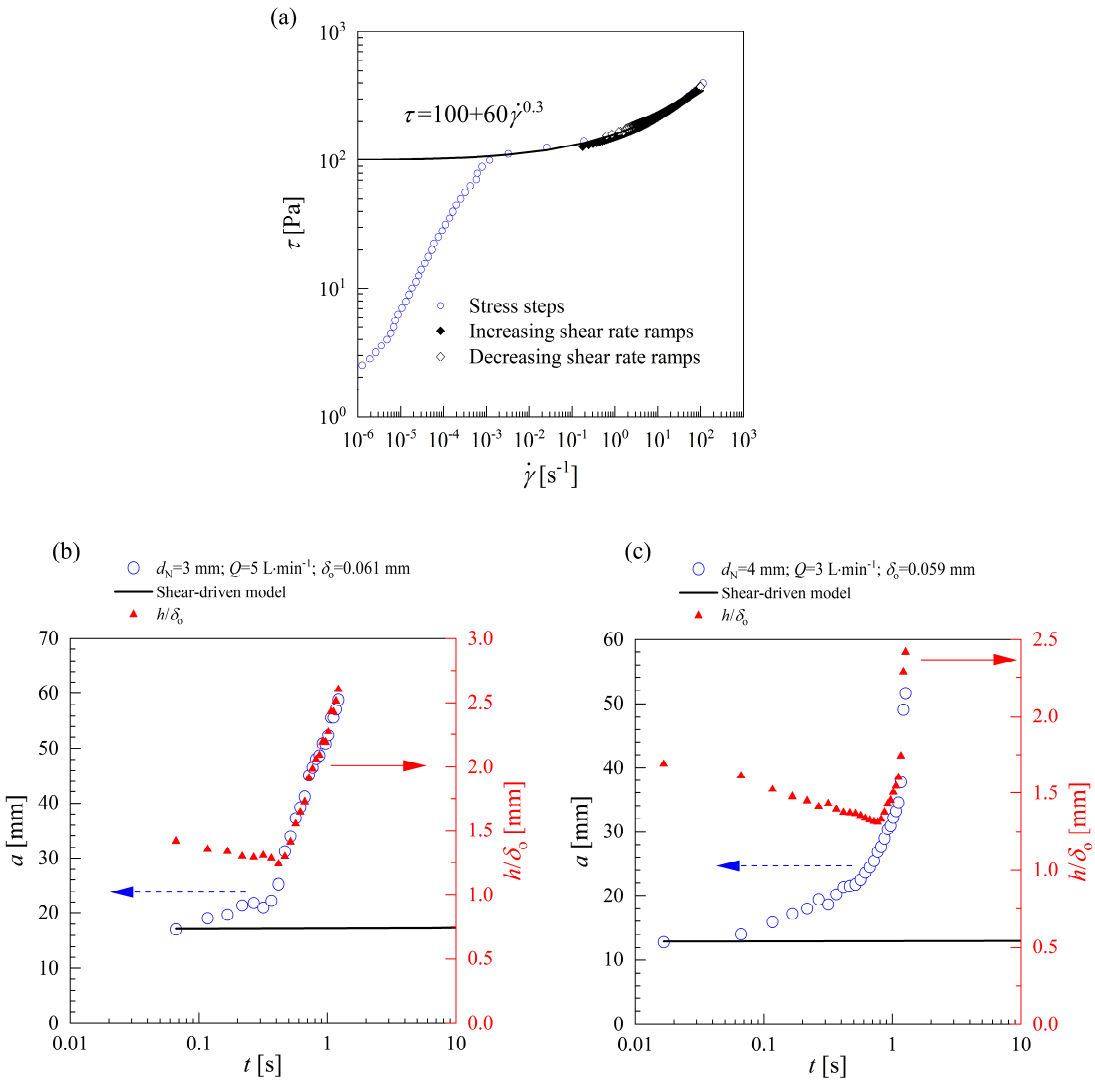

Figure 6.28 – (a) Static and dynamic flow curves of the hair gel, highlighting its non-thixotropic nature. (b) and (c) show a (blue) and $\frac{h}{\delta_o}$ (red) as a function of time for experiments performed with (b) $d_N = 3$ mmm, Q= 5 l·min^{-1}, $\delta_o = 0.061$ mm and (c) $d_N = 4$ mm, Q= 3 l·min^{-1}, $\delta_o = 0.059$ mm.

The shear-driven model does not consider any coupling between the flows in the liquid film and in the soil layer. The shear stress imposed by the liquid on the layer is calculated by the Bhagat and Wilson (2016) model. If there is significant viscous dissipation within the soil layer the value of $\tau_{\mathrm{int}}(r)$ used in Eq. (6.100) should be different from $\tau_{\mathrm{w,l}}(r)$, the shear stress imposed by a liquid film on a flat, immobile surface.

The energy consumed by viscous dissipation within the soil layer at different times is now estimated and compared to the kinetic power of the liquid film. The model for momentum-driven cleaning of thin soil layers discussed in Section 6.1 assumed that viscous dissipation within the layer takes place only at the cleaning front since the liquid film is deflected by the layer in the cases considered previously. For very thin layers, the liquid film flows over the soil layer and viscous dissipation is expected to occur throughout the whole layer. The total power consumed by viscous dissipation within the soil layer is given by

$$Q_{\mathrm{D}'} = 2\pi \int_0^{\delta} \int_{r_\mathrm{o}}^{r} \tau\dot{\gamma}\, r \,\mathrm{d}r \,\mathrm{d}z \,. \tag{6.102}$$

Since $\tau = \tau(r)$, $\dot{\gamma} = \dot{\gamma}(r)$ and $\delta = \delta(r, z)$, Eq. (6.102) can be written as:

$$Q_{\mathrm{D}'} = 2\pi \int_{r_\mathrm{o}}^{r} \tau\dot{\gamma}\, \delta r \,\mathrm{d}r \tag{6.103}$$

which has units of W.

The local kinetic power of the liquid film is given by:

$$\dot{E}_{\mathrm{k}'} = \frac{1}{2}\dot{m}U^2 \tag{6.104}$$

and also has units of W.

The power consumed by viscous dissipation in the soil was calculated by numerical integration of Eq. (6.103) for the case presented in Figure 6.25 (a). Figure 6.29 (a) shows the ratio $Q_{\mathrm{D}'}/\dot{E}_{\mathrm{k}'}$ as a function of the radial position for selected time steps. At low values of r, *i.e.* close to the impinging point, the kinetic energy of the liquid film is large so $Q_{\mathrm{D}'}/\dot{E}_{\mathrm{k}'} \ll 1$. For all times shown, the fraction of the power consumed by viscous dissipation increases with r as U decreases with the radial expansion of the liquid film (see Figure 2.10 (c)). In the region where $r < a_{\max}$ measured from the experiment, $Q_{\mathrm{D}'}/\dot{E}_{\mathrm{k}'} \ll 1$, meaning that the kinetic power of the liquid film is much larger than the power consumed by the soil.

Similarly to what is shown in Figure 6.25 (c), the shear-driven model assumes that the whole layer is mobilised, including the region where $r > a_{\max}$. The fraction $Q_{\mathrm{D}'}/\dot{E}_{k'}$ also decreases with time: according to Eq. (6.103), the layer near the impinging point has a significant contribution to $Q_{\mathrm{D}'}$. The product $\tau\dot{\gamma}$, which only depends on the radial position, is a strongly

decreasing function of r in this region, as indicated in Figure 6.29 (b). Since the local values of δ near the impinging point decrease over time as the layer thins, $Q_{D'}$ also decreases over time. The values of $Q_{D'}/\dot{E}_{k'}$ are smaller than 1, meaning that the liquid film is not significantly decelerated by the soil. This is consistent with experimental observations, as the liquid flowed above the soil beyond the accumulated berm (see Figure 6.26, where a film jump is visible beyond the cleaning front). This suggests that the deceleration of the liquid film by deformation and flow of the soil layer is not responsible for the failure of the shear-driven model.

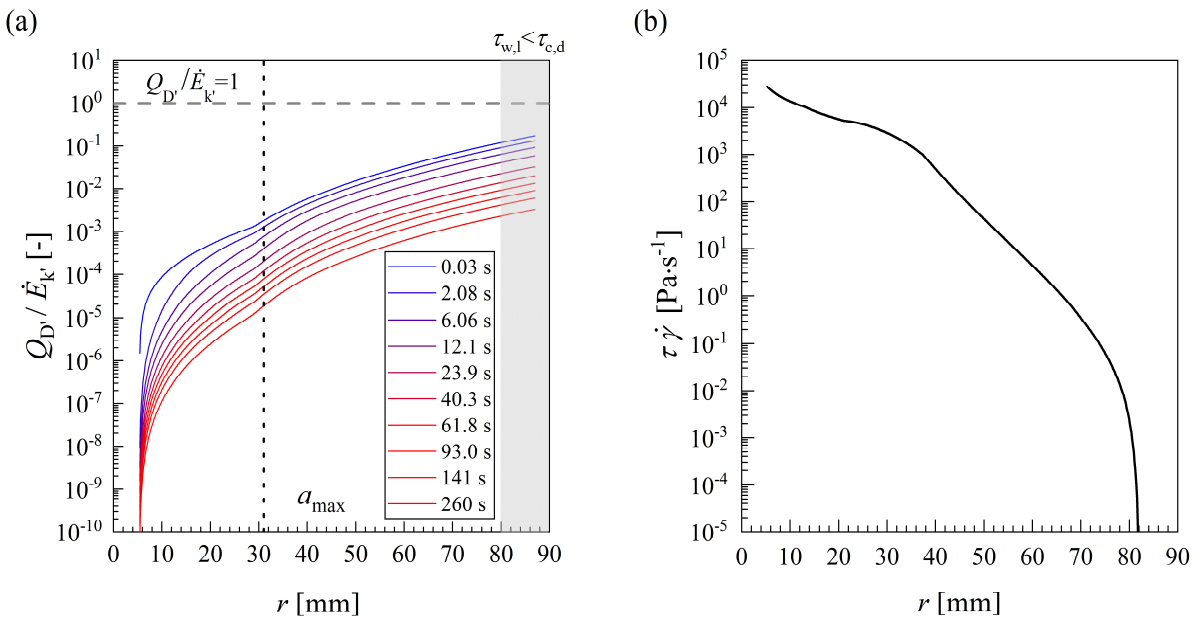

Figure 6.29 – (a) Ratio of the power consumed by viscous dissipation in the soil and the kinetic power of the liquid film at different time steps for the simulation reported in Figure 6.25. The dashed horizontal grey line indicates $Q_{D'}/\dot{E}_{k'} = 1$, dotted vertical black line shows a_{max} from the experiment reported in Figure 6.25 (c). (b) $\tau\dot{\gamma}$ as a function of r for the flow condition reported in (a).

The same analysis is now applied to the cases considered by Yeckel and Middleman (1987). They employed Newtonian soils with viscosities ranging from 0.4 to 1.4 Pa·s, which are five orders of magnitude smaller than the apparent viscosity of the unyielded PJA at shear rates below 10^{-3} s^{-1} (see Figure A.1 in the Appendix). Figure 6.30 shows the solution of their model, Eq. (6.91), for one of their experimental cases solved with the Neumann boundary condition ($\frac{\partial\delta}{\partial r} = 0$ at $r = \frac{d_N}{2}$). The Bhagat and Wilson (2016) model was used to describe the flow in the

liquid film. The profiles for δ as a function of r are qualitatively similar to those reported for the petroleum jelly, showing the displacement of the material steadily outwards. The soil is eventually flushed out of the domain as it does not have a yield stress. The values of $Q_{D'}/\dot{E}_{k'}$ are small over the whole domain at all times, so there is little impact of cleaning on the film energetics. Yeckel and Middleman (1987) did not report the evolution of the cleaned radius over time in their work, so a more thorough comparison with their results is not possible.

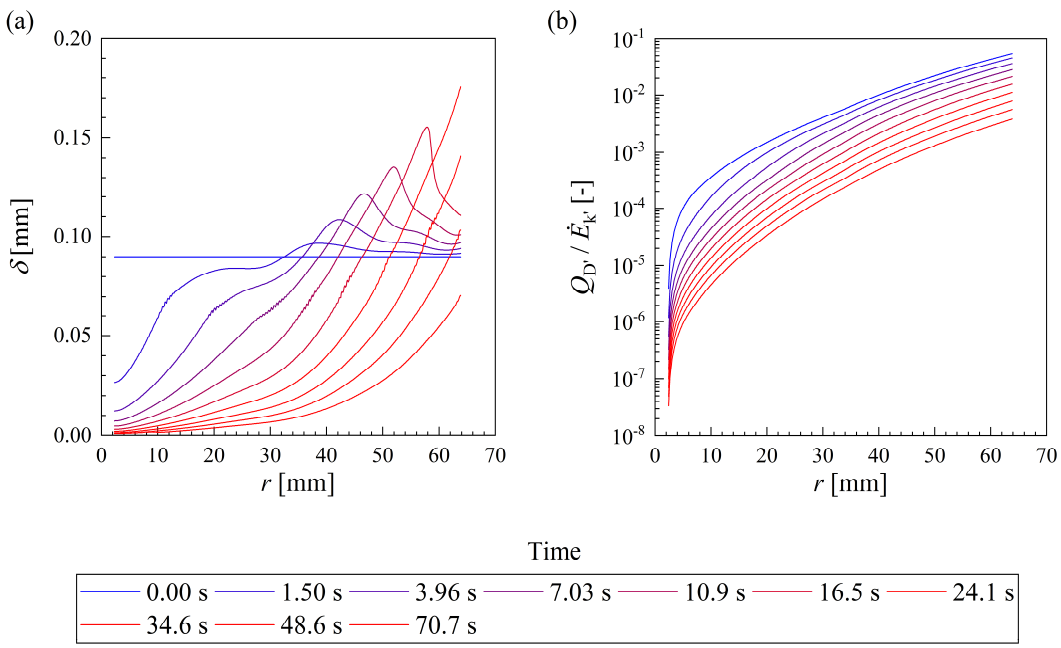

Figure 6.30 – (a) Evolution of the cleaning profiles for one of the experimental conditions reported by Yeckel and Middleman (1987): d_N=4.58 mm, Q=3.3 l·min^{-1}, δ_o=0.09 mm and μ_{so} = 0.48 Pa·s. (b) Ratio of power consumed by viscous dissipation in the soil to the kinetic power of the liquid film at different time steps for the case in (a).

The shear-driven model assumes that the soil layer material behaves as a Herschel-Bulkley fluid. It is possible to manipulate the parameters of the Herschel-Bulkley equation to ensure that the shear-driven model describes the evolution of the cleaned radius accordingly. This is shown in Figure 6.31 (a), where good agreement between the model and two cleaning experiments previously discussed is observed. The parameters of the Herschel-Bulkley equation used in the fits of the shear-driven model lead to descriptions of the shear stress as a function of the shear rate that can be compared to the rheological measurements of the layer material. These are shown in Figure 6.31 (b), where it is evident that the curves lie

between the static and the dynamic flow curves. Different values of τ_c and k_{HB} were employed in each case.

The shear-driven model was fitted to all experiments reported in Table 6.3 and in Figure 6.27, and the parameters employed in the fits are shown in Figure 6.31 (c) and (d). The values of τ_c are essentially the same as the shear stress imposed by the liquid film at the maximum cleaned radius measured in the experiments, $\tau_{w,l}\ (a_{max})$. This makes sense, as in the shear-driven model cleaning takes place only up to the radial position where $\tau_{int} = \tau_c$. It is clear that the values of τ_c employed in the shear-driven model lie between the static and dynamic critical stresses, suggesting that neither of these limiting cases is sufficient to describe the shear-driven removal of the soil. The values of k_{HB} and n_{HB} do not seem to follow any systematic trend, and they were manipulated to ensure an appropriate fit of the model to the experimental data.

The Herschel-Bulkley model assumes a simple viscoplastic behaviour, and so it does not include any contributions from creep below the critical stress or from time-dependent behaviour. Additionally, the shear-driven model does not include any contributions from the effect of the change in topography of the soil layer in the hydrodynamics of the liquid film. Therefore, the usefulness of this model as a predictive tool is limited. A more appropriate solution requires full coupling between the flows in the liquid film and in the soil layer, and a rheological formulation that includes creeping flow for $\tau < \tau_c$ and time-dependent behaviour.

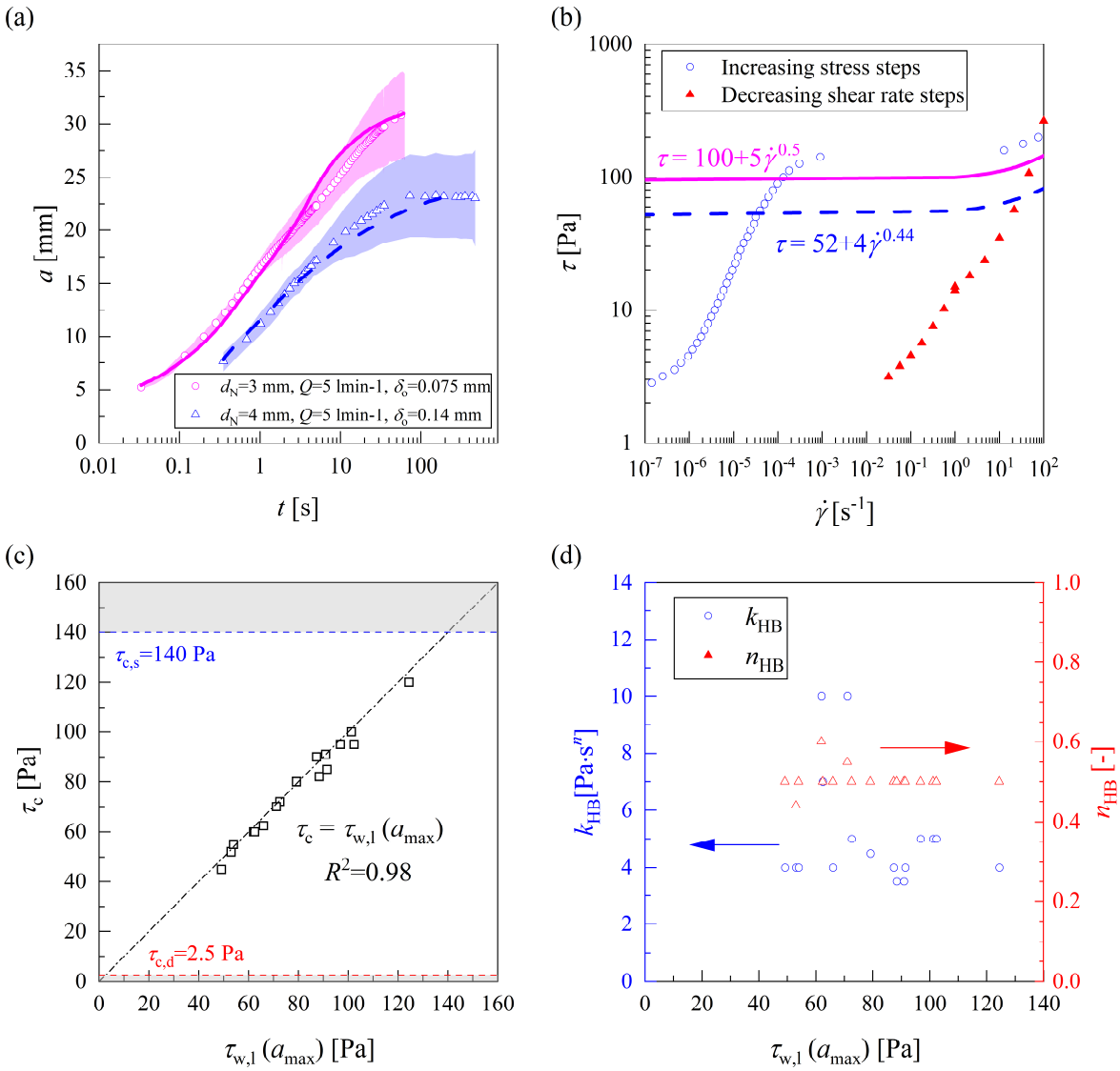

Figure 6.31 – (a) Cleaned radius of layers of the dyed PJA as a function of time for two experimental conditions, along with the solution of the shear-driven model using different combinations of τ_c, k_{HB} and n_{HB}. (b) Static and dynamic flow curves for the dyed PJA, along with the fits of the Herschel-Bulkley equation used in the solution of the shear-driven model reported in (a). Also shown are the values of (c) τ_c and (d) k_{HB} and n_{HB} as a function of $\tau_{w,l}$ at $r = a_{max}$ used in the fits of the shear-driven model to the experiments reported in Table 6.3. Colours of the fitted functions in (a) match those in (b).

6.4 Critique and considerations

In this chapter, different approaches to model the cleaning of viscoplastic soil layers have been presented. The relative thickness of the soil layer to the thickness of the liquid film affects the dynamics of the cleaning operation. A momentum-driven model was developed. It incorporates the rheology of the soil layer and yields a cleaning rate expression similar to the one proposed by Glover *et al.* (2016). Solutions for the Newtonian, power-law, Bingham and Herschel-Bulkley equations were presented. Comparison of the models with experimental data indicates that modelling the rheological behaviour of the viscoplastic soil as a Bingham fluid provides an appropriate description of the cleaning experiments.

The cleaning model based on viscous dissipation at the cleaning front is not able to predict the rate of cleaning *a priori*, as it requires two parameters, ϕ and δ_{i}, which were obtained by fitting to the experimental data. However, unlike previous treatments such as those of Glover *et al.* (2016) and the phenomenological model in Chapter 5, these tuning parameters are now expressed in terms of measurable quantities. Further work remains to be able to predict the values of ϕ and δ_{i}. This would involve identification of the shape of the cleaning front, which requires a rigorous solution of the coupled flow problem involving the liquid film and the soil layer. Modifications of this model were proposed, incorporating the dissipation along the rim and along the material accumulated downstream of the cleaning front. Neither modification enhanced the quality of the fits to the experimental data.

Finally, a shear-driven model used previously was adapted to describe the cleaning of very thin soil layers, when the liquid film flows over the soil layer. This approach did not yield an accurate description of cleaning. The model assumes that the layer is mobilised throughout the radial flow zone, whereas experiments indicated that layer relocation is limited to the cleaning front. Modelling the coupled flow is needed for both cleaning regimes: for thin soil layers, with $h \sim \delta_{\mathrm{o}}$, it is required to predict the shape of the berm. For very thin layers, $h/\delta_{\mathrm{o}} \gg 1$, coupling the liquid and soil flows is needed to work out the interaction between hydrodynamics of the liquid film and the rheology and topography of the layer. The parameters of the Herschel-Bulkley equation can be tweaked to ensure an appropriate description of the evolution of the cleaned radius. This, however, does not appear to have any physical meaning and consisted of an iterative curve-fitting exercise. Quantitative modelling of the coupling of the flows in the liquid and soil requires detailed computational solutions, which has been considered recently by Tsai (2021).

7 Conclusions

The aim of this work was to understand and model the cleaning of viscoplastic soil layers from flat surfaces using coherent impinging turbulent liquid jets. Particular attention was given to how the rheology of the soil layer affects cleaning, which had not been extensively addressed in previous studies. The rheology of different hydrophobic materials used in cleaning experiments was studied in detail using rotational rheometers. Additionally, a method to estimate the yield stress of viscoplastic soil layers *in situ,* using a scraping device instead of a rheometer, was developed and its limitations were discussed. A wide range of cleaning tests were performed, and models were proposed to describe the different cleaning scenarios observed in experiments. Specific conclusions are now discussed for each topic addressed.

7.1 Rheology of soil layer materials

In Chapter 4, experiments were performed to define the sample preparation protocols and to characterise the yielding behaviour of the materials used in the cleaning experiments. All materials showed viscoplastic and time-dependent behaviour. A protocol for preparing the samples was developed by ensuring that the soil layers were in a reproducible state based on the investigation of the ageing of the materials. The yielding regime was investigated through shear stress-controlled experiments. Significant creep below the critical stress was observed for all samples, which agrees with results available in recent literature for other viscoplastic materials (Gibaud *et al.*, 2015; Lidon *et al.*, 2017; Donley *et al.*, 2019).

Viscoplastic soil layers are notably hard to clean due to their yield stress behaviour, so a method to estimate the yield stress of viscoplastic soil layers using a blade-scraping device was developed. Measuring the yield stress of viscoplastic soils *in* situ is important, as removing the materials for analysis in a rheometer might promote structural breakdown of the fragile microstructure which is formed by local conditions at the surface. Fifteen viscoplastic materials were used in this investigation, ranging from the petroleum jellies and soft paraffin that were used in Chapters 5 and 6, to household items and food spreads. Reasonable agreement was obtained between the critical stresses measured in the soil layers and in the stress-controlled rheometer, particularly for materials with larger yield stresses.

7.2 Phenomenological model for cleaning viscoplastic soil layers

In Chapter 5, the cleaning of viscoplastic soil layers was investigated. Cleaning experiments were performed in an impinging jet apparatus, and followed the trend predicted by earlier workers (Glover *et al.*, 2016; Feldung Damkjær *et al.*, 2017; Rodgers *et al.*, 2019): a rapid, initial cleaning near the impinging point, which slows down and reaches a maximum cleaned radius far from the impinging point.

Automated image analysis from the cleaning experiments made it possible to visualize this transition. Close to the impinging point $\mathrm{d}a/\mathrm{d}t$ was proportional to M, as reported by Glover *et al.* (2016). However, when a approached $a_{\max}$ this relationship ceased to be linear, which was not captured by previous models. A phenomenological model was presented to describe the cleaning of thin layers of viscoplastic materials using impinging liquid jets. This model includes a semi-empirical term that describes the deviation from linearity between $\mathrm{d}a/\mathrm{d}t$ and M when $a \to a_{\max}$ and uses the Bhagat and Wilson (2016) model to describe the hydrodynamics of the liquid film. The model was able to describe the evolution of the cleaned radius at several experimental conditions with the PJA, and also for other materials such as the WSP and the PJS. It was incorporated into the model for cleaning by moving nozzles presented by Wilson *et al.* (2015), and shown to give a better description of cleaning than the previously available models.

Fitting the phenomenological model to viscoplastic soils with different rheologies showed that the cleaning rate parameter k' is influenced by the rheology of the soil. k' decreased with τ_{c}, but a systematic decrease of k' with the increase of μ_{c} was not observed.

7.3 Detailed modelling of the cleaning of viscoplastic soil layers

In Chapter 6, different models were developed to describe the cleaning of viscoplastic soil layers incorporating the quantitative description of their rheological behaviour. Different cleaning regimes were identified, namely thin and very thin soil layers, which can be identified from h/δ_{o} in each experiment .

The thin soil layer case occurs when the thickness of the liquid film is of similar magnitude to the thickness of the soil layer. Cleaning was assumed to follow a momentum-driven mechanism, in which the liquid film with thickness h pushes the soil layer away from the impinging point. This is a similar mechanism to the one discussed in previous cleaning

models (Wilson *et al.*, 2014; Glover *et al.*, 2016), where a lumped cleaning rate constant k' had been found by fitting the model to the $\mathrm{d}a/\mathrm{d}t$ vs M data. Although a quantitative estimation of M_y had been proposed by *Glover et al*. (2016) by making a force balance in the horizontal direction at the maximum cleaned radius, k' remained an experimentally fitted rate constant prior to this thesis.

An argument based on the viscous dissipation at the cleaning front was proposed to explain the factors that influence k'. Dissipation was assumed to be limited to the region of the cleaning front where $\delta \leq h$. This allowed incorporating different constitutive equations to describe the viscous dissipation, and expressions that related $\mathrm{d}a/\mathrm{d}t$ to M were obtained for soil layers described by the Newtonian, power-law, Bingham and Herschel-Bulkley models. These expressions provided a framework to describe the parameter k' in terms of measurable quantities, namely the angle of the cleaning front, the thickness of the residual layer left in the substrate and the plastic viscosity in the post-yielding regime. Experimental results were compared to the Bingham model for cleaning layers of three viscoplastic materials and shown to give an appropriate description of the evolution of the cleaned radius. Extensions to this model were also proposed, including dissipation where $\delta > h$ and in the material accumulated at the rim, but these did not provide good descriptions of the experiments.

Experiments reported in Chapter 5 revealed that k' decreases with the increase of τ_c, but this behaviour is not predicted by the model. The model does not describe the decrease in k' with the increase of τ_c because the angle ϕ is assumed to be constant throughout cleaning. Description of the transient morphology of the rim requires solution of the coupled flow between the liquid film and the soil layer.

The very thin soil layer case occurs when the soil layer is thinner than the liquid film, such that the liquid flows over the soil layer. A model describing the cleaning of very thin soil layers was developed by assuming that cleaning in these cases is a result of a shear-driven mechanism, where the soil layer is relocated as a result of the shear stress of the liquid film that flows above it. This is an extension of the model proposed for cleaning very thin Newtonian soils proposed by Yeckel and Middleman (1987). It yielded a partial differential equation that describes the thickness of the residual layer over time for a Herschel-Bulkley soil.

The model did not agree well with the experimental data since key features of the experiments (a fast cleaning rate at short times followed by an asymptotic slow cleaning at longer times) were not predicted. A simple yield stress fluid description, such as the Herschel-Bulkley equation, was not sufficient to describe the cleaning of a time-dependent soil such as the hydrophobic jellies used. Describing the cleaning of a simple (non-thixotropic) yield stress material was attempted with the shear-driven model, but without success. An energetic analysis was also performed and showed that the power consumed by viscous dissipation of the soil is small when compared to the kinetic power of the liquid film. The shear-driven model was able to describe the evolution of the cleaned data when the parameters of the Herschel-Bulkley equation were chosen to lie between the static and the dynamic flow curves. However, this consisted of a curve-fitting exercise and so the usefulness of this model as a predictive tool is limited.

7.4 Recommendations for future work

7.4.1 Evaluation of more realistic cleaning scenarios

Some assumptions were made in the models presented in this thesis. For instance, it was assumed in Chapter 6 that the shape of the cleaning front remains the same throughout the cleaning process. As shown in Chapter 5, the angle of the front changes slightly during cleaning, and this should be incorporated in the detailed cleaning model. Additionally, incorporating the effect of creep such as done in the phenomenological model from Chapter 5 in the detailed model for cleaning thin layers discussed in Chapter 6 appears to be a feasible challenge.

Truly predictive models were not developed since these require the solution of the coupling of the flows in the liquid film and in the soil layer, in both the thin and very thin soil regimes. Lu *et al.* (2020) recently reported a study on cleaning submerged Newtonian layers using computational fluid dynamics (CFD). This suggests that numerical solutions can be useful to ensure the coupling of the liquid film, the material rheology and the air-liquid interface to obtain predictive results for cleaning based on the rheology of the soil layer.

This work considered cleaning by coherent water jets impinging normally on the surface. Investigating more complicated hydrodynamic conditions, such as inclined and non-coherent jets, is needed for many industrial applications. Significant advances in cleaning by non-

coherent jets have recently been reported (Feldung Damkjær *et al.*, 2017; Chee *et al.*, 2018; Yang *et al.*, 2019b; Chee & Wilson, 2021). However, only empirical studies have been reported so far for cleaning with sprays (Burfoot & Middleton, 2009; Rodgers *et al.*, 2019), and so modelling these processes represents a logical next step.

Another area that can be explored is the cleaning of soils that interact with the cleaning solution. Recent studies have reported experimental observations (Rodgers *et al.*, 2019) and a phenomenological model (Yang *et al.*, 2019a) to describe the cleaning of reactive soils. A detailed model that considers the changes in the properties of reactive soils following contact with the cleaning solution has not been proposed yet.

7.4.2 Cleaning of thick soil layers

When a liquid jet first hits a soiled surface, the jet penetrates the soil layer and when it reaches the substrate it starts to clean the material within the radial flow zone. The current models available in the literature consider cleaning in the RFZ, but the penetration of liquid jets in thick soil layers of different rheologies is an interesting (and so far largely unexplored) field of research. Some phenomenological results were presented by Uth and Deshpande (2013), but there is still little understanding in this area. Fluid-structure interactions seem to be responsible for different regimes in the jet penetration (Uth & Deshpande, 2013; Semenov & Wu, 2016), and the rheology of the soils is expected to play a significant role in this phenomenon.

The cleaning of thick soil layers has been studied experimentally by Tuck *et al.* (2020). So far, no argument has been presented to explain the different mechanisms involved, which range from the formation of blisters for the Carbopol® layers reported by Tuck *et al.* (2020) to cratering for the greases investigated by Uth and Deshpande (2013).

7.4.3 Cleaning of layers with different rheologies

The cleaning of soils with other rheological behaviours has not been explored in much depth. The impact of liquid jets on surfaces coated with shear-thinning and viscoelastic fluids were experimentally studied by Fuller and co-workers (Walker *et al.*, 2012; Hsu *et al.*, 2014), but these remain as the only studies to my knowledge that attempted to investigate this. Analytical models for these flows have not been developed.

References

Aguilar-Zárate, M., Macias-Rodriguez, B. A., Toro-Vazquez, J. F., & Marangoni, A. G. (2019). Engineering rheological properties of edible oleogels with ethylcellulose and lecithin. *Carbohydr. Polym.*, **205**, 98–105.

Ahuja, A., Lu, J., & Potanin, A. (2019). Rheological predictions of sensory attributes of lotions. *J. Texture Stud.*, **50** (4), 295–305.

Ahuja, A., Luisi, G., & Potanin, A. (2018). Rheological measurements for prediction of pumping and squeezing pressures of toothpaste. *J. Non-Newton. Fluid Mech.*, **258**, 1–9.

Ahuja, A., & Potanin, A. (2018). Rheological and sensory properties of toothpastes. *Rheol. Acta*, **57** (6–7), 459–471.

Akono, A. T., Reis, P. M., & Ulm, F. J. (2011). Scratching as a fracture process: From butter to steel. *Phys. Rev. Lett.*, **106** (20), 2–5.

Alba, K., & Frigaard, I. A. (2016). Dynamics of the removal of viscoplastic fluids from inclined pipes. *J. Non-Newton. Fluid Mech.*, **229**, 43–58.

Ali, A., De'Ath, D., Gibson, D., Parkin, J., Alam, Z., Ward, G., & Wilson, D. I. (2015). Development of a 'millimanipulation' device to study the removal of soft solid fouling layers from solid substrates and its application to cooked lard deposits. *Food Bioprod. Process.*, **93**, 256–268.

Andrade, D. E. V., & Coussot, P. (2019). Brittle solid collapse to simple liquid for a waxy suspension. *Soft Matter*, **15** (43), 8766–8777.

Andrade, D. E. V., & Coussot, P. (2020). Thermal fatigue and collapse of waxy suspensions. *Rheol. Acta*, **59** (5), 279–289.

Aouad, W., Landel, J. R., Dalziel, S. B., Davidson, J. F., & Wilson, D. I. (2016). Particle image velocimetry and modelling of horizontal coherent liquid jets impinging on and draining down a vertical wall. *Exp. Therm. Fluid Sci.*, **74**, 429–443.

Ardakani, H. A., Mitsoulis, E., & Hatzikiriakos, S. G. (2011). Thixotropic flow of toothpaste through extrusion dies. *J. Non-Newton. Fluid Mech.*, **166** (21–22), 1262–1271.

Ashokkumar, S., & Adler-Nissen, J. (2011). Evaluating non-stick properties of different surface materials for contact frying. *J. Food Eng.*, **105** (3), 537–544.

Astarita, G. (1990). Letter to the Editor: The engineering reality of the yield stress. *J. Rheol.*, **34** (2), 275–277.

Azuma, T., & Hoshino, T. (1984). The Radial Flow of a Thin Liquid Film : 1st Report, Laminar-Turbulent Transition. *Bull. JSME*, **27** (234), 2739–2746.

Ballauff, M., Brader, J. M., Egelhaaf, S. U., Fuchs, M., Horbach, J., Koumakis, N., Krüger, M., Laurati, M., Mutch, K. J., Petekidis, G., Siebenbürger, M., Voigtmann, T., & Zausch, J. (2013). Residual stresses in glasses. *Phys. Rev. Lett.*, **110** (21), 1–5.

Balmforth, N. J., Frigaard, I. A., & Ovarlez, G. (2014). Yielding to Stress: Recent Developments in Viscoplastic Fluid Mechanics. *Annu. Rev. Fluid Mech.*, **46** (1), 121–146.

Barnes, H. A. (1997). Thixotropy - a review. *J. Non-Newton. Fluid Mech.*, **70** (97), 1–33.

Barnes, H. A. (1999a). A brief history of the yield stress. *Appl. Rheol.*, **9** (6), 262–266.

Barnes, H. A. (1999b). The yield stress—a review or ‘παντα ρει’—everything flows? *J. Non-Newton. Fluid Mech.*, **81** (1–2), 133–178.

Barnes, H. A. A., & Nguyen, Q. D. D. (2001). Rotating vane rheometry - a review. *J. Non-Newton. Fluid Mech.*, **98** (1), 1–14.

Barnes, H. A., Hutton, J. F., & Walters, K. (1989). *An Introduction to Rheology*, 1 edn, Amsterdam: Elsevier.

Barnes, H. A., & Walters, K. (1985). The yield stress myth? *Rheol. Acta*, **24** (4), 323–326.

Basso, M., Simonato, M., Furlanetto, R., & De Nardo, L. (2017). Study of chemical environments for washing and descaling of food processing appliances: An insight in commercial cleaning products. *J. Ind. Eng. Chem.*, **53**, 23–36.

Bekkour, K., Leyama, M., Benchabane, A., & Scrivener, O. (2005). Time-dependent rheological behavior of bentonite suspensions: An experimental study. *J. Rheol.*, **49** (6), 1329–1345.

Belblidia, F., Tamaddon-Jahromi, H. R., Webster, M. F., & Walters, K. (2011). Computations with viscoplastic and viscoelastoplastic fluids. *Rheol. Acta*, **50** (4), 343–360.

Ben Azouz, K., Bekkour, K., & Dupuis, D. (2016). Influence of the temperature on the rheological properties of bentonite suspensions in aqueous polymer solutions. *Appl. Clay Sci.*, **123**, 92–98.

Bergman, T. L., Lavine, A. S., Incropera, F. P., & Dewitt, D. P. (2011). *Fundamentals of heat and mass transfer*, 7th edn, Hoboken: John Wiley & Sons.

Bertola, V., Bertrand, F., Tabuteau, H., Bonn, D., & Coussot, P. (2003). Wall slip and yielding in pasty materials. *J. Rheol.*, **47** (5), 1211.

Bhagat, R. K., Jha, N. K., Linden, P. F., & Wilson, D. I. (2018). On the origin of the circular hydraulic jump in a thin liquid film. *J. Fluid Mech.*, **851**, R5.

Bhagat, R. K., Perera, A. M., & Wilson, D. I. (2017). Cleaning vessel walls by moving water jets: Simple models and supporting experiments. *Food Bioprod. Process.*, **102**, 31–54.

Bhagat, R. K., & Wilson, D. I. (2016). Flow in the thin film created by a coherent turbulent water jet impinging on a vertical wall. *Chem. Eng. Sci.*, **152**, 606–623.

Bingham, E. C. (1922). *Fluidity and plasticity*, 1 edn, New York: McGraw-Hill New York.

Bird, R. B., Armstrong, R. C., & Hassager, O. (1987). *Dynamics of Polymeric Liquids, Volume 1: Fluid mechanics*, 2 edn, New York: John Wiley & Sons.

Bonacci, F., Chateau, X., Furst, E. M., Fusier, J., Goyon, J., & Lemaître, A. (2020). Contact and macroscopic ageing in colloidal suspensions. *Nat. Mater.*, **19** (7), 775–780.

Bonn, D., & Denn, M. M. (2009). Yield Stress Fluids Slowly Yield to Analysis. *Science (80-.).*, **324** (5933), 1401–1402.

Bonn, D., Denn, M. M., Berthier, L., Divoux, T., & Manneville, S. (2017). Yield stress materials in soft condensed matter. *Rev. Mod. Phys.*, **89** (3), 035005, Soft Condensed Matter.

Bonn, D., Kellay, H., Tanaka, H., Wegdam, G., & Meunier, J. (1999). Laponite: what is the difference between a gel and a glass? *Langmuir*, **15** (14), 7534–7536.

Boujlel, J., & Coussot, P. (2012). Measuring yield stress: a new, practical, and precise technique derived from detailed penetrometry analysis. *Rheol. Acta*, **51** (10), 867–882.

Bourne, M. C., & Jennings, W. G. (1963a). Kinetic studies of detergency. I. Analysis of cleaning curves. *J. Am. Oil Chem. Soc.*, **40** (10), 517–523.

Bourne, M. C., & Jennings, W. G. (1963b). Kinetic studies of detergency. II. Effect of age, temperature, and cleaning time on rates of soil removal. *J. Am. Oil Chem. Soc.*, **40** (10), 523–530.

Brechet, Y., & Néda, Z. (1999). On the circular hydraulic jump. *Am. J. Phys.*, **67** (8), 723–731.

Breidinger, S. L., & Steffe, J. F. (2001). Texture map of cream cheese. *J. Food Sci.*, **66** (3), 453–456.

Briscoe, B. J., Pickles, M. J., Julian, K. S., & Adams, M. J. (1995). Erosion of surface coatings in hydrodynamic flows. *Wear*, **181–183** (PART 2), 759–765.

Briscoe, B. J., Pickles, M. J., Julian, K. S., & Adams, M. J. (1997). Erosion of polymer-particle composite coatings by liquid water jets. *Wear*, **203–204**, 88–97.

Burfoot, D., & Middleton, K. (2009). Effects of operating conditions of high pressure washing on the removal of biofilms from stainless steel surfaces. *J. Food Eng.*, **90** (3), 350–357.

Bush, J. W. M., Aristoff, J., & Hosoi, A. E. (2006). An experimental investigation of the stability of the circular hydraulic jump. *J. Fluid Mech.*, **558**, 33.

Bush, J. W. M., & Aristoff, J. M. (2003). The influence of surface tension on the circular hydraulic jump. *J. Fluid Mech.*, **489**, 229–238.

Carotenuto, C., & Minale, M. (2013). On the use of rough geometries in rheometry. *J. Non-Newton. Fluid Mech.*, **198**, 39–47.

Chang, C., Boger, D. V, & Nguyen, Q. D. (1998). The yielding of waxy crude oils. *Ind. Eng. Chem. Res.*, **37** (4), 1551–1559.

Chee, M. W. L., Ahuja, T. V., Bhagat, R. K., Taesopapong, N., Wan, S. A., Wigmore, R. L., & Wilson, D. I. (2018). Impinging jet cleaning of tank walls: effect of jet length, wall

curvature and related phenomena. *Food Bioprod. Process.*, 1–12.

Chee, M. W. L., & Wilson, D. I. (2021). Cleaning viscous soil layers off walls by intermittent impinging jets. *J. Clean. Prod.*, **283**, 124660.

Cheng, D. C.-H. (1986). Yield stress: A time-dependent property and how to measure it. *Rheol. Acta*, **25** (5), 542–554.

Chew, J. Y. M., Cardoso, S. S. S., Paterson, W. R., & Wilson, D. I. (2004a). CFD studies of dynamic gauging. *Chem. Eng. Sci.*, **59** (16), 3381–3398.

Chew, J. Y. M., Paterson, W. R., & Wilson, D. I. (2004b). Fluid dynamic gauging for measuring the strength of soft deposits. *J. Food Eng.*, **65** (2), 175–187.

Chilukuri, R., & Middleman, S. (1984). Cleaning of a Rough Rigid Surface: Removal of a Dissolved Contaminant by Convection-Enhanced Diffusion and Chemical Reaction. *J. Electrochem. Soc.*, **131** (5), 1169–1173.

Chin, D.-T., & Tsang, G.-H. (1978). Mass Transfer to an Impinging Jet Electrode. *J. Electrochem. Soc.*, **125** (9), 1461.

Choi, J., & Rogers, S. A. (2020). Optimal conditions for pre-shearing thixotropic or aging soft materials. *Rheol. Acta*, **59** (12), 921–934.

Citerne, G. P., Carreau, P. J., & Moan, M. (2001). Rheological properties of peanut butter. *Rheol. Acta*, **40** (1), 86–96.

Cloitre, M., & Bonnecaze, R. T. (2017). A review on wall slip in high solid dispersions. *Rheol. Acta*, **56** (3), 283–305.

Cloitre, M., Borrega, R., & Leibler, L. (2000). Rheological Aging and Rejuvenation in Microgel Pastes. *Phys. Rev. Lett.*, **85** (22), 4819–4822.

Cohen-Addad, S., & Höhler, R. (2014). Rheology of foams and highly concentrated emulsions. *Curr. Opin. Colloid Interface Sci.*, **19** (6), 536–548.

Coussot, P. (2014). Yield stress fluid flows: A review of experimental data. *J. Non-Newton. Fluid Mech.*, **211**, 31–49.

Coussot, P. (2017). Bingham's heritage. *Rheol. Acta*, **56** (3), 163–176.

Coussot, P. (2018). Slow flows of yield stress fluids: yielding liquids or flowing solids? *Rheol. Acta*, **57** (1), 1–14.

Coussot, P., & Gaulard, F. (2005). Gravity flow instability of viscoplastic materials: The ketchup drip. *Phys. Rev. E*, **72** (3), 1–5.

Coussot, P., Nguyen, Q. D., Huynh, H. T., & Bonn, D. (2002a). Avalanche behavior in yield stress fluids. *Phys. Rev. Lett.*, **88**, 175501.

Coussot, P., Nguyen, Q. D., Huynh, H. T., & Bonn, D. (2002b). Viscosity bifurcation in thixotropic, yielding fluids. *J. Rheol.*, **46** (3), 573–589.

Coussot, P., Tabuteau, H., Chateau, X., Tocquer, L., & Ovarlez, G. (2006). Aging and solid or liquid behavior in pastes. *J. Rheol.*, **50** (6), 975–994.

Cuckston, G. L., Alam, Z., Goodwin, J., Ward, G., & Wilson, D. I. (2019). Quantifying the effect of solution formulation on the removal of soft solid food deposits from stainless steel substrates. *J. Food Eng.*, **243**, 22–32.

Czibulya, Z., Tombácz, E., Szegi, T., Michéli, E., & Zsolnay, A. (2010). Standard state of soil dispersions for rheological measurements. *Appl. Clay Sci.*, **48** (4), 594–601.

Da Cruz, F., Chevoir, F., Bonn, D., & Coussot, P. (2002). Viscosity bifurcation in granular materials, foams, and emulsions. *Phys. Rev. E*, **66** (5), 051305.

Daubert, C. R., Tkachuk, J. A., & Truong, V. D. (1998). Quantitative measurement of food spreadability using the vane method. *J. Texture Stud.*, **29** (4), 427–435.

de Cagny, H., Fazilati, M., Habibi, M., Denn, M. M., Bonn, D., Denn, M. M., & Habibi, M. (2019). The yield normal stress. *J. Rheol.*, **63** (2), 285–290.

De Gennes, P. G. (1985). Wetting: Statics and dynamics. *Rev. Mod. Phys.*, **57** (3), 827–863.

Denn, M. M., & Bonn, D. (2011). Issues in the flow of yield-stress liquids. *Rheol. Acta*, **50** (4), 307–315.

Derec, C., Ajdari, A., Ducouret, G., & Lequeux, F. (2000). Rheological characterization of

aging in a concentrated colloidal suspension. *Comptes Rendus l'Académie Des Sci. - Ser. IV - Phys.*, **1** (8), 1115–1119.

Deshpande, A. P., Krishnan, J. M., & Sunial Kumar, P. B. (2010). *Rheology of Complex Fluids*, New York: Springer.

Dimitriou, C. J., Ewoldt, R. H., & McKinley, G. H. (2013). Describing and prescribing the constitutive response of yield stress fluids using large amplitude oscillatory shear stress (LAOStress). *J. Rheol.*, **57** (1), 27.

Dimitriou, C. J., & McKinley, G. H. (2014). A comprehensive constitutive law for waxy crude oil: a thixotropic yield stress fluid. *Soft Matter*, **10** (35), 6619–44.

Dimitriou, C. J., McKinley, G. H., & Venkatesan, R. (2011). Rheo-PIV Analysis of the Yielding and Flow of Model Waxy Crude Oils. *Energy & Fuels*, **25** (7), 3040–3052.

Dimonte, G., Nelson, D., Weaver, S., Schneider, M., Flower-Maudlin, E., Gore, R., Baumgardner, J. R., & Sahota, M. S. (1998). Comparative study of viscoelastic properties using virgin yogurt. *J. Rheol.*, **42** (4), 727–742.

Dinkgreve, M., Bonn, D., & Denn, M. M. (2017). "Everything flows?" Elastic effects on start-up flows of yield stress fluids. *Rheol. Acta*, **56** (3), 189–194.

Dinkgreve, M., Fazilati, M., Denn, M. M., & Bonn, D. (2018). Carbopol: From a simple to a thixotropic yield stress fluid. *J. Rheol.*, **62** (3), 773–780.

Dinkgreve, M., Paredes, J., Denn, M. M., & Bonn, D. (2016). On different ways of measuring "the" yield stress. *J. Non-Newton. Fluid Mech.*, **238**, 233–241.

Donley, G. J., de Bruyn, J. R., McKinley, G. H., & Rogers, S. A. (2019). Time-resolved dynamics of the yielding transition in soft materials. *J. Non-Newton. Fluid Mech.*, **264**, 117–134.

Donley, G. J., Singh, P. K., Shetty, A., & Rogers, S. A. (2020). Elucidating the G″ overshoot in soft materials with a yield transition via a time-resolved experimental strain decomposition. *Proc. Natl. Acad. Sci.*, **117** (36), 21945–21952.

Dragolici, C., & Dragolici, F. (2014). Introduction in means and methods used in chemical,

biological, Radiological, and nuclear decontamination. *Rom. J. Phys.*, **59** (9–10), 920–929.

Duarte, J. C., Schellart, W. P., & Cruden, A. R. (2014). Rheology of petrolatum–paraffin oil mixtures: Applications to analogue modelling of geological processes. *J. Struct. Geol.*, **63**, 1–11.

Duchesne, A., Andersen, A., & Bohr, T. (2019). Surface tension and the origin of the circular hydraulic jump in a thin liquid film. *Phys. Rev. Fluids*, **4** (8), 084001 1–7.

Duisterwinkel, A. (2010). Water - a most powerful detergent? *Eur. Clean. J.*, 1.

Dumouchel, C. (2008). On the experimental investigation on primary atomization of liquid streams. *Exp. Fluids*, **45** (3), 371–422.

Dzuy, N. Q., & Boger, D. V. (1985). Direct Yield Stress Measurement with the Vane Method. *J. Rheol.*, **29** (3), 335–347.

Energy saving trust. (2014). *At home with water. Analysis from the Energy Saving Trust's water energy calculator*, London.

Evans, I. D. (1992). Letter to the editor: On the nature of the yield stress. *J. Rheol.*, **36** (7), 1313.

Ewoldt, R. H., & McKinley, G. H. (2017). Mapping thixo-elasto-visco-plastic behavior. *Rheol. Acta*, **56** (3), 195–210.

Ewoldt, R. H., Winter, P., Maxey, J., & McKinley, G. H. (2010). Large amplitude oscillatory shear of pseudoplastic and elastoviscoplastic materials. *Rheol. Acta*, **49** (2), 191–212.

F-16.net. (2020). US Air Force - AFMC F-16s. Retrieved November 23, 2020, from <http://www.f-16.net/g3/f-16-photos/album38/album66/831172>

Fang, L. C. (2003). Effect of mixed convection on transient hydrodynamic removal of a contaminant from a cavity. *Int. J. Heat Mass Transf.*, **46** (11), 2039–2049.

Feldung Damkjær, N., Adler-Nissen, J., Jensen, B. B. B., & Wilson, D. I. (2017). Flow pattern and cleaning performance of a stationary liquid jet operating at conditions relevant for industrial tank cleaning. *Food Bioprod. Process.*, **101**, 145–156.

Fernandes, R. R., Andrade, D. E. V., Franco, A. T., & Negrão, C. O. R. (2016). Correlation between the gel–liquid transition stress and the storage modulus of an oil-based drilling fluid. *J. Non-Newton. Fluid Mech.*, **231**, 6–10.

Fernandes, R. R., Andrade, D. E. V., Franco, A. T., & Negrão, C. O. R. (2017a). The yielding and the linear-to-nonlinear viscoelastic transition of an elastoviscoplastic material. *J. Rheol.*, **61** (5), 893–903.

Fernandes, R. R., Andrade, D. E. V., Franco, A. T., & Negrão, C. O. R. (2017b). Influence of pre-shearing on rheometric measurements of an oil-based drilling fluid. *Rheol. Acta*, **56** (9), 743–752.

Fernandes, R. R., Oevermann, D., & Wilson, D. I. (2019). Cleaning insoluble viscoplastic soil layers using static and moving coherent impinging water jets. *Chem. Eng. Sci.*, **207**, 752–768.

Fernandes, R. R., & Wilson, D. I. (2020). Modelling the cleaning of viscoplastic layers by impinging coherent turbulent water jets. *J. Non-Newton. Fluid Mech.*, **282**, 104314.

Fernandez-Feria, R., Sanmiguel-Rojas, E., & Benilov, E. S. (2019). On the origin and structure of a stationary circular hydraulic jump. *Phys. Fluids*, **31** (7), 072104.

Ferry, J. D. (1980). *Viscoelastic properties of polymers*, 3 Edn, New York: John Wiley & Sons.

Fickak, A., Al-Raisi, A., & Chen, X. D. (2011). Effect of whey protein concentration on the fouling and cleaning of a heat transfer surface. *J. Food Eng.*, **104** (3), 323–331.

Fitzgerald, A. M., Barnes, O. J., Smart, I., & Wilson, D. I. (2001). Measurement of particle size distribution of tripalmitin crystals in a model solution using a laser diffraction method. *JAOCS, J. Am. Oil Chem. Soc.*, **78** (10), 1013–1020.

Fox, R. W., McDonald, A. T., & Pritchard, P. J. (2011). *Introduction to fluid mechanics*, 8th edn, Hoboken: John Wiley & Sons.

Fryer, P. J., & Asteriadou, K. (2009). A prototype cleaning map: A classification of industrial cleaning processes. *Trends Food Sci. Technol.*, **20** (6–7), 255–262.

Fryer, P. J., Christian, G. K., & Liu, W. (2006). How hygiene happens: Physics and chemistry of cleaning. *Int. J. Dairy Technol.*, **59** (2), 76–84.

Fuchs, E., Boye, A., Murcek, R., & Majschak, J.-P. (2015). An experimental comparison of film flow parameters and cleaning behaviour of falling liquid films for different tilt angles. *Food Bioprod. Process.*, **93** (October), 318–326.

Fuchs, E., Köhler, H., & Majschak, J.-P. (2019a). Measurement of the Impact Force and Pressure of Water Jets under the Influence of Jet Break-up. *Chemie Ing. Tech.*, (4), 1–13.

Fuchs, E., Kricke, S., Schöhl, E., & Majschak, J. P. (2019b). Effect of industrial scale stand-off distance on water jet break-up, cleaning and forces imposed on soil layers. *Food Bioprod. Process.*, **113**, 129–141.

Geri, M., Venkatesan, R., Sambath, K., & McKinley, G. H. (2017). Thermokinematic memory and the thixotropic elasto-viscoplasticity of waxy crude oils. *J. Rheol.*, **61** (3), 427–454.

Gibaud, T., Frelat, D., & Manneville, S. (2010). Heterogeneous yielding dynamics in a colloidal gel. *Soft Matter*, **6** (15), 3482–3488.

Gibaud, T., Perge, C., Lindstrom, S. B., Taberlet, N., & Manneville, S. (2015). Multiple yielding processes in a colloidal gel under large amplitude oscillatory stress, (AUGUST). Retrieved from http://arxiv.org/abs/1508.05772

Globo News. (2020). Contra coronavírus, Exército faz limpeza de área externa de hospitais públicos do DF. Retrieved November 23, 2020, from <https://g1.globo.com/df/distrito-federal/noticia/2020/03/31/contra-coronavirus-exercito-faz-desinfeccao-de-area-externa-de-hospitais-publicos-do-df.ghtml>

Glover, H. W., Brass, T., Bhagat, R. K., Davidson, J. F., Pratt, L., & Wilson, D. I. (2016). Cleaning of complex soil layers on vertical walls by fixed and moving impinging liquid jets. *J. Food Eng.*, **178**, 95–109.

Goode, K. R., Asteriadou, K., Robbins, P. T., & Fryer, P. J. (2013). Fouling and Cleaning Studies in the Food and Beverage Industry Classified by Cleaning Type. *Compr. Rev. Food Sci. Food Saf.*, **12** (2), 121–143.

Gould, P. (2003). Smart, clean surfaces. *Mater. Today*, **6** (11), 44–48.

Grower, M. F., & Bhaskar, S. N. (1972). Effect of Pulsating Water Jet Lavage on Radioactive Contaminated Wounds. *J. Dent. Res.*, **51** (2), 536–538.

Habibi, M., Dinkgreve, M., Paredes, J., Bonn, D., & Denn, M. M. (2016). Normal stress measurement in foams and emulsions in the presence of slip. *J. Non-Newton. Fluid Mech.*, **238**, 33–43.

Hammelmann. (2020). Typical applications in cleaning technology: Retrieved November 23, 2020, from <https://www.hammelmann.com/en/industries/chemical-industry.php>

Hartnett, J. P., & Hu, R. Y. Z. (1989). Technical note: The yield stress—An engineering reality. *J. Rheol.*, **33** (4), 671.

Herrera-Márquez, O., Serrano-Haro, M., Vicaria, J. M., Jurado, E., Fraatz-Leál, A. R., Zhang, Z. J., Fryer, P. J., & Avila-Sierra, A. (2020). Cleaning maps: A multi length-scale strategy to approach the cleaning of complex food deposits. *J. Clean. Prod.*, **261**, 121254.

Herschel, W. H., & Bulkley, R. (1926). Measurement of consistency as applied to rubber-benzene solutions. In *ASTM Proceeding*, Vol. 26, pp. 621–633.

Hou, L. (2012). Experimental study on yield behavior of Daqing crude oil. *Rheol. Acta*, **51**, 603–607.

Hsu, T. T., Walker, T. W., Frank, C. W., & Fuller, G. G. (2011). Role of fluid elasticity on the dynamics of rinsing flow by an impinging jet. *Phys. Fluids*, **23** (3), 033101.

Hsu, T. T., Walker, T. W., Frank, C. W., & Fuller, G. G. (2014). Instabilities and elastic recoil of the two-fluid circular hydraulic jump. *Exp. Fluids*, **55** (1), 1645.

Hui, Y. H., Bruinsma, L. B., Gorham, J. R., Nip, W.-K., Tong, P. S., & Ventresca, P. (2003). *Food Plant Sanitation*. (Y. H. Hui, L. B. Bruinsma, J. R. Gorham, W.-K. Nip, P. S. Tong, & P. Ventresca, Eds.), 1 edn, New York: Marcel Dekker.

Husband, D. M., Aksel, N., & Gleissle, W. (1993). The existence of static yield stresses in suspensions containing noncolloidal particles. *J. Rheol.*, **37** (2), 215–235.

Hyun, K., Wilhelm, M., Klein, C. O., Cho, K. S., Nam, J. G., Ahn, K. H., Lee, S. J., Ewoldt,

R. H., & McKinley, G. H. (2011). A review of nonlinear oscillatory shear tests: Analysis and application of large amplitude oscillatory shear (LAOS). *Prog. Polym. Sci.*, **36** (12), 1697–1753.

IChemE. (2014). *Water management in the food and drink industry*. *IChemE green paper*, London.

James, D. F. (2009). Boger Fluids. *Annu. Rev. Fluid Mech.*, **41** (1), 129–142.

Joppa, M., Köhler, H., Kricke, S., Majschak, J. P., Fröhlich, J., & Rüdiger, F. (2019). Simulation of jet cleaning: Diffusion model for swellable soils. *Food Bioprod. Process.*, **113** (1993), 168–176.

Joppa, M., Köhler, H., Rüdiger, F., Majschak, J.-P., & Fröhlich, J. (2020). Prediction of Cleaning by Means of Computational Fluid Dynamics: Implication of the Pre-wetting of a Swellable Soil. *Heat Transf. Eng.*, **41** (2), 178–188.

Joppa, M., Köhler, H., Rüdiger, F., Majschak, J. P., & Fröhlich, J. (2017). Experiments and Simulations on the Cleaning of a Swellable Soil in Plane Channel Flow. *Heat Transf. Eng.*, **38** (7–8), 786–795.

Joyner (Melito), H. S. (2018). Explaining food texture through rheology. *Curr. Opin. Food Sci.*, **21**, 7–14.

Kaye, P. L., Pickles, C. S. J., Field, J. E., & Julian, K. S. (1995). Investigation of erosion processes as cleaning mechanisms in the removal of thin deposited soils. *Wear*, **186–187** (PART 2), 413–420.

Keentok, M. (1982). The measurement of the yield stress of liquids. *Rheol. Acta*, **21** (3), 325–332.

Kelessidis, V. C., Hatzistamou, V., & Maglione, R. (2010). Wall slip phenomenon assessment of yield stress pseudoplastic fluids in Couette geometry. *Appl. Rheol*, **20**, 52656.

Kugge, C., Vanderhoek, N., & Bousfield, D. W. (2011). Oscillatory shear response of moisture barrier coatings containing clay of different shape factor. *J. Colloid Interface Sci.*, **358** (1), 25–31.

Kuyumcu, H. Z., & Rolf, L. (2004). Application of high-pressure waterjets for comminution. *Int. J. Miner. Process.*, **74S**, S191–S198.

Kwak, M. S., Ahn, H. J., & Song, K. W. (2015). Rheological investigation of body cream and body lotion in actual application conditions. *Korea Aust. Rheol. J.*, **27** (3), 241–251.

Larson, R. G., & Wei, Y. (2019). A review of thixotropy and its rheological modeling. *J. Rheol.*, **63** (3), 477–501.

Legnani, A., Santos, T. G. M., Andrade, D. E. V., & Negrão, C. O. R. (2020). Waxy oils: Deformation-dependent materials. *J. Non-Newton. Fluid Mech.*, **285**, 104378.

Lelieveld, H. L. M. (2014). *Hygiene in Food Processing*. (H. L. M. Lelieveld, M. A. Mostert, J. Holah, & B. White, Eds.)*Hygiene in Food Processing*, 1st edn, Cambridge: Elsevier. Retrieved from https://linkinghub.elsevier.com/retrieve/pii/C20130162526

Leonard, B. P. (1979). A stable and accurate convective modelling procedure based on quadratic upstream interpolation. *Comput. Methods Appl. Mech. Eng.*, **19** (1), 59–98.

Leonard, B. P. (1995). Order of accuracy of QUICK and related convection-diffusion schemes. *Appl. Math. Model.*, **19** (11), 640–653.

Lepore, E., Brianza, S., Antoniolli, F., Buono, M., Carpinteri, A., & Pugno, N. (2008). Preliminary In Vivo Experiments on Adhesion of Geckos. *J. Nanomater.*, **2008** (1), 1–5.

Lidon, P., Villa, L., & Manneville, S. (2017). Power-law creep and residual stresses in a carbopol gel. *Rheol. Acta*, **56** (3), 307–323.

Liu, H., Lu, Y., & Zhang, J. (2018a). A comprehensive investigation of the viscoelasticity and time-dependent yielding transition of waxy crude oils. *J. Rheol.*, **62** (2), 527–541.

Liu, H., Zhang, J., & Lu, Y. (2018b). Yielding characterization of waxy gels by energy dissipation. *Rheol. Acta*, **57** (6–7), 473–480.

Liu, W., Aziz, N. A., Zhang, Z., & Fryer, P. J. (2007). Quantification of the cleaning of egg albumin deposits using micromanipulation and direct observation techniques. *J. Food Eng.*, **78** (1), 217–224.

Liu, W., Christian, G. K., Zhang, Z., & Fryer, P. J. (2002). Development and use of a

micromanipulation technique for measuring the force required to disrupt and remove fouling deposits. *Food Bioprod. Process. Trans. Inst. Chem. Eng. Part C*, **80** (4), 286–291.

Liu, W., Christian, G. K., Zhang, Z., & Fryer, P. J. (2006a). Direct measurement of the force required to disrupt and remove fouling deposits of whey protein concentrate. *Int. Dairy J.*, **16** (2), 164–172.

Liu, W., Fryer, P. J., Zhang, Z., Zhao, Q., & Liu, Y. (2006b). Identification of cohesive and adhesive effects in the cleaning of food fouling deposits. *Innov. Food Sci. Emerg. Technol.*, **7** (4), 263–269.

Liu, W., Zhang, Z., & Fryer, P. J. (2006c). Identification and modelling of different removal modes in the cleaning of a model food deposit. *Chem. Eng. Sci.*, **61** (22), 7528–7534.

Lu, J., Corvalan, C. M., & Huang, J. (2020). Deformation and removal of viscous thin film by submerged jet impingement. *AIChE J.*, **66** (1). doi:10.1002/aic.16745

Ma, L., & Barbosa-Cánovas, G. V. (1995). Rheological characterization of mayonnaise. Part I: Slippage at different oil and xanthan gum concentrations. *J. Food Eng.*, **25** (3), 397–408.

Macosko, C. W. (1994). *Rheology: principles, measurements, and applications*, New York: Wiley - VCH.

Magens, O. M., Liu, Y., Hofmans, J. F. A., Nelissen, J. A., & Wilson, D. I. (2017). Adhesion and cleaning of foods with complex structure: Effect of oil content and fluoropolymer coating characteristics on the detachment of cake from baking surfaces. *J. Food Eng.*, **197**, 48–59.

Mahaut, F., Chateau, X., Coussot, P., & Ovarlez, G. (2008). Yield stress and elastic modulus of suspensions of noncolloidal particles in yield stress fluids. *J. Rheol.*, **52** (1), 287–313.

Maillard, M., Mézière, C., Moucheront, P., Courrier, C., & Coussot, P. (2016). Blade-coating of yield stress fluids. *J. Non-Newton. Fluid Mech.*, **237**, 16–25.

Malone, S., Roy, S., Eapen, L., Choan, E., MacRae, R., Perry, G., Bowen, J., Samant, R., Morgan, S., Craig, J., Malone, K., & Grimes, S. (2020). Prevalence of Surface

Contamination With SARS-CoV-2 in a Radiation Oncology Clinic. *J. Clin. Oncol.*, **38** (6), 593–601.

Marchesini, F. H. (2012). *Rheology of waxy crude oils*, Pontifícia Universidade Católica do Rio de Janeiro, Rio de Janeiro.

Marchesini, F. H., Naccache, M. F., Abdu, A., Alicke, A. A., Souza Mendes, P. R., & de Souza Mendes, P. R. (2015). Rheological characterization of yield-stress materials: Flow pattern and apparent wall slip. *Appl. Rheol.*, **25** (5). doi:10.3933/APPLRHEOL-25-53883

Marchesini, F. H., Oliveira, R. M., Althoff, H., & de Souza Mendes, P. R. (2019). Irreversible time-dependent rheological behavior of cement slurries: Constitutive model and experiments. *J. Rheol.*, **63** (2), 247–262.

Marinho, T. O., Barbato, C. N., Freitas, G. B., Duncke, A. C., De Oliveira, M. C. K., & Nele, M. (2018). Interaction Effects of Predominantly Linear and Branched Waxes on Yield Stress and Elastic Modulus of Waxy Oils. *Energy and Fuels*, **32** (8), 8057–8068.

Martinie, L., Buggisch, H., & Willenbacher, N. (2013). Apparent elongational yield stress of soft matter. *J. Rheol.*, **57** (2013), 627.

Mason, T. G., Bibette, J., & Weitz, D. A. (1996). Yielding and flow of monodisperse emulsions. *J. Colloid Interface Sci.*, **179** (2), 439–448.

McGuire, P. J. (1985). Nuclear reactor vessel decontamination systems, United State of America: United States Patent and Trademark Office.

Mendes, R., Vinay, G., Ovarlez, G., & Coussot, P. (2015). Modeling the rheological behavior of waxy crude oils as a function of flow and temperature history. *J. Rheol.*, **59** (3), 703–732.

Mewis, J., & Wagner, N. J. (2009). Thixotropy. *Adv. Colloid Interface Sci.*, **147**–**148**, 214–227.

Mickaily, E. S., & Middleman, S. (1993). Hydrodynamic cleaning of a viscous film from the inside of a long tube. *AIChE J.*, **39** (5), 885–893.

Micro-Epsilon. (2018). ConfocalDT Catalog, Ortenburg: Micro-Epsilon, p. 12.

Mohan, L., Bonnecaze, R. T., & Cloitre, M. (2013). Microscopic origin of internal stresses in jammed soft particle suspensions. *Phys. Rev. Lett.*, **111** (26), 1–5.

Møller, P. C. F., Fall, A., & Bonn, D. (2009a). Origin of apparent viscosity in yield stress fluids below yielding. *Europhysics Lett.*, **87** (3), 38004.

Møller, P. C. F., Fall, A., Chikkadi, V., Derks, D., & Bonn, D. (2009b). An attempt to categorize yield stress fluid behaviour. *Philos. Trans. A. Math. Phys. Eng. Sci.*, **367** (1909), 5139–5155.

Møller, P. C. F., Mewis, J., & Bonn, D. (2006). Yield stress and thixotropy: on the difficulty of measuring yield stresses in practice. *Soft Matter*, **2** (4), 274.

Møller, P. C. F., Rodts, S., Michels, M. a J., & Bonn, D. (2008). Shear banding and yield stress in soft glassy materials. *Phys. Rev. E*, **77** (4), 1–5.

Morison, K., & Thorpe, R. (2002). Liquid Distribution from Cleaning-in-Place Sprayballs. *Food Bioprod. Process.*, **80** (4), 270–275.

Morrison, F. A. (2001). *Understanding Rheology*, First, New York: Oxford University Press.

Motl, J. (2017). Rotate an image around a point, MATLAB Central File Exchange. Retrieved from https://uk.mathworks.com/matlabcentral/fileexchange/40469-rotate-an-image-around-a-point

Mujumdar, A., Beris, A. N., & Metzner, A. B. (2002). Transient phenomena in thixotropic systems. *J. Non-Newton. Fluid Mech.*, **102** (2), 157–178.

N'Gouamba, E., Goyon, J., & Coussot, P. (2019). Elastoplastic behavior of yield stress fluids. *Phys. Rev. Fluids*, **4** (12), 1–18.

Nakoryakov, V. E., Pokusaev, B. G., & Troyan, E. N. (1978). Impingement of an axisymmetric liquid jet on a barrier. *Int. J. Heat Mass Transf.*, **21** (9), 1175–1184.

NASA. (2015). Engineers clean mirror with carbon dioxide snow. Retrieved November 23, 2020, from <http://www.nasa.gov/image-feature/goddard/engineers-clean-mirror-with-carbon-dioxide-snow>

Nelson, A. Z., & Ewoldt, R. H. (2017). Design of yield-stress fluids: A rheology-to-structure inverse problem. *Soft Matter*, **13** (41), 7578–7594.

Nelson, A. Z., Schweizer, K. S., Rauzan, B. M., Nuzzo, R. G., Vermant, J., & Ewoldt, R. H. (2019). Designing and transforming yield-stress fluids. *Curr. Opin. Solid State Mater. Sci.*, **23** (5), 100758.

Nguyen, Q. D., & Boger, D. V. (1983). Yield stress measurement for concentrated suspensions. *J. Rheol.*, **27** (4), 321–349.

Nguyen, Q. D., & Boger, D. V. (1992). Measuring the flow properties of yield stress fluids. *Annu. Rev. Fluid Mech.*, **24** (1), 47–88.

Oevermann, D., Bhagat, R. K., Fernandes, R. R., & Wilson, D. I. (2019). Quantitative modelling of the erosive removal of a thin soil deposit by impinging liquid jets. *Wear*, **422**–**423**, 27–34.

Ogita, Y., Takahashi, Y., Iwata, M., Sasatsu, M., Onishi, H., Hashimoto, S., & Machida, Y. (2010). Comparison of physical properties and drug-releasing characteristics of white petrolatums. *Pharmazie*, **65** (11), 801–804.

Oldroyd, J. G. (1947). A rational formulation of the equations of plastic flow for a Bingham solid. *Math. Proc. Cambridge Philos. Soc.*, **43** (1), 100–105.

Olsson, R. G., & Turkdogan, E. T. (1966). Radial spread of a liquid stream on a horizontal plate. *Nature*, **211** (5051), 813–816.

Ong, S. W. X., Tan, Y. K., Chia, P. Y., Lee, T. H., Ng, O. T., Wong, M. S. Y., & Marimuthu, K. (2020). Air, Surface Environmental, and Personal Protective Equipment Contamination by Severe Acute Respiratory Syndrome Coronavirus 2 (SARS-CoV-2) from a Symptomatic Patient. *JAMA - J. Am. Med. Assoc.*, **323** (16), 1610–1612.

Ovarlez, G., Cohen-Addad, S., Krishan, K., Goyon, J., & Coussot, P. (2013). On the existence of a simple yield stress fluid behavior. *J. Non-Newton. Fluid Mech.*, **193**, 68–79.

Ovarlez, G., Mahaut, F., Deboeuf, S., Lenoir, N., Hormozi, S., & Chateau, X. (2015). Flows of suspensions of particles in yield stress fluids. *J. Rheol.*, **59** (6), 1449–1486.

Owens, C. E., Hart, A. J., & McKinley, G. H. (2020). Improved rheometry of yield stress fluids using bespoke fractal 3D printed vanes. *J. Rheol.*, **64** (3), 643–662.

Palabiyik, I., Lopez-Quiroga, E., Robbins, P. T., Goode, K. R., & Fryer, P. J. (2018). Removal of yield-stress fluids from pipework using water. *AIChE J.*, **64** (5), 1517–1527.

Palabiyik, I., Olunloyo, B., Fryer, P. J., & Robbins, P. T. (2014). Flow regimes in the emptying of pipes filled with a Herschel–Bulkley fluid. *Chem. Eng. Res. Des.*, **92** (11), 2201–2212.

Park, E.-K., & Song, K.-W. (2010a). Rheological evaluation of petroleum jelly as a base material in ointment and cream formulations: Steady shear flow behavior. *Arch. Pharm. Res.*, **33** (1), 141–150.

Park, E.-K., & Song, K.-W. (2010b). Rheological evaluation of petroleum jelly as a base material in ointment and cream formulations with respect to rubbing onto the human body. *Korea Aust. Rheol. J.*, **22** (4), 279–289.

Park, S.-Y., Kim, K.-H., Shin, S.-Y., Koo, K.-T., Lee, Y.-M., Chung, C.-P., & Seol, Y.-J. (2015). Decontamination Methods Using a Dental Water Jet and Dental Floss for Microthreaded Implant Fixtures in Regenerative Periimplantitis Treatment. *Implant Dent.*, **24** (3), 1.

Park, Y. S., & Liu, P. L. F. L.-F. L. F. (2010). Oscillatory pipe flows of a yield-stress fluid. *J. Fluid Mech.*, **658** (2010), 211–228.

Peralta, J. M., Meza, B. E., & Zorrilla, S. E. (2019). Draining of films on a quasivertical plate using viscous dissipation. *Phys. Fluids*, **31** (8), 083108.

Perge, C., Taberlet, N., Gibaud, T., & Manneville, S. (2014). Time dependence in large amplitude oscillatory shear: A rheo-ultrasonic study of fatigue dynamics in a colloidal gel. *J. Rheol.*, **58** (5), 1331–1357.

Petekidis, G., Vlassopoulos, D., & Pusey, P. N. (2003). Yielding and flow of colloidal glasses. *Faraday Discuss.*, **123** (1), 287–302.

Piau, J. M. (2007). Carbopol gels: Elastoviscoplastic and slippery glasses made of individual swollen sponges. Meso- and macroscopic properties, constitutive equations and scaling laws. *J. Non-Newton. Fluid Mech.*, **144** (1), 1–29.

Puisto, A., Mohtaschemi, M., Alava, M. J., & Illa, X. (2015). Dynamic hysteresis in the rheology of complex fluids. *Phys. Rev. E*, **91** (4), 042314.

Putz, A. M. V, & Burghelea, T. I. (2009). The solid-fluid transition in a yield stress shear thinning physical gel. *Rheol. Acta*, **48** (6), 673–689.

Rabideau, B. D., Lanos, C., & Coussot, P. (2009). An investigation of squeeze flow as a viable technique for determining the yield stress. *Rheol. Acta*, **48** (5), 517–526.

Ranz, W. E. (1956). *On sprays and spraying*, Pensylvannia State University.

Rao, V. N. M., Hamann, D. D., & Humphries, E. G. (1975). FLOW BEHAVIOR OF SWEET POTATO PUREE AND ITS RELATION TO MOUTHFEEL QUALITY. *J. Texture Stud.*, **6** (2), 197–209.

Rayleigh, Lord. (1914). On the theory of long waves and bores. *Proc. R. Soc. London. Ser. A, Contain. Pap. a Math. Phys. Character*, **90** (619), 324–328.

Renou, F., Stellbrink, J., & Petekidis, G. (2010). Yielding processes in a colloidal glass of soft star-like micelles under large amplitude oscillatory shear (LAOS). *J. Rheol.*, **54** (6), 1219.

Richefeu, V., El Youssoufi, M. S., & Radjaï, F. (2006). Shear strength properties of wet granular materials. *Phys. Rev. E - Stat. Nonlinear, Soft Matter Phys.*, **73** (5), 1–11.

Rodgers, A., de Boer, G., Murray, B., Scott, G., & Kapur, N. (2019). An investigation in to batch cleaning using wash racks. *Food Bioprod. Process.*, **113**, 118–128.

Rouyer, F., Cohen-Addad, S., & Höhler, R. (2005). Is the yield stress of aqueous foam a well-defined quantity? *Colloids Surfaces A Physicochem. Eng. Asp.*, **263** (1-3 SPEC. ISS.), 111–116.

Saikhwan, P., Mercadé-Prieto, R., Chew, Y. M. J., Gunasekaran, S., Paterson, W. R., & Wilson, D. I. (2010). Swelling and dissolution in cleaning of whey protein gels. *Food Bioprod. Process.*, **88** (4), 375–383.

Santarpia, J. L., Rivera, D. N., Herrera, V. L., Morwitzer, M. J., Creager, H. M., Santarpia, G. W., Crown, K. K., Brett-Major, D. M., Schnaubelt, E. R., Broadhurst, M. J., Lawler, J.

V., Reid, S. P., & Lowe, J. J. (2020). Aerosol and surface contamination of SARS-CoV-2 observed in quarantine and isolation care. *Sci. Rep.*, **10** (1), 1–8.

Saramito, P. (2007). A new constitutive equation for elastoviscoplastic fluid flows. *J. Non-Newton. Fluid Mech.*, **145** (1), 1–14.

Saramito, P. (2009). A new elastoviscoplastic model based on the Herschel-Bulkley viscoplastic model. *J. Non-Newton. Fluid Mech.*, **158** (1–3), 154–161.

Schurz, J. (1990). The yield stress - An empirical reality. *Rheol. Acta*, **29** (2), 170–171.

Semenov, Y. A., & Wu, G. X. (2016). Cratering of a solid body due to liquid impact. *J. Eng. Math.*, **101** (1), 71–85.

Shaw, M. C. (2005). *Metal cutting principles*, 2 Edn, Oxford: Oxford University Press.

SMCjet. (2020). Ship Maintenance Industries. Retrieved November 23, 2020, from <https://www.smcjet.com/2017/05/28/ship-maintenance-industries/>

Smith, E. R., Theodorakis, P. E., Craster, R. V., & Matar, O. K. (2018). Moving Contact Lines: Linking Molecular Dynamics and Continuum-Scale Modeling. *Langmuir*, **34** (42), 12501–12518, review-article.

Souza Mendes, P. R. (2009). Modeling the thixotropic behavior of structured fluids. *J. Non-Newton. Fluid Mech.*, **164** (1–3), 66–75.

Souza Mendes, P. R. (2011). Thixotropic elasto-viscoplastic model for structured fluids. *Soft Matter*, **7** (6), 2471.

Souza Mendes, P. R., & Thompson, R. L. (2013). A unified approach to model elasto-viscoplastic thixotropic yield-stress materials and apparent yield-stress fluids. *Rheol. Acta*, **52** (7), 673–694.

Souza Mendes, P. R., Thompson, R. L., Alicke, A. a., & Leite, R. T. (2014). The quasilinear large-amplitude viscoelastic regime and its significance in the rheological characterization of soft matter. *J. Rheol.*, **58** (2), 537–561.

Stafussa, A. P., Rampazzo, V., Fernandes, R. R., Franco, A. T., Bona, E., Maciel, G. M., & Haminiuk, C. W. I. (2019). Multi-block analysis for the correlation of physico-chemical

and rheological data of 42 fruit pulps. *J. Texture Stud.*, **50** (2), 114–123.

Sterling, A. M., & Sleicher, C. A. (1975). The instability of capillary jets. *J. Fluid Mech.*, **68** (3), 477–495.

Stickel, J. J., Knutsen, J. S., & Liberatore, M. W. (2013). Response of elastoviscoplastic materials to large amplitude oscillatory shear flow in the parallel-plate and cylindrical-Couette geometries. *J. Rheol.*, **57** (6), 1569.

Stokes, J. R., & Telford, J. H. (2004). Measuring the yield behaviour of structured fluids. *J. Non-Newton. Fluid Mech.*, **124** (1–3), 137–146.

Stortz, T. A., & Marangoni, A. G. (2014). The replacement for petrolatum: thixotropic ethylcellulose oleogels in triglyceride oils. *Green Chem.*, **16** (6), 3064–3070.

Tabi, I. (1949). Water jump in the boundary layer. *J. Phys. Soc. Japan*, **4**, 212–215.

Tabilo-Munizaga, G., & Barbosa-Cánovas, G. V. (2005). Rheology for the food industry. *J. Food Eng.*, **67** (1–2), 147–156.

Tarcha, B. A., Forte, B. P. P., Soares, E. J., & Thompson, R. L. (2015). Critical quantities on the yielding process of waxy crude oils. *Rheol. Acta*, **54** (6), 479–499.

Thomas, S. K., Cassoni, R. P., & MacArthur, C. D. (1996). Aircraft anti-icing and de-icing techniques and modeling. *J. Aircr.*, **33** (5), 841–854.

Thompson, R. L. (2020). The eagle and the rat: Non–equilibrium dynamics in time-dependent materials. *J. Non-Newton. Fluid Mech.*, **281**, 104313.

Thompson, R. L., Sica, L. U. R., & de Souza Mendes, P. R. (2018). The yield stress tensor. *J. Non-Newton. Fluid Mech.*, **261** (April), 211–219.

Tiu, C., & Boger, D. V. (1974). Complete rheological characterization of time-dependent food products. *J. Texture Stud.*, **5** (3), 329–338.

Todkari, V. C., & Kate, R. P. (2019). Numerical and experimental investigations on a circular hydraulic jump due to normal impinging free liquid jet on a flat horizontal target plate. *Fluid Dyn. Res.*, **51** (2), 025508.

Trinh, L., Willey, A. R., Martin, P. J., Ashley, J., Tothill, I. E., & Rodgers, T. L. (2017). Rate-Based Approach to Cleaning-in-Place. *Ind. Eng. Chem. Res.*, **56** (23), 6695–6702.

Tsai, J.-H. (2021). *Measurement and modelling of soft solid layers in cleaning applications*, PhD thesis, University of Cambridge.

Tsai, J. H., Cuckston, G. L., Hallmark, B., & Wilson, D. I. (2019). Fluid-dynamic gauging for studying the initial swelling of soft solid layers. *AIChE J.*, **65** (9), 1–13.

Tsai, J. H., Fernandes, R. R., & Wilson, D. I. (2020). Measurements and modelling of the 'millimanipulation' device to study the removal of soft solid layers from solid substrates. *J. Food Eng.*, **285**, 110086.

Tuck, J. P., Alberini, F., Ward, D., Gore, B., & Fryer, P. J. (2020). Cleaning of thick viscoplastic surface deposits using an impinging jet: Effect of process variables. *J. Food Eng.*, **266**, 109699.

Tuladhar, T. R., Paterson, W. R., Macleod, N., & Wilson, D. I. (2000). Development of a novel non-contact proximity gauge for thickness measurement of soft deposits and its application in fouling studies. *Can. J. Chem. Eng.*, **78** (5), 935–947.

Uhlherr, P. H. T., Guo, J., Tiu, C., Zhang, X. M., Zhou, J. Z. Q., & Fang, T. N. (2005). The shear-induced solid-liquid transition in yield stress materials with chemically different structures. *J. Non-Newton. Fluid Mech.*, **125** (2–3), 101–119.

Uth, T., & Deshpande, V. S. (2013). Unsteady penetration of a target by a liquid jet. *Proc. Natl. Acad. Sci.*, **110** (50), 20028–20033.

Valette, R., Hachem, E., Khalloufi, M., Pereira, A. S., Mackley, M. R., & Butler, S. A. (2019). The effect of viscosity, yield stress, and surface tension on the deformation and breakup profiles of fluid filaments stretched at very high velocities. *J. Non-Newton. Fluid Mech.*, **263**, 130–139.

Van Asselt, A. J., Van Houwelingen, G., & Te Giffel, M. C. (2002). Monitoring System for Improving Cleaning Efficiency of Cleaning-in-Place Processes in Dairy Environments. *Food Bioprod. Process.*, **80** (4), 276–280.

Visintin, R. F. G., Lapasin, R., Vignati, E., D'Antona, P., & Lockhart, T. P. (2005).

Rheological behavior and structural interpretation of waxy crude oil gels. *Langmuir*, **21** (14), 6240–6249.

Walder, D. N., Weaver, J. P. A., & Evans, A. (1969). An apparatus to detect a yield stress in blood. *Biorheology*, **6** (1), 23–32.

Walker, T. W., Hsu, T. T., Frank, C. W., & Fuller, G. G. (2012). Role of shear-thinning on the dynamics of rinsing flow by an impinging jet. *Phys. Fluids*, **24** (9), 093102.

Wang, T., Davidson, J. F., & Wilson, D. I. (2013a). Effect of surfactant on flow patterns and draining films created by a static horizontal liquid jet impinging on a vertical surface at low flow rates. *Chem. Eng. Sci.*, **88**, 79–94.

Wang, T., Davidson, J. F., & Wilson, D. I. (2015). Flow patterns and cleaning behaviour of horizontal liquid jets impinging on angled walls. *Food Bioprod. Process.*, **93**, 333–342.

Wang, T., Faria, D., Stevens, L. J., Tan, J. S. C., Davidson, J. F., & Wilson, D. I. (2013b). Flow patterns and draining films created by horizontal and inclined coherent water jets impinging on vertical walls. *Chem. Eng. Sci.*, **102**, 585–601.

Wang, Y., & Khayat, R. E. (2019). The role of gravity in the prediction of the circular hydraulic jump radius for high-viscosity liquids. *J. Fluid Mech.*, **862**, 128–161.

Ward, R. K. (2014). *Handbook of Food Allergen Detection and Control*. (S. Flanagan, Ed.)*Woodhead Publishing Series in Food Science, Technology and Nutrition*, 1st edn, Cambridge. doi:10.1016/0167-5699(87)90020-x

Wardhaugh, L. T., & Boger, D. V. (1991). The measurement and description of the yielding behavior of waxy crude oil. *J. Rheol.*, **35** (6), 1121–1156.

Watson, E. J. (1964). The radial spread of a liquid jet over a horizontal plane. *J. Fluid Mech.*, **20**, 481.

White, F. M. (1999). *Fluid mechanics*, 4th ed, London: McGraw-Hill.

Wildfowl & Wetlands Trust. (2019). *PR19 Challenge Report #5*, London. Retrieved from <https://s3-eu-west-1.amazonaws.com/mollyhandley/WWT/Challenge+reports+/wwt-pr19+report+5-3.pdf>

Willenbacher, N. (1996). Unusual thixotropic properties of aqueous dispersions of Laponite RD. *J. Colloid Interface Sci.*, **182** (2), 501–510.

Wilson, D. I. (2005). Challenges in Cleaning: Recent Developments and Future Prospects. *Heat Transf. Eng.*, **26** (1), 51–59.

Wilson, D. I., Atkinson, P., Köhler, H., Mauermann, M., Stoye, H., Suddaby, K., Wang, T., Davidson, J. F., & Majschak, J. (2014). Cleaning of soft-solid soil layers on vertical and horizontal surfaces by stationary coherent impinging liquid jets. *Chem. Eng. Sci.*, **109**, 183–196.

Wilson, D. I., Köhler, H., Cai, L., Majschak, J.-P., & Davidson, J. F. (2015). Cleaning of a model food soil from horizontal plates by a moving vertical water jet. *Chem. Eng. Sci.*, **123**, 450–459.

Wilson, D. I., Le, B. L., Dao, H. D. A., Lai, K. Y., Morison, K. R., & Davidson, J. F. (2012). Surface flow and drainage films created by horizontal impinging liquid jets. *Chem. Eng. Sci.*, **68** (1), 449–460.

Yan, J.-F. F., Sáez, A. E., & Grant, C. S. (1997). Removal of oil films from stainless steel tubes. *AIChE J.*, **43** (1), 251–259.

Yang, J., Bhagat, R. K., Fernandes, R. R., Nordkvist, M., Gernaey, K. V., Krühne, U., & Wilson, D. I. (2019a). Cleaning of toothpaste from vessel walls by impinging liquid jets and their falling films: Quantitative modelling of soaking effects. *Chem. Eng. Sci.*, **208** (8), 115148.

Yang, J., Kjellberg, K., Jensen, B. B. B., Nordkvist, M., Gernaey, K. V., & Krühne, U. (2019b). Investigation of the cleaning of egg yolk deposits from tank surfaces using continuous and pulsed flows. *Food Bioprod. Process.*, **113**, 154–167.

Yang, Q., Ali, A., Shi, L., & Wilson, D. I. (2014). Zero discharge fluid dynamic gauging for studying the thickness of soft solid layers. *J. Food Eng.*, **127**, 24–33.

Yeckel, A., & Middleman, S. (1987). Removal of a viscous film from a rigid plane surface by an impinging liquid jet. *Chem. Eng. Commun.*, **50** (1–6), 165–175.

Yeckel, A., Middleman, S., & Klumb, L. A. (1990). The removal of thin liquid films from

periodically grooved surfaces by an impining jet. *Chem. Eng. Commun.*, **96** (1), 69–79.

Yeckel, A., Strong, L., & Middleman, S. (1994). Viscous film flow in the stagnation region of the jet impinging on planar surface. *AIChE J.*, **40** (10), 1611–1617.

Yoshimura, A., & Prud'homme, R. K. (1988). Wall Slip Corrections for Couette and Parallel Disk Viscometers. *J. Rheol.*, **32** (1), 53–67.

Zhang, Z., Ferenczi, M. A., Lush, A. C., & Thomas, C. R. (1991). A novel micromanipulation technique for measuring the bursting strength of single mammalian cells. *Appl. Microbiol. Biotechnol.*, **36** (2), 208–210.

Appendix A – Rheological characterisation of commercial fast-moving consumer goods

The millimanipulation device was used to estimate the yield stress of different fast-moving consumer goods in Section 4.2. The estimates of the yield stress obtained with the MM3 device were compared to measurements performed in the Kinexus stress-controlled rotational rheometer. This appendix presents the data for the rheological characterisation of the materials listed in Table 4.2. Results are provided for increasing shear stress ramps and steps in Figures A.1 to A.14 (a), and for oscillatory shear stress amplitude sweeps in Figures A.1 to A.14 (b). The experimental set-up follows the same protocols defined in Section 4.2: shear stress ramps were performed with a constant rate of increase of the shear stress, $\dot{\tau}$ =50 Pa·min^{-1}, whereas shear stress steps were conducted by applying a constant shear stress over 30 s in each step. The oscillatory measurements were conducted at the frequency $\omega = 1$ Hz. All experiments were performed with serrated parallel plates to avoid wall slip effects, at 20 °C. In the insets of (a), dark diamonds indicate the values of τ_y^{e1} calculated using Eq. (4.2) at the characteristic shear rate $\dot{\gamma}_{ch} = V/s$ for the millimanipulation experiments, whereas shaded region indicate the range of values of τ_y^{e3} calculated with Eq. (4.4).

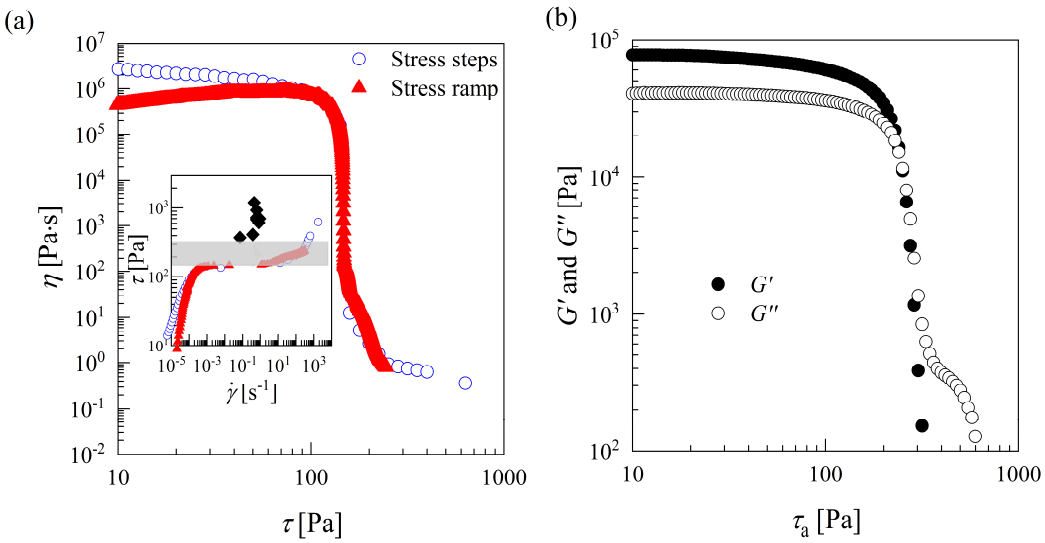

Figure A.1 - PJA. (a) Apparent viscosity as a function of the imposed shear stress, for stress steps and stress ramp; (b) G′ and G″ as a function of the stress amplitude for the oscillatory shear stress amplitude sweep.

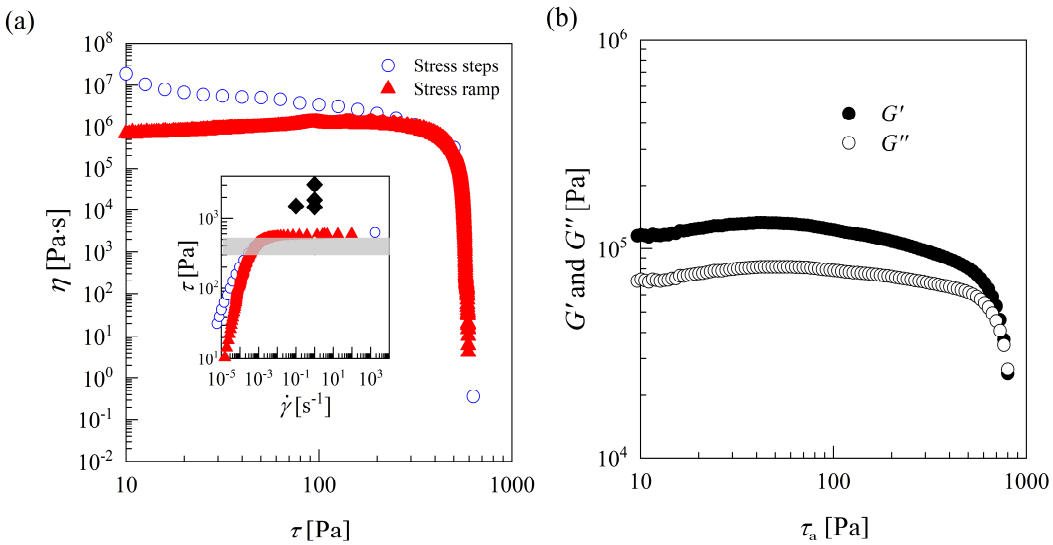

Figure A.2 - PJS. (a) Apparent viscosity as a function of the imposed shear stress, for stress steps and stress ramp; (b) G' and G'' as a function of the stress amplitude for the oscillatory shear stress amplitude sweep.

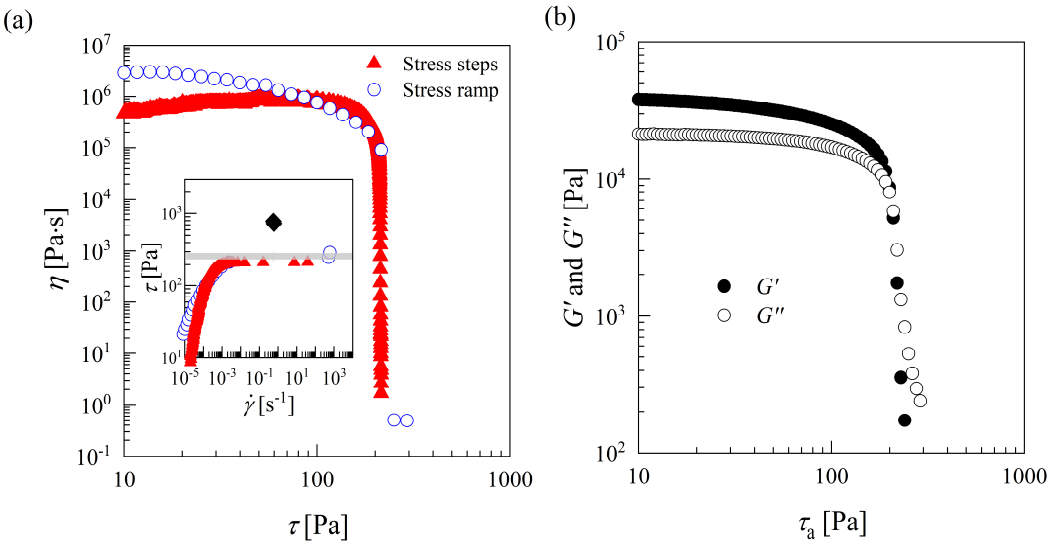

Figure A.3 - PJT. (a) Apparent viscosity as a function of the imposed shear stress, for stress steps and stress ramp; (b) G' and G'' as a function of the stress amplitude for the oscillatory shear stress amplitude sweep.

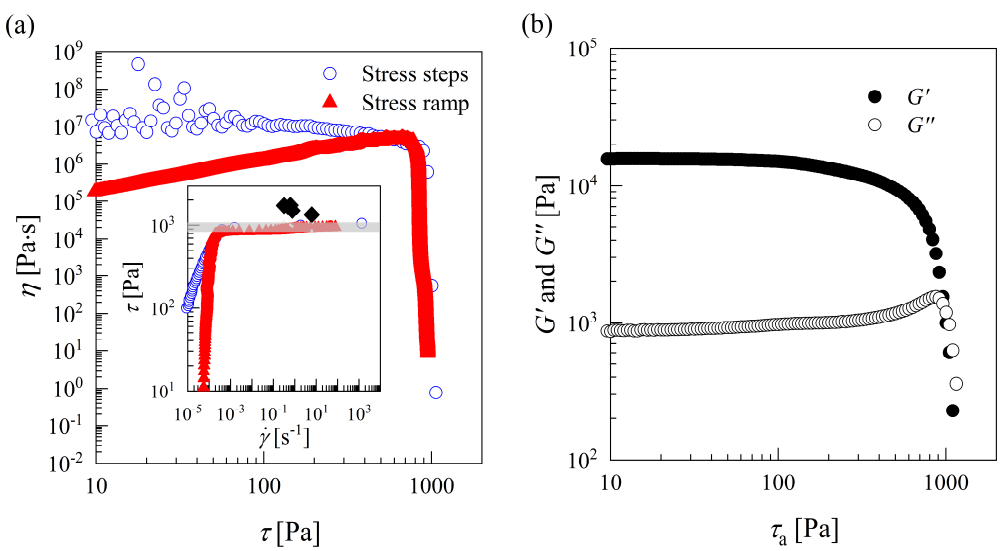

Figure A.4 - Nivea hand cream. (a) Apparent viscosity as a function of the imposed shear stress, for stress steps and stress ramp; (b) G' and G'' as a function of the stress amplitude for the oscillatory shear stress amplitude sweep.

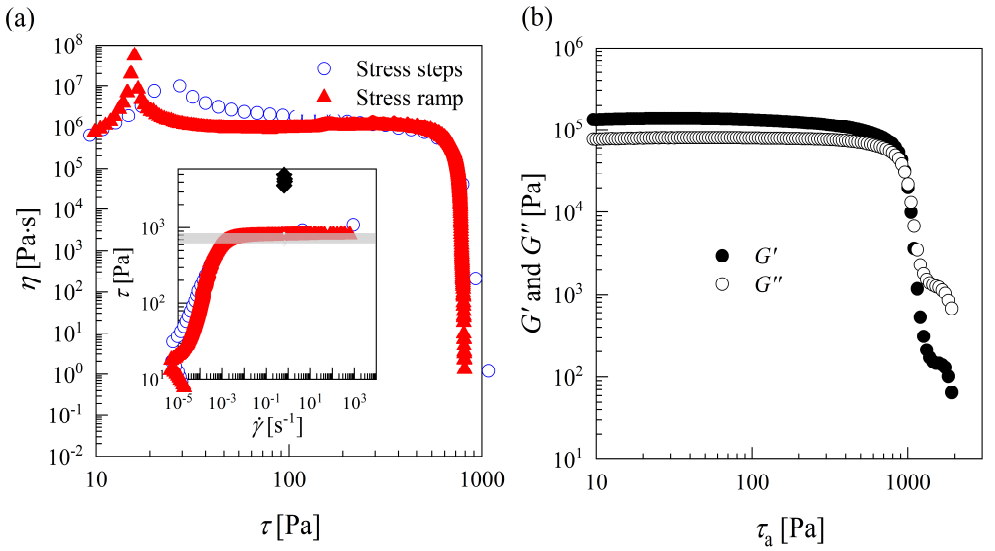

Figure A.5 - Hair wax: (a) Apparent viscosity as a function of the imposed shear stress, for stress steps and stress ramp; (b) G' and G'' as a function of the stress amplitude for the oscillatory shear stress amplitude sweep.

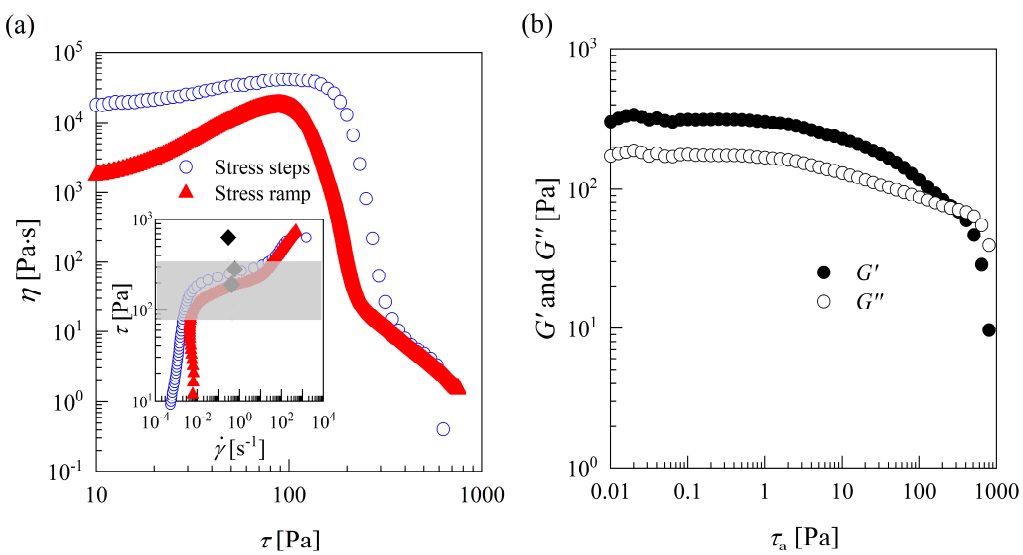

Figure A.6 - Colgate toothpaste. (a) Apparent viscosity as a function of the imposed shear stress, for stress steps and stress ramp; (b) G' and G'' as a function of the stress amplitude for the oscillatory shear stress amplitude sweep.

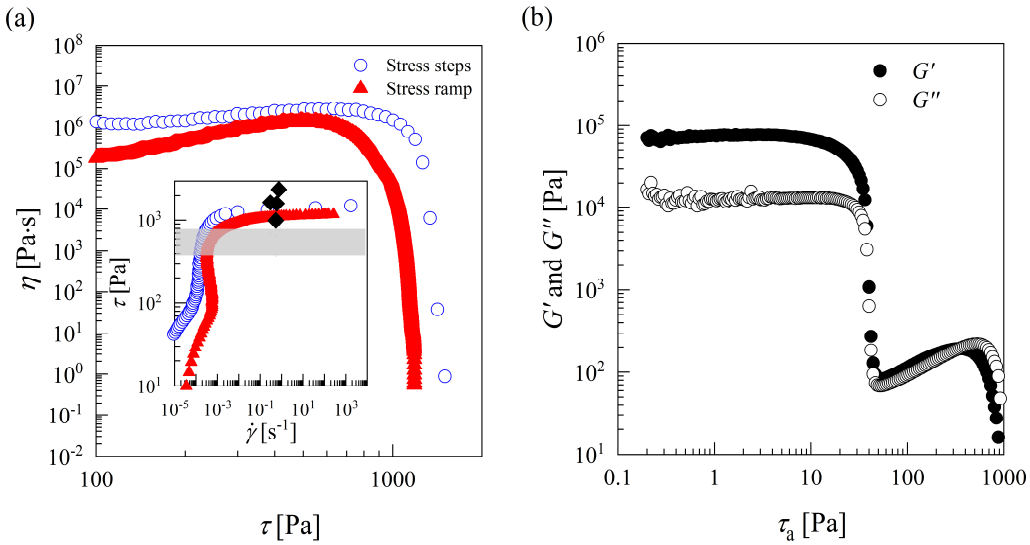

Figure A.7 - Peanut butter. (a) Apparent viscosity as a function of the imposed shear stress, for stress steps and stress ramp; (b) G' and G'' as a function of the stress amplitude for the oscillatory shear stress amplitude sweep.

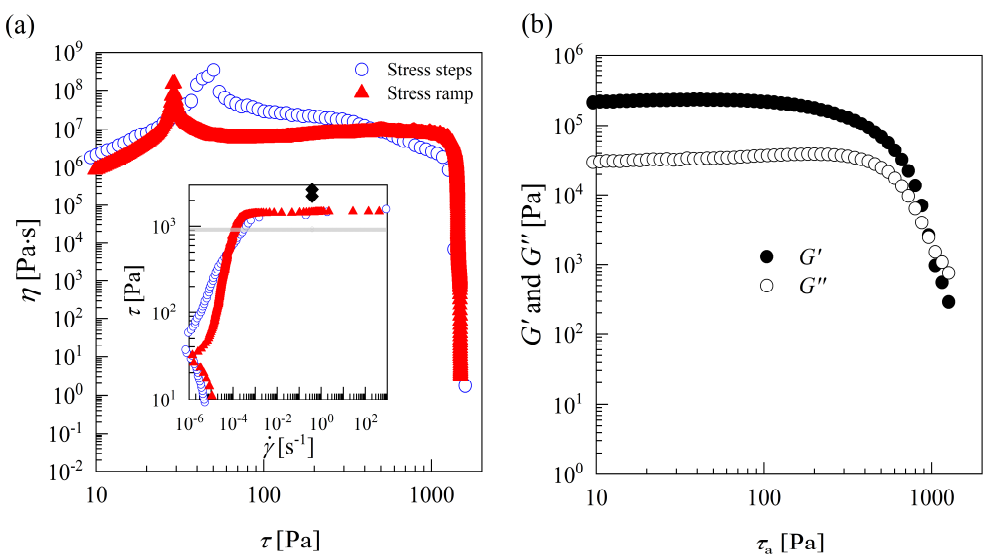

Figure A.8 - Butter. (a) Apparent viscosity as a function of the imposed shear stress, for stress steps and stress ramp; (b) G' and G'' as a function of the stress amplitude for the oscillatory shear stress amplitude sweep.

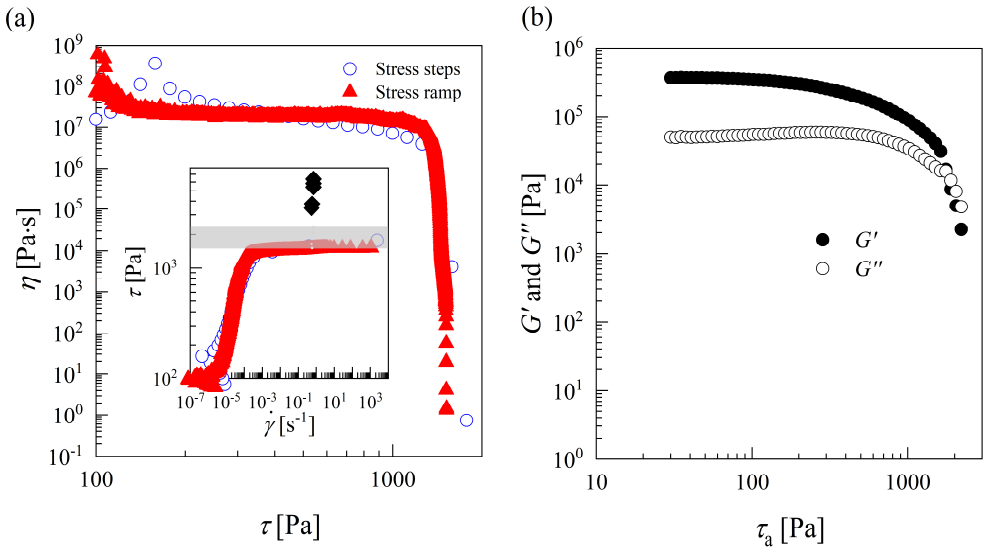

Figure A.9 - Lard. (a) Apparent viscosity as a function of the imposed shear stress, for stress steps and stress ramp; (b) G' and G'' as a function of the stress amplitude for the oscillatory shear stress amplitude sweep.

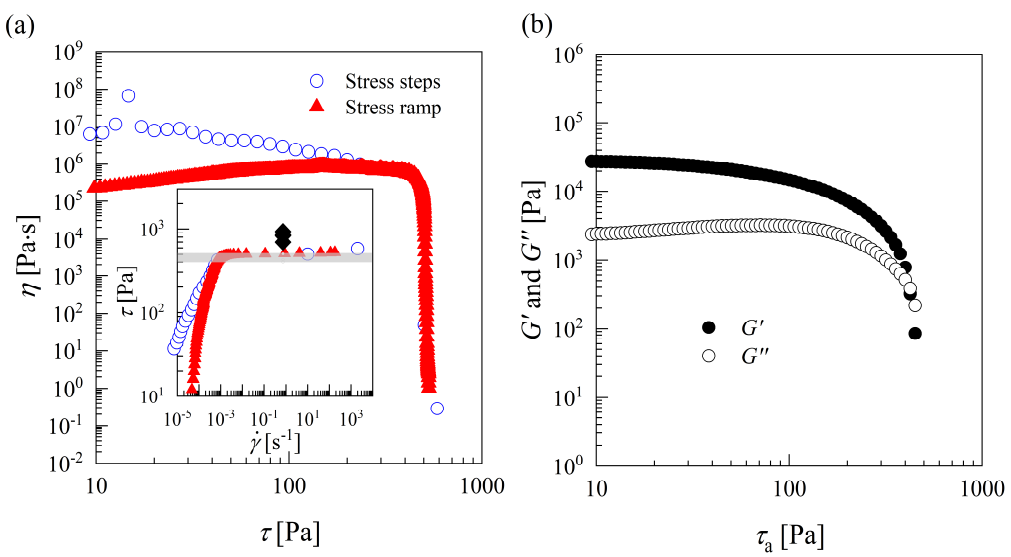

Figure A.10 - Margarine: (a) Apparent viscosity as a function of the imposed shear stress, for stress steps and stress ramp; (b) G' and G'' as a function of the stress amplitude for the oscillatory shear stress amplitude sweep.

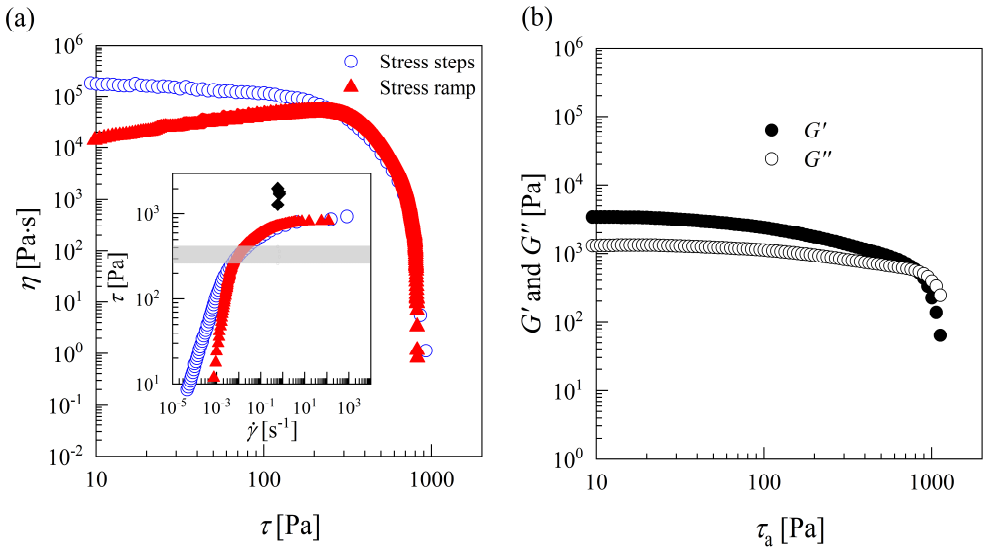

Figure A.11 - Cheese spread. (a) Apparent viscosity as a function of the imposed shear stress, for stress steps and stress ramp; (b) G' and G'' as a function of the stress amplitude for the oscillatory shear stress amplitude sweep.

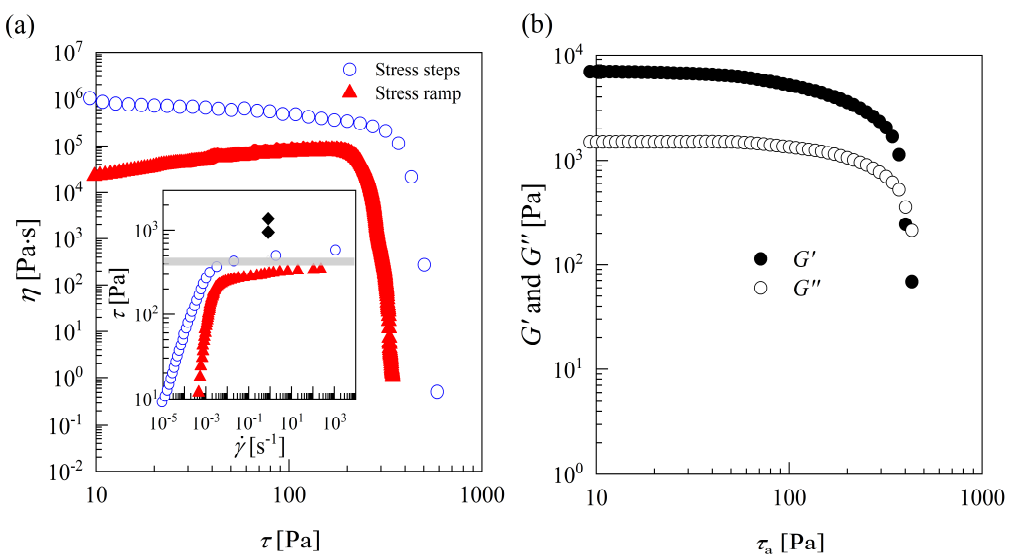

Figure A.12 - Cream cheese. (a) Apparent viscosity as a function of the imposed shear stress, for stress steps and stress ramp; (b) G' and G'' as a function of the stress amplitude for the oscillatory shear stress amplitude sweep.

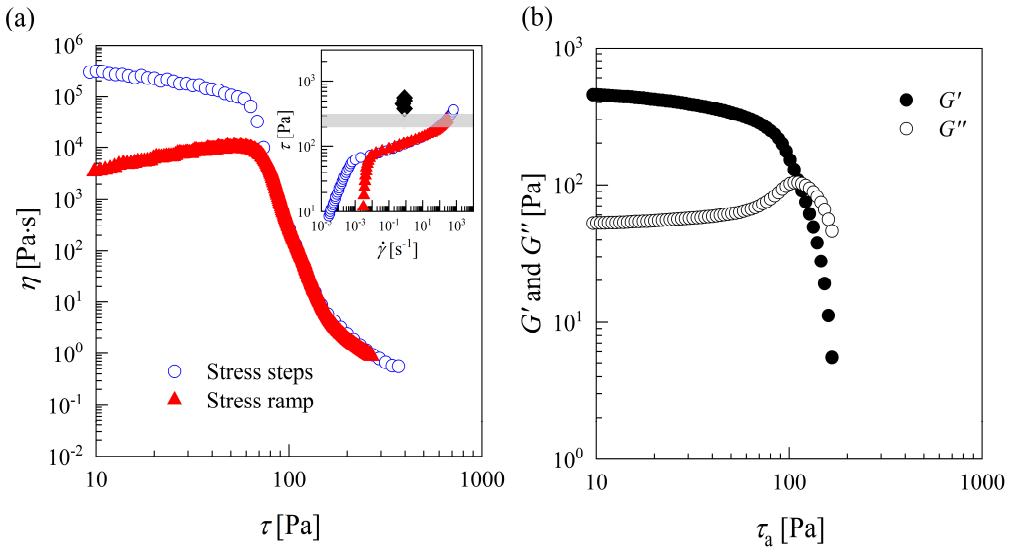

Figure A.13 - Mayonnaise. (a) Apparent viscosity as a function of the imposed shear stress, for stress steps and stress ramp; (b) G' and G'' as a function of the stress amplitude for the oscillatory shear stress amplitude sweep.

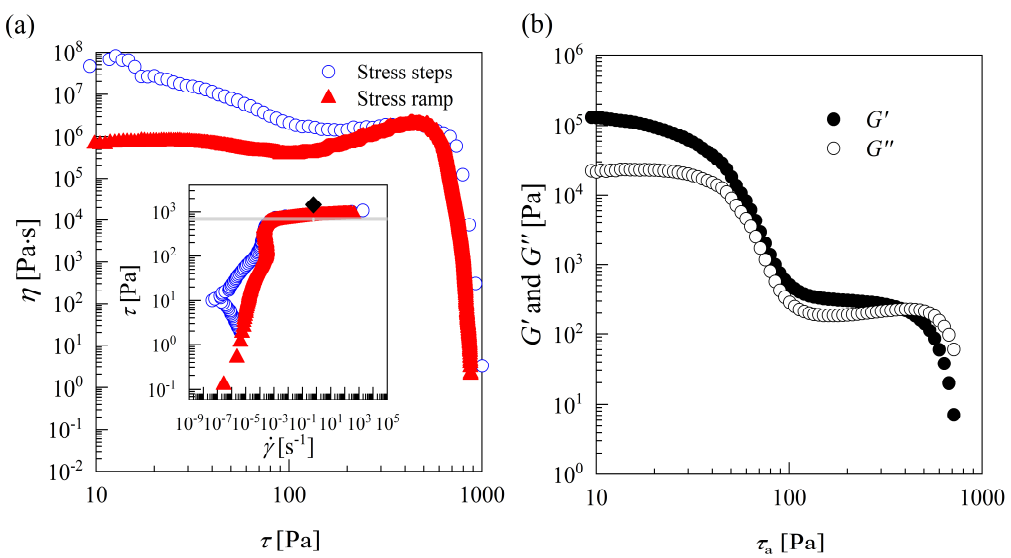

Figure A.14 - Biscoff spread. (a) Apparent viscosity as a function of the imposed shear stress, for stress steps and stress ramp; (b) G' and G'' as a function of the stress amplitude for the oscillatory shear stress amplitude sweep.